Petrogenetic Evolution, Geometries and Intrusive Styles of the Early Cenozoic Saucer-Shaped Sills of the Faroe Islands

HANSEN, JOGVAN

Petrogenetic Evolution, Geometries and Intrusive Styles of the Early Cenozoic Saucer-Shaped Sills of the Faroe Islands

Jógvan Hansen

Petrogenetic Evolution, Geometries and Intrusive Styles of the Early Cenozoic Saucer-Shaped Sills of the Faroe Islands

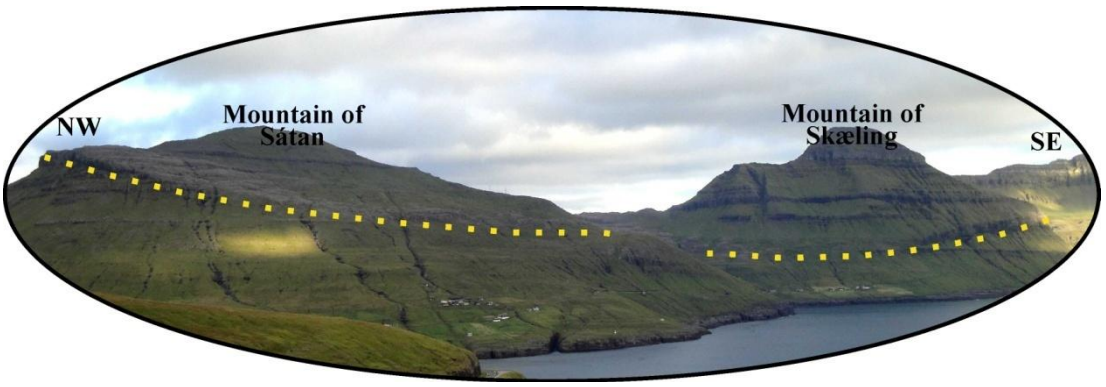

Jógvan Hansen

A thesis submitted for the degree of Doctor of Philosophy

Durham University

Department of Earth Sciences

2011

Acknowledgements

This thesis would not have come into being without the encouragement, good ideas and help from a number of people and establishments.

First of all I would like to thank my supervisors Dr. Dougal A. Jerram and Dr. Simon R. Passey for outlining the project in the first place and for the raising of necessary funding. Also, prompt and thorough reviews by supervisors Dr. Dougal A. Jerram, Dr. Ken J. W. McCaffrey and Dr. Simon R. Passey, on manuscripts intended to build up thesis chapters as well as papers to be submitted for publication, improved their contents substantially.

The professional and kind guidance from Dr. Mike Widdowson and John Watson during my stay at the Open University in Milton Keynes, in connection with whole-rock geochemical analyses of all collected rock samples, made this part of the project particularly pleasant.

Skilful handling and advanced techniques during analyses of selected rock samples by professional staff at Durham University have resulted in the most satisfactory and interesting results.

Richard Walker and Catherine Nelson are acknowledged for helpful assistance in the use of basic ArcGIS functions and for the provision of written material useful in structuring the process of thesis writing respectively.

I am indebted to my family back in the Faroe Islands, as their help with accommodation etc. were critical factors that eventually led to a successful completion of the ever important fieldwork done in the Faroe Islands.

A thorough review on geochemistry and isotope geology chapters by professor Jon Davidson, who stepped in during a critical phase of thesis production due to unforeseen circumstances, improved the thesis substantially and is gratefully acknowledged. Likewise, director of postgraduate studies Dr. Jonathan Imber is thanked for all sorts of support, particularly during the final phases of thesis production.

Last but not least, funding from BP, Chevron and Geysir Petroleum, through Jarðfeingi (Faroese Earth and Energy Directorate) under the Faroese Competence Uplift Scheme, made this project possible and is greatly appreciated.

Abstract

Geometries of sills intruded into the lava pile of the Faroe Island Basalt Group (FIBG), which were targeted in this study, were mostly recorded by conventional mapping methods where measured distances and positions were plotted onto accurate topographic maps aided by the use of high-quality photos of relevant outcrops. These data were subsequently used to manually plot 2D profiles along selected tracks and to produce electronic 3D maps using ArcGIS software.

The general geometries of the investigated sills, measured at lateral scales ranging from a few metres to a few kilometres and at vertical scales ranging from a few metres to a few hundred metres, differ somewhat from typical sill geometries reported previously for sills intruded into sedimentary successions. The ubiquitous saucer-shapes of the sills from this study, which generally curve upwards in a gradual manner from inner sub-horizontal sections to steeper outer margins, contrast with the common angular transitions from inner sub-horizontal to outer steeper sections of sills reported from sedimentary host-rocks. In this thesis we explore possible alternatives to already existing theories on sill emplacement in sedimentary successions.

Major and trace element compositions for samples representing most of the sills exposed in the Faroe Islands have been determined by means of XRF and ICP-MS analyses. Geochemically most of these sills can be grouped into two main categories characterised either by high or by low TiO_2 contents. Different sorts/types of metasomatism of source rocks to high-TiO_2 versus low-TiO_2 sills are indicated by different Nb and Ta anomalies. Modelling by means of REE and other trace elements suggest that much of the compositional differences between these two main categories can be explained by various degrees of partial melting of broadly similar mantle sources. Additional fractionation and accumulation of plagioclase modified some of the melts that gave rise to the actual sills. The initial partial melting event probably occurred at depths slightly shallower than the lower limit of the garnet stability field at ~85 km while plagioclase crystallisation/accumulation most likely occurred at depths shallower than ~18 km. Isotopic compositions may point to very slight contamination of some sills with crustal material.

Contents

mm

Appendices

1. Transfer of field data to 3D electronic maps (ArcGIS software)
2. XRF analysis methodology
3. ICP-MS analysis methodology
4. MC-ICP-MS analysis methodology

Subsidiary matter in support of candidate

1. Geological Magazine: paper
2. Journal of the Geological Society, London: paper

List of figures

List of tables

Chapter One

1. Introduction

1.1. Prelude to chapter one

Sills have been reported from a wide variety of geological settings with or without previous histories of surface basaltic magmatism. In theory, sills can form at any location experiencing igneous activity as long as certain physical criteria within the affected crust are fulfilled. This thesis endeavours to clarify which processes and physical actions governed intrusion styles and geometries of the saucer-shaped sills of the Faroe Islands, and to comprehensively interpret/detect which igneous processes prevailed from initial melt generation at depth to ultimate magma solidification in the fully inflated sills, i.e. an investigation of the entire plumbing system at all levels. In order to achieve these goals a twofold approach is employed; i) sill geometries and field occurrences/measurements are utilised to interpret/detect relevant emplacement processes, and ii) geochemical compositions, aided by isotope characteristics, are used to track the actions of igneous processes at depth.

This chapter contains a brief outline of sill occurrences and some common emplacement theories (1.2), as well as an evaluation of the processes used to obtain the relevant data on sill geometries and field evidences in general (1.3). In sub-section 1.4 the physical conditions necessary to produce basaltic melts are briefly discussed and appropriate methods of obtaining and interpret geochemical data are looked at in 1.5.

1.2. Occurrences of sheet intrusions

Dykes are generally thought of as sub-vertical tabular bodies cutting bedding planes at right angles, and they may occur over lengths ranging from a few metres to hundreds of kilometres (Hall, 1996; Gudmundsson and Marinoni, 1999). They may display thickness variations ranging from a few centimetres to more than 100 m, although thicknesses of a few tens of centimetres to a few metres are most common (Hall, 1996). Sills can range in size from <1 m thick small sheets to several hundred metres thick major intrusions underlying hundreds of square kilometres and they may occur as sub-horizontal concordant sheets or as partly discordant bodies (Hall, 1996).

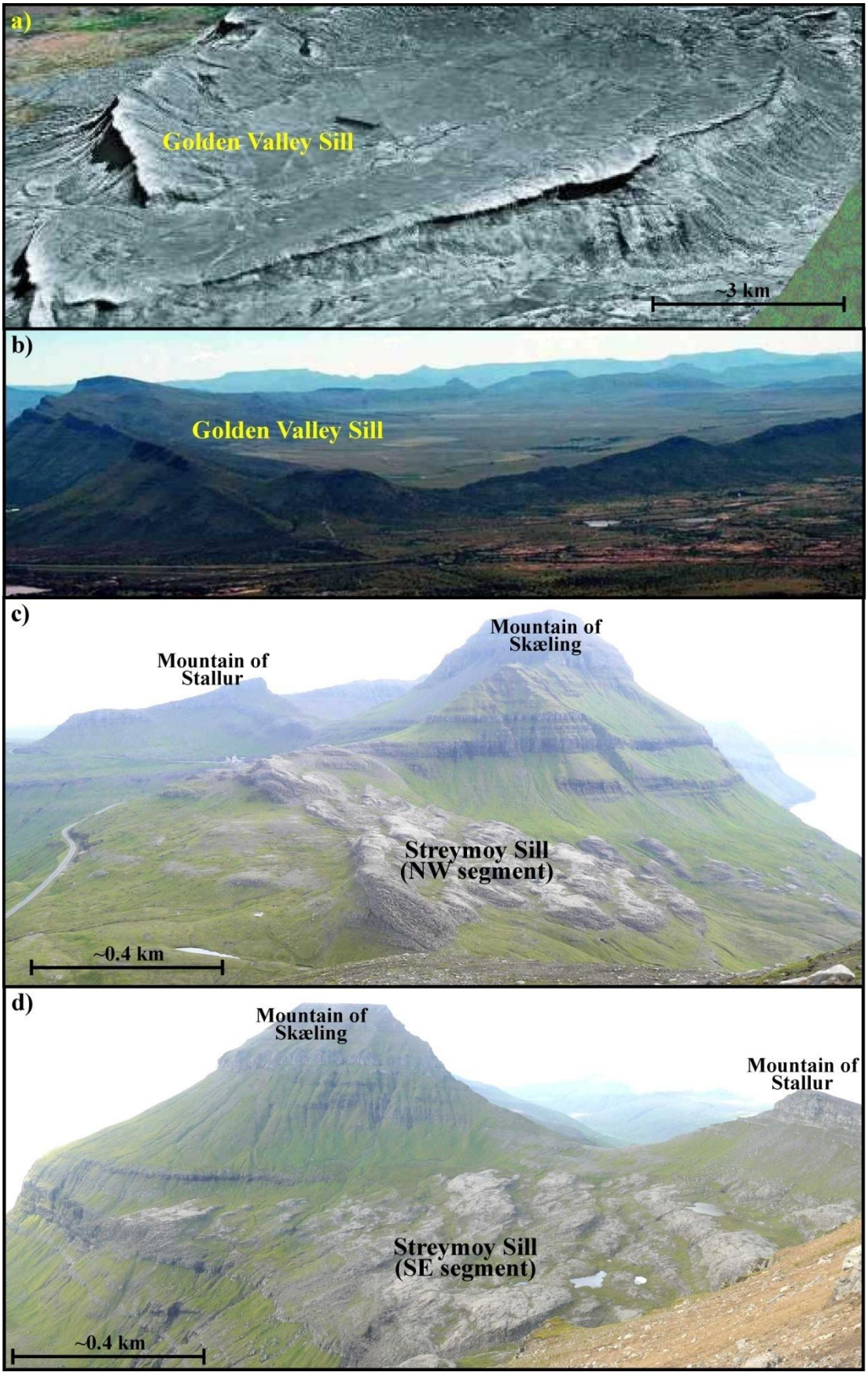

Figure 1.1. a) The large saucer-shaped Golden Valley Sill, South Africa, which is intruded into sedimentary successions, is made up of a sub-horizontal inner section and discordant outer margins

(from: www.nickschofield.co.uk). b) Same as in a), but from a different angle (from: www.fys.uio.no). c) The large saucer-shaped Streymoy Sill, Faroe Islands, slices through tabular basaltic lava flows at the mountain of Skæling on the island of Streymoy. d) Same as in c), but from the opposite side of the mountain of Skæling.

Very large sills can be matched in volume by multiple smaller sill intrusions in large intrusive complexes, which commonly occur in sedimentary basins as well as in volcanic successions (Walker, 1992; Hall, 1996; Hansen, 2006) (e.g. Fig. 1). Sills occurring in sedimentary basins are commonly divided into groups according to their geometries, some of which include radially or bilaterally symmetrical saucer-shaped sills in addition to sub-horizontal or inclined tabular sheets (e.g. Galland et al., 2003, Malthe-Sørensen et al., 2004; Thomson and Hutton, 2004; Galland et al., 2006; Thomson, 2007; Galland et al., 2009) (Fig. 1.2a; Fig. 1.2b; Fig. 1.2c). Saucer-shaped sills commonly consist of sub-horizontal inner sections that give way to inclined middle or outer sections that in some cases again give way to sub-horizontal outer margins (e.g. Chevallier and Woodford, 1999; Thomson and Hutton, 2004; Thomson, 2007; Polteau et al., 2008). In addition to the linear slopes often displayed by steeply inclined outer sill sections associated with uplift/folding of overburden and sill climbing (Thomson, 2007), inclined sill sections may also show step-and-stair geometries (Francis, 1982; Goulty, 2005) or they may occur as interconnected lobes that gradually curve upwards away from the base of the sill in question (Thomson, 2004; Hansen and Cartwright, 2006).

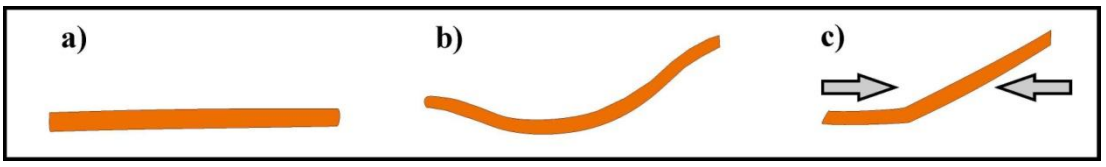

Figure 1.2. a) Tabular sub-horizontal sill sheets resulting from lateral intrusion at very low or very high pressures (e.g. Malthe-Sørensen et al., 2004). b) Saucer-shaped geometry from sill intrusion into static crust (Galland et al., 2006). c) Sub-horizontal basal sill sections give way to linearly inclined sheets during sill intrusion into a crust experiencing compression (Galland et al., 2006).

1.3. Data acquisition in 3D

In theory, the use of precise printed topographic maps supplemented by GPS satellite navigation equipment and aerial photos can be used to acquire accurate 2D data (in the sub-horizontal plane) that in turn can be plotted onto pre-defined electronic

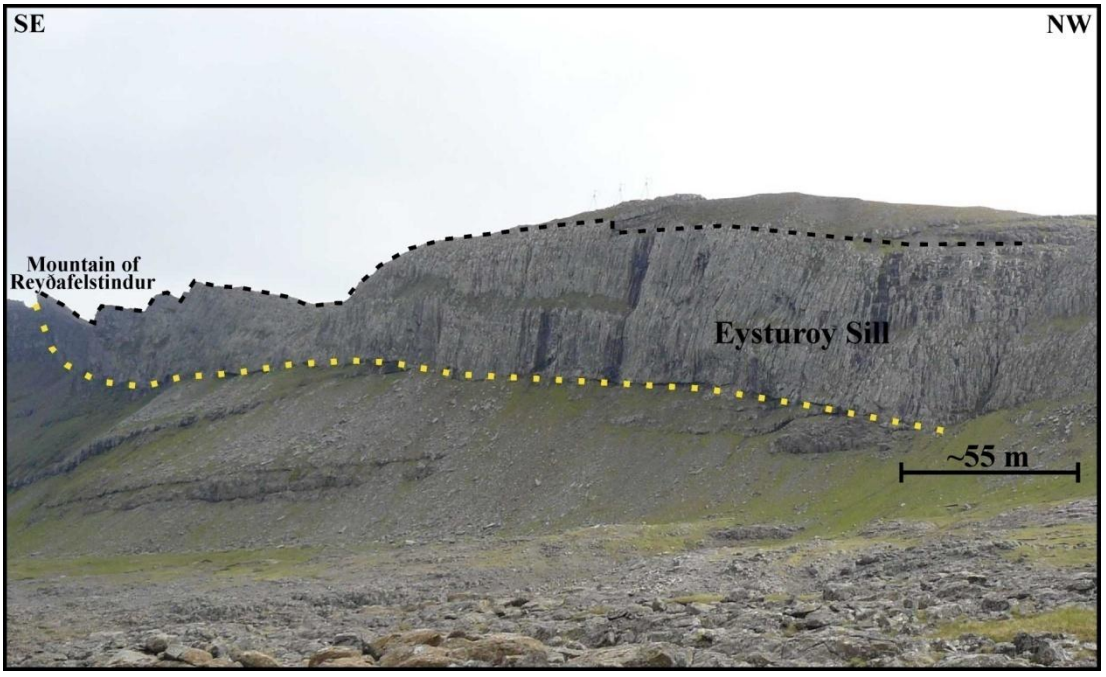

Figure 1.3. Sub-vertical NE margin of the Eysturoy Sill where a smooth lower contact (Dotted yellow line) is well preserved as opposed to the more eroded upper contact (Dashed black line).

ArcGIS maps in order to obtain 3D models of the targeted topographic features. However, measurements by means of GPS devices may yield inaccurate or invalid data particularly if these need to be acquired from lower sill contacts where half of the sky is obscured by vertical cliffs, as would be the case if upper sill contacts are heavily eroded and surrounding host rocks have been removed in consequence to weathering/erosion (e.g. Fig. 1.3). Also, sub-vertical views from aerial photos may not be able to distinguish between sills and their host basalts, and so are not always good alternatives to careful/detailed fieldwork and precise printed topographic maps. The raw pre-defined electronic ArcGIS topographic maps available to this study are composed of lateral contours drawn at elevation intervals of 10 m, with each contour being interconnected to its nearest neighbours with lines drawn orthogonal to these. If a contour is cut of (e.g. Fig. 1.4a), the orthogonal lines from the nearest underlying contour are automatically connected to the nearest overlying contour. If several successive contours are missing, the geometry of the vacant space from the missing contours will therefore define a uniform slope between the nearest underlying and overlying contours, which will not necessarily be identical to the actual surface (Fig. 1.4b; Fig. 1.4c). Consequently, reliable altitudes cannot be extracted from electronic pre-defined ArcGIS topographic maps for known positions in areas where the

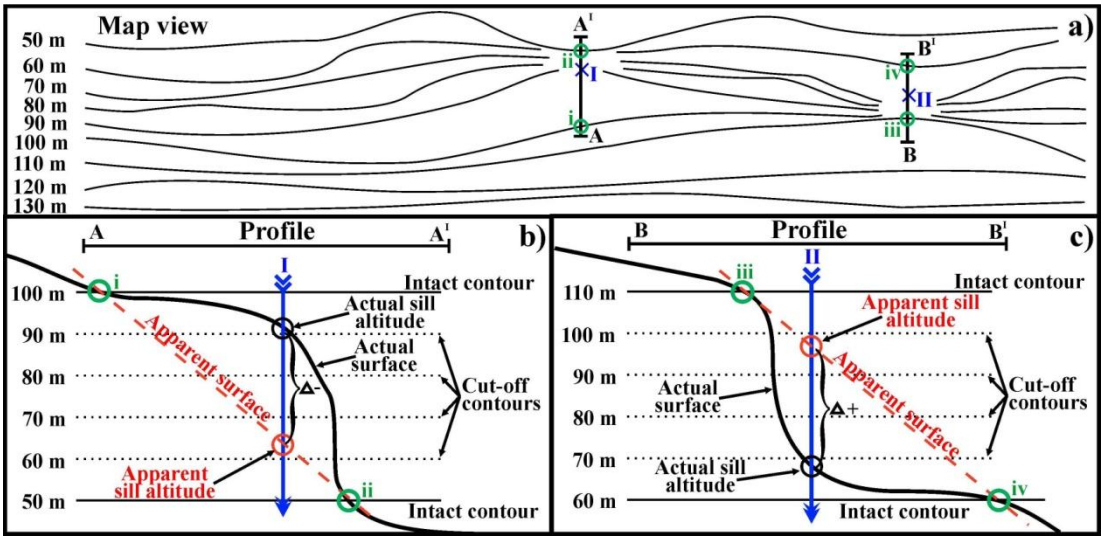

Figure 1.4. a) The artificial topographic map section shows how some altitude contours, drawn at 10 metres intervals, are cut off in the steepest parts of the imaginary landscape. The green circles labelled i, iii and ii, iv represent nearest intact upper and lower contours respectively that enclose the area where contours are cut off. Blue crosses (arrows in b and c) labelled I and II represent points plotted on lower sill margins. b) This vertical profile represent the track from A to A^{I} in a) and demonstrates how the position labelled I intersects the artificial surface that connects i and ii, thus yielding an apparent altitude that that is Δ- lower than the actual altitude. c) This vertical profile represent the track from B to B^{I} in a) and demonstrates how the position labelled II intersects the artificial surface that connects iii and iv, thus yielding an apparent altitude that is Δ+ higher than the actual altitude.

contours are cut off. Instead, the electronic ArcGIS 3D maps can be used to display sill geometries where all the 3D data have been obtained by other means e.g. accurate printed topographic maps. However, the method of displaying sills as 3D features where exposed sill surfaces, as outlined by accurately measured longitudes/latitudes, are draped on predefined electronic ArcGIS 3D maps include some weak points as well. On the one hand sill surfaces represented by electronic

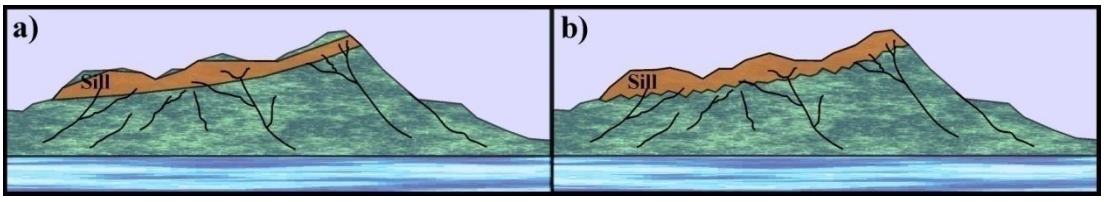

Figure 1.5. a) Draping of sills that are represented by electronic shape-files onto pre-defined electronic 3D maps (ArcGIS) will result in incomplete covering of interior sill surfaces, whereas sill margins will be fairly precisely imaged. b) Draping of sills that are represented by electronic raster-files onto pre-defined electronic 3D maps (ArcGIS) will result in imprecisely imaged sill margins, but will cover all outcrops in the interiors of the sills in question.

shape-files will display fairly accurate outlines, but their interiors tend to cut through protrusive topographic features in the landscape instead covering these (Fig. 1.5a). On the other hand the interiors of sill surfaces represented by electronic raster-files will cover the landscape within their outlines entirely, but their edges are generally irregular and jagged and will give an imprecise picture of sill margins (Fig. 1.5b). Of these two options the sill surfaces represented by draping of raster-files best image the bulk of the actual outcrops representing the sills in question.

1.4. Basalt occurrences

Basalts can be found at both constructive and destructive continental margins, i.e. in mid-ocean ridge and in island arc environments respectively, and they commonly occur as oceanic island basalts and continental basalts in intraplate settings as well (Hall, 1996).

Melting experiments have shown that major elements in basalts and their geochemical compositions in general can vary considerably in consequence to changes in e.g. temperatures (T), pressures (P), degrees of partial melting as well as compositional differences of source rocks during melting (Table 1.1; Fig. 1.6). However, melting of different mantle lithologies at different T and/or P do not necessarily always result in large compositional differences between the produced glasses. In general, basaltic glasses produced from melting of a fertile mantle peridotite/lherzolite (sample PHN1611; Kushiro, 1996) would yield the following basaltic glasses: quartz tholeiites at low T (< 1200° C) and low P (< 0.9 GPa) during low to moderate degrees of melting (< 15%), boninites moderate T (1200 - 1300° C) and at low P (< 0.9 GPa) during moderate to high degrees of melting (10 – 20%), alkalic basalts at high T (> 1200° C) and at high P (> 1 GPa) but low degrees of melting (< 10%), picrites at high T (> 1300° C) and at high P (> 1 GPa) during moderate to high degrees of melting (10 – 20%) and tholeiitic basalts at moderate to high T (1200 – 1400° C) and at low to high P (0.8 – 2.5 GPa) with the degrees of melting ranging from 0 to 28% (Kushiro, 1996; 2001). The much larger stability fields of tholeiitic basalts with respect to both pressures and temperatures relative to other basalt types may explain why tholeiites are the most common basalt type occurring worldwide. Tholiitic basalts are themselves commonly grouped into three categories according to their silica content where silica undersaturated rocks occur as nepheline tholiites, silica saturated rocks occur as olivine tholiites while silica

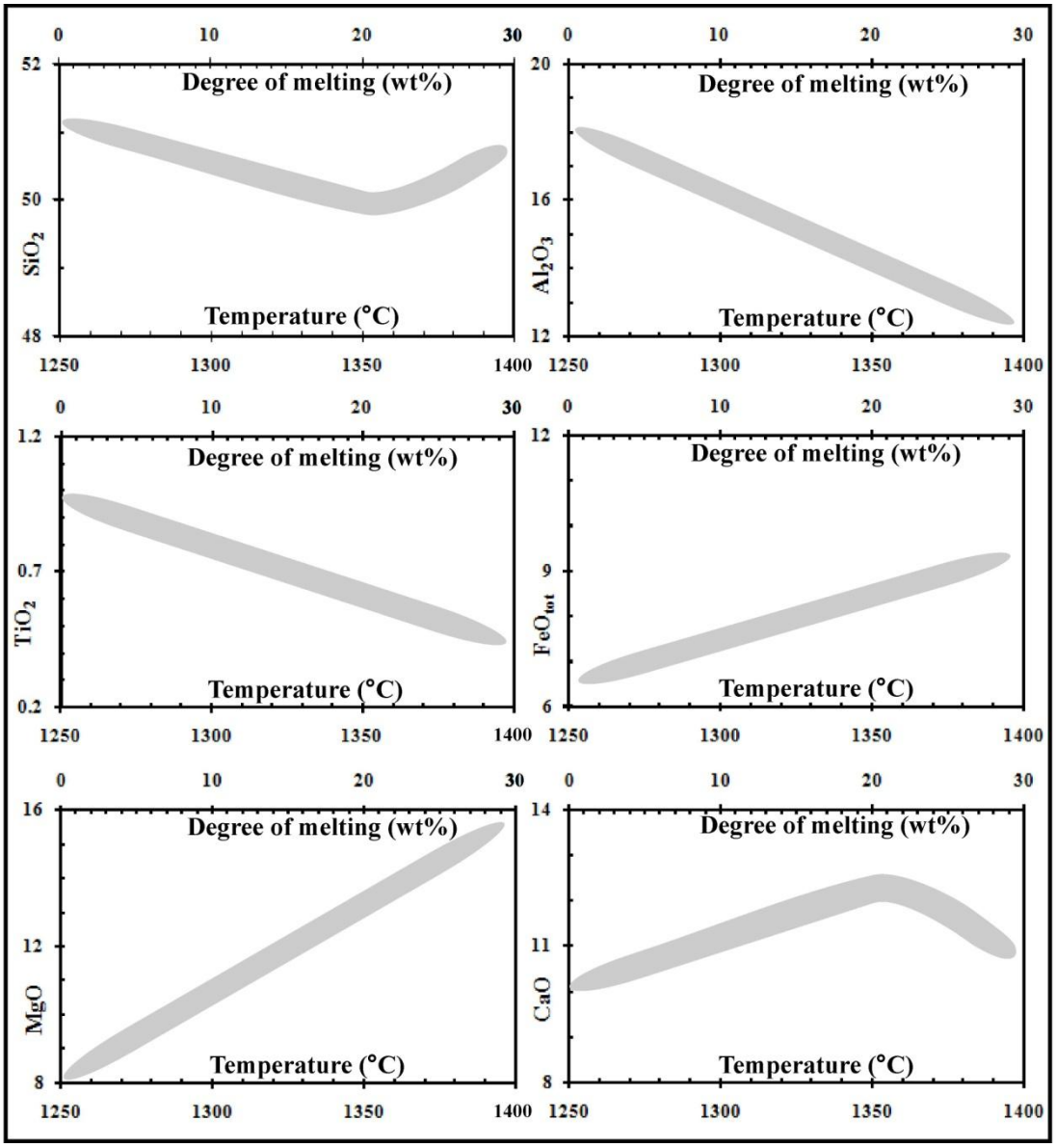

Figure 1.6. The diagrams indicate variations in major element compositions (Thick grey shaded lines) as functions of differences in temperatures (Approximate values based on melting of a "primitive upper mantle" of Baker and Stolper, 1994) and the degrees of partial melting (Approximate values based on melting of a "natural spinel lherzolite" of Hirose and Kawamoto, 1995). See also table 1.

oversaturated rocks occur as quartz tholeiites (Yoder and Tilley, 1962).

1.5. Obtaining data on basalt geochemistry

The procedure of obtaining geochemical data generally starts with careful collection of representative rock samples in the field. The next step will most often involve mechanical processing where samples first are crushed to fine gravel and subsequently ground to fine rock powder. Major elements and selected trace

Table 1.1. Changes in solidus temperatures, melt percentages and major element compositions as functions of changes in physical conditions during formation of basaltic magmas.

	[a, b]Increasing fertility (Added basic material?)	[c; d; e; f]Increasing temperature (Fix. Press.)	[a; e; f]Increasing pressure (Fix. temperature)	[f; g; b]Increasing melting % (Fix. temp. and press.)	[g; h]Increasing H_2O content (Metasom.?)
Solidus	Decreasing	----------	Increasing	----------	Decreasing
Melt %	Increasing	Increasing	decreasing	----------	Increasing
SiO_2	----------	[i]Decreasing [j]Increasing	Decreasing	[k]Decreasing [l]Increasing	----------
Al_2O_3	----------	decreasing	----------	Decreasing	decreasing
FeO_{tot}	Increasing	Increasing	Increasing	Increasing	Increasing
MgO	----------	Increasing	----------	Increasing	Increasing
CaO	----------	[i]Increasing [j]Decreasing	----------	[k]Increasing [l]Decreasing	----------
Na_2O	----------	Decreasing	----------	Decreasing	----------
TiO_2	----------	Decreasing	----------	Decreasing	----------

Superscript letters from a to h indicate studies of: [a]Yaxley (2000); [b]Kogiso et al. (1998); [c]Baker and Stolper (1994); [d]Ulmer (2001); [e]Falloon et al. (2008); [f]Hirose and Kushiro (1993); [g]Hirose and Kawamoto (1995); [h]Green and Falloon (2005). [i]Valid at temperatures below ~1350° C; [j]Valid at temperatures above ~1350° C; [k]Valid at melting percentages lower than ~15%; [l]Valid at melting percentages larger than ~15%.

elements are commonly analysed by means of X-ray fluorescence spectrometry (XRF). Here the trace elements are determined on discs from pressed rock powder whereas major elements are determined on glass beads made from powdered rock samples fused with a flux of lithium metaborate or tetraborate (e.g. Rollinson, 1998 and references therein). Inductively coupled plasma emission mass spectrometry (ICP-MS) is frequently employed for accurate determination of REE and trace elements in addition to being used for isotopic analysis. Finely ground rock powder from samples to be analysed by this method are processed through a number of dissolution sequences where the targeted material is exposed to various acid mixtures until it is dissolved to individual elements (ions) in a solution that is ready to be analysed.

1.6. Main objectives and thesis framework

The first major objective of this thesis is to gain information regarding sill emplacement mechanisms in general and, if possible, to provide constraints on the particular intrusive processes that ultimately led to the emplacements of the saucer-shaped sills exposed in the Faroe Islands. In order to achieve this goal the approach has been to obtain a thorough knowledge of the general geometries of individual sills as well as their lateral extent and to investigate if individual sills can be grouped into

distinct categories according to their geometries. Also, the geometries of sills from this study are contrasted against those of sills reported from other settings in an attempt to detect possible discrepancies between sills emplaced into volcanic versus sedimentary strata. Field investigations/measurements of sills and dykes at more detailed scales, i.e. from a few centimetres and up to a few tens of metres, are employed in order to identify feeders to the sills, to determine sill dimensions (thicknesses) and to establish contact relationships between host rocks and intrusive rocks as well as exact relationships between sills and dykes. Finally, all acquired data/evidences are correlated in order to achieve the best explanation of emplacement mechanisms. With the purpose of circumventing the data acquisition problems, as mentioned in section 1.2, most 3D data collections were done with the aid of high-precision printed topographic maps in addition to detailed field measurements and conventional photos of relevant exposures. The acquired data were displayed as 3D maps, using ArcGis software, and as 2D profiles along selected tracks to better illuminate general sill geometries and/or particular geometric characteristics of the sills in question.

The second major objective of this thesis is to gain a thorough knowledge of most aspects with respect to the petrogenetic history of the saucer-shaped sills of the Faroe Islands, i.e. to constrain the course of magmatic evolution from the embryonic stages of primary melt formation at depth through possible crystal fractionation and/or contamination in the crust to the final magma solidification in the investigated sills and dykes. The approach to achieve this goal has involved geochemical interpretations based on major elements, trace elements, including REE, and the characteristics of selected isotopes. The major element composition is used to classify these sills and to obtain information of their source rocks. Selected trace elements, including REE, are used to obtain a more detailed picture of potential processes that were active during various stages of magmatic evolution, in addition these are used in calculations/modelling aiming at quantification of partial melting and fractionation/accumulation percentages, which ultimately gave rise to the magmas that intruded the lava pile of the Faroe Islands. Trace elements, including REE, as well as Sr, Nd and Pb isotopes are used to detect and quantify potential contamination of the sills with crustal material. Finally, all geochemical and isotopic data/evidence are correlated to achieve reliable interpretations of how the plumbing system underneath the Early Cenozoic Faroe Islands worked at depth.

1.7. Thesis summary

Chapter 1: A brief introduction to occurrences of sheet intrusions and basalts in general and an overview of some common methods of acquiring relevant physical/geochemical data. A brief outline of the general idea and motivation behind the project complete this chapter.

Chapter 2: A brief review on the tectonomagmatic evolution of the North Atlantic Igneous Province (NAIP) and the Faroe Island Basalt Group (FIBG).

Chapter 3: Field description of the actual sills and associated dyke networks with emphasis on intrusive relationships at macroscopic, mesoscopic, hand specimen and microscopic scales and their implications on intrusive styles. Similarities and/or dissimilarities with sills from sedimentary settings are evaluated.

Chapter 4: Compositions of major and trace elements including REE and their implications on the petrogenetic evolution of the saucer-shaped sills of the Faroe Islands. What was the nature of the palaeo plumbing system at depth? Isotopic compositions of the investigated sills in addition to a few selected local basalts from the literature are used to detect/interpret the nature of source rocks and the extent and nature of potential crustal contamination.

Chapter 5: A brief overview of the results obtained in the physical and geochemical investigations of sills/dykes. How do these results coincide with already existing theories and what is the status of the sills in a regional and/or provincial context? Proposed future research topics related to the current project include: (1) Whole-rock ICP-MS analyses of additional sill samples. (2) Microprobe (electron/ion) analyses of plagioclase phenocrysts/inclusions and of other mineral grains of unknown composition that potentially could be of crustal/exotic origin. (3) Argon–Argon and/or the Rhenium–Osmium dating of all the investigated sills. (4) Additional geochemical analyses. (5) Comprehensive mechanical modelling to test the effect of systematic depth-related variations of Young's modulus on sill emplacement.

Appendices:

1. Brief overview of workflow during plotting of sills on electronic ArcGIS maps.

2. Brief overview of XRF analytical techniques (major and trace elements).

3. Brief overview of ICP-MS analytical techniques (trace elements including REE).

4. Brief overview of techniques employed during isotope analyses (Sr, Nd and Pb).

5. Tabulated results from partial melting and fractionation/accumulation modelling.

Chapter Two

2. Tectonomagmatic evolution of the North Atlantic Igneous Province (NAIP) including the Faroe Islands Basalt Group (FIBG)

2.1. Prelude to chapter two

The basaltic rocks of the Faroe Islands and the surrounding shelf formed in Early Cenozoic times (Waagstein et al., 2002; Abrahamsen, 2006; Storey et al., 2007) and represent an onshore/offshore manifestation of the igneous activity associated with the generation of the N Atlantic Igneous Province (NAIP), the magmatism of which affected vast onshore/offshore areas of the N Atlantic during this period (Saunders et al., 1997; Meyer et al,. 2007). The NAIP can be categorised as a large igneous province (LIP) and is itself a manifestation of the vast melt production associated with the formation of large magmatic provinces at a global scale (e.g. Fig. 2.1). The term LIP was previously assigned to igneous provinces of predominantly mafic compositions covering surface areas of more than 10^5 km^2 (Coffin and Eldholm, 1992), but more recent studies have suggested that igneous provinces of mainly silicic compositions should be included in the LIP family based on the same criterions as those that are valid for their mafic counterparts (Bryan and Ernst, 2008). More specifically, a revision on LIP definition suggest that they are magmatic provinces that are blanketing surfaces of more than 10^5 km^2 each, they comprise igneous volumes of more than 10^5 km^3 each, their maximum life spans are less than ~50 million years and they are characterised by igneous peaks of short duration (Generally 1 to 5 million years), during which most of the total igneous volume is produced (Bryan and Ernst, 2008). Other studies have suggested that the term LIP should be used in broader terms for all igneous provinces, irrespective of petrogenesis or compositional affinity, which are exposed over a minimum area of around 50000 km^2 (Sheth, 2007). LIP exposures have been documented on continents, on oceanic plateaus, on ocean basins, on submarine ridges, on ocean islands/seamount chains and at volcanic rifted margins (Bryan and Ernst, 2008). Well known onshore examples of basaltic LIP include the NAIP, the Deccan Traps and the

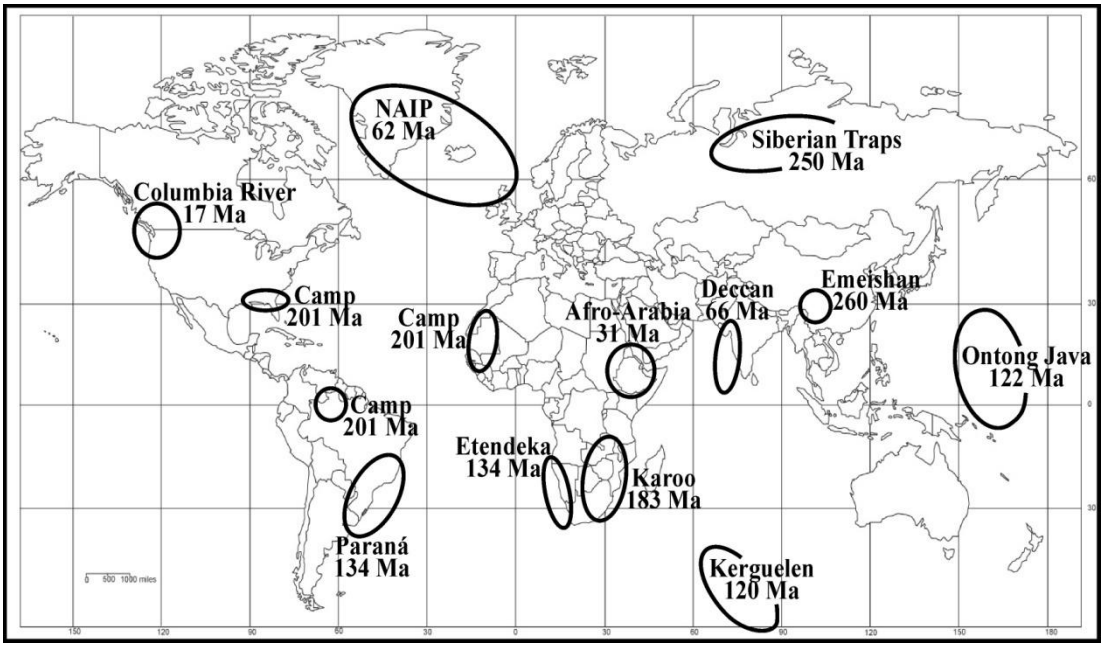

Figure 2.1. The ellipses on the Mercator map indicate a few (out of numerous) parts of the Earth that have been affected by the actions of well known basaltic Large Igneous Provinces (LIP) previously. Numbers refer to approximate timing for initiation of magmatism (Ages are from the compilation of Bryan and Ernst, 2008). See text.

Paraná – Etendeka basalts, which formed in rift-related settings, and the Siberian Traps in addition to the Columbia River flood basalts (Fig. 2.1), the generation of which were do not appear to be linked to such rifted continental settings (Coffin and Eldholm, 1992).

This chapter contains a general description of the North Atlantic Igneous Province (NAIP) (2.2) and of the Faroe Islands Basalt Group (FIBG) (2.3). Earlier theories and petrogenetic models on the NAIP formation are discussed (2.4) followed by a description of the geological settings within the province based on earlier publications on the subject (2.5). Particularities of individual regions within the province are briefly outlined (2.6) and the NAIP is considered in the context of rift geometries (2.7) and in the context of global and provincial plate tectonic processes (2.8) A brief summary with concluding remarks bring this chapter to an end (2.9).

2.2. General characteristics of the North Atlantic Igneous Province

The North Atlantic Igneous Province (NAIP) is a classic Large Igneous Province (LIP) associated with a volcanic rifted margin. It has traditionally been considered to comprise the voluminous Palaeogene igneous rocks occurring at the conjugate E

Greenland – NW European margins and in the W Greenland – Baffin Bay area (Upton, 1988; Saunders et al., 1997; Meyer et al., 2007 and references therein). However, other contemporaneous magmatism also occurred in the northernmost parts of Greenland (Kap Washington Group at ~64 ± 3 Ma, Estrada et al., 2001) and in the W Barents Sea (Vestbakken Volcanic Province, ~54 Ma, Tsikalas et al., 2002) (Fig. 2.2). In general, the bulk of the Early Palaeogene NAIP rocks can be grouped into the following regions: W Greenland – Baffin Island, SE Greenland, (central – east) CE Greenland, NE Greenland, Vøring margin, Møre margin, Faroe Islands, Rockall – Hatton area, Faroe – Shetland Basin, Rockall Trough and the NW British Isles (e.g. Saunders et al., 1997) (Fig. 2.2). Other contemporaneous, but smaller and more isolated, parts of the NAIP are also shown in Figure 2.2. The CE Greenland – Faroe Islands Ridge and Iceland formed subsequent to the onset of seafloor spreading within the province (Meyer et al., 2007). Exposed and submerged basaltic rocks of the NAIP extend in a roughly NE–SW direction for more than 2000 km along the conjugate East Greenland – NW European margins (Saunders et al., 1997) (Fig. 2.2). The extrusive rocks of the NAIP cover a surface area of at least ~1.3×10^6 km^2, while extrusive and intrusive rocks of all regions of the province combined have been estimated to comprise a volume of ~6.6×10^6 km^3 (Eldholm and Grue, 1994). The surface area of the onshore lava pile of the Faroe Islands is a mere ~1400 km^2, but when offshore igneous successions are included, the total area overlain by the basalts of this region is estimated at ~120000 km^2 (Passey and Jolley, 2009). The rocks of the NAIP occur in a variety of modes each reflecting the environments that dominated the actual source regions during the time of emplacement. Most of the extrusive rocks at the conjugate E Greenland – NW European margins (the Faroe Islands; Rockall – Hatton and Vøring – Møre) were extruded in subaerial or shallow-marine environments onto continental crust (e.g. Boldreel and Andersen, 1998; Natland and Winterer, 2005). Also, the majority of the Early Palaeogene W Greenland igneous products were emplaced onto/into continental crust (Larsen et al., 1999a) and in subaerial or shallow marine environments (Storey et al., 1998).

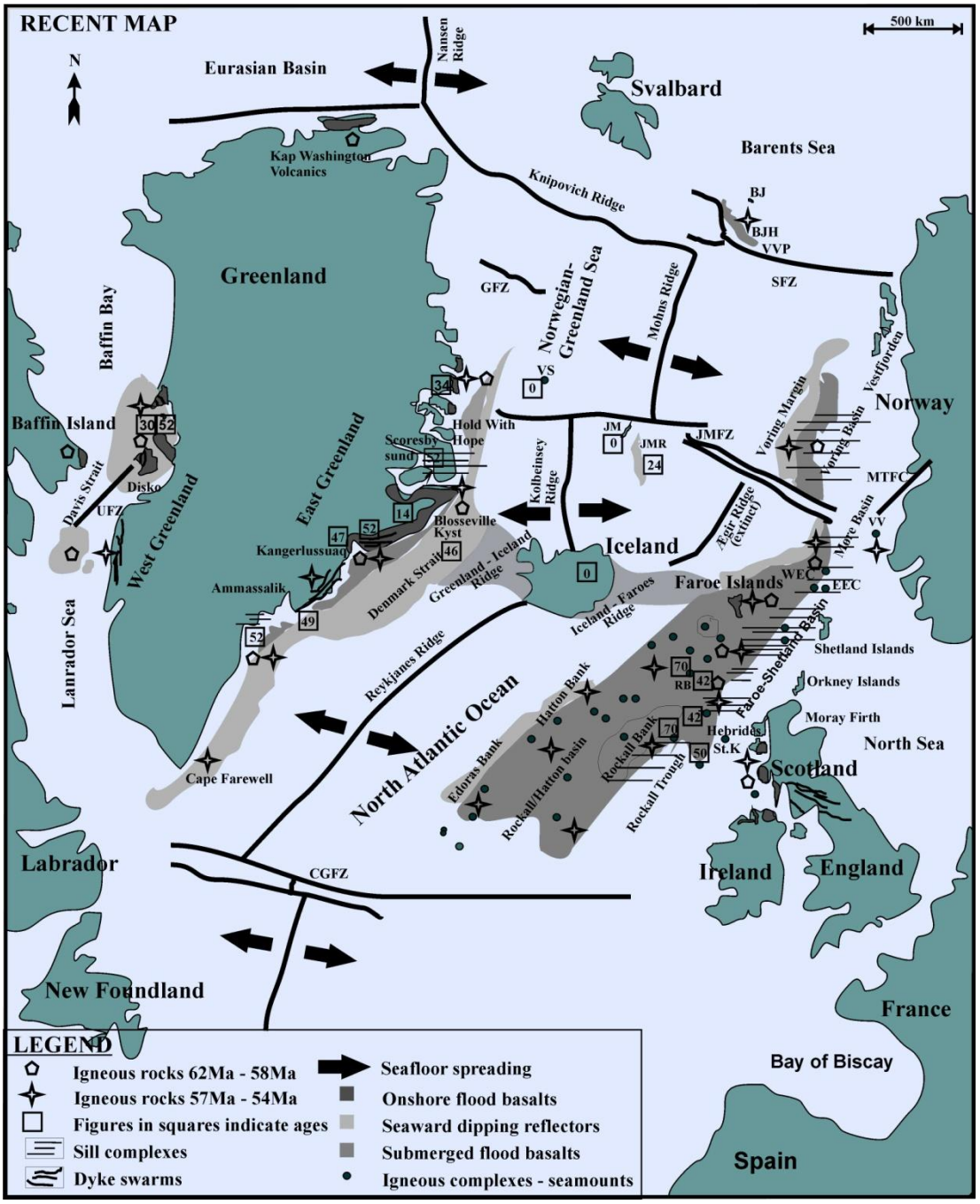

Figure 2.2. Simplified map showing the extent of the North Atlantic Igneous Province and surrounding areas modified from Saunders et al. (1997); Nielsen et al. (2002); Nielsen et al. (2007). The central igneous complexes and/or seamounts are modified from Bull and Masson (1996); Ritchie et al. (1997); Naylor et al. (1999); Edwards (2002); Hitchen (2004); Archer et al. (2005). Figures in the open squares indicate ages of magmatism occurring prior to or subsequent to the peak of igneous activity in the province at ~62 to ~53 Ma. Abbreviations: BJ – Bjørnøya; BJH – Bjørnøya High; CGFZ – Charlie Gibbs Fracture Zone; EEC – East Erlend Complex; GFZ – Greenland Fracture Zone; JM – Jan Mayen; JMFZ – Jan Mayen Fracture Zone; JMR – Jan Mayen Ridge; MTFC – Møre–Trøndelag Fault Complex; RB – Rosemary Bank; SFZ – Senja Fracture Zone; UFZ – Ungava Fracture Zone; VS – Vesteris Seamount; VV – Vestbrona Volcanic rocks; VVP – Vestbakken Volcanic Province; WEC – West Erlend Complex. See text.

2.3. General characteristics of the Faroe Island Basalt Group (FIBG)

The emplacement of the Faroe Island Basalt Group (FIBG) at the NW European margin occurred in Early Cenozoic times (Waagstein et al., 2002; Abrahamsen, 2006; Storey et al., 2007), meaning that it was a central part of the contemporaneous NAIP magmatism (Upton, 1988; Waagstein, 1988; Saunders et al., 1997; Meyer et al., 2007). Previous geophysical studies of the archipelago and surrounding areas suggested that the Early Cenozoic basalts building up the Faroese block rest on a ~30 km thick continental crust that in turn form part the Rockall – Faroe Islands microcontinent (Bott et al., 1974). More recent seismic interpretations indicate that the Moho reaches a maximum thickness of 40 – 46 km beneath the Faroe Islands. Here, the Early Cenozoic basalts probably rest on some Palaeozoic and Mosozoic cover material to ~30 km of stretched Archaean continental crust, which in turn is underplated by and perhaps also intruded by additional Early Cenozoic basaltic material (Richardson et al., 1998). The total stratigraphic thickness of exposed and drilled lavas of this region (the layers of which generally dip gently [~2°] towards the ESE or SE in the main study area) measure ~6.6 km (Rasmussen and Noe-Nygaard, 1969; Rasmussen and Noe-Nygaard, 1970; Waagstein, 1988; Passey and Bell, 2007; Passey and Jolley, 2009) (Fig. 2.3). The onshore lava succession covers an area of ~1400 km^2 (Fig. 2.3), but as offshore basalt sequences also extend from the Faroe Islands and into the Faroe-Shetland basin the total area overlain by the rocks of this basalt group is estimated at ~120000 km^2 (Passey and Jolley, 2009). The basalts of the FIBG were grouped into Upper, Middle and Lower Series basalts previously (Rasmussen and Noe-Nygaard, 1970; Waagstein, 1988), but recent studies have resulted in a revised nomenclature where the volcanic successions are grouped into seven formations (Passey and Bell, 2007; Passey and Jolley, 2009). Starting from the base of the lava pile and upwards these formations are: the ~1075 m thick volcaniclastic Lopra Formation; the ~3250 m thick Beinisvørð Formation composed of tabular lava flows; the ~9 m thick sedimentary Prestfjall Formation; the 40 – 50 m thick sedimentary Hvannhagi Formation; the 1250 – 1350 m thick Malinstindur Formation mostly composed of compound lava flows; the ~30 m thick sedimentary Sneis Formation and the ~900 m thick Enni Formation composed of compound and tabular lava flows (Passey and Bell, 2007; Passey and Jolley, 2009 and refs. therein) (See stratigraphic column in Fig. 2.3). Individual lava flows of the thicker crystalline

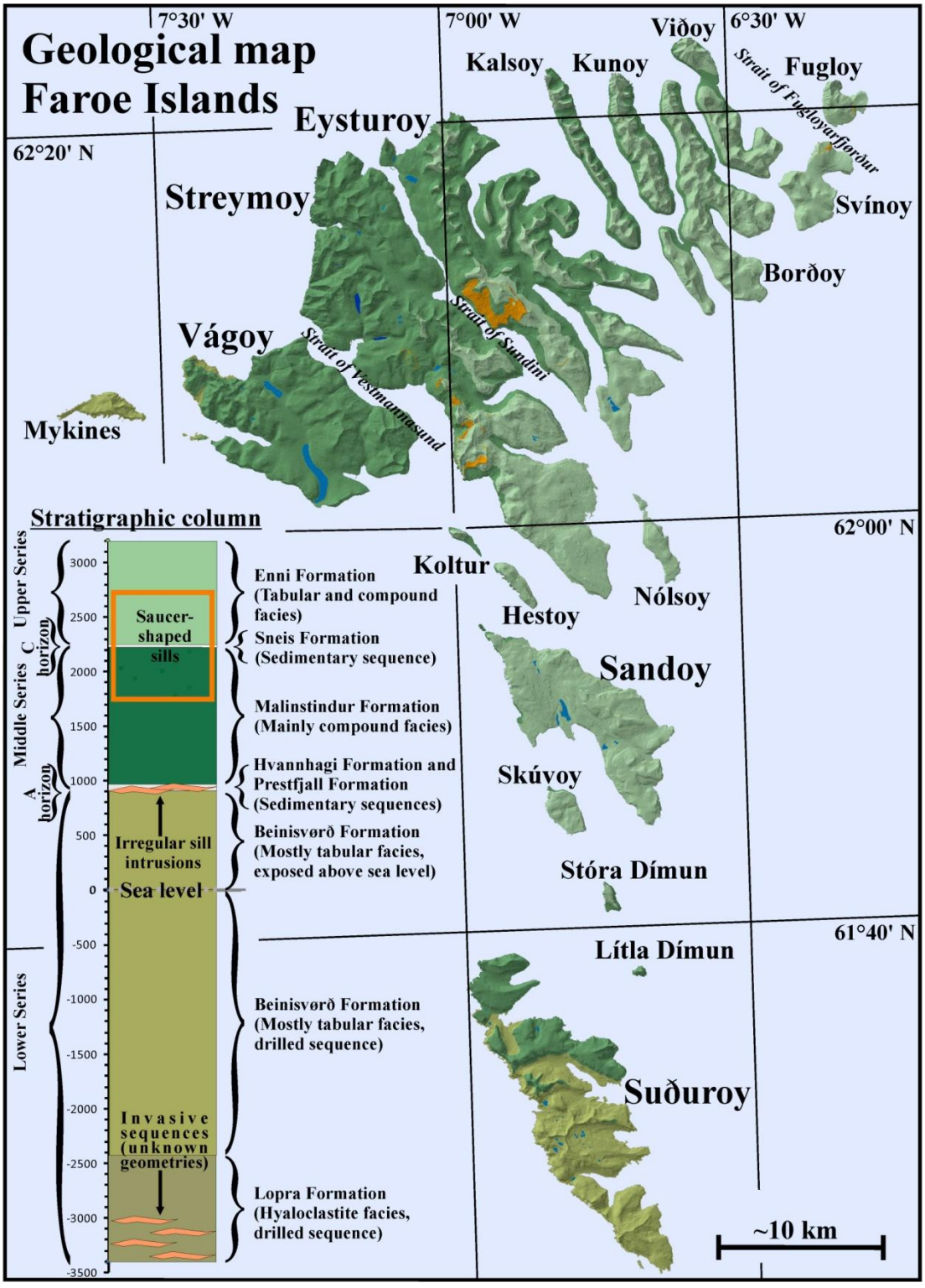

Figure 2.3. The geological map and stratigraphic column of the Faroe Islands are mainly based on studies of Rasmussen and Noe-Nygaard (1970) and Passey and Bell (2007). Initial nomenclature from Noe-Nygaard and Rasmussen (1968); Rasmussen and Noe-Nygaard (1970) and Waagstein (1988) is indicated to the left of the stratigraphic column whereas recent revised nomenclature from Passey and Bell (2007) is shown to the right. Only the major lava formations are displayed on the map, but the thinner sedimentary formations are shown in the stratigraphic column. Sills from this study are indicated by orange colour on the map and their total vertical extent is indicated by orange rectangle

on the stratigraphic column. Dark blue fields indicate local freshwater lakes. The 3D map, produced by means of ArcGIS software, is shown in orthogonal projection onto UTM net (only nautical grid is shown) WGS 1984 – 29N. See text.

formations are commonly separated by thin volcaniclastic lithologies and/or weathering surfaces mostly measuring a few centimetres to a few tens of centimetres in thickness, but occasionally these can be measured in metres (Rasmussen and Noe-Nygaard, 1970; Passey and Bell, 2007; Passey and Jolley, 2009). The crystalline rocks that represent the Beinisvørð Formation are generally aphyric whereas those belonging to the Malinstindur and Enni formations include both olivine and plagioclase phyric rocks in addition to aphyric basalts (Rasmussen and Noe-Nygaard, 1969; Waagstein, 1988; Passey and Jolley, 2009 and references therein).

The lavas of the Faroe Islands are commonly grouped into two main categories according to their geochemical compositions where high-TiO_2 lavas (TiO_2 >1.5 wt%) make up most of the volume in the lowermost ~5.5 km of the lava pile and low-TiO_2 lavas (TiO_2 <1.5 wt%) are becoming increasingly common in the remaining upper parts (Rasmussen and Noe-Nygaard, 1969; Hald and Waagstein, 1984; Waagstein, 1988; Passey and Jolley, 2009 and references therein; Søager and Holm, 2009, 2011). Dykes are ubiquitous at all levels of the lava pile while saucer-shaped sills are confined to the uppermost parts of the Malinstindur Formation, the Sneis Formation and the lowermost parts of the Enni Formation (Rasmussen and Noe-Nygaard, 1970; Passey and Bell, 2007; Passey and Jolley, 2009) (Fig. 2.3). Invasive sills or dykes? of unknown extent/geometries can be found in the lowermost ~400 m of the Lopra Formation (Passey and Bell, 2007). Like the local lavas, dykes and sills are often categorised according to their TiO_2 content (Hald and Waagstein, 1991; Holm et al., 2001). While high-TiO_2 dykes and lavas occur throughout the archipelago, low-TiO_2 dykes and lavas are mostly concentrated in the northern parts of the islands (Hald and Waagstein, 1991; Søager and Holm, 2011). The sills display a geochemical trend being somewhat different, with low-TiO_2 intrusions occurring towards the SW and those with high-TiO_2 content occurring towards the NE (Hald and Waagstein, 1991).

2.4. Competing theories on the NAIP petrogenesis

A number of theories and geodynamic models seeking to define the nature of common mechanisms, which can explain all aspects of the Early Cenozoic

magmatism that eventually resulted in the igneous products making up the NAIP (and other LIPs), have been proposed pr

eviously. These have often been grouped into two end member categories, one of which argue in favour of rifting and magmatism in response to the ascent of large plumes from the deep mantle (e.g. White and McKenzie, 1989; Campbell and Griffiths, 1990) whereas the other infer lithospheric control on these processes (e.g. Ziegler, 1992).

Although a variety of plume models for the NAIP genesis have been proposed earlier (e.g. Meyer et al., 2007 and references therein) most are ultimately based on one of two models: 1) The White and McKenzie (1989) "static" plume model, infer a plume that rises passively from the mantle-core boundary in a whole-mantle convectional regime, and upon reaching the lithosphere generates temperatures of up to ~200ºC above those of the ambient mantle in a circular area extending up to ~2000 km in diameter (Fig. 2.4a). The resulting surface uplift then triggers crustal rifting, which in turn is accompanied by extensive igneous activities. 2) The Campbell and Griffiths (1990) "impinging" plume model, suggests that a plume with a bulbous head and a narrow feeder conduit ascend from the lower mantle propelled by thermal buoyancy (in a whole-mantle convectional regime), and upon impinging at the lower lithosphere generates a large crustal uplift with associated rifting and relatively brief but vigorous magmatism over a comparable area of 2000-2500 km across (Fig. 2.4a). This model infers high temperature MgO-rich melts to be generated only above the hot narrow plume stem, and the associated rifting requires pre-existing heterogeneities in the lithosphere.

In accordance with previous inferences for general LIP genesis by extension from global scale plate movements and associated decompression melting (e.g. Ziegler, 1992), Korenaga (2004) and Lundin and Doré (2005a; 2005b) invoke lithospheric control on both rifting and magmatism of the NAIP. These authors suggested that both the Early Cenozoic NAIP and the present day Iceland magmatism represented a "top down" effect of extension from plate tectonic processes, where decompression melting of upper mantle source rocks generated the rocks of the NAIP (Fig. 2.4b). Other studies have suggested that the present day "Iceland Hotspot" extends to no greater depths than the bottom of the upper mantle (e.g. Foulger et al. 2001). Korenaga and Keleman (2000) and Lundin and Doré (2005a, 2005b) have interpreted the wide range in geochemical and isotopic compositions in both Early Cenozoic

NAIP rocks, as well as in recent Icelandic melts to result from partial melting of a heterogeneous fertile upper mantle. Recent re-interpretations of rifting processes in the Early Cenozoic NAIP have suggested a slightly different variant of lithospheric control in connection with global plate reorganisations. Here, numerous local sites of extension, resulting from cessation/relaxation of earlier compressional stress regimes that were unevenly distributed within the affected tectonic plates, are dispersed over plate-wide areas where they initiate rifting and associated LIP magmatism (Nielsen et al., 2007).

Other potential processes that are not directly related to global plate reorganisations or large plumes from the deep mantle, but which are sometimes thought to initiate large-scale partial melting include: i) spontaneous upwellings that are initiated by crustal/lithospheric perturbations could generate excessive decompression melting in near-solidus buoyant material of the upper mantle (Raddick et al., 2002); ii) delamination of lower crustal rocks into the upper mantle provide fertile material that melt at lower temperatures relative to the surrounding mantle; iii) edge-driven convection cells in the upper mantle result in extensive decompression melting to produce flood basalts (e.g.Meyer et al., 2007 and references therein) (Fig. 2.4c).

These LIP studies seem to suggest that the most notable differences between the source materials of the early "plume" models and the "lithospheric" models are their presumed origin in the deep mantle and in the upper mantle respectively. However, still other studies have suggested that the sources to large basaltic provinces worldwide originated in at least three distinct levels in the sub-lithospheric mantle (Courtillot et al., 2003) (Fig. 2.4). Such tapping of compositionally diverse basaltic magmas from different mantle levels could point to some degree of ***mantle heterogeneity*** at the vertical scale.

On the assumption that magmas were produced by partial melting of material originating at any depths in the sub-lithospheric mantle, earlier studies have suggested that the ability/***strength of the lithosphere*** to resist penetration of ascending melts was a critical factor that has influenced the ultimate magma volumes of many LIPs (e.g. Coffin and Eldholm, 1992). These authors also stated that the velocities of lithospheric plates, which experience lateral motion above these ascending magmas, were an important factor in determining ultimate magma volumes of mantle-derived basaltic melts.

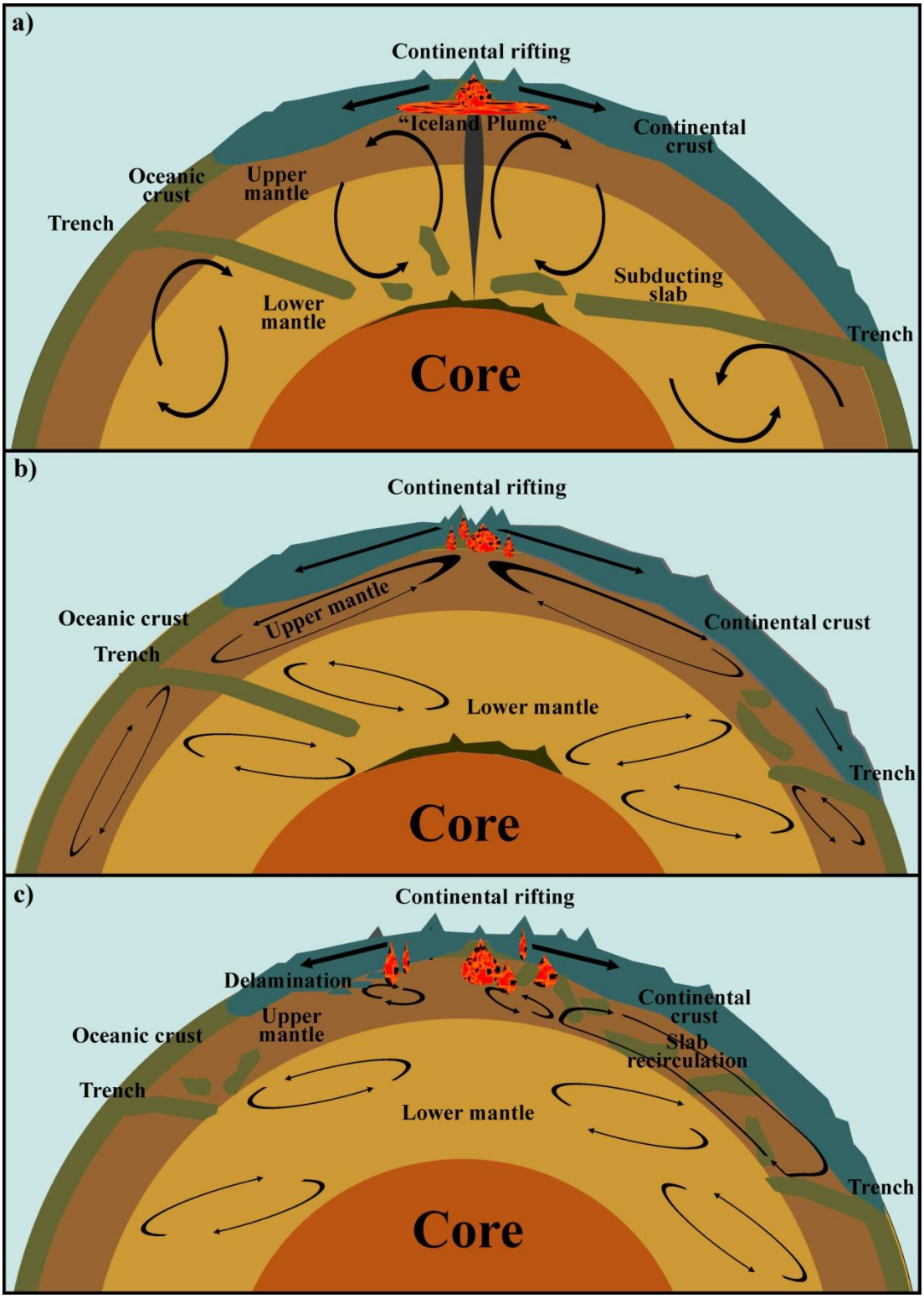

Figure 2.4. Possible scenarios during continental break-up and NAIP formation. a) Rifting occur in response to the activity of a large mantle plume originating at the mantle-core boundary in a whole-mantle convectional regime. b) Rifting and decompression melting in the sub-continental lithospheric mantle (SCLM) occur in response to (far-field) extension and mantle drag. c) Rifting and upper mantle melting occur in response to activity of upper mantle plume(s) where slab recirculation or crustal delamination enriched igneous products in an upper-mantle convectional regime. See text.

2.4.1. Mantle heterogeneity

There is a general consensus amongst most geologists that the entire compositional variation occurring in basaltic rocks world-wide both in large flood basalt provinces and in comparatively smaller igneous events, cannot result from differences in melt-forming processes alone, but require some compositional heterogeneities of the presumed mantle sources to these basalts.

A variety of causal mechanisms/processes have been suggested to explain mantle heterogeneities, these include: 1) Gravity induced decoupling/settling of oceanic lithosphere originating from subduction zones provide oceanic crust to the mantle in regions adjacent to active or extinct subduction zones (Alberede and Van der Hilst, 2002; Meibom et al., 2003; Donnely et al., 2004; Anderson, 2006). 2) Delamination of the lower crust/lithosphere due to extension, thermal erosion and/or density contrast to provide the upper mantle with oceanic (eclogitic) crust (Anderson, 2005; Lustrino, 2005).

(1) The exact fates of subducted oceanic crust with attached sediments/fluids have been longstanding themes of debate amongst many geologists. The main issue is whether subducted materials inevitably plunge right down to the mantle-core boundary, due to their large negative buoyancies, or if subducted lithosphere material sometimes is distributed in higher levels of the mantle as well. Interpretations from seismic tomography and numerical modelling seem to suggest that old and relatively cold oceanic lithosphere from subduction zones can eventually find their way down to the lowermost 200 km of the mantle i.e. the "D" layer (Zhao, 2004; Lay, 2005). Consequently, the addition of mostly oceanic crustal material to the lowermost few hundred kilometres of the mantle are assumed to have resulted in a heterogeneous region within the "D" layer (Hedlin et al., 1997; Helffrich and Wood, 2001; Alberede and Van der Hilst, 2002; Lay, 2005). Based on low velocity zones and/or presumed temperature anomalies in the middle mantle, some authors argue in favour of a heterogenous zone at this level as well in response to the addition of subducted oceanic crust (Hedlin et al., 1997; Helffrich and Wood, 2001; Courtillot et al., 2003; Zhao, 2004). Korenaga (2004) argued that the crustal part of subducting slabs become strongly buoyant below the 660 km discontinuity zone and so are expected to be entrained at levels no deeper than this zone. Remnants of young and hot oceanic lithosphere that are too buoyant to be subducted to great mantle depths may

come to rest in the upper mantle when decoupled from their subducting slab, thus probably resulting in upper mantle heterogeneities as well (e.g. Alberede and Van der Hilst, 2002; Meibom et al., 2003; Anderson, 2006).

(2) Delamination processes have previously been interpreted to occur in a number of ways: i) Rayleigh-Taylor instabilities in the lower crust result in detachment of slices of dense hydrated material that descend down into hotter mantle environments where it is exposed to partial melting and dehydration, the products of which in turn trigger hydrous melting of overlying mantle material thus initiating a chain reaction (Elkins-Tanton, 2005). ii) Extension related ascent of MOHO can cause lateral thermo-mechanical erosion of the surrounding lithosphere on its flanks thus resulting in decoupling and descent/settling of slices of lithospheric material (Morency and Doin, 2004). iii) Mechanical thickening and shortening of the lithosphere induced by compression can enhance gravitational instability of cold and dense lithospheric roots that finally become detached from the lithosphere due to lateral thermal attenuation from the increasingly hot surroundings (Kay and Kay, 1993; Conrad, 2000; Lustrino, 2005). iv) As the density of cold eclogitic rocks at the base of thick continental/oceanic crust is 3 to 10 % denser than normal mantle peridotites, some authors infer that delamination of the eclogites can occur due to density differences alone, if the eclogitic layer is sufficiently thick (Zegers and Van Keken, 2001; Anderson, 2005).

Perhaps of equal importance, compared to compositional heterogeneities in the upper mantle, is the possible presence and distribution of fluids/water, which has the potential of greatly enhancing partial melting (Hirose and Kawamoto, 1995; Green and Falloon, 2005). The origin of water in the mantle could be subducted oceanic crust or fluids expelled during earlier small-scale melting events in the mantle (Nichols et al., 2002). Small-scale heterogeneities (ranging from metres to a few kilometres) due to metasomatism in the lithospheric mantle are also inferred to have developed in response to transport of water and enriched material via deep lithospheric shear zones (Bonatti, 1990; Downes, 1990; Donnely et al., 2004). Other authors have argued in favour of the existence of water-rich cold plume-like structures in the upper mantle, which are inferred to have obtained their water from pristine mantle regions or from stalled oceanic subducted crust above the 660 or 410 km discontinuity zones (Dixon et al., 2002; Gerya and Yuen, 2003). With respect to

the NAIP, Jamtveit et al. (2001) detected elevated H_2O content in Early Cenozoic igneous products of W Greeenland; CE Greenland; NE Greenland; Iceland and the Faroe Islands. Similarly, Nichols et al. (2002) recorded elevated H_2O contents in rocks from the Iceland area that systematically increase northwards along the offshore Reykjanes Ridge towards the most active igneous regions of onshore Iceland where the largest values were measured.

2.4.2. Lithospheric strength

A relevant issue to be addressed in complex and diverse extension-related large igneous provinces like the NAIP is: what caused the magmatism to be so wide-spread until a relatively narrow seafloor-spreading zone finally was established? Obviously, the strength of certain parts of the lithosphere and its relative capability to resist stretching, rupture and/or intrusion of magmas must have played a major role. The strength of the lithosphere depends on a few main factors. Clearly, certain mineral assemblages are less resistant to fracturing/penetration than other e.g. sedimentary and quartzo-felspathic igneous rocks, typical for the upper continental crust/lithosphere, are considerably weaker than olivine dominated rocks that are common for the lower lithosphere (Kohlstedt et al., 1995; Kusznir and Park, 2002). The presence of water and increased fluid pressure in general further weakens all affected rock assemblages in the lithosphere (Kohlstedt et al., 1995; Hirth and Kohlstedt, 1996; Jackson et al., 2008). As many parts of the lithosphere often have had a complex magmatic/tectonic history, lateral as well as vertical compositional heterogeneities are of common occurrence (Kohlstedt et al., 1995; Harry and Bowling, 1999) rendering some sections of the crust/lithosphere prone to rifting at lower extensional stresses than is the case for the average lithosphere. Also, tectonic activities commonly leave complex assemblages of shear zones in the lithosphere which in turn may facilitate rifting both by enhancing partial melting and by reactivation of these old shear zones (Kohlstedt et al., 1995; Holdsworth et al., 1997; Ryan and Dewey, 1997; Harry and Bowling, 1999). In the context of lithospheric strength, the "soft-point model" (Corti et al., 2001; Callot et al., 2002; Geoffroy, 2005) suggests that magmas ascending from the sub-lithospheric mantle in regions already undergoing extension, will penetrate the lithosphere at locations that are pre-weakened by previous small-scale igneous activity. Callot et al. (2002); and Geoffroy (2005) further suggested that the configurations of such pre-weakened zones in the

North Atlantic region prior to the final seafloor spreading event exerted significant control on the geometry of rift propagation and the spatial distribution of igneous centres/regions building up the NAIP.

Extensional strain rates and general changes in heat flow are important factors in governing whether the affected lithosphere experiences a net strengthening or a net weakening in a laterally homogeneous and relatively undeformed lithosphere, which is exposed to extensional forces (Kohlstedt et al., 1995; Hirth and Kohlstedt, 1996; Kusznir and Park, 2002; Jackson et al., 2008). These authors suggested that when a laterally homogeneous lithosphere experiences stretching from lateral extension, the high temperature MOHO will temporarily ascend in the area(s) of locus, and if minerals are given time enough to re-crystallise (strain hardening) and temperatures are given enough time to re-equilibrate, the MOHO will eventually descend to its previous level again leaving strong olivine dominated rocks in the lower crust, hence resulting in a net lithospheric strengthening. Conversely, high strain rates will not allow minerals to re-crystallise (strain softening) or temperatures to re-equilibrate and will eventually result in necking of the lithosphere (Kohlstedt et al., 1995; Hirth and Kohlstedt, 1996; Kusznir and Park, 2002; Jackson et al., 2008). The former process would probably cause the locus of stretching to shift to a new preferred and weaker location (e.g. Sonder and England, 1989; Harry and Bowling, 1999; Kusznir and Park, 2002).

2.5. Geological settings

In the context of large igneous provinces, it is relevant to consider relevant tectonic events within the area of interest and to consider potential temporal and spatial links between igneous products formed within the LIP in question. With respect to the structural settings, tectonic signatures and effects associated with the closure of the Iapetus Ocean in Silurian – Devonian times and the subsequent collapse of the Caledonian Orogen in Devonian times (Roberts, 2003) may be of particular relevance, as the bulk of the Early Cenozoic magmatism that eventually gave rise to the NAIP occurred in those parts of the proto-North Atlantic area that were affected by these events in some ways.

2.5.1. Tectonic settings

In the period from the collapse of the Caledonian Orogen and until the final break-up in Early Cenozoic times, various extensional systems were active for shorter or longer periods during a total time span of ~350 Ma, which resulted in the formation of widespread sedimentary basins (Doré et al., 1999; Skogseid et al., 2000). Early Cenozoic exploitation/reactivation of both Precambrian and Palaeozoic Caledonian shear zones/structures have been inferred previously (Doré et al., 1997, 1999; Skogseid et al., 2000). Following the closure of the Iapetus Ocean and the collapse of the Caledonian Orogen in Silurian–Devonian times (Roberts, 2003), the proto-North Atlantic area to the south of the Caledonian front was characterised by a patchwork of Archaean and Proterozoic terranes (Dickin, 1992). Early Cenozoic magma formation by melting/recycling of fertile source material that originated from tectonic activities associated with Precambrian orogens have been suggested earlier for some parts of the NAIP (e.g. Lundin and Doré, 2005a).

The main structures that formed during the various post-Caledonian tectonic events in the proto-North Atlantic, i.e. at the conjugate E Greenland – NW European margins, and at the W Greenland margin are introduced below.

2.5.1.1. Carboniferous – Triassic

During this time span, broadly E-W directed lithospheric extension between Eurasia and Greenland resulted in the formation of large half-graben basins that become widely dispersed in the proto N Atlantic area and which were subsequently filled with thick successions of continental sediments (Ziegler, 1989; Surlyk et al., 1990; Brekke et al., 1999; Doré et al., 1999). In Permian – Triassic times this extension was non-orogenic and linked to basin subsidence in response to thermal relaxation of the lithosphere (Ziegler, 1989). In the latest part of this period the area north of N Greenland was exposed to moderate NNW directed extensional stress (Ziegler, 1989).

2.5.1.2. Jurassic – Cretaceous

Extensional activity in the proto N Atlantic area that was related to sea-floor spreading in Mid Jurassic between West Africa and North America (Wilson, 1997) resulted in faulting and subsidence in regions off Mid-Norway (Blystad et al., 1995). Surlyk et al. (1981) argued in favour of extensional activity throughout Jurassic times

for NE Greenland. Late Jurassic E–W extension, possibly linked to rifting in central Europe and seafloor spreading in the Tethys (Ziegler, 1989), resulted in stretching and subsidence of the Rockall Trough, the Faroe – Shetland Basin and the Vøring – Møre basins (Ziegler, 1989; Brekke et al., 1999; Cole and Peachey, 1999). In the Early Cretaceous the central Atlantic spreading ridges propagated northward and reached the northern parts of Spain and probably caused a considerable NW–SE extensional stress to be built up in the already stretched northern parts of the proto N Atlantic area, thus causing further extension and rapid subsidence in the existing sedimentary basins listed above (Cole and Peachey, 1999; Doré et al., 1999). The switch from Tethyan seafloor spreading to subduction at its northern margin caused the tectonics on the future N Atlantic margin to change from rifting in broadly N-S directions to one dominated by NE-SW directed rifting during this period (Doré et al., 1999). Shrivastava and Tapscott (1986) suggested that spreading in the Rockall Trough occurred during the Mid Cretaceous (Albian time, 100-105 Ma), whereas Knott et al. (1993) proposed that spreading occurred in the Rockall Trough in the time span from Late Carboniferous to Late Cretaceous times and that the Rockall Plateau detached from Greenland at around 83 Ma. Surlyk et al. (1981) argued in favour of the occurrence of extension in NE Greenland throughout the Cretaceous. Being located between E Greenland and NW Europe, extension across the Rockall Plateau in Cretaceous times was accommodated by stretching of the Rockall – Hatton area (Bull and Masson, 1996; Tate et al. 1999). On the one hand, Roest and Shrivastava (1989) and Rumph et al. (1993) suggested that E–W extension between Greenland and North America in Late Cretaceous times caused rifting to propagate rapidly from the proto Bay of Biscay area and northward, thus initiating the formation of the Labrador Sea, on the other hand Ziegler (1989) interpreted this extensional event to have taken place in Late Jurassic–Early Cretaceous times. However, Chalmers (1991) and Chalmers and Laursen (1995) opposed these authors and pointed out that the most likely timing for the onset of sea-floor spreading in the Labrador region was in the Early Palaeocene times rather than in the Late Cretaceous, thus reducing the estimated amount of new sea-floor formed, compared to previous calculations. Throughout this period the area north of N Greenland was exposed to moderate NNW directed extensional stresses (Ziegler, 1989).

2.5.1.3. Pre-rift Cenozoic

Some of the most recent theories regarding the evolution of the NE Atlantic suggest that a weak NE–SW directed, relatively short-lived, extensional episode occurred at around 60 Ma causing NW directed rifting in a relatively narrow area reaching from the British Isles via the Faroe Islands and CE Greenland to the Disko area in W Greenland, and possibly linked to spreading centres in the Baffin Bay (Lundin and Doré, 2005a, 2005b). Early Palaeogene extension across the Rockall – Hatton area has been inferred previously (Doré et al., 1999; Tate et al., 1999), and Edwards (2002) suggested an increasing degree of extension across the Rockall – Hatton area from the north towards the south during this period. Cole and Peachey (1999) interpreted extension to have occurred across the Rockall Trough in Early Paleocene times, an extensional event that probably continued into the Eocene as well. Frequent episodes with short WNW-ESE or NW-SE directed extension with various loci of rifting occurred in the Faroe-Shetland Basin in Early and Mid Paleocene times (Dean et al., 1999), and Lundin and Doré (1997) likewise inferred broadly NW-SE directed extension to have occurred in the Møre and Vøring basins during this period. Timewise, the NE-SW directed extension discussed at the start of this sub-section (Lundin and Doré, 2005a, 2005b) seems to be at odds with the NW-SE extension suggested for large parts of the N Atlantic during this period by other authors. Supplementary to the interpretations by these authors, Harrison et al. (1999) suggested that all of the NW European offshore basins were the sites of one continuous rift with sinistral strike-slip movements in the Mid Paleocene. Two sub-parallel sinistral strike-slip events occurring at around 62 Ma have been inferred for the E Greenland margin in a line that broadly coincides with the subsequent Early Eocene break-up trend and for the NW European margin from the Vøring Basin in the north to the Rockall Trough in the south Nielsen et al. (2007).

Ziegler (1989) argued in favour of considerable extensional NNW directed extensional stresses off N Greenland in the Late Palaeocene and Harrison et al. (1999) also suggested considerable N directed extensional stresses for Greenland in in general in Late Paleocene and Earliest Eocene times.

Regional vertical movements and the formation of transient domal uplifts preceded the main phases of Early Palaeogene igneous activities in many parts of the NAIP (e.g. Maclennan and Jones, 2006; Meyer et al., 2007; Saunders et al., 2007).

Table 2.1. Early Palaeogene transient uplifts have been reported for many regions within the North Atlantic Igneous Province (NAIP)

Regions	Cited authors
Disko area, W Greenland	Japsen et al. (2005)
Ammassalik area, SE Greenland	Clift et al. (1995); Larsen and Saunders (1998)
Kangerlussuaq area, CE Greenland	Peate et al. (2003)
Scoresby Sund area, CE Greenland	Mathiesen et al. (2000)
Hold With Hope, NE Greenland	Thomson et al. (1999)
Vøring margin, off mid Norway	Ren et al. (2003)
Møre margin, off mid Norway	Brekke et al. (1999)
Northern North Sea Basin	Nadin et al. (1997)
Faroe-Shetland Basin	Nadin et al. (1997); Rudge et al. (2008)
North Rockall Trough	Archer et al. (2005)
Moray Firth to Shetland	Mackay et al. (2005); Rudge et al. (2008)
NW British Isles (Scotland)	Green et al. (1993); Mudge and Jones (2004)
Irish Sea	Cope (1994)
Porcupine Basin	Jones et al. (2001)

Published examples of some regional domal uplifts are listed in Table 2.1. Without constraining the depth of origin, Saunders et al. (2007) suggested that the ascent of narrow hot mantle jets and broadly contemporaneous rifting in areas of uplifts within the NAIP resulted in crustal doming.

A number of Early Cenozoic tectonic events occurred in the Faroe Islands and surrounding areas some of which are exposed onshore as displacements along dyke/fault systems (Rasmussen and Noe-Nygaard, 1970; Geoffroy et al., 1994). Based on measurements onshore of the Faroe Islands Geoffroy et al. (1994) reported two Paleocene strike slip and one compressional event that was contemporaneous with the latest stages of magmatism in the area. Hald and Waagstein (1991) and Waagstein (1988) suggested that the emplacement of the sills of the Faroe Islands was related to tectonically induced doming in the area during the latest stages of or immediately following the final volcanic activity in the area, whilst Geoffroy et al. (1994) more specifically suggested sill emplacement in response to reverse faulting in a NE-SW directed compressional environment shortly prior to the onset of the N Atlantic opening. Localised NE-SW directed extension at 59 – 55 Ma was proposed for the Faroe Islands region by Walker et al. (2011). Ellis et al. (2009) speculated that the positions of the larger sills adjacent to narrow fjords in the actual area could be explained by the involvement of deep-seated lineaments, occurring in these fjords, in the igneous processes during emplacement of these sills.

2.5.1.4. Syn-rift Cenozoic

At around 56-54 Ma the focus of the broadly E-W directed crustal stretching in the proto N Atlantic area, which had previously been accommodated in a relatively wide NNE–SSW trending zone including the Rockall Trough, the Rockall – Hatton area, the Faroe – Shetland Basin and the Møre and Vøring basins as well as at the NE Greenland margin, was re-located into a zone west of the Hatton – Rockall area, the Faroe Plateau and the Vøring Margin on the European side and to the east of the E Greenland margin as seafloor spreading was initiated (Roest and Srivastava, 1989; Saunders et al., 1997; Brekke et al., 1999). At the same time extension between Greenland and North America continued in the Labrador Sea, forming a triple junction with the NE Atlantic rifting south of S Greenland (Roest and Srivastava, 1989). Transform movements between Greenland and N America, which also occurred during this period, were accommodated by the Ungava Fault Zone (Chalmers et al., 1995). The combined spreading on the E and W side of Greenland caused it to move in a roughly northward direction relative to the European and American continents (Roest and Shrivastava, 1989; Geoffroy et al., 1994; Harrison et al., 1999). Late Paleocene to Early Eocene roughly NW-SE trending compressional structures, perhaps related to the northward movement of Greenland during this period of incipient rifting, have been recorded in the northern parts of the Faroe Islands, the Hatton Bank, the N Rockall Trough and in the Faroe-Shetland Basin (Boldreel and Andersen, 1993; Geoffroy et al., 1994; Boldreel and Andersen, 1998; Dean et al., 1999). It is unclear whether similar contemporaneous and perhaps related compressional structures have been recorded at the conjugate E Greenland margin. The Earliest Eocene onset of seafloor spreading in the Norwegian-Greenland Sea and in the Eurasian Basin (Shrivastava and Tapscott, 1986; Ziegler, 1992) were also accompanied by a clockwise rotation of Greenland relative to N America and Eurasia, thus causing compressional deformation in NW Greenland and in the W Barents Shelf (the Eurekan and Spitsbergen orogens) and differences in the rate of seafloor spreading in the initial N Atlantic Ocean (Ziegler, 1992). High spreading rates during the initial phases of seafloor opening of the N Atlantic have been suggested by structural and geochronological studies on pseudotachylites in E Greenland (Larsen and Jakobsdóttir, 1988; Karson et al., 1998). Broadly N – S directed extension has been inferred for the region encompassing the Faroe Islands at ~55 Ma (Walker et al., 2011).

2.5.1.5. Post-rift Cenozoic

Seafloor spreading in the Labrador Sea dissipated prior to about 36 Ma and the main axis of spreading migrated to the existing NE Atlantic spreading ridge (Roest and Srivastava, 1989; Saunders et al., 1997).

Following the peak of igneous and tectonic activity, associated with the formation of the majority of the NAIP in Palaeocene/Eocene times, parts of the crust on both sides of the NE Atlantic rifted margin experienced some comparatively less violent, but in some cases significant, tectonic events in e.g. Mid Cenozoic times often involving vertical movements from local compressional stress regimes, possibly related to intraplate transpression from the actively spreading Mid-Ocean Ridge (MOR) or regional movements in the European plate (Boldreel and Andersen, 1993, 1998; Brekke et al., 1999; Doré et al., 1999). Onshore structural evidences recorded in the Faroe Islands have pointed to the occurrences of broadly NW – SE directed local extension at ~48 Ma and broadly NW – SE oriented compression at ~20 Ma (Walker et al., 2011). In Early Neogene times, dome-shaped uplifts occurred in many places on both sides of the continental margins of the NAIP area (e.g. Japsen and Chalmers, 2000 and references therein; Lundin and Doré, 2002). Asthenospheric diapirism caused by Rayleigh-Taylor instability has been suggested as a causal mechanism for these domal uplifts earlier (e.g Rohrman and Van der Beek, 1996).

2.5.2. Igneous settings

The igneous rocks of the NAIP cover a compositional spectrum ranging from ultramafic picrites to silicic rocks (Table 2.2), but the vast majority of the rocks encountered in the province today are of basaltic compositions. Rocks having been contaminated with crustal material typically occur at or close to the base of volcanic successions in of the basaltic sequences of this province (Larsen et al., 1998; Gibson, 2002). The igneous products occur in a wide variety of modes including fissure or point-source fed lava-flows (e.g. Peate et al., 2003; Single and Jerram, 2004) and ignimbrites as well as plutonic or sheet intrusions (sills/dykes) (Table 2.2), each reflecting the processes and crustal environment that prevailed in that particular area during emplacement of these melts. Most of the igneous activities of the NAIP occurred in the time span from around 64 Ma to around 52 Ma. Two main periods of melt emplacement have been inferred for the NAIP representing overlapping ages at around 62 Ma to 58 Ma and at around 57 Ma to 54 Ma with detectable peaks at ~60

Ma and at ~55 Ma, respectively (e.g. Saunders et al., 1997; Jerram and Widdowson, 2005) (Table 2.2). Igneous activity on smaller scales preceded these main igneous periods in e.g. the N Rockall Trough (Morton et al., 1995; O'Connor et al., 2000) and continued subsequently in many parts of the NAIP area for tens of millions of years (Storey et al., 1998; O'Connor et al., 2000; Tegner et al., 2008) and may still be encountered today on Iceland and on the island of Jan Mayen (Trønnes et al., 1999) (Table 2.2).

2.5.2.1. Early-Middle Paleocene

In a reconstructed map of the NAIP region, intended to show the spatial distribution of the igneous activities for the Early to Middle Paleocene (Fig. 2.5; Table 2.2), the magmatic regions and/or centres at the conjugate E Greenland – NW European margins seem to form irregular and roughly NNE–SSW directed trends, from just to the north of Hold With Hope and southwards to the Ammassalik area along the E Greenland margin and from the Vøring area and southwards to the NW British Isles area at the NW European margin, converging at the CE Greenland–Faroe Islands area (Fig. 2.2; Fig. 2.5). According to current published data the igneous activities in N and W Greenland were spatially isolated from these events.

It is noticeable that regions of the NAIP where igneous activities have been recorded for the Early-Middle paleocene, coincide well with regions that experienced transient uplifts during this period (Fig 2.5.; Table 2.1; Table 2.2). Also, it appears that both the uplifted regions and those parts of the NAIP that experienced the most voluminous igneous production during this period, namely the NW British Isles, the Faroe Islands, the central-east Greenland (CE Greenland) and the Disko region in W Greenland (Upton, 1988; Saunders et al., 1997; Meyer et al., 2007), occurred in the vicinity of old orogenic sutures or fronts from the Palaeozoic Caledonian Orogen at the conjugate E Greenland – NW European margins, from Archaean–Proterozoic orogens at the conjugate E Greenland – NW European margins and from Archaean Nagssugtoqidian–Rinkian Orogen at the conjugate W Greenland – N America margins, i.e. in the Disko – Baffin Island area (Fig. 2.4.; Fig. 2.5.).

2.5.2.2. Late Paleocene and Early Eocene

The inferred trends of igneous activities at the conjugate E Greenland–NW European margin from the Early-Middle Paleocene seem to be more or less repeated in the

Table 2.2. Summary of Early Palaeogene ages for key regions of the North Atlantic Igneous Province. Overlapping ages are commonplace.

Regions	Rock compositions: modes of emplacements	Cited authors
British Isles: ~61 to ~55 Ma	Ultramafic, mafic, silicic: volcanic, plutons, sills, dykes	Gamble et al. (1999); Chambers et al. (2005); Storey et al. (2007)
Rockall-Hatton margin: ~58 to ~53 Ma	Mafic, silicic: volcanic, plutons, sills, dykes	Sinton and Duncan (1998); Hitchen (2004)
Rockall Trough: ~70 to ~54 Ma	Mafic, silicic: volcanic, sills	Hitchen and Ritchie (1993); Morton et al. (1995); Sinton et al. (1998); O'Connor et al. (2000); Archer et al. (2005);
Faroe-Shetland Basin: ~61 to ~55 Ma	Mafic, silicic: volcanic, sills, dykes	Hitchen and Ritchie (1993); Trude et al. (2003)
Vøring margin: ~61 to ~55 Ma	Mafic, silicic: volcanic, sills, dykes	Skogseid et al. (1992); Sinton et al. (1998); Planke et al. (2005)
Møre Margin: ~56 to ~55 Ma	Mafic: sills	Planke et al. (2005)
Faroe Islands: ~61 to ~55 Ma	Ultramafic, mafic: volcanic, sills, dykes	Waagstein et al. (2002); Storey et al. (2007)
NE Greenland: ~59 Ma to ~53 Ma	Ultramafic, mafic: volcanic, sills, dykes	Upton et al. (1995); Price et al. (1997)
CE Greenland: ~61 to ~53 Ma	Ultramafic, mafic, silicic: volcanic, plutons, sills, dykes	Karson et al. (1998); Tegner et al. (1998a); Hald and Tegner (2000); Lenoir et al. (2003); Peate et al. (2003); Storey et al. (2007)
SE Greenland: ~62 Ma to ~55 Ma	Ultramafic, mafic, silicic: volcanic, sills, dykes	Sinton and Duncan (1998); Sinton et al. (1998); Tegner and Duncan (1999); Storey et al. (2007)
W Greenland: ~61 Ma to ~54 Ma	Ultramafic, mafic, silicic: volcanic, dykes	Storey et al. (1998); Larsen et al. (1999a); Geoffroy et al. (2001)
N Greenland: ~64 Ma	Mafic, silicic: volcanic, dykes	Estrada et al. (2001)
Bjørnøya Marginal High: ~54 Ma	Mafic: volcanic	Tsikalas et al. (2002)
Vestbrona, off SW Norway: ~55 Ma	Mafic: volcanic	Bugge et al. (1980)

The ages presented in this table reflect only the main phases of NAIP magmatism. Earlier and subsequent magmatism occurred in many of the same regions as those presented in this table (e.g. Morton et al., 1995; Storey et al., 1998; O'Connor et al., 2000; Tegner et al., 2008 and references in these papers).

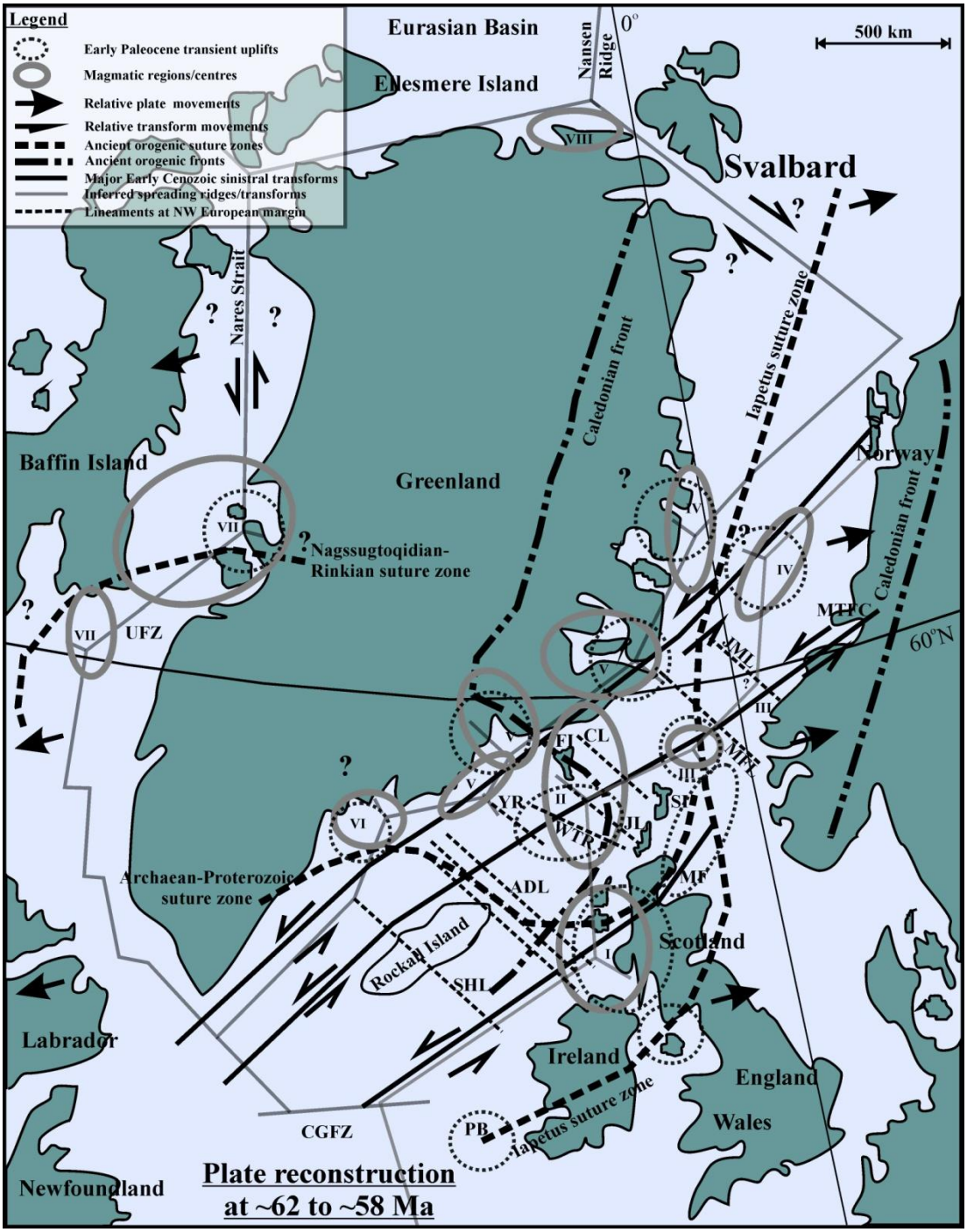

Figure 2.5. Simplified map of the NAIP at around 62 to 58 Ma based on Torsvik et al. (2001a, 201b). The inferred locations of the Caledonian fronts and the Iapetus suture zone are from: Bott (1987); Soper et al. (1992); Ziegler (1992); Masson et al. (1999); Skogseid et al. (2000); Hansen and Brooks (2002); Roberts (2003); Cocks (2005); Foulger et al. (2005a, 2005b). The inferred Archaean–Proterozoic suture zone in the Rockall–Hatton–NW Britain area is modified from Dickin (1992). The inferred Nagssuqtocidian–Rinkian suture zone in the Disko region is modified from Connelly et al. (2006). The three major NE-SW trending sinistral transforms are modified from Nielsen et al. (2007). Broadly NW-SE trending lineaments at the NW European margin are from Kimbell et al. (2005). General spreading directions are from Harrison et al. (1999) and Nielsen et al. (2007). Abbreviations: ADL – Anton Dohrn Lineament; CGFZ – Charlie Gibbs Fracture Zone; CL – Claire Lineament; JL –

Judd Lineament; JML – Jan Mayen Lineament; FI – Faroe Islands; MF – Moray Firth; MFL – Marflo Lineament; MTFC – Møre–Trøndelag Fault Complex; PB – Porcupine Basin; SHL – South Hatton Lineament; SI – Shetland Islands; UFZ – Ungave Fault Zone;WTR –Wyville-Thomson Ridge; YR – Ymir Ridge. Roman numbers I to VIII refer to igneous regions. See text for further explanation.

Late Paleocene and Early Eocene (Fig. 2.6.), apart from a westward relocation of magmatism at the Vøring margin, an eastward relocation of magmatism at the Blosseville Kyst and the establishment of volcanism in the W Barents Sea. Final sea-floor spreading just north of the Faroe Islands occurred farther to the east at ~54 Ma (Bott, 1985). Each part of the double zigzag geometry for the inferred Early Palaeogene magmatic trends of the NAIP in the NE Atlantic area seem to resemble classic rifting trends associated with the embryonic stages of continental rifting where the surface expression of the rift processes appears as interconnected triple junctions at various stages of development (Burke and Dewey, 1973; Ziegler, 1989; Park, 1995; Sears et al., 2005).

The ages and the emplacements of the igneous products of the Rockall-Hatton area have hitherto been poorly constrained although Late Paleocene and/or Early Eocene ages (around 57-55 Ma) are indicated for the Rockall and Hatton banks (Table 2.2). O'Reilly et al. (1998) detected major thermal anomalies west of the Rockall Bank that overprinted all signatures, generated by previous extensional events. As the latest extensions recorded for this area occurred in Early/Mid Paleocene times (Lundin and Doré, 1997; Doré et al., 1999; Tate et al., 1999) it is suggested that, if they formed broadly contemporaneously, the majority of the lavas and central igneous complexes occurring in the Rockall-Hatton area could have been emplaced in the Late Paleocene/Earliest Eocene.

2.5.2.3. Post-rift Cenozoic

Palaeogene post-rift igneous activity within the NAIP in the form of central igneous complexes, sills/dykes/plutons or volcanics of modest volumes of various ages have been reported from W Greenland, E Greenland, NW British Isles and in the N Rockall-Trough (e.g. Storey et al., 1998; O'Connor et al., 2000; Tegner et al., 2008 and references in these papers) and these rocks were emplaced in the same areas as those experiencing voluminous igneous activity in the Paleocene and Early Eocene.

Although the only documented igneous activity in Neogene times outside the Iceland

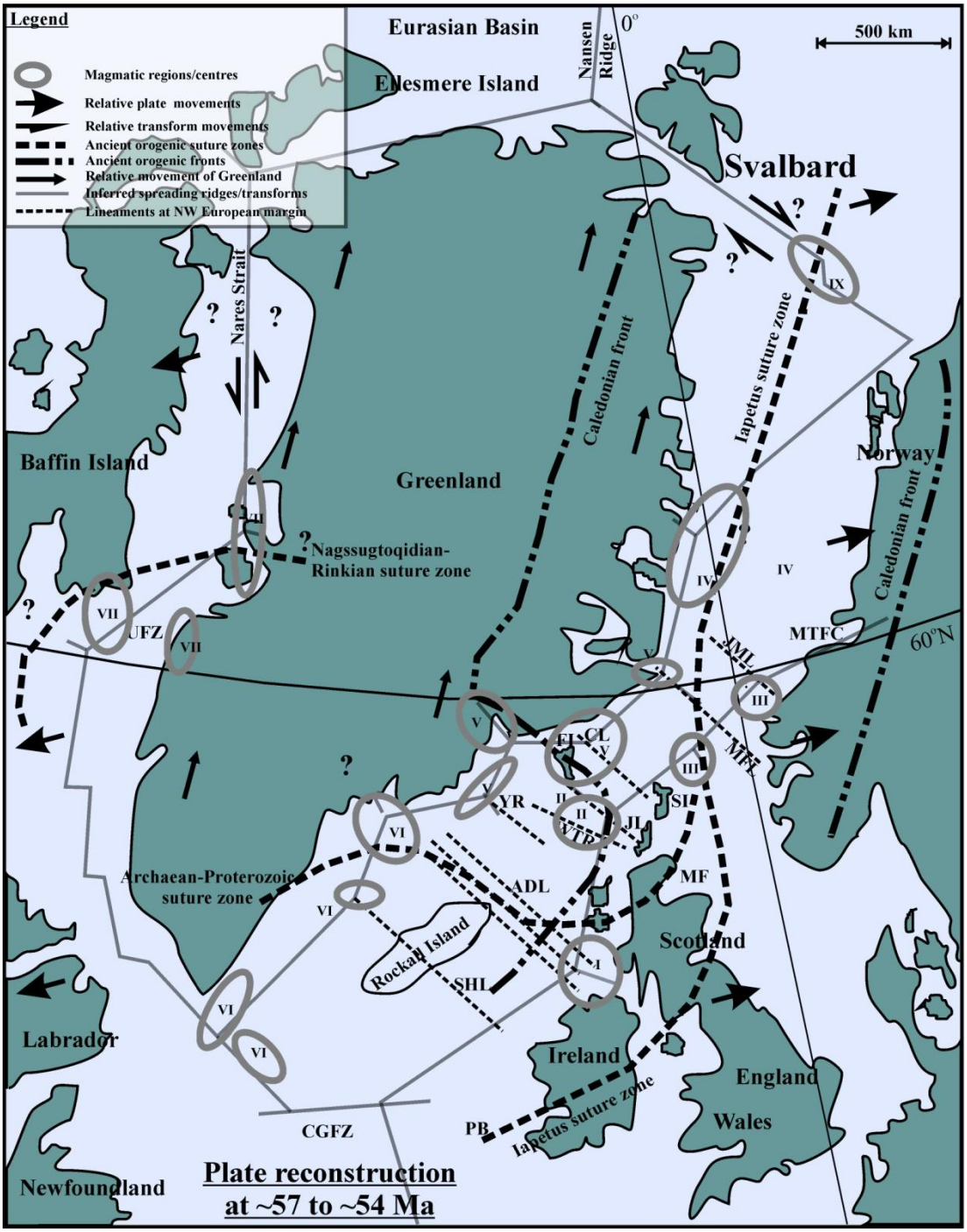

Figure 2.6. Simplified map of the NAIP at around 57 to 54 Ma based on Torsvik et al. (2001a; 2001b). Roman numbers I to IX refer to igneous regions. Other explanation and abbreviations as in Figure 2.3. See text for further explanation.

region occurred on the Jan Mayen Ridge in the Norwegian-Greenland Sea (Gudlaugsson et al., 1988), it is noticable that widespread uplifts within the NAIP during this period were confined to regions, which experienced the most voluminous igneous activity in the Early Palaeogene (Japsen and Chalmers, 2000).

Other late NAIP magmatism, including Iceland and the Faroe-Greenland Ridge, occurred in regions with previous Palaeogene magmatism or they were related to relatively recent NAIP plate reorganisations and the current Iceland igneous region.

2.6. Brief considerations on individual regions of the NAIP

2.6.1. The NW British Isles (Fig. 2.2; I in Fig. 2.5 and Fig. 2.6)

Previous studies have suggested that magmatic centres, concentrated around an Early Palaeogene triple junction in the Hebrides – Ireland area, were instrumental in propelling the contemporaneous magmatism in the NW British Isles (Burke and Dewey, 1973; Geoffroy et al., 1996). The observed NW-SE directed orientation of widespread Paleocene dykes in the NW British Isles (e.g. Speight et al., 1982; England, 1988) point to roughly NE-SW directed extension during emplacement of these intrusions (England, 1988; Geoffroy et al., 1996) and Geoffroy et al. (1996) further proposed that the dyke swarms represented a SE branch (failed arm) of a triple junction that was located in the NW parts of this area. The later Eocene extension in NW Britain (England, 1988; Geoffroy et al., 1996) has been interpreted to result from broadly NW–SE-directed crustal extension associated with the opening of the North Atlantic (Geoffroy et al., 1996). The Early Palaeogene magmatism in NW Britain has previously been associated with melting of the "Iceland Plume" (Upton et al., 2002), although Nadin et al. (1997) tentatively suggested that a separate distinct mantle source may have been active in the NW Britain area during this period. Tectonic activity has also been invoked by some authors to have facilitated melt generation in the area (Upton et al., 2002; Chambers et al., 2005).

2.6.2. The Faroe Islands – N Rockall Trough (Fig. 2.2; II in Fig. 2.5 and Fig. 2.6, as well as V in Fig. 2.6)

Geoffroy et al. (1994) argued in favour of an Early Palaeogene triple junction that was more or less centred on the Faroe Islands, while Burke and Dewey (1973) proposed that a contemporaneous triple junction was situated in the Faroe Island – N Rockall Trough area with associated magmatic centres in the N Rockall Trough and to the SSW and/or SW off the Faroe Islands. This accords with inferences by Waagstein (1988) suggesting that the depocentre that provided igneous products to the Beinisvørð Formation (formerly lower basalt series: e.g. Passey and Bell, 2007) in the Faroe Islands was located in the southern or central part of the Faroe Islands

shelf. A number of NW-SE trending lineaments have been reported for this region (Kimbell et al., 2005) and sub-parallel igneous emplacement trends of contemporaneous central igneous complexes in the SW parts of the area have been interpreted to result from control by local lineaments (e.g. Archer et al., 2005). In theory, failed NW-SE trending rift arms or leaky transforms from a triple junction that migrated within this region during Paleocene and Eocene times could have generated some of these sub-parallel igneous trends. If potential triple junctions located in the Faroe Islands area and off NW Britain were joined by extensional/transform faults, these would presumably have been sub-parallel to the N–S-trending contemporaneous dykes reported for mainland Scotland to the E and S of Skye as reported by Speight et al. (1982). Morton et al. (1995) tentatively suggested that volcanism at the Rosemary Bank in the N Rockall Trough was due to a separate underlying source, and Hitchen et al. (1997) likewise argued in favour of a local source for the Early Palaeogene rocks in the same area. Other authors have associated the Early Cenozoic magmatism in this area with the "Iceland plume" (Holm et al. 2001; Archer et al. 2005).

2.6.3. The NE Faroe – Shetland Basin; N North Sea; offshore SW Norway (Fig. 2.2; III in Fig. 2.5 and Fig. 2.6)

Previous studies have suggested that a triple junction to the NNE off the Shetland Isles was operational in Paleocene times (Burke and Dewey, 1973) and farther to the NNE, i.e. off the SW Norwegian coast, a magmatic centre was active during Late Paleocene and Early Eocene (Bugge et al., 1980). While Kanaris-Sotiriou et al. (1993) interpreted Paleocene basaltic and intermediate volcanic rocks of the Erlend Complex in the northern North Sea to be a result of volcanism induced by extension in the area, Mudge and Jones (2004) and Rudge et al. (2008) attributed contemporaneous uplifts and igneous activity, recorded in the northern North Sea and the NE Faroe – Shetland Basin area, to the activity of the "Iceland Plume". Active involvement of a Paleocene precursor to the Jan Mayen Fracture Zone during the formation of the igneous products at the Vestbrona area offshore SW Norway has been inferred previously (Torske and Prestvik, 1991). The Møre – Trøndelag Fault Complex, which intersects the same area offshore the SW Norwegian coast, was probably active during this period as well (Doré et al., 1997; Redfield et al., 2004).

2.6.4. The Vøring margin; NE Greenland (Fig. 22; IV in Fig. 2.5 and Fig. 2.6)

Inferred magmatic activity at the Vøring margin in Early Paleocene times occurred at some distance to the east of the future break-up zone, but it migrated westwards with time (Eldholm et al., 1989). Early Eocene magmatism in NE Greenland and at the Vøring margin were closely related spatially (Viereck et al., 1988; Upton et al., 1995) and recent studies have revealed a continuous Early Eocene igneous complex that directly linked these two regions together in the earliest stages of sea-floor spreading (Olesen et al., 2007). The volume and rock types of Early Cenozoic igneous products of the Vøring margin resemble those commonly found in the Rockall Trough (Upton, 1988) and on the NW British Isles (Viereck et al., 1988 and references therein). Volumes of igneous products from this period decreased from the central Vøring margin towards the south and north respectively (Berndt et al., 2001), thus perhaps indicating melt supplies from a relatively confined central magmatic source. On the one hand, an "Iceland Plume" origin has been inferred previously for the magmatism in NE Greenland and at the Vøring margin (Skogseid et al., 1992; Upton et al., 1995); on the other hand, Eldholm et al. (1989) and Van Wijk et al. (2001) suggested that decompression melting triggered by extension/rifting was responsible for the magma generation at the Vøring margin. Recent re-interpretations of available magnetic, bathymetric, gravity and seismic data from the Vøring margin strongly suggest local Eocene magmatism related to an Azores-type triple junction, linked to the embryonic stages of sea-floor spreading in the Norwegian–Greenland Sea (Gernigon et al., 2008).

2.6.5. The (central-east) CE Greenland (Fig. 2.2; V in Fig. 2.5 and Fig. 2.6)

The voluminous and widespread Early Cenozoic igneous products in this region may have been produced by the activities of several contemporaneous magmatic centres (Callot et al., 2002). Localities of active triple junctions for this period have been suggested previously for the region off Kangerlussuaq (Burke and Dewey, 1973; Karson and Brooks, 1999; Tegner et al., 2008), but other potential sites of tectonomagmatic activity may be inferred from Early Paleocene magmatism and uplifts reported for this area in previous studies (Larsen and Watt, 1985; Nielsen, 1987; Mathiesen et al., 2000; Callot et al., 2002; Peate et al., 2003). This vast area was characterized by Early Cenozoic episodic igneous activity and frequent migration of magmatic centres (Larsen and Watt, 1985; Peate et al., 2003), and at

least three distinct Early Cenozoic rifting events have been recorded for this region, some of which occurred far inland (Nielsen, 1987; Olesen et al., 2007). The bulk of the rift-related magmatism in CE Greenland and the Faroe Islands at ~55 Ma occurred close to the Blosseville Kyst (Nielsen, 1987; Larsen and Watt, 1985; Larsen et al., 1999b), which is in accordance with previous inferences suggesting that the magmas of the younger basalt formations of the then neighbouring Faroe Islands were supplied from the north during this period (Waagstein, 1988; Larsen et al., 1999b). The onset of final sea-floor spreading at latitudes intersecting the Blosseville Kyst occurred farther to the east along the now extinct Ægir Ridge at ~54 Ma (Bott, 1985). On the one hand, Larsen and Marcussen (1992) and Hanghøj et al. (2003) considered the Early Cenozoic magmatism in CE Greenland to be linked to extension in the area; on the other hand Tegner et al. (2008 and references therein) suggested that the same magmatism resulted from actions of the "Iceland Plume".

2.6.6. The Hatton – Edoras margin; SE Greenland (Fig. 2.2; VI in Fig. 2.5 and Fig. 2.6)

Only parts of this extensive area have been investigated in details, but their close proximity in Early Cenozoic times may suggest that these two margins perhaps shared some magmatic centres prior to the sea-floor spreading in the region. Sites of potential Early Cenozoic triple junctions within this region have been implied previously (Burke and Dewey, 1973; Bull and Masson, 1996; Karson and Brooks, 1999; Nielsen et al., 2002; Nielsen et al., 2007) while contemporaneous separate magmatic centres and domal uplifts recorded within this region previously (e.g. Morgan and Barton, 1990; Barton and White, 1997; Larsen and Saunders, 1998; Elliot and Parson, 2008) could point to separate events that involved tectonomagmatic activities outside potential sites of triple junctions of this region as well. The occurrences of major lineaments within the actual region (Kimbell et al., 2005) could potentially have facilitated igneous activity if these were active during the actual time span. Morgan and Barton (1990) detected a large separate magmatic centre that was active on the NW Hatton Bank in the Early Cenozoic, and recent work by Elliot and Parson (2008) suggested that the Hatton rifted margin could be divided into three separate segments, each of which with a distinct magmatic evolution. These authors tentatively suggested that the northern parts of the Hatton margin only experienced diffuse spreading in the Early Eocene prior to Chron 21

(~50 Ma) when regular coherent spreading was established. The phenomenon of diffuse sea-floor spreading has previously been interpreted to reflect low obliquity rifting in a magmatically starved environment (Corti et al. 2001). In the southernmost parts of this margin, Elliot and Parson (2008) recorded relatively concentrated syn- to post-break-up volcanism. Most authors infer the "Iceland Plume" to be the main source for the magmatism at these two margins (Barton and White, 1997; Fitton et al., 2000), but Edwards (2002) considered any "Iceland Plume" dominated processes occurring further eastwards toward the Rockall – Hatton Basin to be problematic, and Barton and White (1997) suggested that there was no major long-distance lateral migration of the melt supplies to the magmatism at the Edoras Bank.

2.6.7. TheWest Greenland – Baffin Island area (Fig. 2.2; VII in Fig. 2.5 and Fig. 2.6)

Reported trends of major faults that presumably were active in the W Greenland – Baffin Island area in Early Cenozoic times (Chalmers et al., 1995; Geoffroy et al., 2001; Callot et al., 2002; Skaarup et al., 2006) together with reported locations of concentrated contemporaneous igneous activities and doming (Chalmers et al., 1995; Callot et al., 2002; Japsen et al., 2005; Skaarup et al., 2006) suggest that magmatism was confined to areas adjacent to kinks in the contemporaneous rifting trends. These areas of concentrated tectonomagmatic activity include the southern tip of the Ungava Fault System and the area in the vicinity of the islands of Ubekendt Ejland and Disko. Another kink or potential triple junction between major faults interpreted to have been active during the same period occurred further to the north between Baffin Island, Ellesmere Island and W Greenland (Burke and Dewey, 1973; Torsvik et al., 2001; Nielsen et al., 2007). Gill et al. (1995) associated the high-temperature melting required for the generation of Early Cenozoic picrites in this region with a separate hot "Baffin Bay Plume" rather than with a distant asymmetric/irregular "Iceland Plume" as suggested by e.g. Chalmers (1997) and Storey et al. (1998). The generation of Eocene dykes in SW Greenland and the volcanism along the Ungava Fault System have been attributed to melting in response to plate reorganizations in the area during that period of time (Storey et al., 1998; Larsen et al., 1999a; Skaarup and Pulvertaft, 2007 and references therein).

2.6.8. N Greenland (Fig. 2.2; VIII in Fig. 2.5)

The Early Cenozoic Kap Washington Group is thought to have been generated in response to continental rifting related to the break-up of the Laurasian plate (Estrada et al., 2001). A contemporaneous active triple junction off Kap Washington would be in accordance with studies of Torsvik et al. (2001a, 2001b) and Nielsen et al. (2007).

2.6.9. The W Barents region (Fig. 2.2; IX in Fig. 2.6)

Volcanic rocks in the W Barents Sea (Vestbakken Volcanic Province) located at the inferred trace of the Caledonian suture zone are interpreted to have formed in response to Early Eocene transtension associated with plate reorganizations in this region (Tsikalas et al., 2002).

2.6.10. Recent magmatism NE Atlantic (Fig. 2.2)

Apart from Iceland, which is considered to be the embodiment of the "Iceland plume" by many authors, recent volcanism in the NAIP area occurring on Jan Mayen and at the Vesteris Seamount have been interpreted to result from extension-related decompression melting, where enhanced melting has been inferred for the Jan Mayen magmatism due to elevated water content in the source region (Haase and Devey, 1994; Haase et al., 1996).

2.7. The NAIP in the context of rift geometries

The overall geometry of the NAIP with apparent double zigzag trends of igneous activities at the conjugate NW European – E Greenland margins (Fig. 2.4; Fig. 2.5) and the longevity of the igneous activity, together with the involvement of the Faroe Islands – Rockall microcontinent and the Jan Mayen microcontinent in the rift processes (Roberts and Searle, 1979; Kodaira et al., 1998; Edwards, 2002; Mjelde et al., 2008), seem to suggest a complex and discontinuous break-up history. A comparable complex rifting evolution has been reported for the recent Afar (E **Af**rican – **Ar**abian) Volcanic Province where migration of magmatic centres and triple junctions have been of common occurrences and where microcontinents (Danakil and Aisha) have been involved in the rifting/igneous processes and not uncommonly have defined their own secondary triple junctions with associated magmatism (Tesfaye et al., 2003; Wolfenden et al., 2004; Garfunkel and Beyth, 2006).

Individual large mantle plumes have been linked to the magmatism, rifting and triple junction formation in the Afar Volcanic Province previously (Garfunkel and Beyth, 2006), but other authors have argued that the East African rift system in general developed in response to global plate reorganizations (e.g. Wolfenden et al., 2004). The association between enhanced magmatism and rift geometry, that is, triple junctions (Sears et al., 2005) or kinks in rifting trends (Abdel-Rahman and Nassar, 2004; Wolfenden et al., 2004), is well known. In this context the evolution of the proto-Iceland region may be of relevance for the Early Palaeogene NAIP magmatism, as a great increase in the volume of magma production in that area in Middle Palaeogene times (Foulger and Anderson, 2005) coincided with the establishment of the ridge – ridge – transform triple junction (Reykjanes ridge – Kolbeinsey ridge – Faroe transform fault) as recorded by Bott (1985). Indeed, the present rifting trend of the N Atlantic displays a pronounced anticlockwise rotation in going from south to north across Iceland (Fig. 2.2), and a recent study has pointed to the potential existence of a current active E-W trending transform fault underneath Iceland (Foulger, 2006), i.e. the Iceland area could in fact still harbour an active triple junction. The common occurrences of dissimilar geochemical and isotopic signatures in rift-related basalts produced within constricted periods of time and within confined areas in: the East African rift system (Barrat et al., 1998; Orihashi et al., 1998; Rogers et al., 2000; George and Rogers, 2002; Keranen and Klemperer, 2008); in Iceland (Kitagawa et al., 2008); in E Greenland (Hanghøj et al., 2003; Peate and Stecher, 2003), around the N Rockall Trough (Hitchen et al., 1997) and in the Azores (Beier et al., 2008) may point to heterogeneous compositions of their respective mantle reservoirs.

2.8. The NAIP in the context of plate tectonic processes in adjacent areas

In the context of Early Cenozoic global plate-tectonic processes, it is noteworthy that the relative convergence of Africa and Iberia with respect to W Europe and the associated compression between these two tectonic plates came to a standstill from the earliest Paleocene to the Early Eocene (Rosenbaum et al., 2002), that is, in the same time interval as the occurrence of most of the Early Cenozoic NAIP magmatism and the initial stages of continental break-up of the proto N Atlantic area. The causal mechanism for the standstill in relative plate convergence has previously been interpreted to result from a contemporaneous continental collision in the Alps

between the African and European plates (eastern parts) at around 65 Ma (Jolivet and Faccenna, 2000; Rosenbaum et al., 2002). A recent complementary tectonic model suggested termination of compression and promotion of extension in the NW Atlantic area in the Early Palaeogene in response to major left-lateral displacements between Greenland and NW Europe, which ultimately resulted in narrowing (contraction) and retreat of the European plate relative to the African plate (Nielsen et al., 2007). In a rifting perspective, Lundin and Doré (2005) argued that the Early Cenozoic igneous–tectonic activities in the proto N Atlantic area that generated the NAIP were merely a result/expression of the final phases of the ongoing break-up of Pangaea, spatially and temporally linking the Early Paleocene central Atlantic rifting (Ziegler, 1989, 1992) in the south with the Early Eocene rifting in the Eurasian Basin to the north (Srivastava, 1985; Brown et al., 1987).

2.9. Summary of chapter 2 and concluding remarks

In this chapter a brief review has been attempted on the key magmatic centres of the NAIP presented in a geodynamic framework, focusing on their interrelationships and the tectonic developments during the onset of the NAIP. The specific conditions directly prior to the onset of the NAIP and the continued development of the region during the Palaeogene, based on the findings of the present study, can be highlighted as follows:

(1) The onset of the rifting and igneous activity of the NAIP area was a temporal and spatial continuation of the rifting in the adjacent central Atlantic Ocean to the south and a precursor for the rifting in the Eurasian Basin to the north. The main igneous and tectonic activities in the NAIP in Early Palaeogene times coincide with contemporaneous changes in the relative motion between the European and African plates, which perhaps halted the previous compressional regimes in the NW Atlantic during this time span.

(2) Taken all together, the apparent geometry of the main igneous regions of the NAIP at the conjugate E Greenland – NW European margins displays similarities with trends inferred for the embryonic stages of classic continental rifting regimes consisting of numerous more or less interconnected triple junctions. The occurrences of numerous smaller central igneous complexes and/or seamounts that are widely scattered at the NW European margin may not

be entirely in accordance with a simple rifting model, if most of these formed contemporaneously with the larger igneous regions of the NAIP.

(3) The close proximity between ancient orogenic sutures/fronts and regions of the NAIP that experienced Early Cenozoic magmatism and/or transient uplifts may indicate that the embryonic stages of magmatism and continental rifting within these areas could have been facilitated by lithospheric heterogeneities and/or weaknesses commonly associated with such tectonic features, irrespective of whether global plate reorganizations or a single large mantle plume were the driving forces for the onset of the NAIP.

Chapter Three

3. Field occurrences and geometries of sills and associated dyke networks

3.1. Prelude to chapter three

Flood basalt provinces and associated volcanic rifted margins remain some of the largest manifestations of igneous activity at the Earth's surface (Chapter 2). They are generally emplaced as an initial onset phase, through a main eruptive sequence and finally a waning phase and intrusive equivalents can be emplaced throughout these phases (Jerram and Widdowson, 2005). The intrusive networks or "plumbing systems" that underpin flood basalt systems can be extensive and varied (e.g. Ernst et al., 2005; Cartwright and Hansen, 2006) and provide important information on how the magmas reach the surface. Large sill complexes have been reported for many of the large igneous provinces such as Karoo (Cox, 1980; Galerne et al., 2008), Etendeka (Thompson et al., 2007) and the NAIP (Bell and Butcher, 2002; Cartwright and Hansen, 2006). Sill emplacement frequently accompanied the Early Cenozoic igneous phases of the NAIP and have been recorded for: several offshore sedimentary basins at the NW Atlantic margin (Hansen, 2006 and references therein), onshore NW Britain (Gibb and Henderson, 2006), onshore Faroe Islands (Rasmussen and Noe-Nygaard, 1970; Passey and Bell, 2007; Passey and Jolley, 2009), at the E Greenland margin (Larsen and Marcussen, 1992) and at the W Greenland margin (Storey et al., 1998) (See also Fig. 2.2). The large sills of the Faroe Islands are intruded into the main lava pile, a phenomenon that is important for several reasons including that it can potentially provide a better understanding of the nature of active plumbing systems during the latest stages of igneous activity in continental flood basalt provinces (CFB). Also, the features of these sills, which crop out in crystalline rocks, can be compared with sills encountered in sedimentary basins/sequences thus perhaps offering additional insights into the formation of sill complexes occurring in sedimentary settings.

While dykes are ubiquitous at most crustal levels in regions that have experienced igneous activity, the role of sills in magmatic plumbing systems that feed igneous

activity on the surface and the exact sill-feeder relationships are more ambiguous. Sills may themselves be fed either by dykes or other adjoining sills (Hansen et al., 2004; Cartwright and Hansen, 2006; Thomson, 2007) and interconnected sills building up intrusive complexes in sedimentary basins could initially have acted as active parts of plumbing systems that fed surface magmatism (Larsen and Marcussen, 1992; Bell and Butcher, 2002; Hansen et al., 2004; Cartwright and Hansen, 2006; Thomson, 2007). While some previous studies have suggested formation of saucer-shaped sills by melts being supplied from marginal dykes that first intrude/inflate the inclined outer sill sections followed by intrusion/inflation of the inner sub-horizontal basal sections (Francis, 1982; Chevallier and Woodford, 1999) (Fig. 3.1a; Fig. 3.1b), more recent models mostly infer melt injection from central sources that first generate sub-horizontal inner sill sections followed by the development of more inclined outer parts (Malthe-Sørensen et al., 2004; Thomson, 2004; Thomson and Hutton, 2004; Hansen and Cartwright, 2006; Goulty and Schofield, 2008) (Fig. 3.1c). Variations in sill shapes may reflect differences in the depth of intrusion and/or differences in the mechanical properties of the host-rocks as well as presence or absence of tectonic activity in the affected area (Galland et al., 2003; Malthe-Sørensen et al., 2004; Galland et al., 2006). Mechanical and numerical modelling studies have shown that melt intruded into static non-deformed homogeneous sediments have the potential to develop into saucer-shaped sills (Galland et al., 2003; Malthe-Sørensen et al., 2004; Galland et al., 2006; Galland et al., 2009) (Fig. 3.1d). It has been argued earlier that the saucer-shape of a sill (sill climbing) results from asymmetries in the local stress fields that develop during sub-horizontal sill propagation in response to interactions between the inflating sill and its overburden and starts to form when the length across the inner section of the sill versus the thickness of the overburden reach a certain factor (e.g. Pollard and Holzhausen, 1979; Fialko, 2001; Malthe-Sørensen et al., 2004; Thomson, 2007; Goulty and Schofield, 2008; Polteau et al., 2008). More specifically, i) Malthe-Sørensen et al. (2004) argued that sills would be flat unless their inner diameter exceeded the intrusion depth by a factor of two or three ii) Pollard and Holzhausen (1979) suggested that sill climbing would be greatly enhanced when intrusion depth divided by sill radius $d/r \leq 2$ while iii) Fialko (2001) interpreted radius versus depth ratios of $r/d > 1$ to be necessary for upward deflections of propagating sill margins to

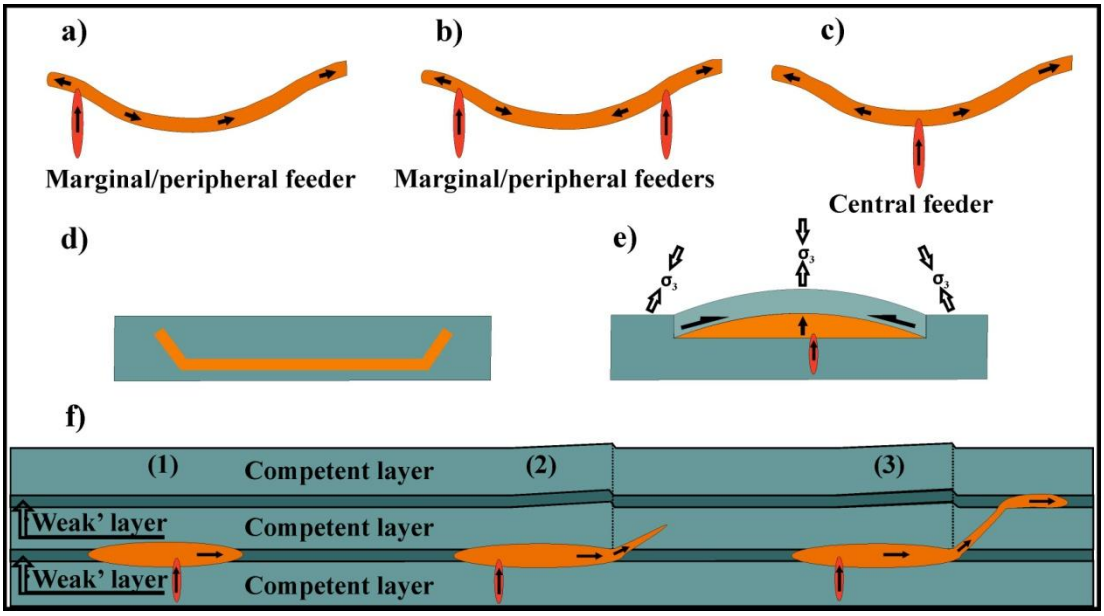

Fig. 3.1. a) Saucer-shaped sill fed from a marginal dyke on one side of the sill (e.g. Francis, 1982). b) Saucer shaped sill fed from more than one marginal dyke (e.g. Chevallier and Woodford, 1999). c) Saucer-shaped sill is fed from a central source (e.g. Rasmussen and Noe-Nygaard, 1970; Malthe-Sørensen et al., 2004). d) Sills intruded into sedimentary basins commonly develop flat inner sections and steeply inclined outer sections (Malthe-Sørensen et al., 2004; Galland et al., 2009). e) Asymmetrical sill inflation in homogeneous material due to displacement/doming of overburden result in extension and rotation of the least principal stress axes (σ_3) at sill margins thus triggering upward deflection of propagating margins (Pollard and Holzhausen, 1979) or tensile failure of overburden above these margins (Goulty and Schofield, 2008). f) Sub-horizontal sill propagation in a relatively 'weak' layer in stratified host rocks (1) gives way to sill climbing through a more competent layer (2), due to asymmetries at sill margins resulting from rupture/folding of overburden, followed by propagation in a 'weak' layer (3) at higher crustal level (Based on: Kavanagh et al., 2006; Thomson 2007; Menand, 2008). Full arrows indicate directions of magma flow. Open arrows indicate direction of least principal stress axes σ_3. One-sided arrows indicate relative shear movements. See text.

occur. In more details, the processes of sill climbing in homogeneous host-rocks, where certain sill sizes versus intrusion depths can be observed, are thought to involve asymmetrical sill inflation in response to larger volumes of magmas being emplaced above an initial sub-horizontal plane of sill emplacement than below the same plane in response to displacement/doming of the Earth's (free) surface (Pollard and Holzhausen, 1979; Fialko, 2001; Goulty and Schofield, 2008) (Fig. 3.1e). The displacement/doming of the overburden should in turn result in sub-horizontal extension and rotation of the least principal stress axes (σ_3) at sill margins (Fig. 3.1e) thus triggering upward deflection of the propagating margins (Pollard and

Holzhausen, 1979) or result in tensile failure of the overburden immediately above these margins (Goulty and Schofield, 2008). If true, these inferences would mean that sills intruded into homogeneous host-rocks at similar crustal levels should possess roughly similar lengths across their inner sections while sills intruded at any crustal depths may take the form of sub-horizontal sheets if the desired radiuses versus depths ratios are not achieved. Broadly similar processes during sill emplacement in stratified sedimentary successions that possess variable mechanical properties would expectedly result in sub-horizontal sill propagation in a relatively 'weak' layers and sill climbing through more competent layers (Kavanagh et al., 2006; Thomson, 2007; Menand, 2008) (Fig. 3.1f). Sill intrusion into unconsolidated sediments may require mechanisms that are different from those suggested for sill emplacements in relatively rigid host-rocks, as volume changes in strata both below and above a propagating sill from sediment compaction and fluid expulsion may match the volume of the intruding sill (Einsele et al., 1980), thus probably nullifying the sill–overburden interactions required to generate asymmetries of the stress fields at sill margins.

In this thesis the first detailed documentation of a sill complex intruded into a basaltic lava pile is presented. Field relationships of the saucer-shaped sills i.e. the Eysturoy Sill, the Streymoy Sill, the Svínoy-Fugloy Sill, the Kvívík Sill, the Morskranes Sill, the Sundini Sill and the (much smaller) Langaregn Sill as well as at the dyke network intersecting the area intruded by these sills are investigated.

This chapter contains a thorough description of the field occurrences of sills from the Faroe Islands at all scales including mapping in electronic 3D maps and in ordinary 2D profiles (3.2) in addition to field descriptions and mapping of dykes/feeders in the actual area (3.3). Particularities of sill margins are described and sill–sill contacts, sill–dyke contacts as well as sill–host rock contacts are dealt with (3.4). Tectonic effects on host rocks associated with sill emplacement and post-magmatic deformation within the investigated sills are briefly described/interpreted (3.5). Various physical conditions necessary for sill emplacement to occur are considered in a discussion section together with earlier emplacement theories, new proposed emplacement theories as well as host rock environment during emplacement of the actual sills (3.6). The chapter ends with a brief summary and concluding remarks (3.7).

3.2. General sill occurrences and geometries

The investigated sills have been plotted in 3D maps (Fig. 3.2; Fig. 3.3; Fig. 3.4) using ArcGIS software. The workflow during ArcGIS plotting is briefly outlined in appendix 1.

The 7 sills of dealt with in this study underlie an area measuring more than 60 km^2 combined and they can be encompassed within a total sub-vertical distance of ~840 m perpendicular to the layered basalts of the Malinstindur, Sneis and Enni formations, but there is a considerable overlap in the sub-vertical extent at which many of the sills are exposed in the regional stratigraphy (Fig. 3.2; Fig. 3.3). The sedimentary Sneis Formation (Passey and Jolley, 2009) is intersected by the Streymoy, the Eysturoy and the Morskranes sills and perhaps also by the Svínoy-Fugloy Sill (Fig. 3.2). The general appearances of the investigated intrusions indicate sub-horizontal or slightly inclined basal sections for all sills that gradually give way to slightly steeper outer sections without any detectable transition zone(s) between inner and outer sections (Fig. 3.4; Fig. 3.5). The inclinations of the steeper sill sections rarely exceed around 45°, but far the largest parts of these intrusions display inclinations that are less than 15° relative to the horizontal plane. Hence, any specific angles of sill transgression cannot be determined due to the gradual changes in sill inclination.

Although all sills from this study display similar very low-angle contacts between basal sill sections and layered crystalline/sedimentary host-rocks in addition to displaying similarities in their overall saucer-shaped geometries and arcuate inclined margins (e.g. Fig. 3.6), they can be grouped into two distinct categories based on some distinct characteristics.

(1) In accordance with distinct bimodal thickness occurrences and general geometric characteristics, each of the Streymoy and the Eysturoy sills can be divided into two (NW and SE) segments joined roughly halfway along their apparent longitudinal axes (Fig. 3.4; Fig. 3.5). The maximum thicknesses of the NW segments of both these sills measure 25 ± 5 m whereas maximum thicknesses of 45 ± 5 and 55 ± 5 m have been measured for the SE segments of the Streymoy and the Eysturoy sills respectively. As there are only moderate thickness

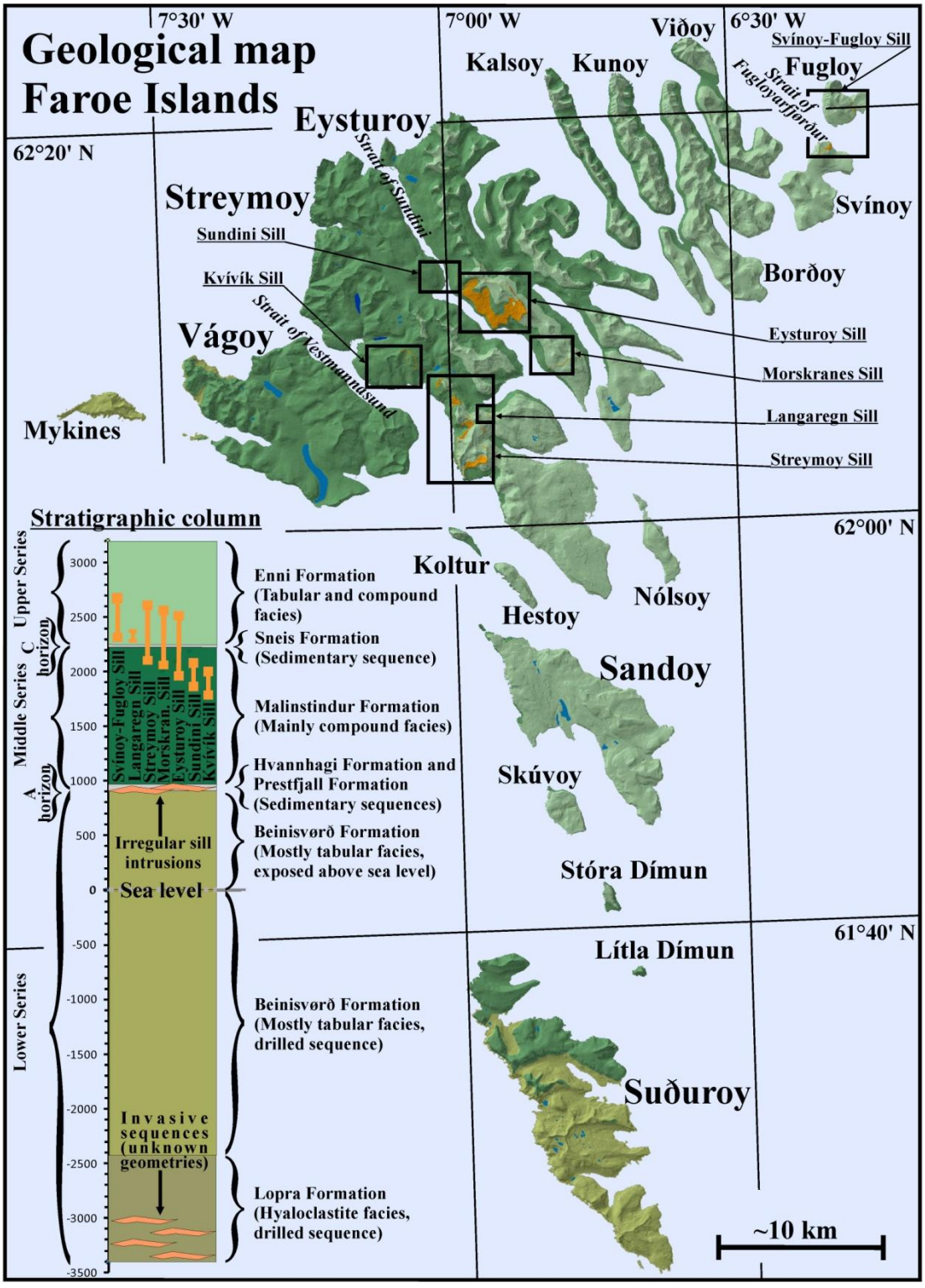

Fig. 3.2. Basaltic formations and stratigraphic column are as in Fig. 2.3. Sills from this study are indicated by labelled rectangles on the map and their vertical extents are indicated by vertical bars on the stratigraphic column. The sills are arranged from left to right in the stratigraphic column according to decreasing altitudes of their basal sections. See text.

variations within each of these segments, similarities in emplacement processes might be envisaged for these two sills. The NW segments of both sills were emplaced at ~200 to ~250 m lower stratigraphic levels relative to their SE counterparts when measured at locations roughly halfway along their respective longitudinal ($A - A^{I} - A^{II}$) profiles (Fig. 3.5a; Fig. 3.5b). These two segmented sills appear to have been preserved in near original extent along their longest axis and parallel alignments of layers in uplifted overburdens relative to layers in the surrounding host basalt suggests sub-vertical uplifts on top of relatively uniformly inflated intrusions. The uniform and relatively great thicknesses along the basal SW margins of the Eysturoy and the Streymoy sills and the NE directed dip of their SW extremities (Fig. 3.3a; Fig. 3.3b) may suggest that the segments building up these sills originally displayed some degree of symmetry with broadly NE directed dip along their presumed missing palaeo SW margins. The NE-SW directed cross-section of the well-preserved SW margin currently exposed of the Svínoy–Fugloy Sill could give a hint to original geometries of these presumed missing SW sections in the Eysturoy/Streymoy sills (Fig. 3.5a; Fig. 3.5b). Reconstructions based on combinations of NE-SW directed cross-sections from all these three sills suggest maximum initial widths of ~5 km ± 0.5 km (Fig. 3.3a; Fig. 3.3b). For the Streymoy Sill the reconstructed area of extent would accordingly be ~45 ± 4.5 km^2, and for the Eysturoy Sill it would approximate ~40 ± 4 km^2 (Fig. 3.3a; Fig. 3.3b). Consequently, estimates of the maximum initial volumes for the reconstructed Streymoy and Eysturoy sills suggest figures in the vicinity of ~2 km^3 for each of these intrusions. Composite sills of comparable sizes are of common occurrences in sedimentary basins along the NW European margin (e.g. Hansen et al., 2004).

(2) The Kvívík, the Morskranes and the Sundini sills all display increased thicknesses from less than 0.5 m at their basal NW or W margins to a maximum of 20 ± 5, 15 ± 5 and ~7 m respectively, at their elevated SE, E or NE margins (Fig. 3.5). There are no evidences of any uplifts of the strata overlying the basal and thinnest parts of these intrusions, suggesting accommodation of intruding melts solely by elastic displacement of the host basalts at these localities. The slightly saucer-shaped geometry of these sills and the low average thicknesses of their basal sections, which commonly are no greater than those of intersecting linear sub-vertical dykes, suggest different intrusion styles for these sills

compared to the dykes they intersect. Also, the very limited thicknesses of the bulk of the saucer-shaped basal parts of these intrusions clearly demonstrate that large-scale sill inflation is not necessarily a precondition for the formation of saucer-shaped sills in basaltic lava piles. The wedging-out of the sills at their basal sections suggests that if these intrusions initially covered a larger area, any potential missing parts were attached to the thicker inclined margins.

It is problematic to determine the exact geometry of the Svínoy-Fugloy Sill, as only parts of it are exposed above sea level. Although most parts of this sill display thicknesses of 30 ± 5 m, reduced thicknesses in the NNE and the SSW parts may suggest similarities with the sills in group (2) even though the intrusion could be

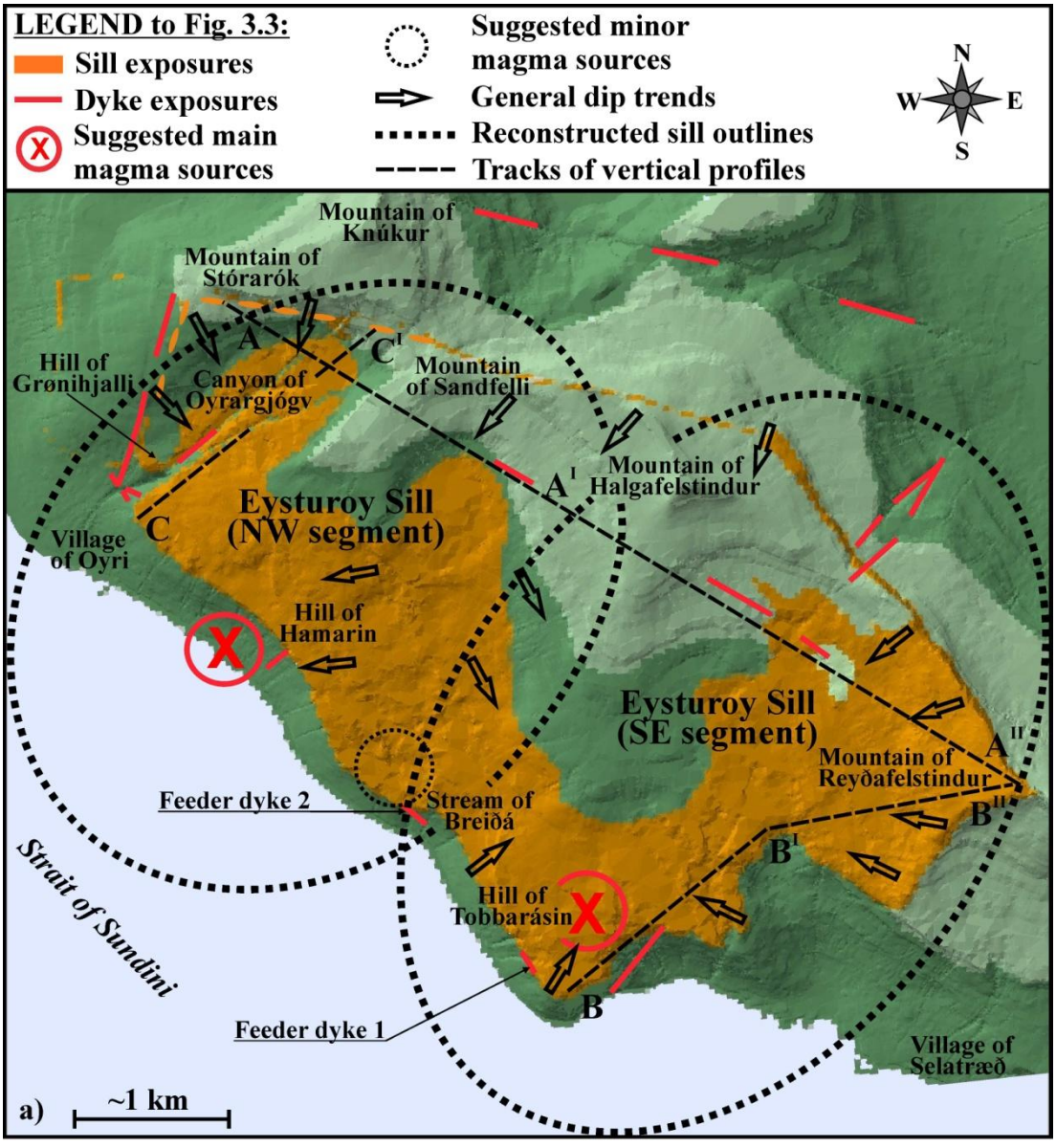

Figure 3.3. (Continued)

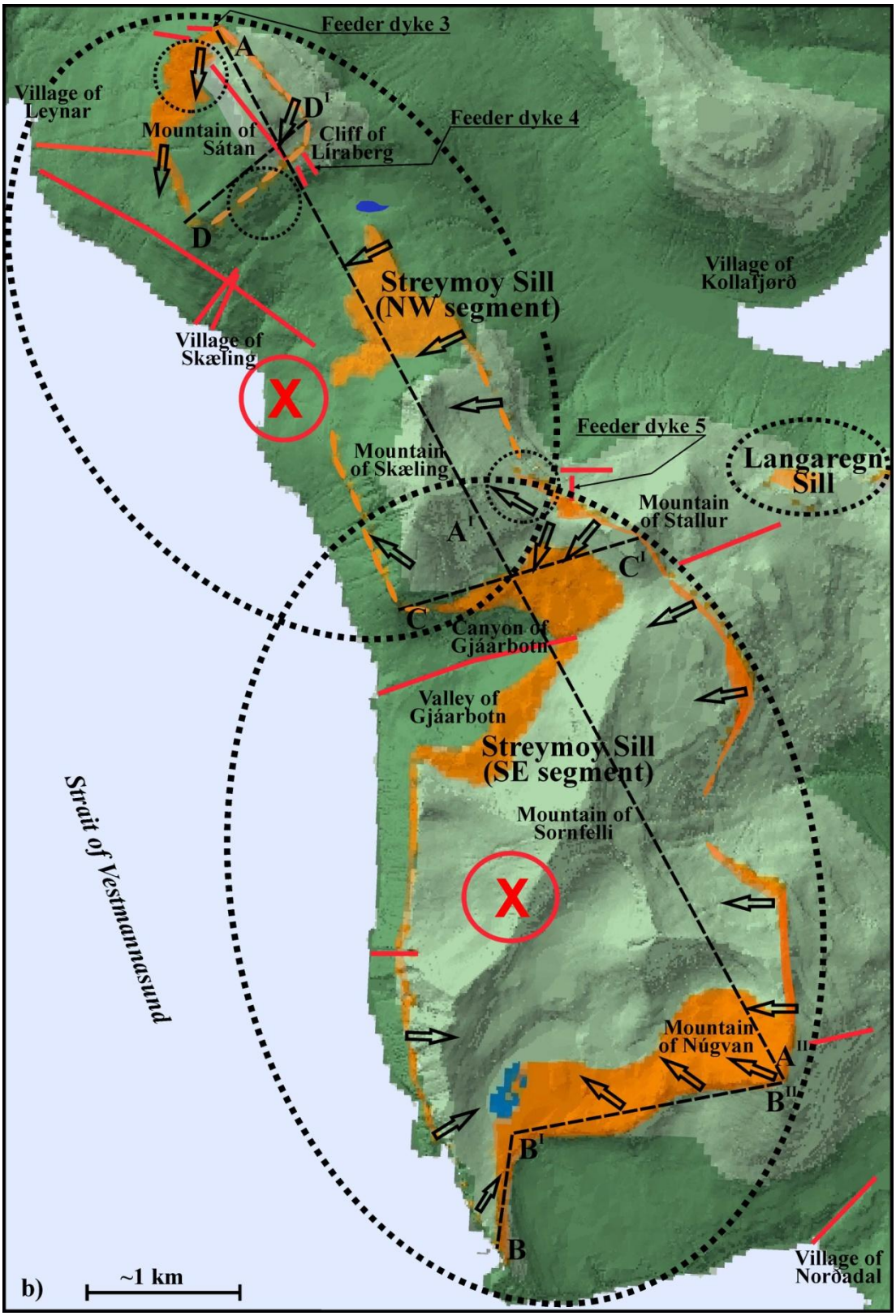

Figure 3.3. (Continued)

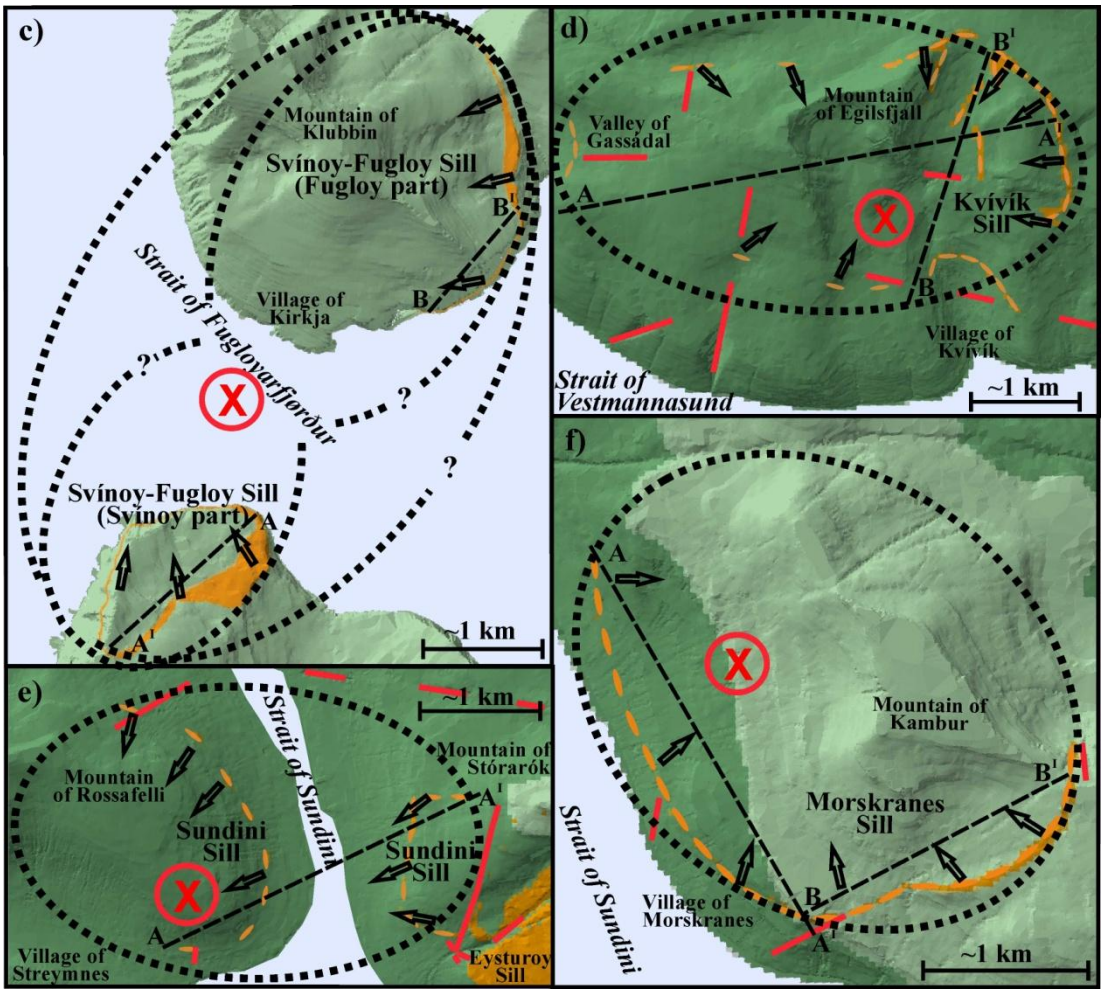

Figure 3.3. The figure show enlarged map views of the individual sills from Fig. 3.2. a) Eysturoy Sill; b) Streymoy Sill and Langaregn Sill; c) Svínoy-Fugloy Sill; d) Kvívík Sill; e) Sundini Sill; f) Morskranes Sill. Main magma sources (open red ellipses with red crosses) are estimated from measured dip and feeder/protrusion directions whereas minor magma sources (dotted open black ellipses) have been determined from sites of thin inclined feeder dykes/sheets. Dip directions of labelled inclined feeder dykes at the immediate dyke/sill contacts are for the Eysturoy Sill: 1 = ~15° → NE; 2 = ~15° → ESE and for the Streymoy Sill: 3 = ~30° → S; 4 = ~45° → SW; 5 = ~30°→ W. The dips of most feeders increase to sub-vertical angles a few metres to a few tens of metres below the dyke/sill contacts. Note the different scales for some individual sills. See text.

composed of two segments. The poorly exposed Langaregn Sill has a uniform thickness of 8 – 10 m in localities were it is well preserved, but it does not appear to fit into any of the two mentioned categories as it is much smaller (Less than ~800 m along its longest axis).

The field occurrences and overall geometries on macroscopic scales for all the sills combined show that apart from similarities in the overall saucer-shaped nature of the

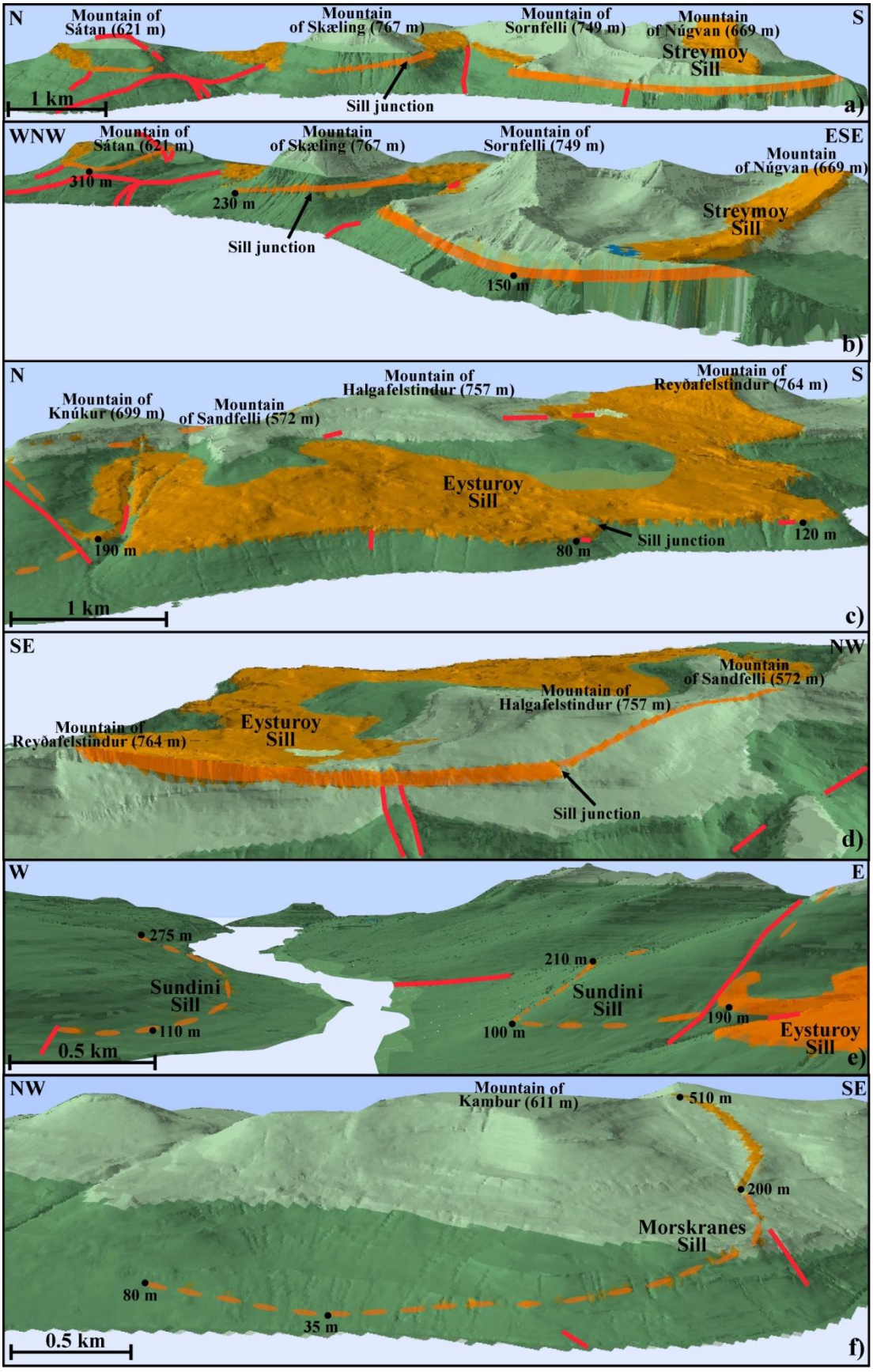

Figure 3.4. Panorama views of some of the sills from Fig. 3.2 and Fig. 3.3. a) and b) The Streymoy Sill. c) and d) The Eysturoy Sill. e) The Sundini Sill. f) The Morskranes Sill. See text.

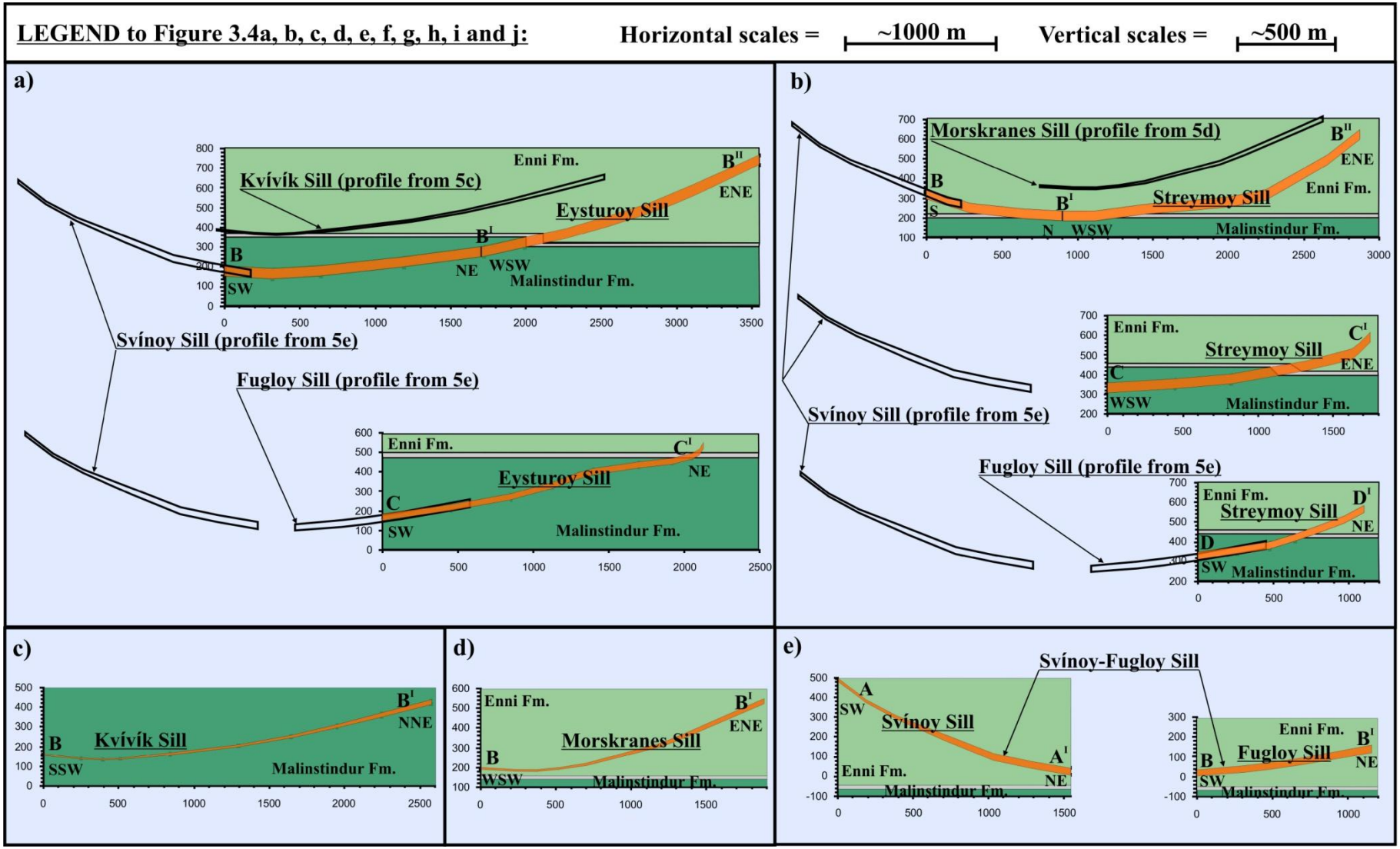
LEGEND to Figure 3.4a, b, c, d, e, f, g, h, i and j:
Horizontal scales = ~1000 m
Vertical scales = ~500 m
a)
Kvívík Sill (profile from 5c)
Enni Fm.
Eysturoy Sill
Svínoy Sill (profile from 5e)
Fugloy Sill (profile from 5e)
Malinstindur Fm.
b)
Morskranes Sill (profile from 5d)
Streymoy Sill
Svínoy Sill (profile from 5e)
Fugloy Sill (profile from 5e)
c)
Kvívík Sill
d)
Morskranes Sill
e)
Svínoy-Fugloy Sill
Svínoy Sill
Fugloy Sill

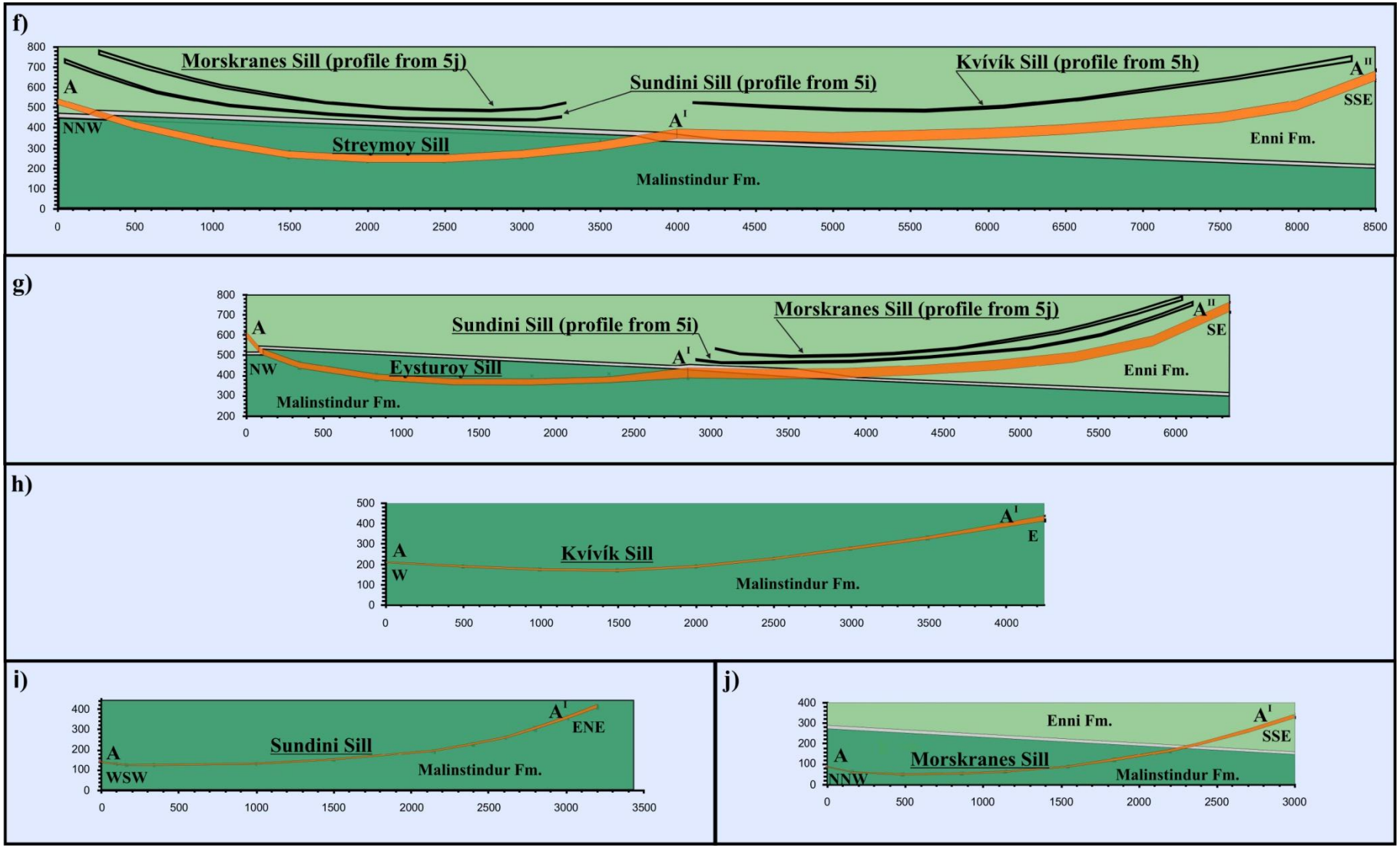
f)
Morskranes Sill (profile from 5j)
Sundini Sill (profile from 5i)
Kvívík Sill (profile from 5h)
A
A I
A II
NNW
SSE
Streymoy Sill
Enni Fm.
Malinstindur Fm.
g)
Sundini Sill (profile from 5i)
Morskranes Sill (profile from 5j)
A
A I
A II
NW
SE
Eysturoy Sill
Enni Fm.
Malinstindur Fm.
h)
Kvívík Sill
A
A I
W
E
Malinstindur Fm.
i)
Sundini Sill
A
A I
WSW
ENE
Malinstindur Fm.
j)
Enni Fm.
Morskranes Sill
A
A I
NNW
SSE
Malinstindur Fm.

Figure 3.5. (Previous two pages). The simplified cross-sections and longitudinal profiles shown in this figure refer to the labelled dashed lines that are indicated on the map sections in Fig. 3.3. a) Cross-sections of the Eysturoy Sill (Profiles: B - B^{I} - B^{II}; C - C^{I} from Figure 3.3a); b) Cross-sections of the Streymoy Sill (Profiles: B - B^{I} - B^{II}; C - C^{I}; D - D^{I} from Figure 3.3b); c) Cross-section of the Kvívík Sill (Profile: B - B^{I} from Figure 3.3d); d) Cross-section of the Morskranes Sill (Profile: B - B^{I} from Figure 3.3f); e) Cross-sections of the Svínoy-Fugloy Sill (Profiles: A - A^{I}; B - B^{I} from Figure 3.3c); f) Longitudinal profile of the Streymoy Sill (Profile: A - A^{I} - A^{II} from Figure 3.3b); g) Longitudinal profile of the Eysturoy Sill (Profile: A - A^{I} - A^{II} from Figure 3.3a); h) Longitudinal profile of the Kvívík Sill (Profile: A - A^{I} from Figure 3.3d); i) Longitudinal profile of the Sundini Sill (Profile: A - A^{I} from Figure 3.3e); j) Longitudinal profile of the Morskranes Sill (Profile: A - A^{I} from Figure 3.3f). Vertical exaggeration is ~1.35 and distances along X and Y axes are indicated in metres. Sill thicknesses indicate maximum values. The stratigraphy is indicated with the same colours as shown in the stratigraphical column of Fig. 2.3 and Fig. 3.2. Comparison between profiles representing the Eysturoy and Streymoy sills with profiles representing the smaller sills of this study (shapes with open black outlines) may hint to original geometries of the Eysturoy and Streymoy sills and to potential similarities in emplacement mechanisms. See text.

investigated sills (Fig. 3.4; Fig. 3.5) relative to sills intruded into sedimentary strata (e.g. Chevallier and Woodford, 1999), the gradual and gently upward-curving geometries displayed by all sills from this study differ from the geometries that are typical for sills intruded into sedimentary successions, where well-defined sub-horizontal inner sections abruptly give way to more steeply inclined middle/outer sections that in turn sometimes give way to flat outer rims (Chevallier and Woodford, 1999; Polteau et al., 2008; Thomson, 2007; Thomson and Hutton, 2004). Comparable relatively abrupt changes of inclination angles in the intrusions from this study have only been observed at a few localities at elevated sill margins (Described below). Hence, it is not possible with any reasonable degree of certainty to categorise the sills/segments of the Faroe Islands into distinct inner, middle and outer sections using the same criteria commonly used for sills intruded into sedimentary strata. However, if those parts of the measured and reconstructed sills that possess inclinations ≤ ~15° with the horizontal plane (Around 70 – 80 %) are considered to match the inner saucers of sills from sedimentary settings, the corresponding maximum inner widths would range from ~3.0 to ~4.0 km. If only the sub-horizontal basal sections of the investigated sills should be considered to match inner saucers of sills from sedimentary settings, these figures would be in the range from 1.5 to 2.0 km.

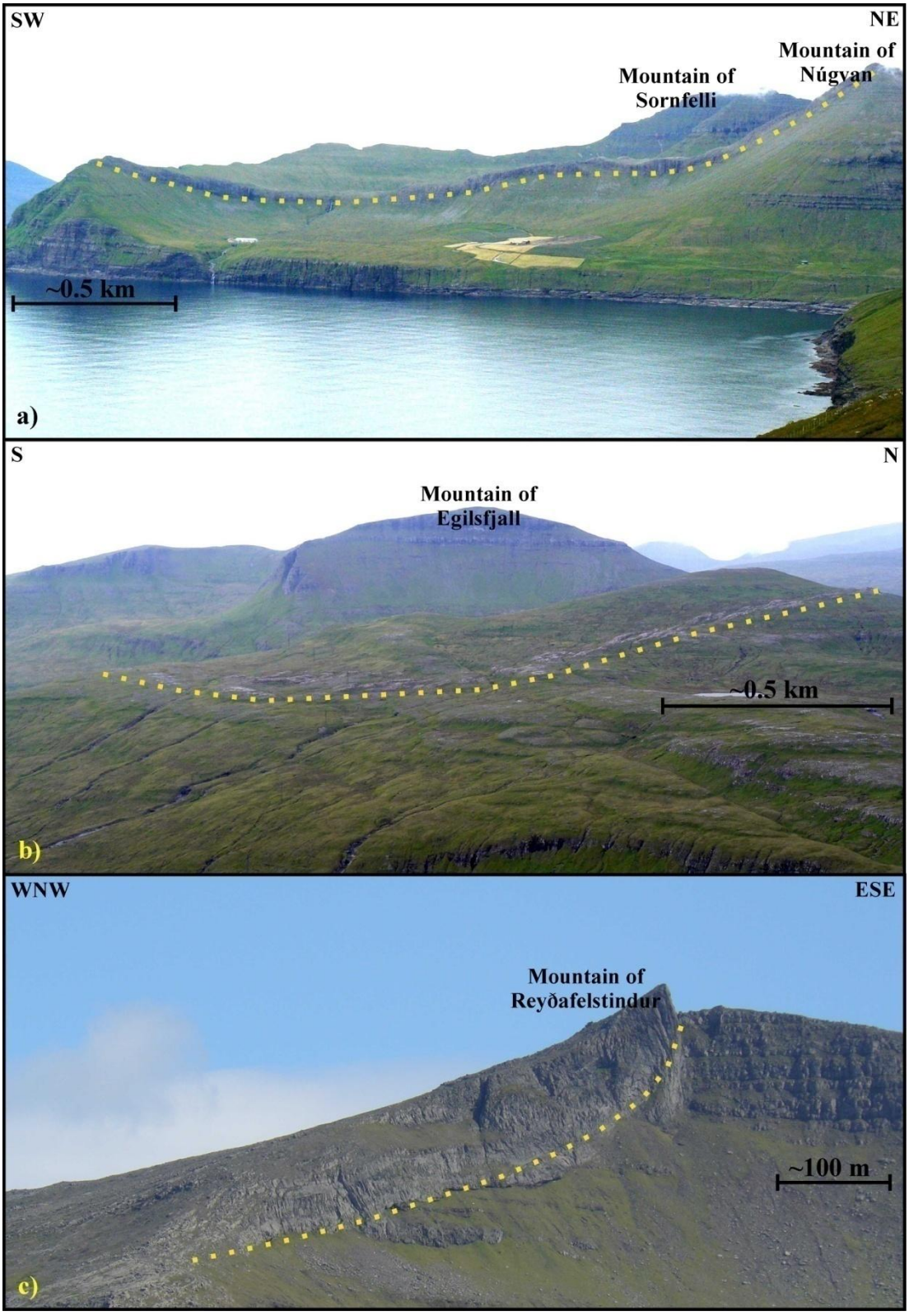

Figure 3.6. Yellow dotted lines indicate lower sill contacts. a) The along-strike view shows the saucer-shaped geometry of the Streymoy Sill (See also figure on title page). b) Arcuate upper margin/rim of the Kvívík Sill. c) Upward-curving termination of the SW parts of the Eysturoy Sill (See also Fig. 1.3). See text.

3.3 Dykes and feeders

A number of dyke systems mostly ranging in thickness from ~0.5 to ~4 m intersect the area underlain by the sills of the Faroe Islands (Fig. 3.3). However, the few exposed accessible dyke-sill contacts of sub-vertical dyke systems in the area suggest that all these systems pre-date the sills. This inference is supported by geochemical constraints (Not shown). A total number of five moderately inclined dykes/sheets, each exposed only for very limited lateral distances and ranging in thickness from ~0.4 to ~2.0 m, have been identified as feeders for the Eysturoy and the Streymoy sills (Fig. 3.3a; Fig. 3.3b). The identification is based partly on field evidences, as shown below, and partly on geochemical constraints (e.g. chapter 4). The inclined feeders dip between ~15° and ~45° at their contacts, but their dip angles are rotated to sub-vertical orientations a few metres to a few tens of metres below the dyke-sill contacts. There are no observations to suggest that any of these inclined dykes acted as conduits for magma transport between individual sills during emplacement. Three of the dykes (labelled 3, 4 and 5 in Fig. 3.3b) apparently fed the uppermost parts of the elevated E, NE and N facing parts of the NW sill segment of the Streymoy Sill. These three dykes strike in directions broadly similar to those of the local sill sections they once fed, and field relationships suggest they supplied melts only to the uppermost ~50 to ~100 metres of the actual sills. The remaining two dykes (labelled 1 and 2 in Fig. 3.3a) probably fed the base of both segments of the Eysturoy Sill. Field evidences show that the thin inclined dykes that presumably fed the NW segments of the Eysturoy and Streymoy sills close to the junctions with their respective SE sill segments (Dyke 2 in Fig. 3.3a and dyke 5 in Fig. 3.3b) apparently only supplied melts to these for lateral distances of less than ~200 m. In spite of direct evidence showing that some parts of the uppermost sections of the Streymoy Sill probably were fed from dykes directly at their elevated and inclined margins, numerous examples of sub-horizontal protrusions from inclined basal sections of this and all the other larger sills, investigated in this study, seem to suggest that the main magma supplies for all sills were channelled via their basal sub-horizontal sections. Inferred magma sources to the sills of the Faroe Islands, are indicated in Fig. 3.3.

3.4. Sill margins and contacts

3.4.1. Distinct features of sill margins

Some of the field relationships encountered in the sill complex of the Faroe Islands

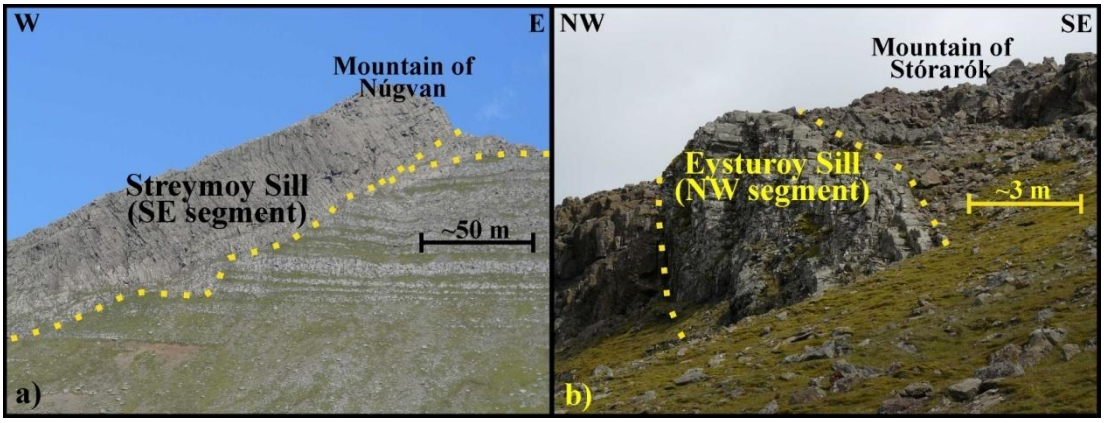

Figure 3.7. a) Sub-horizontal protrusion from the lower contact of the Streymoy Sill at its inclined SE extremity. b) Sub-vertical protrusion from the top of the Eysturoy Sill. Dotted yellow lines indicate lower sill contacts or outlines.

seem to suggest that some of these sills could have been active parts of more extensive plumbing systems. For instance, a thick (>5 m) sub-horizontal layer is branching out from the base of the steeply inclined rim of SE extremity of the the Streymoy Sill on the top of the mountain of Núgvan and proceeds into the host rocks as a layer-parallel sequence (Fig. 3.7a). A kink in the lower sill contact at lower stratigraphic level in the same area could be a manifestation of an earlier failed attempt of sub-horizontal protrusion (Fig. 3.7a). Also, a ~6 m thick vertical dyke-shaped protrusion, attached directly to top the N extremity of the Eysturoy Sill (Fig. 3.7b), suggests vertical magma transport from this sill. Currently, the maximum distances of potential magma transport via these protruding bodies cannot be determined due to erosion, but they could in theory have supplied melts to adjoining sills or perhaps to surface magmatism.

Thinner protrusions (squirts), which terminate a few metres or a few tens of metres at most from their sill sources, have been injected sub-horizontally into the host rocks from the lower margins of many of the investigated sills, particularly the Eysturoy, the Streymoy and the Morskranes sills. A common feature for the sites of these protrusions is that the lower contacts of the main sill bodies that supplied the injected melts display inclined geometries, which may be of various angles with the horizontal plane (Fig. 3.8a; Fig. 3.8b). Another noticeable feature that is characteristic for many of the protrusions in question is that they have been injected laterally into homogeneous crystalline sequences irrespective of the existences of presumed less competent sedimentary sequences above or below the actual levels of

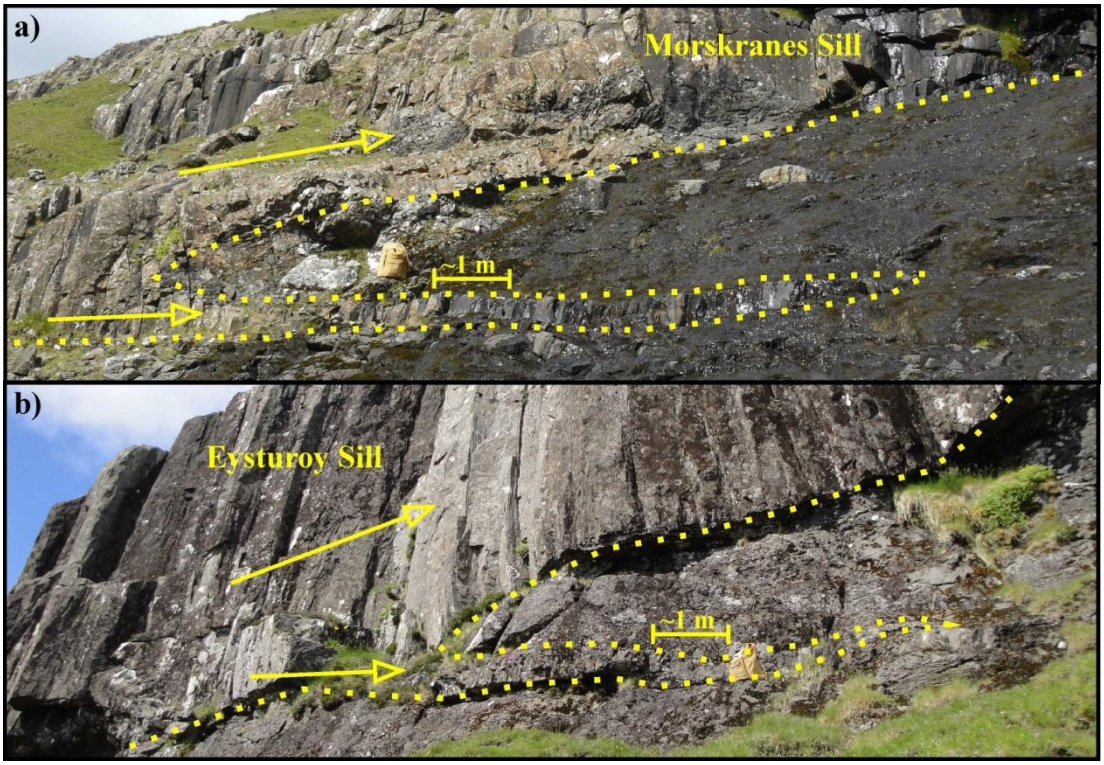

Figure 3.8. a) Thin sub-horizontal protrusion from inclined base of the Morskranes Sill into host basalts. b) Protrusion from the base of the Eysturoy Sill. Yellow arrows suggest direction of palaeo magma flow. Yellow dotted lines show lower sill contacts and outlines of protrusions. See text.

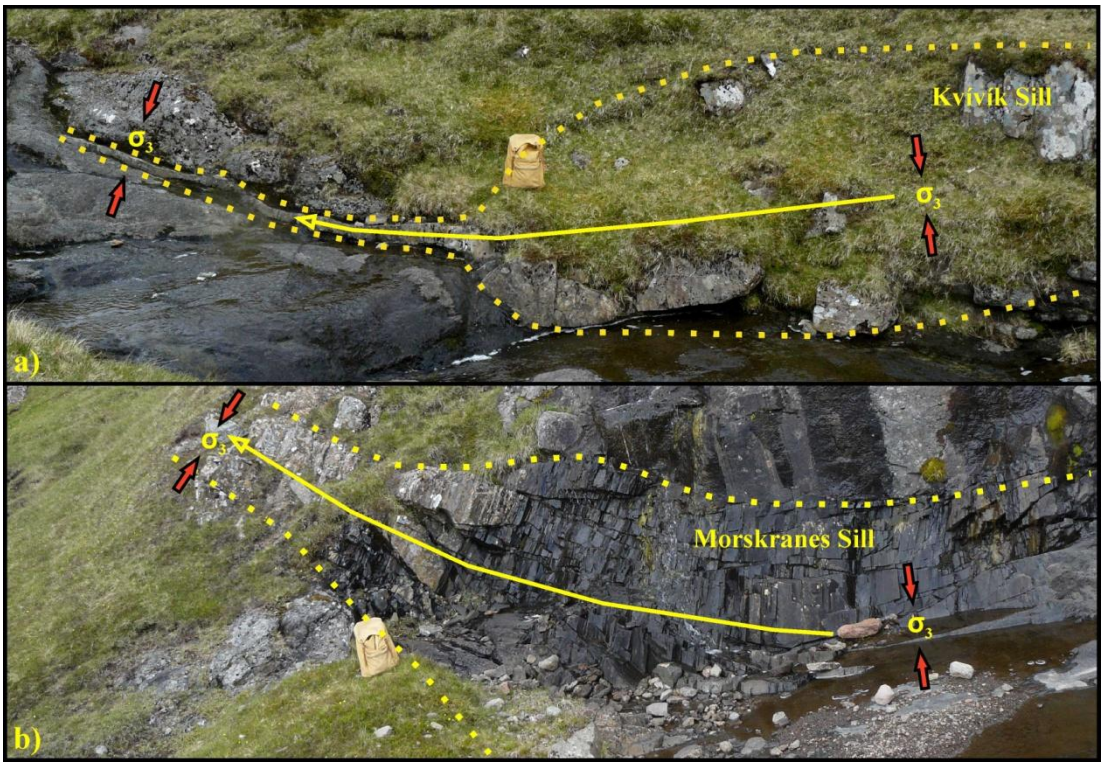

Figure 3.9. Yellow dotted lines indicate sill outlines in a) the Kvívík Sill and b) the Morskranes Sill. Curved yellow arrows suggest directions of initial sill propagation. Red arrows suggest orientations of local least principal local axes σ_3. Rucksack measures ~45 cm. See text.

injection.

The thinnest sections in the basal parts of some of the smaller sills from this study such as the Kvívík and the Morskranes sills (e.g. Fig. 3.5) commonly display irregular margins with slightly protruding tongue-shaped inflated forms that give way to thinner and slightly inclined upward-curving sections on one or both sides (Fig. 3.9). The combined field evidences from these margins seem to suggest that the inclined thinner sections initially propagated out from the more inflated central regions of these protrusions. As these thin margins define terminations of the intrusions, it seems reasonable to assume that their geometries reflect initial intrusion styles with upward-curving fracture propagation from slightly inflated sill sections probably resulting from rotation of least principal stress axes σ_3 (Fig. 3.9).

3.4.2. Sill – sill contacts

Most of the investigated sills are not directly spatially related, but the Eysturoy and the Sundini sills both crop out in the same area in the NW parts of the island of Eysturoy (Fig. 3.2; Fig. 3.3c; Fig. 3.4e). The geochemical compositions of these two sills are identical (Unpublished data) thus perhaps indicating that they may have been derived from a common magma reservoir during the same period of time. The Sundini Sill is exposed at lower stratigraphic levels relative to the Eysturoy Sill in this area, and a ~1.5 m thick sub-vertical dyke separates both sills (Fig. 3.10). Geochemical differences between this dyke and these two sills (Unpublished data) in

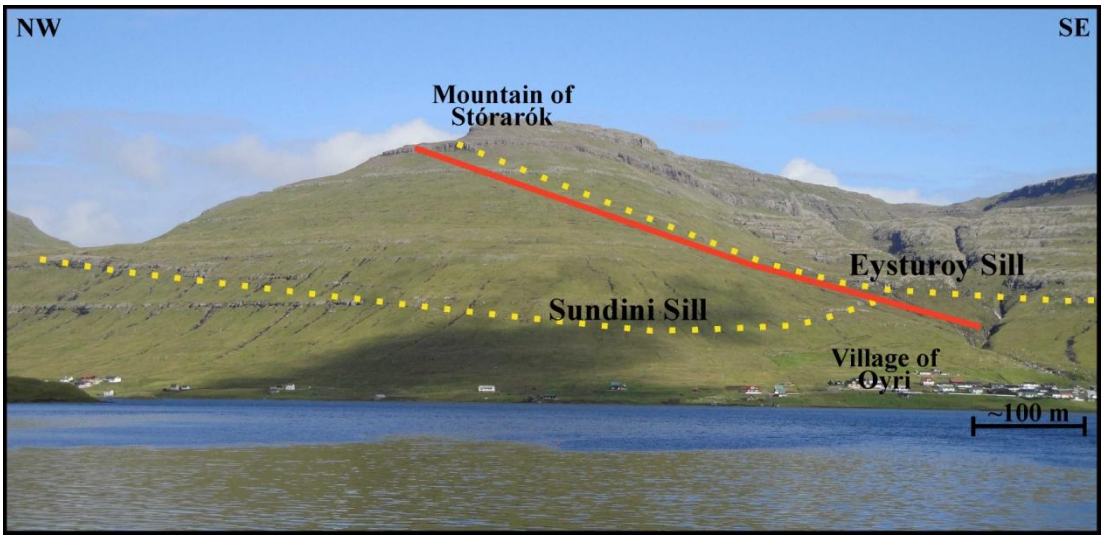

Figure 3.10. Yellow dotted lines indicate the lower contacts of the Eysturoy and Sundini sills. Red line indicates a sub-vertical dyke. See text.

addition to field evidences suggest that these two sills were emplaced subsequent to the dyke intrusion. The very close proximity between these two sills renders it possible that the Sundini Sill could have acted as a feeder to the Eysturoy Sill, if it did penetrate the dyke during emplacement, or they may have been fed from the same dyke network.

Contacts or junctions within individual sills can be encountered in each of the large

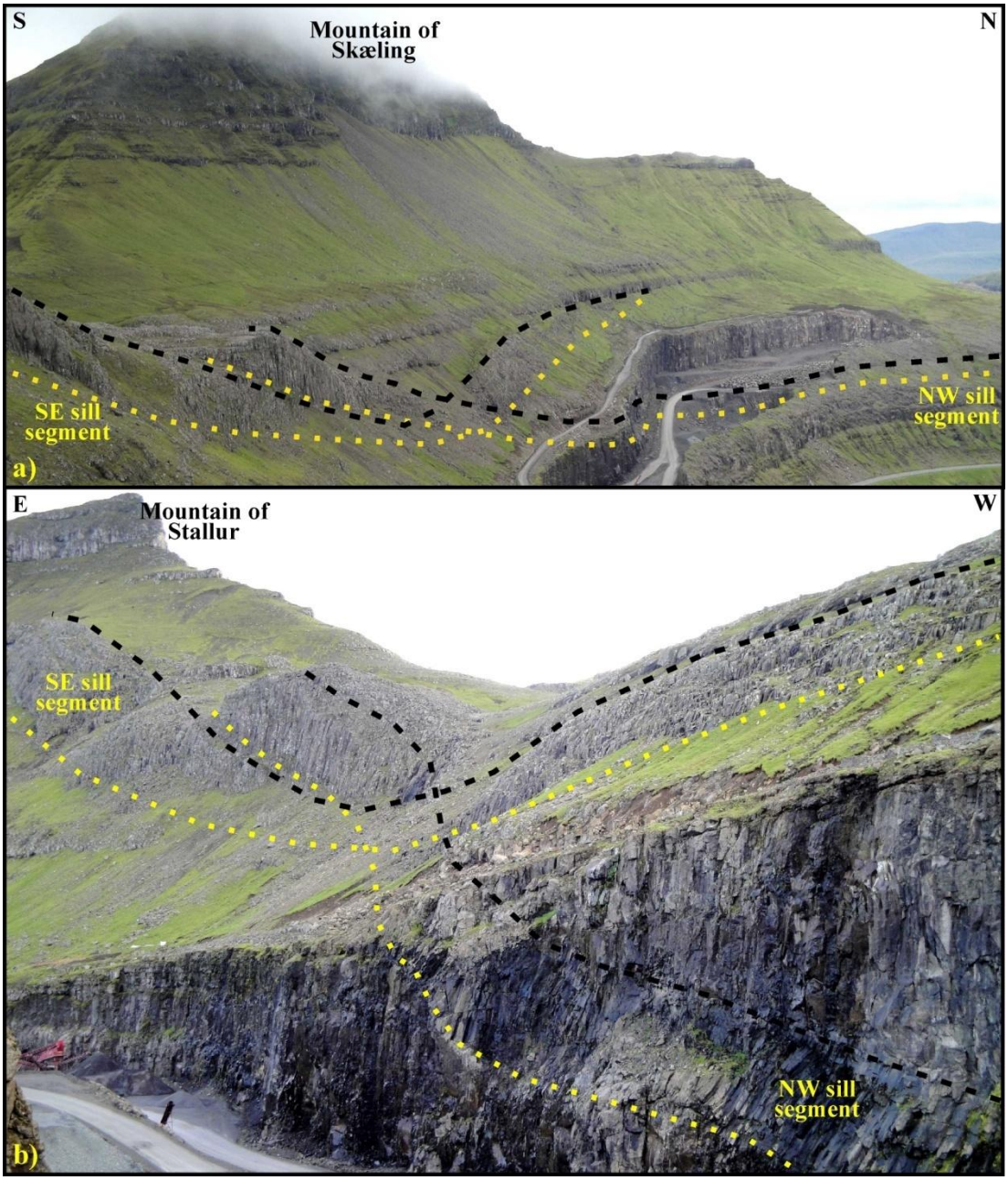

Figure 3.11. Views from two different angles of the same zone of merging between the NW and SE segments of the Streymoy Sill on the NE flank of the mountain of Skæling. a) View from east. b) View from north (closer). Yellow dotted lines indicate lower sill contacts whereas black dashed lines indicate upper boundaries. The quarry measures ~500 m along its longest axis. See text.

Eysturoy and the Streymoy sills at the zones merging between their respective NW Streymoy Sill are crosscutting (Fig. 3.11) and define a particularly good example of a and SE segments. On the NE flank of the mountain of Skæling the segments of the class C" sill junction as described previously using seismic interpretations from offshore sedimentary basins at the NW European margin (Hansen *et al*. 2004, their Fig. 11). The NW sill segment of this sill crops out at ~50 m lower stratigraphic level relative to its SE counterpart in the vicinity of their mutual contact at this locality (Fig. 3.11). Actual centimetre scale contacts of this sill junction are concealed by rock debris. On the SW flank of the mountain of Skæling the contact between these segments is less conspicuous as they do not crosscut at the SW sill margin.

The junction between the NW and SE segments of the Eysturoy Sill is well exposed

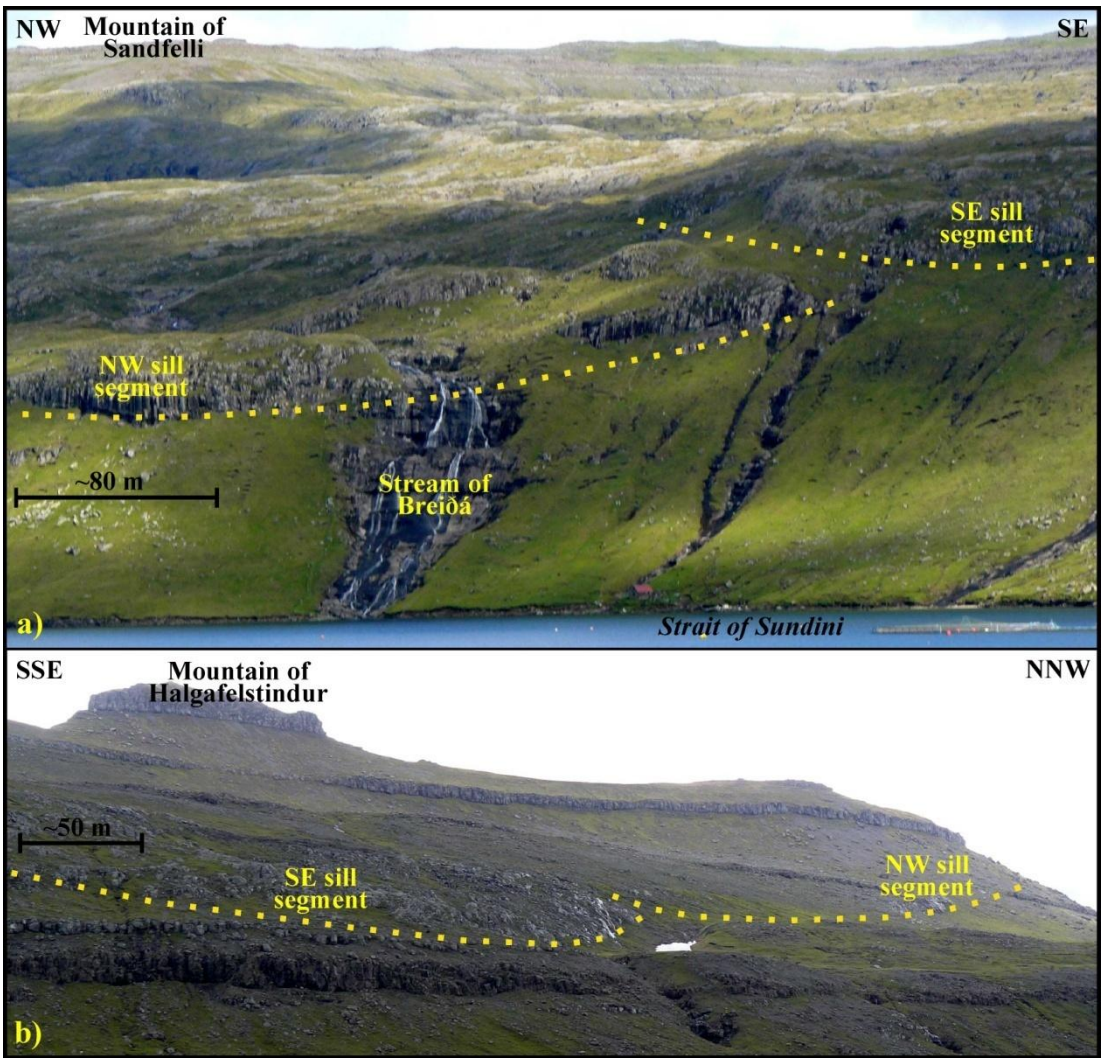

Figure 3.12. Opposite views of the zones of merging between the NW and SE segments of the Eysturoy Sill exposed roughly halfway along the SW and NE margins of this sill. a) View from SW. b) View from ENE. Yellow dotted lines indicate lower sill contacts. See text.

at localities roughly halfway along the SW and NE margins of this sill, whereas it is due to erosion that has masked potential differences in the original upper sill surfaces less conspicuous in the interior of the intrusion due to welding of the segments and (Fig. 3.12a). It is conspicuous that the NW segment is exposed at ~50 m lower stratigraphic levels relative to its SE counterpart close to the junction at the SW sill margin (Fig. 3.12a) whereas the opposite is through with the SE segment being exposed at 40 – 50 m lower levels relative to its NW matching part close to the junction at the NE sill margin (Fig. 3.12b). These features are perhaps best explained by the emplacement of the NW segment farther to the SW relative to its SE neighbour. Consequently, both the NW segment of the Eysturoy Sill and the Sundini Sill display a trend with sinistral dislocation relative to their SE neighbours.

3.4.3. Sill – dyke contacts

A significant number of dykes intersect the investigated sills (Fig. 3.3), but actual contacts are most often concealed beneath earth or rock debris. However, at the vertical cliff of Líraberg a well-exposed intrusive contact shows how the NW segment of the Streymoy Sill cuts through a sub-vertical dyke (Fig. 3.13a; Fig. 3.13b; Fig. 3.14a). The NE leaning geometry of the dyke at the sill-dyke contact could potentially point to magma flow within the sill from the SW towards the NE during the initial phases of emplacement. This inference would be in accordance with the orientations of nearby protrusions from the base of the actual sill. The fact that this dyke protrudes several metres into the sill may suggest that it acted as a temporary barrier to sill/fracture propagation during early stages of sill emplacement, until the intrudinng magma forced its way through it. A similar scenario may be envisaged for parts of the Morskranes Sill, the magmas of which appear to have been guided along a sub-vertical dyke system at its southern rim (Fig. 3.3f). More often than not, the sub-vertical dyke systems are manifested by the occurrences of canyons, being sub-parallel to dyke trends, cutting through sills at locations where they intersect (Fig. 3.13c). As all sub-vertical dykes with exposed contacts to the sills are cut by these, the activities of post-magmatic tectonic events most probably resulted in fracturing of the sills along zones pre-weakened by the dykes. It is noteworthy that while the Streymoy Sill is intact where it has cut a sub-vertical dyke at the cliff of Líraberg on the SE flank of the Mountain of Sátan (Fig. 3.13a; Fig. 3.13b; Fig. 3.14a), it is itself cut by a deep canyon on the NW flank of the Mountain of Sátan, i.e. around 1 km

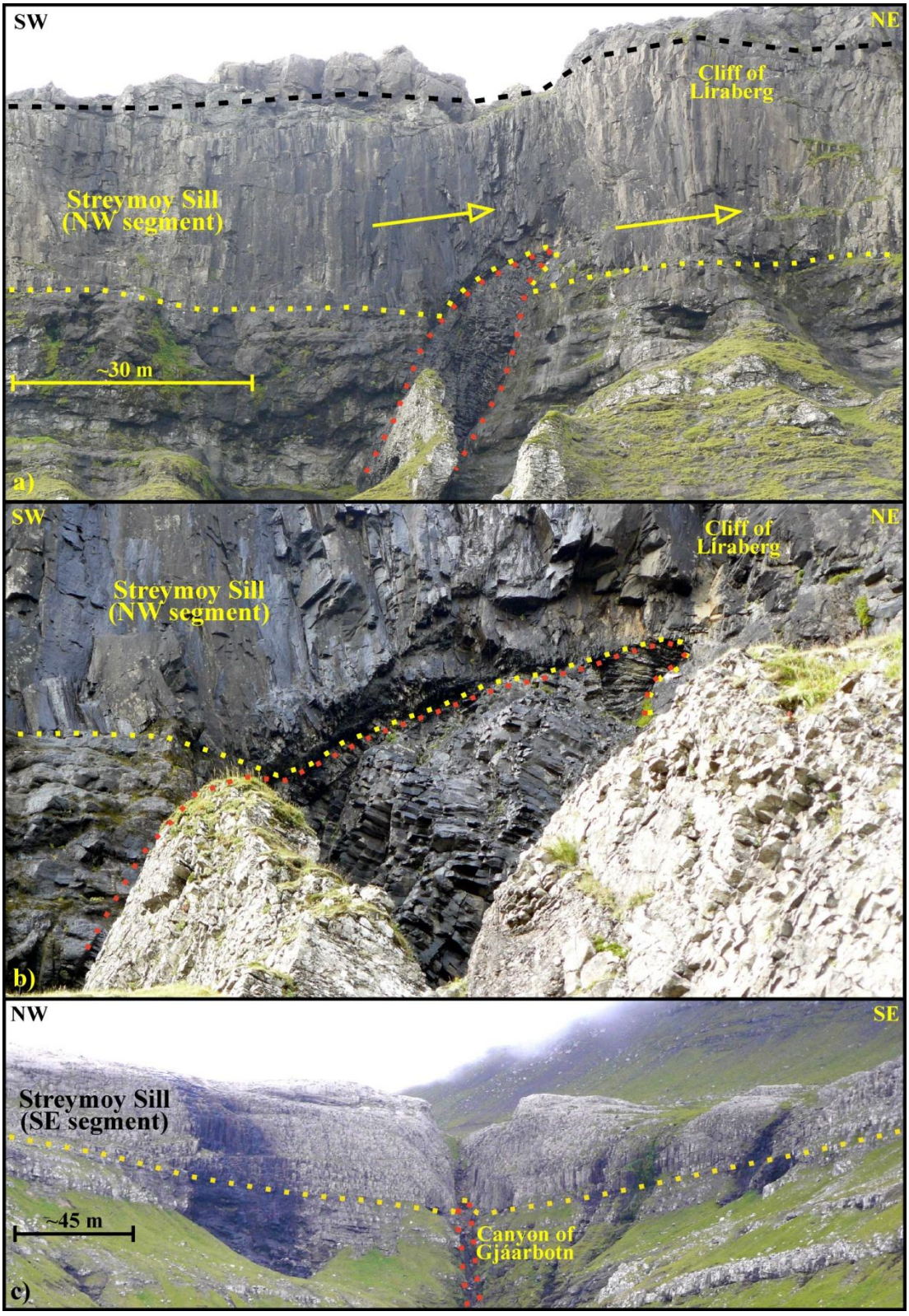

Figure 3.13. a) Sub-vertical en-echelon dyke with dextral steps cut by NW segment of the Streymoy Sill. Yellow arrows suggest direction of palaeo magma flow. b) Same as in a) but showing a close-up view of the sill-dyke contact with foliated chilled sill margin. c) Deep canyon in the SE segment of the Streymoy Sill where it cuts a sub-vertical dyke. Yellow dotted lines indicate lower sill contacts, red dotted lines indicate dyke outlines and black dashed line indicates upper sill contact. See text.

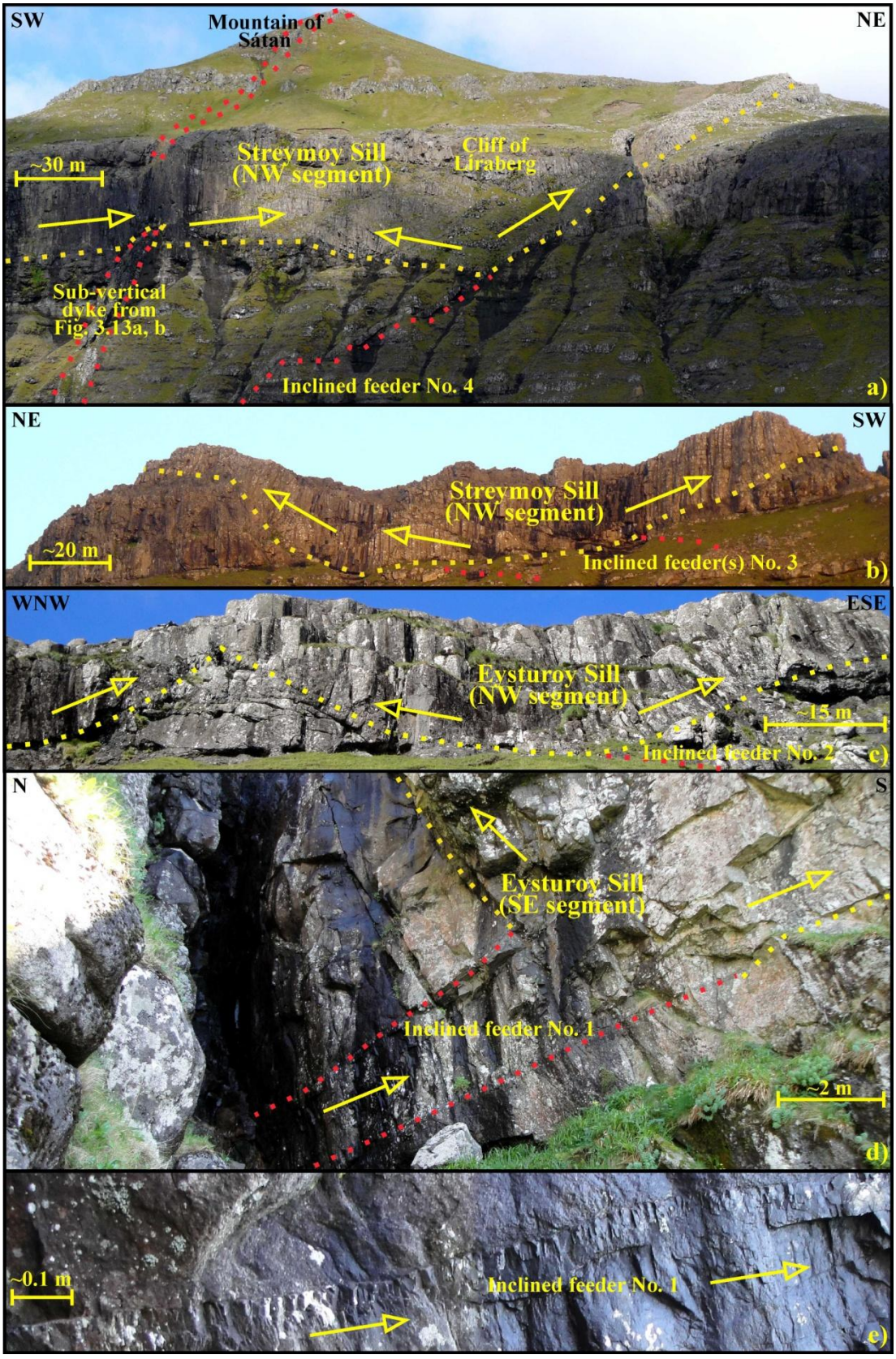

Figure 3.14. Feeders from Fig. 3.3. a) Inclined feeder No. 4 with ramp-flat geometry. b) Inclined feeder(s) No. 3. c) Inclined feeder No. 2. d) Inclined feeder No. 1. e) Upper contact (diagonal from upper right) of inclined feeder No. 1. Yellow dotted lines indicate lower sill contacts, red dotted lines indicate dyke contacts/outlines. Yellow arrows suggest palaeo magma flow directions. See text.

farther to the NW, where a sill – dyke contact to the same dyke is exposed.

Well exposed contact zones between the investigated sills and inclined dykes show, that the lower sill contacts immediately above these presumed feeders invariably display upwards and outwards/upwards sloping geometries (funnel-shaped) away from their inferred feeders (Fig. 3.14). Similar features have not been detected anywhere else within the actual sills. The ~1.5 m thick supposed feeder No. 4 to the Streymoy Sill displays a pronounced ramp-flat geometry and steepens to a sub-vertical orientation a few tens of metres below the sill it may have fed (Fig. 3.14a). It is noteworthy that the dip of this dyke/sheet just below the contact and that of the sill margin to the NE above it are virtually identical and are much steeper than the general dip of the sill to the SW of the sub-vertical dyke shown in Fig. 3.14a. The supposed feeder No. 3 to the Streymoy Sill, which is exposed on the NW flank of the mountain of Sátan, is in fact composed of one main ~1.0 m thick dyke/sheet and few additional <~0.3 m thick sheet intrusions that probably supplied magmas to the NW extremity of this sill (Fig. 3.14b). The ~0.4 m thick supposed feeder No. 2 to the Eysturoy Sill appartently supplied melts to the NW segment for a lateral distance less than ~150 m adjacent to the junction that connect segments of this sill. The site where presumed main magma supplies from the WNW have coalesced with magmas from inferred feeder No. 2 to the NW segment of the Eysturoy Sill crops out as an angular kink (~90°) at the base of the sill ~50 m to the WNW of the feeder-sill contact (Fig. 3.14c). The ~2 m thick supposed feeder No. 1 was probably a major magma source to the SE segment of the Eysturoy Sill, the base of which it is currently attached to (Fig. 3.14d). It is noteworthy that the transition zone between this relatively thick dyke/sheet and the actual sill crops out entirely within a homogeneous crystalline basaltic layer rather than in one of the sedimentary sequences occurring just below the sill-feeder contact. Occasionally, mapping on centimetre scales have been required in order to pin point sites of presumed magma supplies to the investigated sills, as intrusive contacts between inferred feeders and volcanic basaltic host rocks may be elusive due to similarities in rock types, weathering and/or lichen growths (Fig. 3.14e).

3.4.4. Sill – host rock contacts

In general, the contacts between the investigated sills and their host volcanic rocks are sharp and well-defined (Fig. 3.15a), especially if they are compared to contacts of

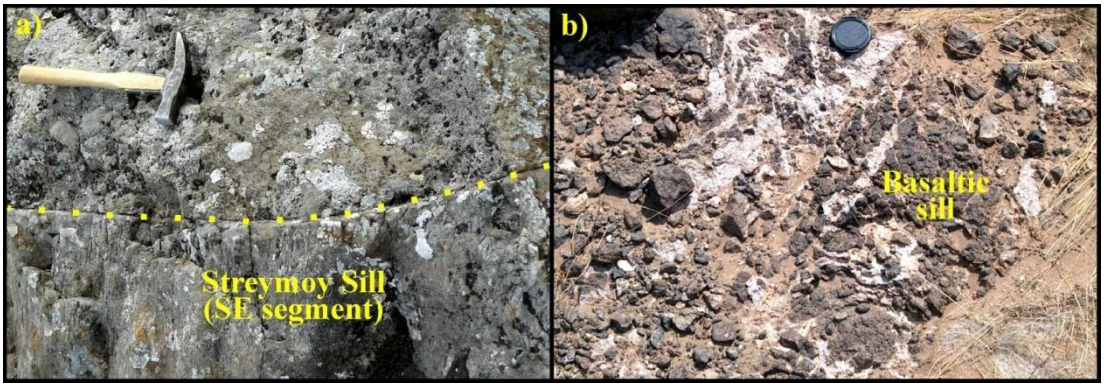

Figure 3.15. Sill – host rock contacts. a) Knife-sharp contact (Yellow dotted line) between the main body of the Streymoy Sill and overlying volcanic strata. The shaft of the hammer measures ~30 cm. b) Peperitic contact zone between a basaltic sill (dark) and sedimentary strata (white) in the Huab Basin, Namibia. Lens cap is for scale. See text.

mafic sills intruded into relatively unconsolidated sedimentary successions, where intrusive contacts commonly can be measured in metres (Fig. 3.15b).

Although relatively large sections of the Eysturoy and Streymoy sills are well exposed (Fig. 3.3a; Fig. 3.3b), most sill surfaces appearing in map view are eroded to lesser or greater degrees. Hence, evidences of the exact nature of upper sill contacts are not of common occurrences even though chilled upper sill margins can be encountered in a few localities. Also, imprints on sill surfaces from protruding irregular features in host basalts may occur locally within very restricted locations, sometimes associated with stoped blocks of roof material (Fig. 3.16a; Fig. 3.16b). The angular or curved imprints of roof rocks in the investigated sill generally occur at scales ranging from a few tens of centimetres to a few metres. The stoped material may occur as blocks that are only partly incorporated in their host sills (e.g. Fig. 3.16a) or it can occur as blocks of sizes ranging from a few tens of centimetres to a few metres that are completely embedded in their host sills (Fig. 3.16b). The latter type of stoped basalt blocks are sometimes hard to distinguish from their host sills in cases where both are affected by weathering and/or lichen growths or if they are of broadly similar consistency and compositions. The preservation of host rocks trapped within sill bodies during magma intrusion into sedimentary sequences that are less refractive than the intruding material may require mechanisms that are different from those applying to sill intrusion into crystalline basaltic host rocks like those of this study. Examples include a sub-horizontal, relatively large (a few hundred m^2) and thin (<1 m thick) layer of silica-rich sediments that have experienced contact

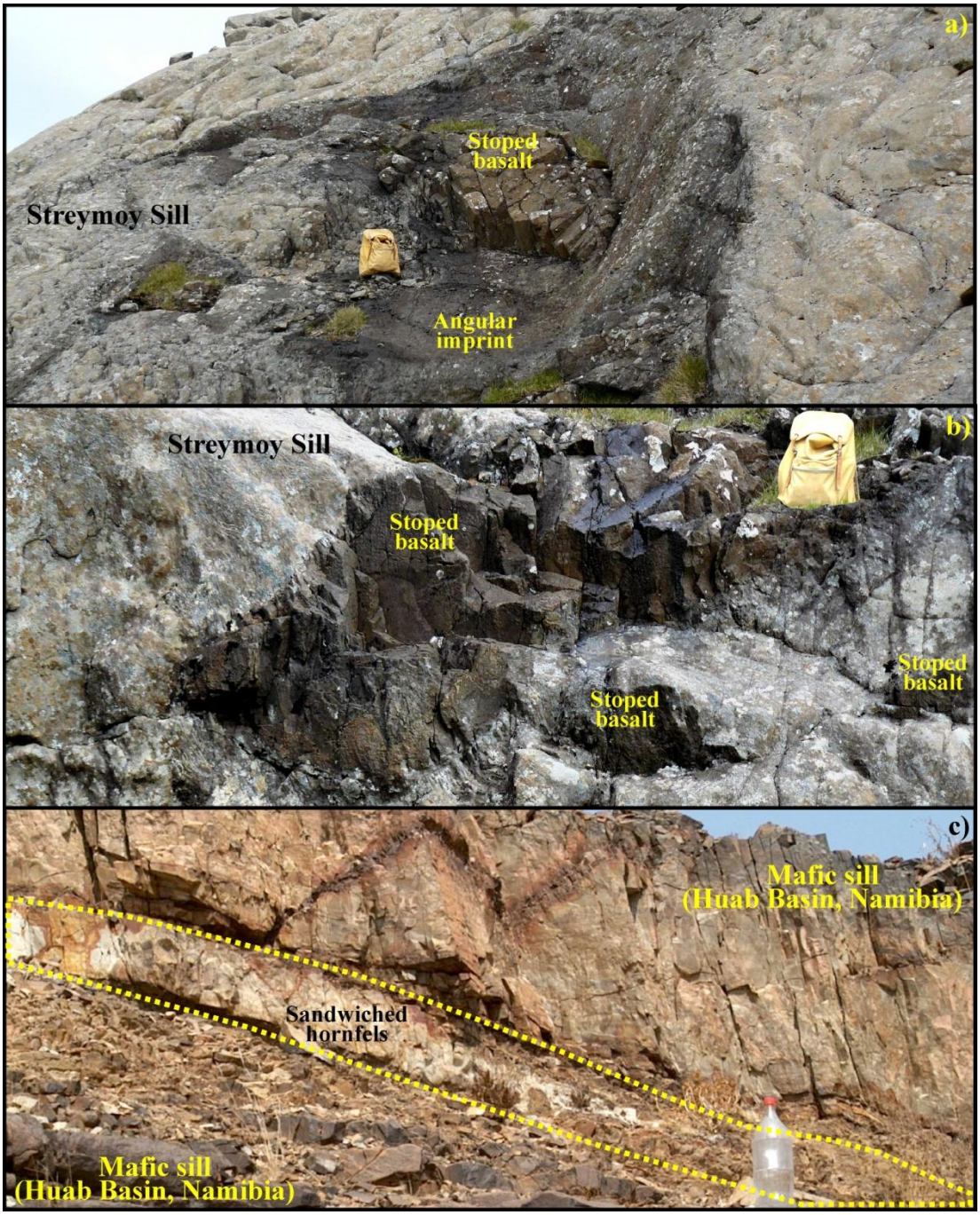

Figure 3.16. a) Partially embedded block of stoped host rock (dark brown) at the centre of an angular imprint (dark grey) in the Streymoy Sill. b) Stoped basalt blocks of various sizes completely embedded in the Streymoy Sill. The rucksack measures ~45 cm. c) Sub-horizontal ~0.6 m thick layer of a silica-rich intensely hornfelsed/baked sedimentary sequence (outlined by yellow dotted line) embedded in a mafic sill cropping out in the Huab Basin, Namibia. See text.

metamorphosis triggered by ascending hot sill material before ultimately being covered/embedded by newer magma pulses (Fig. 3.16c).

The exposed sill-host rock contacts are not uniform throughout the sill boundaries,

but may vary according to the type of host rocks (e.g. crystalline versus sedimentary sequences), and the nature of chilled sill margins may differ between upper versus lower boundaries. Also, various sections of individual sills may have been affected

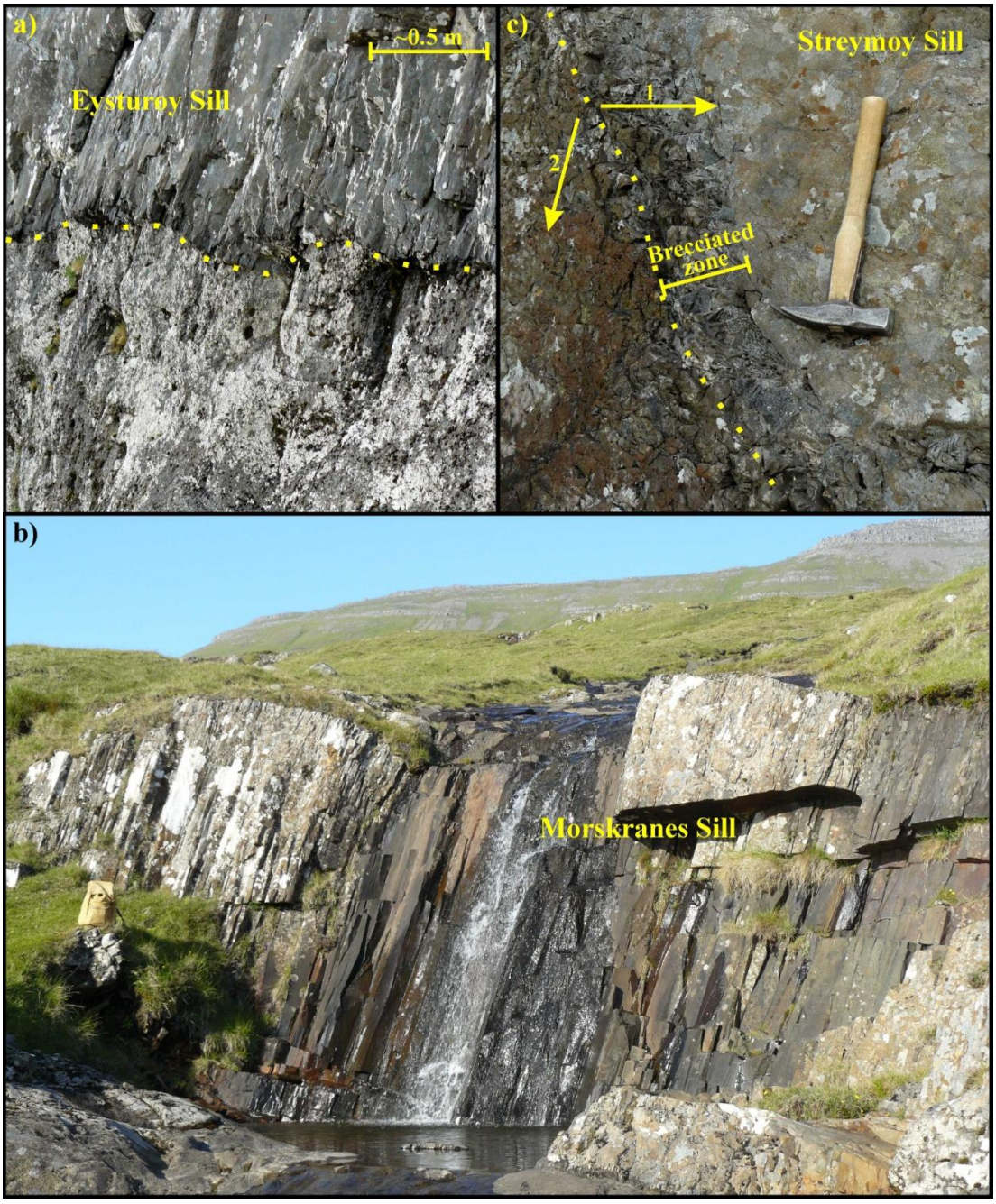

Figure 3.17. a) Densely spaced platy jointing at lower chilled margin of the Eysturoy Sill. Yellow dotted line indicates lower sill contact. b) Platy jointing across the entire thickness of a thin part of the Morskranes Sill. Rucksack measures ~45 cm. c) Brecciated chilled upper margin in an angular outcrop of the Streymoy Sill. Yellow dotted line indicates sill edge. Arrow 1 indicates sub-horizontal direction (including thickness of breccia) whereas arrow 2 indicates sub-vertical direction (the contact surface of the sill). The shaft of the hammer measures ~30 cm. See text.

differently by post-magmatic tectonic events. Hence, the appearances of sill boundaries may differ according to location relative to deformation activities. These differences are sometimes manifested by either welded contact or sills and host rocks can be detached.

A consequence of the different contact styles occurring along the margins of the investigated sills is that both sills and host rocks immediately at their respective contacts may have been affected in different manners by sill emplacement and/or subsequent deformation events.

One feature sometimes occurring at chilled lower sill margins in intrusions apparent from this study, is a more or less well-developed platy jointing, which generally is oriented orthogonal to sill – host rock contacts and frequently reach ~0.5 metres or more into the sills in question (Fig. 3.17a). These lower margin characteristics could perhaps point to some water influx in e.g. non-crystalline layers in host rocks (Lyle, 2000). In localities where sill thicknesses measure less than ~2 metres, platy jointing may occur throughout the sills in question (Fig. 3.17b). In outcrops where chilled upper sill margins display distinctive features, these sometimes occur as zones of

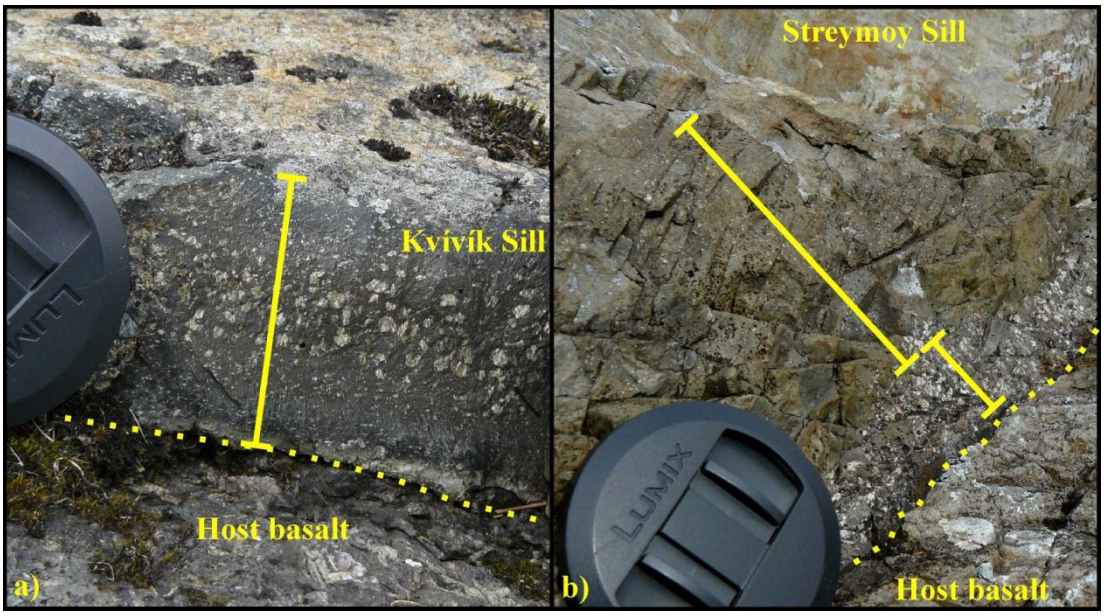

Figure 3.18. a) Relatively large amygdales are concentrated in the central parts of a thin part of the Kvívík Sill. Yellow bar indicates sill thickness. Yellow dotted line indicates lower sill contact. b) Amygdales at the upper margin of the Streymoy Sill. Small yellow bar measures ~2 cm and indicates zone with relatively large amygdales (1 to 4 mm) whereas the larger bar measures 6 – 8 cm and indicates zone with small amygdales (< 1 mm). Yellow dotted line indicates upper sill contact. Lens cap is for scale. See text.

brecciated structures immediately at the contact, the thicknesses of which commonly measure 0.15 to 0.2 metres (Fig. 3.17c).

Amygdaloidal rocks at chilled sill margins are not of common occurrences at the lower margins of the larger sills of the Faroe Islands, but in outcrops where sill thicknesses measure < ~0.5 metres, i.e. in the smaller sills that wedge out at one end, amygdaloidal rocks may be encountered at both lower and upper margins. If a sill section measures < ~0.2 metres in thickness, the largest amygdales tend to be concentrated in the interior of the sills in question (Fig. 3.18a). In these very thin sill sections amygdales commonly make up 15 to 20 percent of the total rock volume (Fig. 3.18a). Amygdaloidal rocks are occasionally encountered at the upper chilled margins of the larger sills where they not uncommonly make up an outer thin (~2 cm thick) zone, with sizes of individual amygdales measuring ~1 to ~4 mm, and an inner thicker (~5 to ~10 cm) zone where individual amygdales generally measure < 1 mm (Indicated with small and large yellow bars respectively in Fig. 3.18b). It is noteworthy that while sizes of amygdales increase with decreased distances to upper contacts of the larger sills, sizes of amygdales in very thin sill sections decrease with decreasing distances to sill contacts (Fig. 3.18a; Fig. 3.18b).

As the host rocks are composed of basalts with geochemical and mineralogical compositions that are comparable to the investigated sills, they have not been particularly susceptible to melting and they have not experienced contact metamorphism at any significant scales in consequence to thermal effects from sill intrusion. Hence, the host rocks along many parts of the margins of sill from this

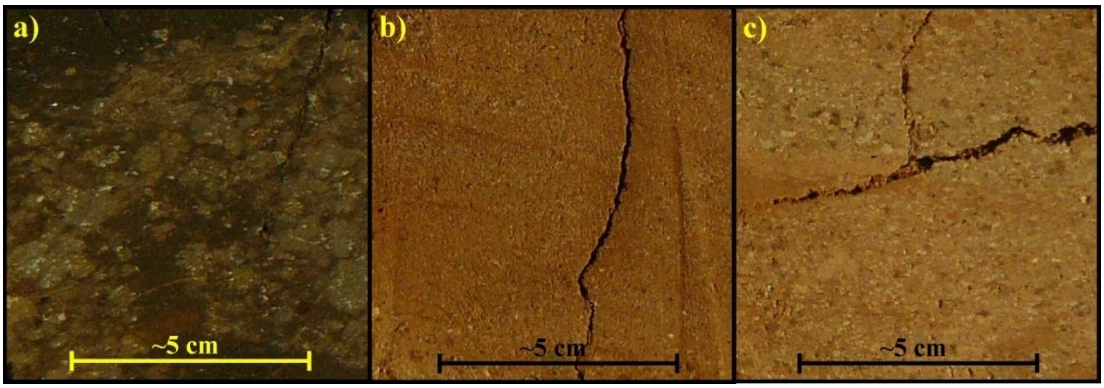

Figure 3.19. Increasing degrees of compaction/baking and discolouring of tuff samples with decreasing distance to the upper contact of the Streymoy Sill. a) Tuff sample collected immediately at sill contact. b) Tuff sample collected ~0.75 metres from the same contact. c) Tuff sample collected ~1.50 metres from the same contact. See text.

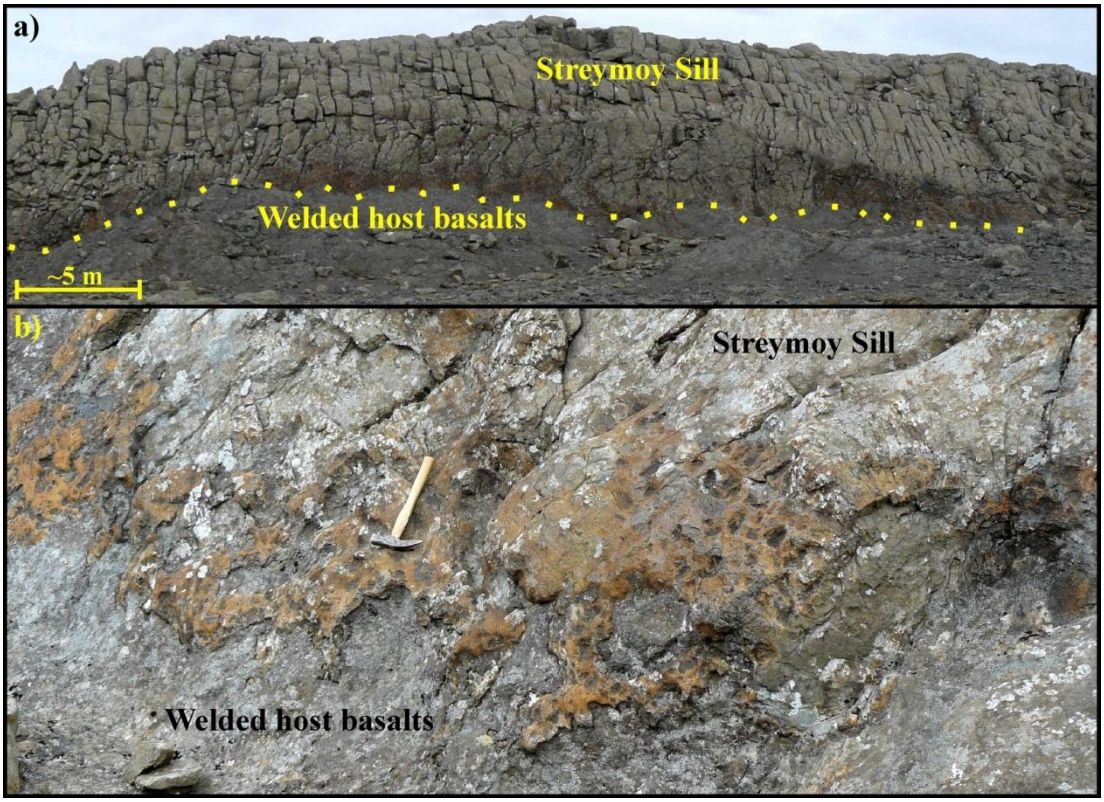

Figure 3.20. a) Host rock (lower parts of photo) is welded to the Streymoy Sill. A brownish coating measuring < 1 cm separates sill and welded basalt. Yellow dotted line indicates the upper sill contact. b) Closer view of the irregular contact from a). Shaft of hammer measures ~30 cm. See text.

study do not display clear/visible signs of intrusive activity. However, baking and compaction of tuffaceous strata immediately at intrusive contacts are occasionally associated with some of the larger sills. In a 1.5 to 2.0 metre thick tuff sequence on top of the NW segment of the Streymoy Sill there is an increasing degree of compaction/baking with decreasing distance to the sill contact. In this location a 10 to 15 cm thick zone immediately at the sill contact is dark coloured (Fig. 3.19a) and has a density approaching that of crystalline basalt. At a distance of ~0.75 metres from the sill contact the tuff is slightly compacted/baked and discoloured (Fig. 3.19b) whereas tuff at a distance of ~1.5 metres from the contact shows no apparent signs of modification from thermal effects (Fig. 3.19c), but has a density and colour similar to material from the same tuff horizon several tens of metres away from the sill contact. Welding of host rocks to sill intrusions is another feature that may be encountered within limited parts of the upper margins of the larger sills from this study (Fig.3.20). The zones of welded basalts rarely reach maximum thicknesses of more than ~1.0 metre, but most often these vary significantly and display jagged surfaces. In many

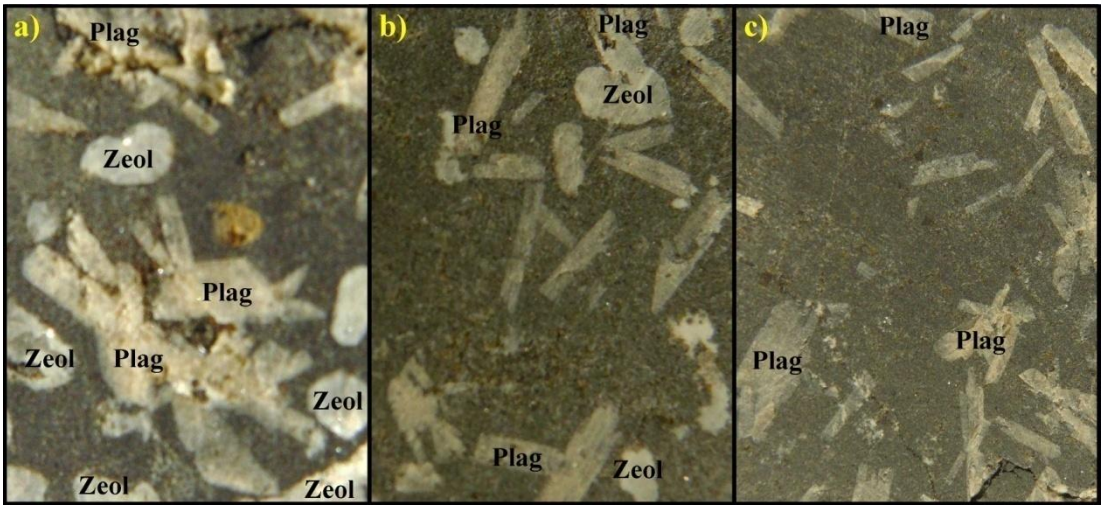

Figure 3.21. Increased amygdale densities in welded basalts with decreasing distances to the upper contact of the Streymoy Sill. a) Basalt sample collected ~0.5 metres from the sill contact. b) Basalt sample collected ~0.75 metres from the same contact. c) Basalt sample collected ~1.0 metres from the same contact. Plag = plagioclase crystals; Zeol = zeolite crystals in amygdales. The larger plagioclase crystals generally measure 1.0 to 1.5 cm. See text.

cases no apparent evidences of metamorphism can be seen in the welded basalts in hand specimen. However, in a way that is comparable to the amygdaloidal zones in sill margins immediately at their upper contacts, welded host rocks may also display various densities of amygdales. Relatively dense amygdale populations commonly occur up to around 0.5 metres away from upper sill contacts (Fig. 3.21a) and less dense populations can also be encountered up to ~0.75 metres away from sill contacts (Fig. 3.21b), but at distances larger than ~1.0 metres from the intrusive contacts these welded basalts are often free of amygdales (Fig. 3.21c). It is noteworthy that no clear signs of amygdales can be observed in host rocks to the very thin parts of the smaller sills of the Faroe Islands. Obviously, the amygdales in the welded host basalts result from gas exsolution/migration across contacts from the sills followed by filling of the resulting vesicles with secondary zeolite minerals.

The best direct evidences of the exact nature of welded sill – host rock contacts and chilled sill/dyke margins in general can be obtained by careful examination of relevant thin sections of actual contacts. Inspection under the microscope of a welded transition zone between an amygdale-free basaltic apophysis in the immediate vicinity of the Streymoy Sill, which it is connected to, and amygdaloidal host basalts reveal an undulating contact where melts with or without small plagioclase crystals have protruded up to 4 – 5 millimetres into the zeolite-bearing host rocks (Fig.

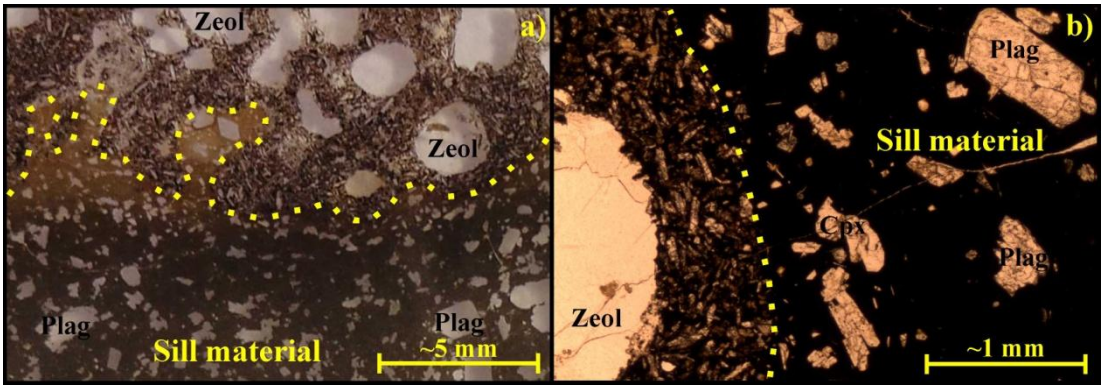

Figure 3.22. a) Ordinary image showing undulating contact (yellow dotted line) between intrusive sill material (generally dark grey glass, but light brown at contact) and host rock. White minerals set in the sill glass are mostly plagioclases and the odd clinopyroxenes. The groundmass of the host rock is composed of fine-grained plagioclase and clinopyroxene. Phenocrysts (amygdales) in host rock are zeolites. b) Image under plane-polarised light showing a closer view of the right hand side of the photo in a), but rotated ~90° anticlockwise. Glass in the sill material (black) is connected to interstitial/interconnected glass (tiny black patches) in the host rock via the intrusive contact (yellow dotted line). Plag = plagioclase; Cpx = clinopyroxene; Zeol = zeolite. See text.

3.22a). An even closer view of this transition zone shows that the apparent contact is in fact itself a transition zone where the melt (glass) in the vein is connected to tiny interconnected interstitial melt (glass) batches in a fine-grained groundmass of plagioclase and clinopyroxene within the host rock, hence explaining the welding (Fig. 3.22b). Clearly, contact metamorphism has resulted in sufficient degrees of melting of the least refractive parts of the fine-grained host rock so as to produce the interconnected network of partial melts (glass) that have acted as cement between intrusive rocks and host rocks.

3.5 Tectonic effects on sills and host rocks

As many of the investigated sills and the host basalts in the immediate vicinity of these sills commonly are characterised by conspicuous deformation structures at various scales, it is pertinent to present a brief introduction of their modes of occurrence and try to determine the nature of causal mechanisms.

3.5.1. Syn-magmatic deformation

Apart from the common occurrences of sub-vertical foliation at lower sill margins in the larger sills (e.g. Fig. 3. 17a), foliation around assimilated blocks of host basalts at a few localities and foliation across entire sill thicknesses in some thin parts of the

smaller sills, deformation associated with sill emplacement does not appear to have affected the intrusions from this study significantly. However, cooling fractures in the form of columnar jointing are of common occurrences in many parts of the investigated sills. In general, these columns/joints are oriented orthogonal to upper/lower sill margins (Fig. 3.23a), but in a few sites the columns define a lower and an upper group where columns of one group are oriented almost perpendicular to

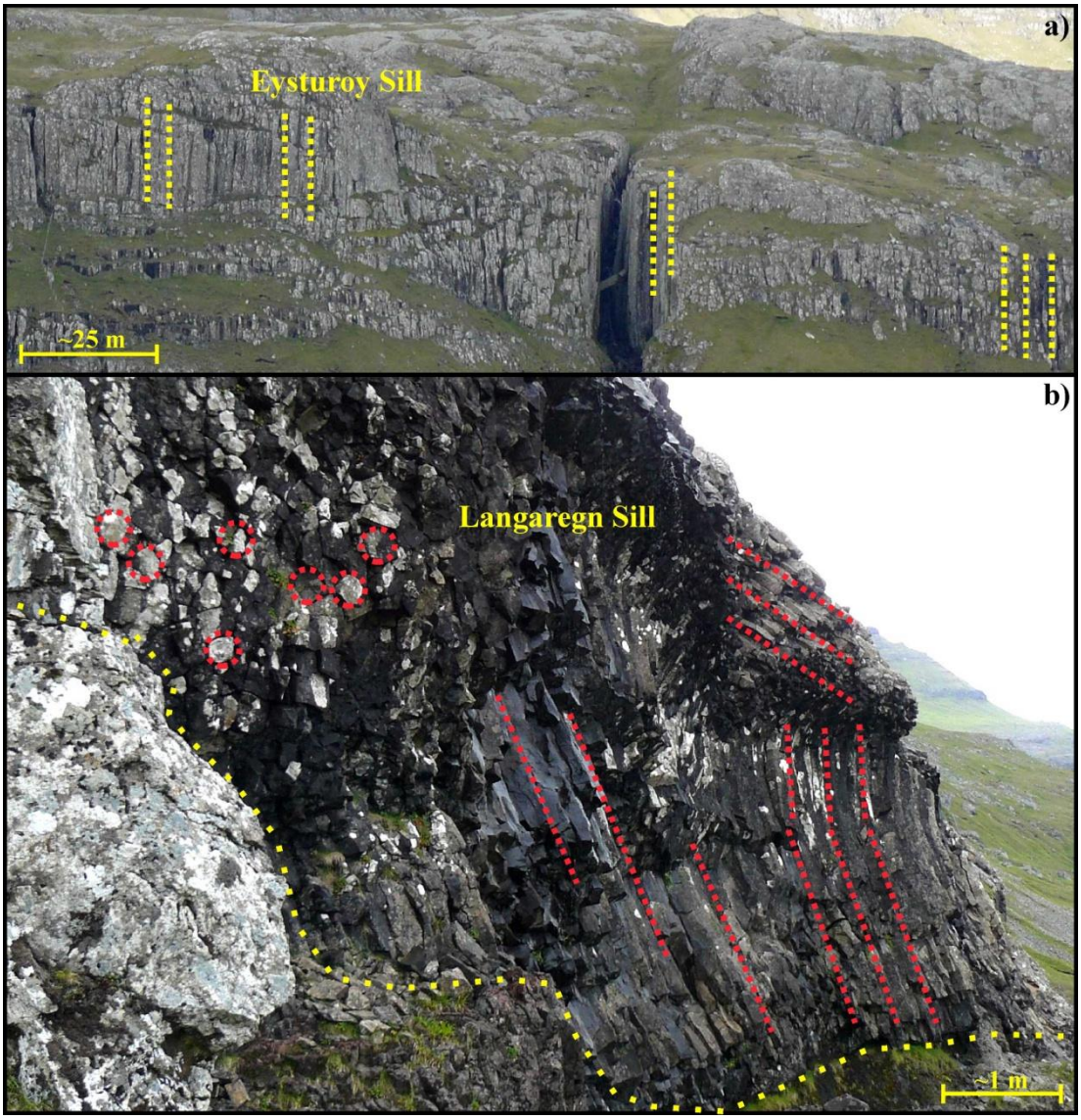

Fig. 3.23. a) Parts of the Eysturoy Sill display sub-vertical columnar jointing oriented orthogonal to sill contacts (yellow dotted lines). The columns are particularly conspicuous in the canyon walls, from where one column has broke loose and tipped over across the canyon. b) Columnar jointing in the Langaregn Sill where columns in the lower parts of the sill are oriented orthogonal to the lower contact in contrast to column in the upper parts that are sub-parallel to the upper contact. Yellow dotted line indicates lower sill contact. Red dotted lines indicate orientations of columns. Red dotted circles indicate ends of some sub-horizontal columns.

columns of the other group (Fig. 3.23b). In the example shown in Fig. 3.23b, the columns in the lower part of the actual sill are oriented at right angles to the lower sill contact whereas those of the upper part are sub-parallel to the upper contact.

The host basalts have been affected by the intrusive activities associated with sill

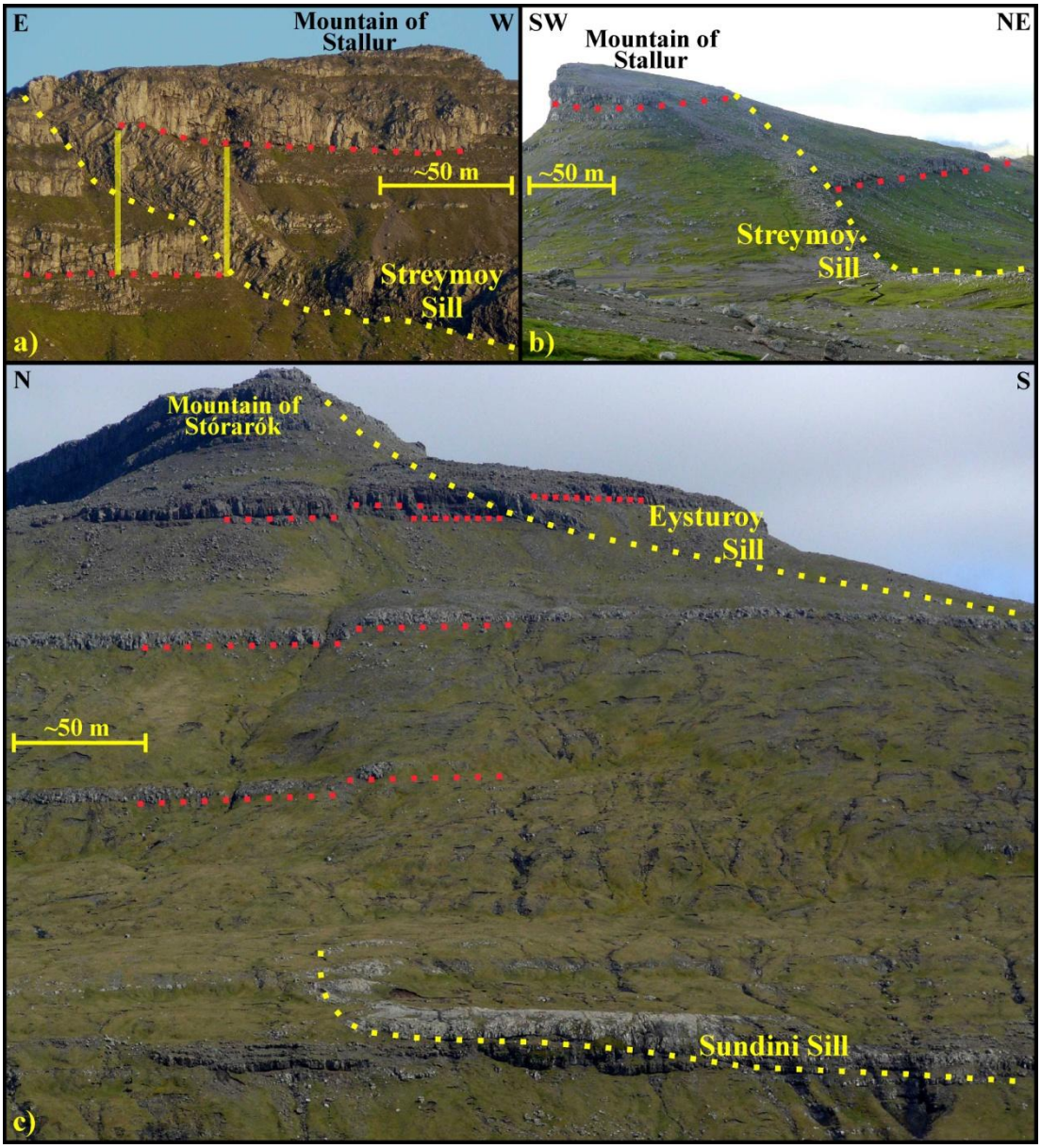

Figure 3.24. a) Marker horizon (red dotted lines) in basaltic overburden has been uplifted vertically (~45 m) by the SE segment of the Streymoy Sill. A 40 to 45 metres sub-horizontal displacement of the overburden towards the east or northeast is suggested by lateral overlap of marker horizons (vertical semi-transparent yellow lines). b) Same as in a), but showing a view from the opposite side of the mountain of Stallur. c) Marker horizon (red lines composed of closely spaced red dots) in host basalts has been uplifted (15 – 20 m) by the NW segment of the Eysturoy Sill. Three marker horizons at different stratigraphic levels (red dotted lines) in the host basalts have been uplifted (6 – 7 m each) by the Sundini Sill. Yellow dotted lines indicate lower sill contacts.

intrusion to various degrees and sometimes display thin zones of densely spaced fracturing/faulting close to sill margins. These fractures are mostly sub-parallel to the sill margins at the actual sites and could be a result of intrusive activities or they formed in response to subsequent tectonic events. However, the most prominent manifestations of intrusive activities in the host basalts are in the form of sub-vertical displacement of strata on top of the sills in question. An especially good example is exposed at the mountain of Stallur, where the SE segment of the Streymoy Sill has displaced a marker horizon upwards by around 45 metres during emplacement/inflation (Fig. 3.24a; Fig. 3.24b). Other good examples include an exposure on the southern flank of the mountain of Stórarók where emplacement of the thinnest parts of the NW segment of the Eysturoy Sill resulted in 15 to 20 metres uplift of the overburden (Fig. 3.24c). Also, uplifted marker horizons (6 to 7 metres) at three distinct stratigraphic levels on top of the thickest sections of the Sundini Sill (Fig. 3.24c) probably owe their displacement to sill inflation. It is likely that some of the uplifted overburdens also "floated" in sub-horizontal directions for short distances during sill emplacement as evidenced by ~40 metres of displacement in easterly direction of the overburden atop the Streymoy Sill at the mountain of Stallur (Fig. 3.24a).

3.5.2. Post-magmatic deformation

All exposed parts of the lava pile of the Faroe Islands have been affected by various regional tectonic events, some of which have been interpreted earlier to have occurred prior to or contemporaneous with sill intrusion in the area (e.g. Geoffroy et al., 1994). However, as the investigated sills represent the latest known phases of igneous activity in the actual region, deformation structures recorded within these intrusions must represent post-magmatic regional or local tectonic events.

A few structural characteristics dominate the deformation features observed within the actual sills. Broadly E–W trending sub-vertical fractures occurring either as closely spaced (2 to 3 cm apart) microscopic joints, which in many cases only become apparent when sill samples are split apart, or as more conspicuous and slightly more distantly spaced fractures appearing as linear sub-parallel surface structures (Fig. 3.25a) are of common occurrences in many parts of the sills from this study. Other prominent signs of tectonic activities that are particularly visible within the Eysturoy and Streymoy sills include well-defined sets of relatively large NNE–

SSW trending faults that often define conjugate sets dipping at low angles with the horizontal plane (Fig. 3.26a). Views at more detailed scales of rocks adjacent to these large faults commonly disclose the occurrences of multiple smaller faults/fractures that define broadly similar trends, but which often also dip at lower angles with the horizontal plane and may occur as individual faults rather than in conjugate sets (Fig. 3. 26b). Clear evidences of reverse movements along some of these faults in ESE direction at the SE margin of the Streymoy Sill (Fig. 3.26b) and in WNW direction at

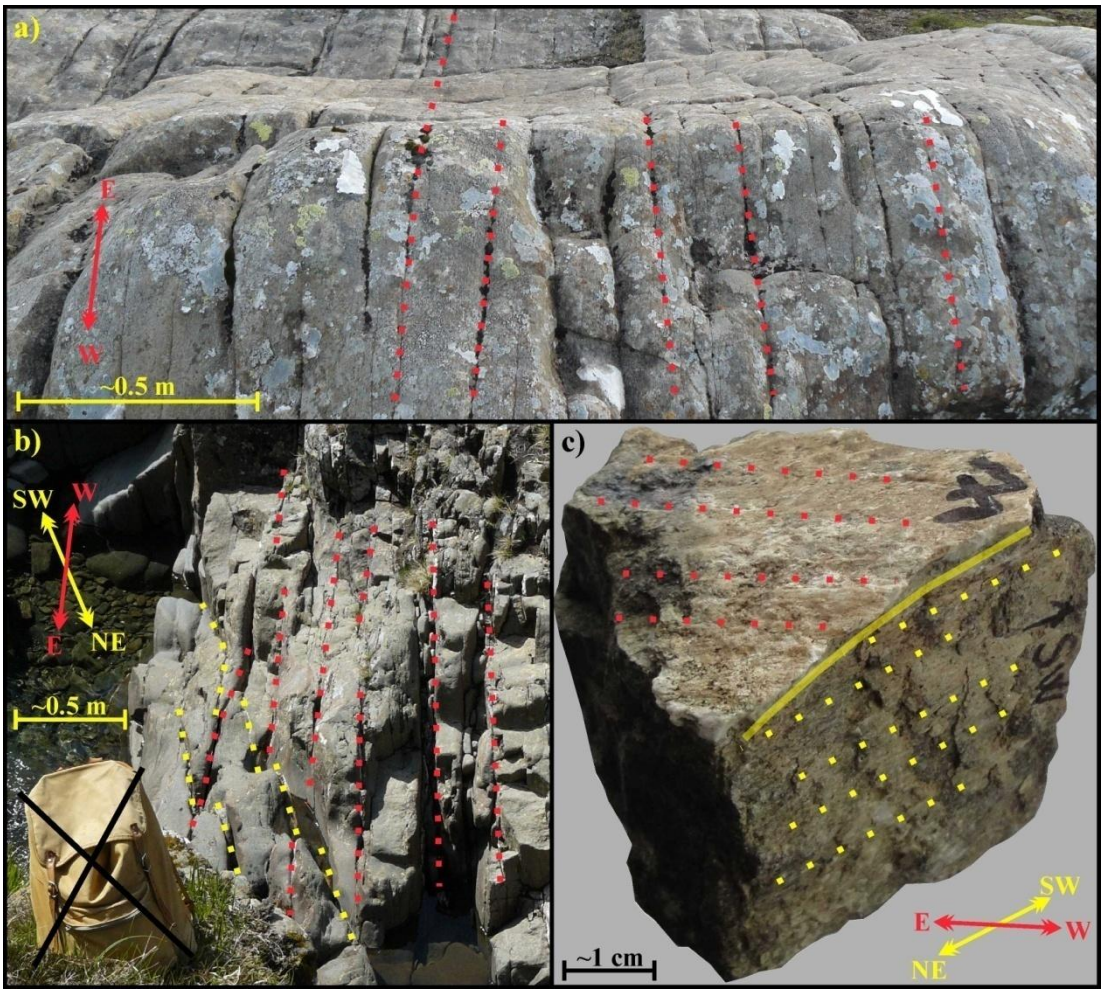

Figure 3.25. a) E–W directed sub-vertical fractures occurring in a more than 10 metres wide zone of the Streymoy Sill. b) In the Eysturoy Sill NE–SW trending millimetre thick sub-vertical mineralised extensional fractures (yellow dotted lines) have been displaced by sinistral strike-slip movements in E–W trending sub-vertical faults (red dotted lines) that appear to have affected the host sill in a semi-plastic manner. c) In the Kvívík Sill, NE–SW trending fibre lineation from sub-vertical dextral strike-slip movements (yellow dotted lines) have been overprinted by sub-horizontal E–W trending fibre liniation (red dotted lines) where the sense of movement (i.e. sinistral versus dextral) cannot be determined. Semi-transparent yellow full line indicates the contact where the face with E–W trending fibre lineation overprints the face with NE–SW trending fibre lineation. See text.

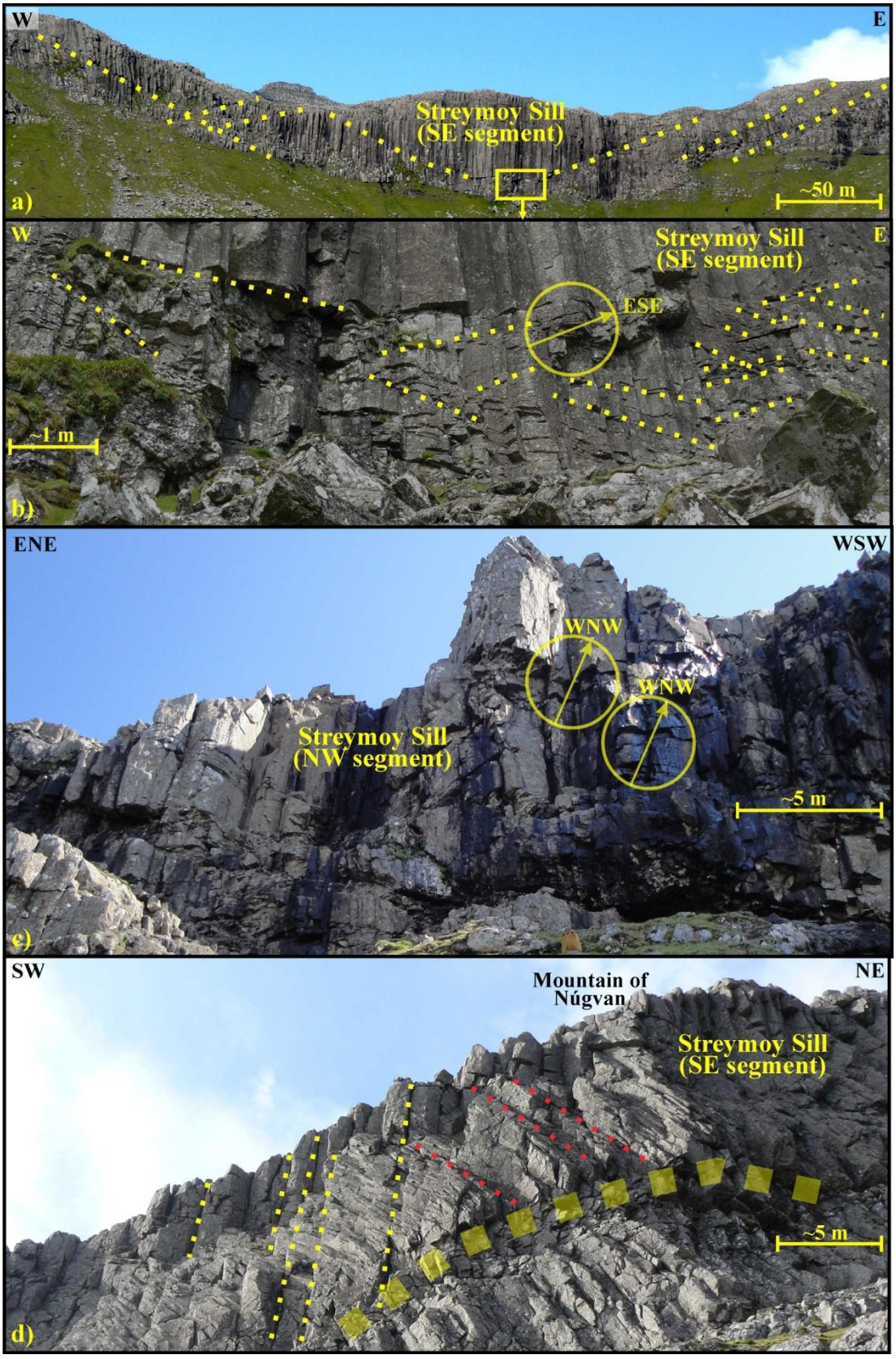

Figure 3.26. a) A number of conjugate faults (yellow dotted lines) that trend in a broadly NNE–SSW direction cut the the Streymoy Sill at low angles with the horizontal plane adjacent to the village of Norðadal. b) A closer view of a) reveal intense fracturing/faulting at all scales. The yellow circle encloses an example of limited reverse movement in a broadly ESE direction (yellow arrow). c) The

yellow circles enclose examples of limited reverse movements in a broadly WNW direction (yellow arrows) at the intensely faulted NW extremity of the Streymoy Sill on the NW flank of the mountain of Sátan. d) Sub-vertical broadly N–S oriented normal faults (yellow dotted lines) have cut initial inclined columnar jointing (red dotted lines), and apparently some of the reverse faults as described above as well (e.g. thick semi-transparent yellow dotted line), at the SE extremity of the Streymoy Sill at the mountain of Núgvan. See text.

the NW extremity of the same sill (Fig. 3.26c) strongly suggest formation of these faults in response to a compressional/shortening event. A succession of sub-vertical broadly N–S trending normal faults cut the original columnar jointing of the Streymoy Sill at its SE extremity on the mountain of Núgvan, as well as parts of the reverse faults described above (Fig. 3.26d). Less conspicuous are NE–SW trending sub-vertical tensile fractures occurring in some sills either as metre thick open faults/canyons, or as millimetre thick mineralised veins (Fig. 3.25b; Fig. 3.25c).

Direct relationships between deformation structures of different orientations within the sills that indicate the temporal sequence of deformation events have only occasionally been recorded in this study. In a narrow NE–SW trending canyon cutting into the Eysturoy Sill, sub-vertical NE–SW trending mineralised thin fractures are intersected by E–W trending sub-vertical fractures that form parts of a ~2 m wide fracture zone. Slight sinistral strike-slip movements within the fracture zone have resulted in slight dislocation of the mineralised NE–SW trending fractures, which themselves together with the canyon, in which the they crop out, probably result from NW–SE directed extension (Fig. 3.25b). Intersecting deformation structures encountered within the Kvívík Sill display a slightly different angle of the same aspect, where a sub-vertical face with NE–SW trending fibre lineation from dextral strike-slip motion is overprinted by a sub-horizontal face that contains E–W trending fibre lineation (Fig. 3.25c). Hence, these two exposures suggest that the observed E–W trending deformation structures were generated or reactivated subsequent to formation of the NE–SW trending deformation structures. The broadly E–W directed extension required to generate the observed normal sub-vertical faults could be of local origin e.g. sagging faults, but if they are of regional origin there may exist a link between these normal faults and the E–W directed strike-slip faults described previously.

Altogether, the combined field evidences on deformation structures recorded within the investigated sills in the course of this study do not yield conclusive results with

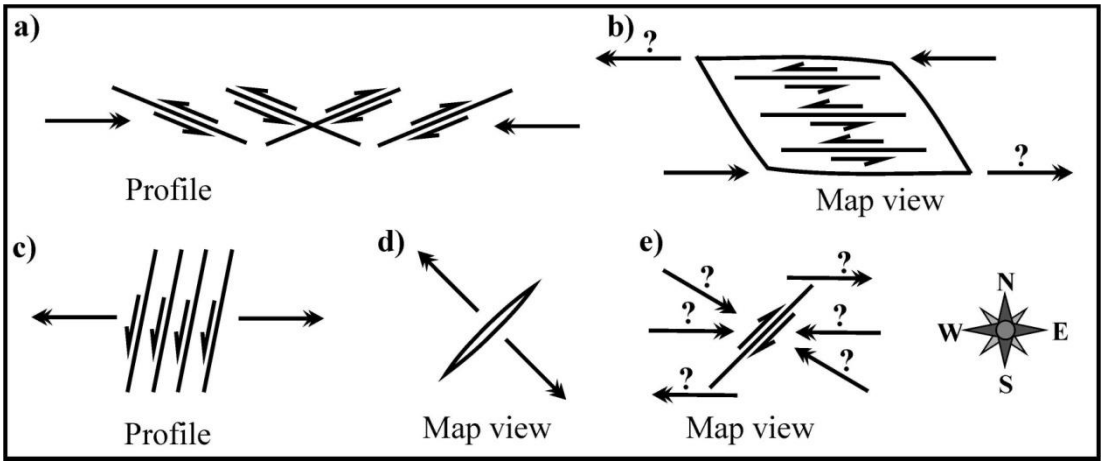

Figure 3.27. Simplified drawings of presumed deformation events. a) Reverse faulting from WNW–ESE or E–W directed compression. b) E–W directed compression-transpression or extension-transtension generates E–W trending strike-slip faults. c) Normal faulting from E–W directed extension. d) NW–SE directed extension generates NE–SW trending faults. e) Broadly E–W directed compression-transpression, extension-transtension or WNW–ESE compression-transpression on pre-existing NE–SW trending fractures can generate dextral strike-slip movements along the fracture planes. Full arrows = compression-extension; one-sided arrows = shear movements. See text.

respect to the temporal relationships between the observed features, apart from the overprinting of NE–SW trending structures by E–W directed movements (Fig. 3.25b; Fig. 3.25c). However, these observations provide strong indications on some palaeo stress directions in the actual area. Briefly, these can be listed as: Broadly WNW–ESE or E–W directed compression/shortening resulted in the formation of low-angle conjugate reverse faults in the Streymoy and Eysturoy sills in particular (Fig. 3.26a; Fig. 3.26b; Fig. 3.27a). Transpression and strike-slip faulting/jointing from this same compression event may have had the potential to generate the pervasive sub-vertical E–W directed joints that are of common occurrence in most of the sills from this study (Fig. 3.25a; Fig. 3.27b). E–W directed extension resulted in relatively closely spaced sub-vertical N–S trending normal faults at the inclined SE margin of the Streymoy Sill (Fig. 3.26d; Fig. 3.27c). Overprinting of sub-vertical NE–SW trending fibre lineation by sub-horizontal E–W directed fibre lineation (Fig. 3.25c) was probably generated by broadly E–W directed compression/transpression or extension/transtension. Roughly NW–SE directed extension produced NE–SW trending sub-vertical faults/joints in some of the sills (Fig. 3.25b; Fig. 3.25c; Fig 3.27d). Broadly E–W directed stresses (compression/transpression or extension/transtension?) could be responsible for slight sinistral displacements of

sub-vertical NE – SW trending mineralised fractures within narrow sub-vertical E–W trending fracture zones in e.g. the Eysturoy Sill (Fig. 3.25b; Fig.3.27b) and for fibre lineation on NE–SW trending fractures (Fig. 3.25c; Fig. 3.27e).

It would require a more extensive investigation of surrounding host basalts to establish whether all the observed deformation structures are of regional extent or if some of them are of more local character.

3.6. Discussion

The geometries of the investigated sills in addition to their general field occurrences may hint to particular emplacement styles and mechanisms, which are not necessarily entirely in accordance with earlier models proposed for sills intruded into sedimentary successions. However, a few ***physical criteria*** need to be satisfied for sill emplacement to occur irrespective of the nature of their host rocks.

3.6.1. Physical conditions and emplacement criteria for sheet intrusions

Some of the criteria that govern magma transport and emplacement of sheet intrusions include: (1) excess magma pressure in the melting region in addition to positive buoyancy/gravity of the intruding magmas contribute to the development of and, (2) principal stresses encountered in the intruded host-rocks and (3) elasticity and cohesive strength of the host rocks contribute to the inhibition of sill evolution (Bradley, 1965; Delaney et al., 1986; Gudmundsson, 1986; Lister and Kerr, 1991; Rubin, 1995; Kavanagh et al., 2006; Burchardt, 2008).

(1) Regions experiencing partial melting are sometimes interpreted to be the ultimate sources of excess magma pressures (Bradley, 1965), as melts + residues combined are expected to possess larger volumes compared to their unmelted source rocks (e.g. Maaløe, 2003). Newly generated magmas are expected to possess large positive buoyancies relative to their source rocks, which will exert upward-directed stresses on the lower parts of their plumbing systems (Morgan, 1997; Raddick et al. 2002), whereas magmas in dykes and sills at very shallow crustal levels may exert gravity-induced lateral stresses on their surroundings (Lister and Kerr, 1991; Varga et al. 1998).

(2) In homogeneous non-deformed host rocks, magmas in sheet intrusions are expected to propagate in planes perpendicular to the least principal stress σ_3 (Pollard, 1973; Geoffroy et al., 1994; Valentine and Krogh, 2006), meaning that

for sub-vertical dykes σ_3 lay in the sub-horizontal plane (Valentine and Krogh, 2006). For sill intrusions to be initiated, σ_3 is expected to have near vertical orientations where the lithostatic load of the overburden $pgz_{overburden}$ (p = bulk density of the overburden; g = gravity and z = depth) exert stress on the intrusion (Kavanagh et al., 2006; Valentine and Krogh, 2006; Motoki and Sichel, 2008). Hence, for melts intruded from sub-vertical or oblique feeder dykes in relatively homogeneous host rocks, sill emplacement would be expected to occur at a depth range where a localised rotation of σ_3 from a sub-horizontal or inclined orientation to a sub-vertical orientation has taken place (Valentine and Krogh, 2006). Melt injection and fault propagation in any dyke or sill regime require a magmatic pressure P_m that is greater than σ_3, and in cases where the P_m of intruding melts is larger than the greatest principal stress σ_1 and the cohesive strength σ_c of the host rock combined, sheet intrusions oriented at angles other than 90° relative to the regional σ_3 can be formed (Rubin, 1995; Valentine and Krogh, 2006). The invasion of magmas into pre-existing fractures can sometimes lead to sheet intrusions oriented at angles other than 90º relative to σ_3 as long as P_m exceed the normal components of any regional σ_3 resolved on the invaded fracture planes (Delaney et al., 1986; Baer et al., 1994; Rubin, 1995; Valentine and Krogh, 2006). At crustal levels with near-vertical σ_3, sill emplacement is commonly thought to occur preferably in "weak" layers when intruded into host-rocks composed of sub-horizontal strata of contrasting mechanical properties (Bradley, 1965; Kavanagh et al., 2006; Burchardt, 2008).

Fracture propagation and emplacement of sheet intrusions into relatively homogeneous non-deformed host rocks require a P_m that is greater than σ_3 and the ability of the host rock to resist compression/stretching and possible fracturing combined (Gudmundsson, 1986; Menand and Tait, 2002; Valentine and Krogh, 2006). The thickness of a young sub-horizontal sill, prior to wholesale failure and uplift of the overlying strata, depends on the elastic properties of the host-rocks i.e. their capacity to expand/compress without fracturing (Pollard, 1973; Gudmundsson, 1986; Rubin, 1995) (e.g. Fig. 3.28).

The change in thickness of a vertical column of uniform rocks, in response to applied symmetrical compressional-extensional vertical forces, can in its simplest form be expressed as (Ohanian, 1989):

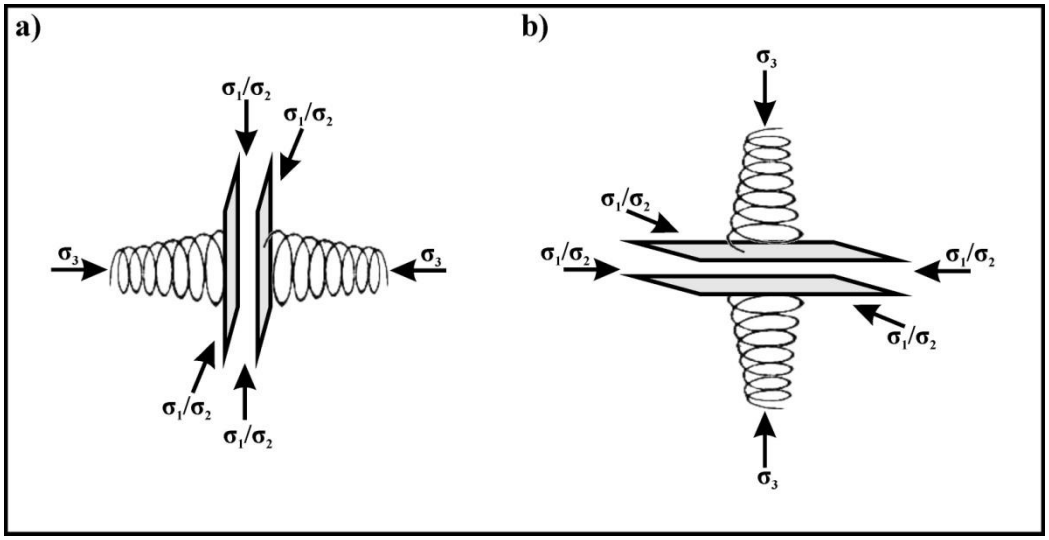

Figure 3.28. a) Dyke intrusion by elastic displacement of host rocks requires a sub-horizontal orientation of σ_3. b) Sill intrusion by elastic displacement of host rocks requires a sub-vertical orientation of σ_3. Intrusion thicknesses prior to rupture of wallrocks/overburdens depend on sizes of σ_3 and the capacities of host rocks to contract/expand elastically. See text.

$$\Delta v = ((1/E) \times (F/A)) \times v \quad (1)$$

where v represents the vertical extent of affected host-rocks, Δv is the total vertical change in thickness of affected host-rocks (same as change in sill thickness during inflation), E is the Young's modulus of affected rocks, A is the sub-horizontal area at the end(s) of rock column(s) (equal to surface area of sill during inflation) and F (negative for compression) is the total vertical force acting on the affected rocks i.e. for sill intrusion F equals magmatic pressure P_m (for a Newtonian liquid) per area unit times the whole sill area: $F = P_m \times A$ Equation (1) then reduces to:

$$\Delta v = (P_m/E) \times v \quad (2)$$

The elastic response of a rock to shear stress of any direction may play an additional role for sill emplacement and can be expressed as (Ohanian, 1989):

$$\Delta v = ((1/S) \times (F/A)) \times v \quad (3)$$

or in reduced version:

$$\Delta v = (P_m/S) \times v \quad (4)$$

where Δv is change of rock dimensions (thickness), S is the Shear modulus, which is two to three times smaller than E for most materials (Ohanian, 1989).

Apart from the vertical stress σ_v, and the cohesive strength of the host-rocks σ_c, an additional barrier to be overcome during sill intrusion is the horizontal stress e_h expressed as (Fyfe et al., 1978):

$$\sigma_h = \sigma_v(\mathrm{m}-1)^{-1} \pm e_h E \quad (5)$$

where σ_v is the vertical stress (load of overburden), m is Poisson's number (reciprocal to Poisson's ratio), e_h is the horizontal strain (compressive strain is positive) and E is the Young's modulus. This means that prior to rupture of the overburden the vertical inflation of any sills emplaced at specific magmatic pressures rely on E in particular in addition to the vertical extent of affected host-rocks as critical factors in governing the accommodation of these intrusive bodies by elastic displacement.

3.6.2. Application of earlier emplacement theories

It is not straightforward to compare the investigated sills with sills from other similar settings, as emplacements of saucer-shaped sills into igneous host-rocks have not been described in the published literature earlier (to this students knowledge), but the emplacements of tabular sub-horizontal sills in volcanic successions from NE and E Iceland have been interpreted to result from rotation of σ_3 from sub-horizontal to sub-vertical orientations due to contrasting mechanical properties in layered host-rocks (Burchardt, 2008; Gudmundsson, 2011). While the feeders from this study display similarities with the inclined dykes/sheets that fed these Icelandic sills, magma intrusions along sub-horizontal mechanical boundaries like those reported from Iceland (Burchardt, 2008) has only been observed in a feeder to the Streymoy Sill that displays a ramp-flat geometry (Fig. 3.14a) and in a few localities where magmas of propagating and otherwise climbing sills may have been guided along sub-horizontal weakness zones for very short distances (Fig. 3.6a; Fig. 3.14a). It remains an open question if the interaction mechanism between a sill and its total overburden mechanism, which has been interpreted to generate the asymmetry necessary for climbing of saucer-shaped sills with distinct sub-horizontal inner and steeply inclined middle/outer sections (e.g. Malthe-Sørensen et al., 2004; Thomson, 2007; Goulty and Schofield, 2008; Polteau et al., 2008), is applicable for the formation of saucer-shaped sills where the saucer gradually curve upwards all the way from the sub-horizontal base to the inclined rim. If hypothetic diameters of low-

angle inner sections (≤ ~15°) of the smaller sills and individual sill segments from the Faroe Islands measure ~3.0 to ~4.0 km (section 3.2) and if it is assumed that the diameter of these hypothetic inner sills were ~4 times the overburden (e.g. Polteau et al., 2008) their emplacement depths would accordingly have ranged from ~800 to ~1000 m, i.e. at equal or just slightly shallower depths than the estimated values of ~1000 m indicated by measurements of palaeo thicknesses in the area intruded by the Svínoy-Fugloy Sill (Jørgensen, 2006). Using these same hypothetical inner sill diameters on other expressions for length of inner sill sections versus intrusion depths, i.e. depth/radius ≤ 2 (Pollard and Holzhausen, 1979) and radius/depth ≥ 1 (Fialko, 2001) would yield intrusion depths of 3 – 4 km and 1.5 – 2 km respectively. According to previous studies on palaeo thicknesses of the basalt formations of this region (Jørgensen, 2006), such intrusion depths would be unrealistically high. If the Streymoy and the Eysturoy sills were intruded as homogeneous single elliptic intrusions, the maximum diameters of their inner sill sections that possess inclination angles less than ~15° would have approached ~7.5 km and ~5.0 km respectively, meaning that these intrusions would have been intruded at depths ranging from ~1400 to ~2000 m, when an inner diameter versus overburden ratio of ~4 is assumed. As these depths also exceed the actual palaeo thicknesses indicated for the actual basalt sequences (Jørgensen, 2006), it is unlikely that each of these two sills formed as single elliptic intrusions, if the criterion with a diameter/overburden ratio of ~4 is valid within reasonable margins. If depth estimates are only based on sub-horizontal innermost sill/segment sections measuring 1.5 – 2km across (section 3.2), a diameter/overburden ratio of ~4 (Polteau et al., 2008) would yield maximum overburden thicknesses of only 0.4 to 0.5 km whereas the ratios depth/radius ≤ 2 (Pollard and Holzhausen, 1979) and radius/depth ≥ 1 (Fialko, 2001) would yield intrusion depths of 1.5 – 2 km and 0.75 – 1 km respectively. Consequently, only depth estimates from the expression of Fialko (2001) approach realistic values in this particular case. It remains an open question whether the sills from this study owe their saucer-shaped geometry to symmetrical wholesale uplifts of sill overburdens in response to certain intrusion sizes versus intrusion depths, as the actual sizes of these sills commonly vary, even though they are intruded at similar stratigraphic levels. Also, the asymmetrical nature of both smaller sills and individual segments of the larger sills as well as common occurrences of gradual and continuous upward-

curving geometries all the way from central sections of the actual sills seem to suggest the actions of other emplacement mechanisms.

3.6.3. Exploring other potential emplacement mechanisms

As each of the Kvívík, Morskranes and Sundini sills have only been inflated to relatively great thicknesses at their inclined margins and approach zero thicknesses in their opposite ends at lower altitudes, the development of these sills may have been halted prematurely before they reached their full potential when compared to the much thicker and uniformly inflated Streymoy and Eysturoy sills. The magmas building up the two uniformly inflated Streymoy and Eysturoy sills must have supported their overburdens entirely in contrast to the magmas of the three (four?) partially inflated sills, which could only have supported the bulk of their overburdens at their thickest ends. If these three partly inflated intrusions do indeed represent less evolved stages of sill formation compared to the neighbouring Streymoy and Eysturoy sills, they may offer important and unique insights into the embryonic stages of sill emplacement into relatively rigid host-rocks. The asymmetric saucer-shapes and systematic thickness variations of these three intrusions suggest that physical conditions, such as sizes and directions of the principal stress axes acting on the sills, underwent temporal and spatial variations during their development. If the orientations of thin sub-horizontal protrusions into host basalts from slightly inclined basal sections, common to all the studied sills (Fig. 3.8), can be taken as indications of magma transport directions, these seem to suggest that the actual intrusions initially developed radially outwards at slightly inclined angles from their lowermost stratigraphic levels. Indeed, previous studies have suggested that additional fracture/magma propagation from the margins of developing sheet intrusions primarily take place in directions that possess the largest values of a parameter *K*, expressed as (Baer, 1991):

$$K = P_d(\pi l)^{1/2} \quad (6)$$

where P_d is the driving pressure and l is the distance to the magma source. As is suggested from equation 6, continued propagation of dyke/sill margins or protrusions from these would predominally be directed away from their respective magma sources. Determination of the most probable directions of palaeo magma flows from orientations of protrusions from larger sheet intrusions have also been utilised earlier,

e.g. in a study of the Great Whin and Midland Valley dolerite sills (Goulty, 2005) and in other studies of sheet intrusions in general (Correa-Gomes et al., 2001, and refs. therein). Similar growth models for saucer-shaped sills have sometimes been inferred for sills intruded into sedimentary successions as well (Thomson, 2004; Thomson and Hutton, 2004; Hansen and Cartwright, 2006). Also, Pollard and Johnson (1973) stated that rocks around developing sheet intrusions would pull apart in plane continous with the length of the actual intrusions. The very restricted lateral extent of exposed feeder/sill transition zones (e.g. Fig. 3.14) indicate that these sills were fed from point sources rather than laterally extensive dykes/fissures.

As no crustal uplifts have been detected in the overburdens above the thin basal parts of the Kvívík, the Morskranes and the Sundini sills, their overall saucer-shaped geometries and upward-curving propagation trends (Fig. 3.9) cannot readily be explained by a mechanism with sill climbing due to wholesale uplifts/doming of their respective overburdens that generated the asymmetries at their propagating margins, as discussed above for sills occurring in sedimentary strata. Instead we envisage continuous mechanisms that occur at much smaller scales involving interactions between the invading magmas and the intruded strata above and below the propagating sill margins.

Due to the effect of lithostatic load the values of E for crustal rocks increase with depths in a non-linear manner where the relative increase of E for fixed distance

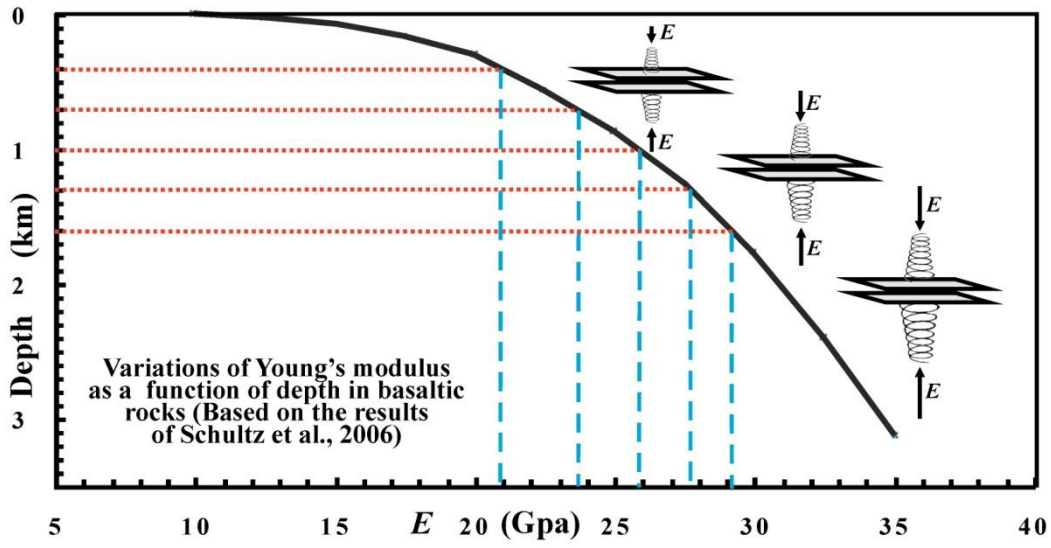

Figure 3.29. The values of Young's modulus for basaltic crustal rocks increase systematically with increasing depths in a non-linear fashion with the largest relative increase occurring at relatively shallow depths. (Based on the study of Schultz et al., 2006). See text.

intervals is largest at relatively shallow crustal levels (Schultz et al., 2006) (Fig. 3.29). As E is expected to be constant at fixed depths in laterally homogeneous host-rocks, no noticeable variations in elasticity of host-rocks should be expected in the sub-horizontal plane. Hence, for a young sill propagating laterally into host-rocks that behave as isotropic units on vertical scales of a few hundreds of metres (e.g. Hatcher, 1995), the variations of E (Fig. 3.29) should render the strata atop the ambientintrusion more prone to elastic stretching/compression compared with a similar rock suite below it. During inflation/dilation of sheet intrusions behind existing single extension fractures, the nature of the stress fields within host-rocks adjacent to both sides of the propagating tips/margins may be be influenced by the invading magmas. Such effects on the host material may include a drop in pressures immediately behind the propagating tip (Rubin, 1995) and rearrangements of principal stress axes/trajectories in the immediate vicinity of the intruding sheets relative to orientations of these axes within ambient host-rocks (Pollard, 1973). Accordingly, a previous study (Pollard, 1973) suggested that the local largest principal stress axes/trajectories σ_1 adjacent to an embryonic sheet intrusion were rotated from orientations being sub-parallel to the plane of the intruding sheet just in front of the propagating margin to orientations broadly orthogonal to the developing intrusion behind the advancing tip (Fig. 3.30a). Correspondingly, the local least principal stress axes/trajectories σ_3 are expected to be near-vertical on both sides of the very tip of the developing sheet intrusion immediately at the fracture plane and then gradually have their farther end rotated inwards behind the propagating tip (Pollard, 1973) (Fig. 3.30a). Based on Fig. 3.30a, two inferences can be made. 1) The configuration of the local σ_1 and σ_3 as shown in Fig. 3.30a renders it unlikely that propagation direction of potential magma protrusion near such a propagating sheet margin would deviate substantially from the general direction of margin propagation. 2) The probable increase in local values of Young's modulus E in host-rocks on both sides of an inflating/propagating sheet intrusion due to compression would most probably reduce the likelihood of magma protrusions in directions opposite to the general direction of margin propagation. These two arguments support previous inferences, suggesting that orientations of protrusions from sills of this study probably point to approximate directions of palaeo magma flows (See also discussion around equation 6 above).

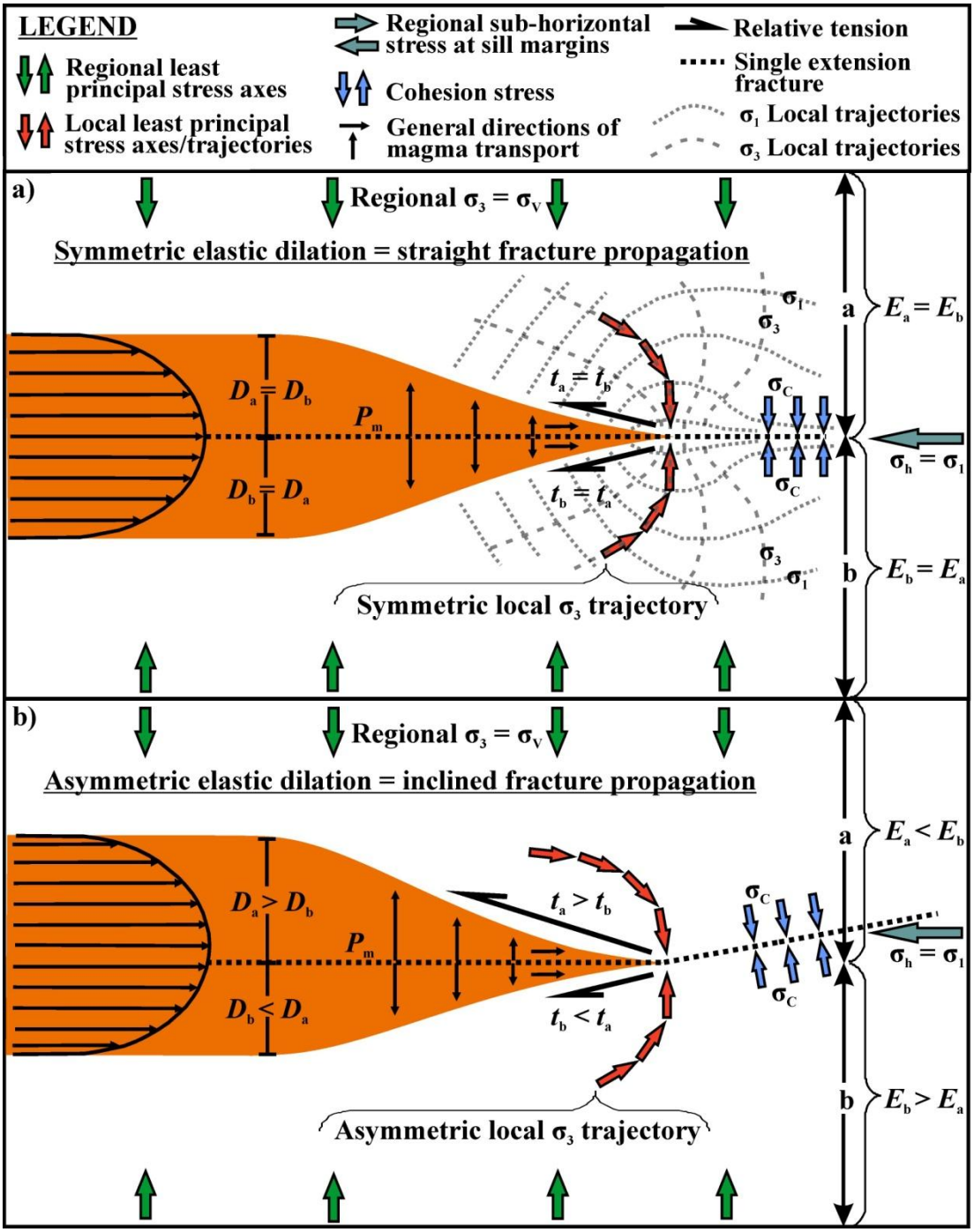

Figure 3.30. a) Symmetric sill inflation (radial?) with sub-horizontal fracture propagation. b) Asymmetric sill inflation with inclined fracture propagation. a and b = host rocks above and below single extension fractures respectively; D_a, t_a, E_a = values of dilation, tension and Youngs modulus respectively in host rocks above a single extension fracture; D_b, t_b, E_b = values of dilation, tension and Youngs modulus respectively in host rocks below a single extension fracture; P_m = magmatic pressure; σ_1, σ_3, σ_v, σ_c and σ_h = largest principal, least principal, vertical, cohesion and horizontal stress axes respectively. Dotted and dashed semi-transparent grey lines/curves of different orientations, shown in a) represent local σ_1 and σ_3 trajectories respectively, which result from interaction between intruding magmas and their host-rocks (Trajectories adopted from Pollard, 1973). See text.

Gravity-induced differences in elastic properties of isotropic host-rocks on either side of a laterally propagating single extension fracture could in theory cause a young sill to inflate disproportionally behind the propagating tip, with relatively larger melt volumes being emplaced above a vertically fixed initial plane of propagation than GPa, 1000 - 1300 m = 26.8 GPa) are used, show that the dilation above the initial plane of propagation for this theoretical sill is ~7.5% larger than it is below it. below it (in accordance with equation 2). It may be envisaged that such asymmetric dilation could lead to a slightly larger drop in the relative least principal stress above the propagating tip than below it, thus resulting in asymmetries of the local σ_3 trajectories that would trigger an upward deflection of the propagating tip relative to the previous plane of propagation (Fig. 3.30b). A testing of this scenario by means of equation 2, where a sill is being intruded at a depth of ~1000 m with ~300 m of host-rocks above and below this embryonic intrusion being affected by the sill dilation and where average values of Young's modulus from Fig. 3.29 (700 - 1000 m = 24.8 Although this inferred process of sill climbing is interpreted to occur at much smaller scales and to take place at the very sill margins, the principle is quite similar to a mechanism where propagating sill margins are interpreted to be deflected upwards in response to stress asymmetries at sill margins, due stretching of entire overburdens ocurring in response to asymmetrical inflation of entire sills, associated with displacement or doming of the Earth's (free) surface on top of developing intrusions (Pollard and Holzhausen, 1979; Fialko, 2001; Goulty and Schofield, 2008) (e.g. Fig. 3.1e). As the relative increase of E for fixed vertical distances becomes lesser with increasing depth (Schultz et al., 2006) (Fig. 3.29), asymmetric sill inflation, as inferred above, should be expected to become less prevalent with increasing depths. The result of these depth-dependant differences should in turn result in less inclined and successively larger basal sill sections with increasing depths, which is in accordance with previous interpretations on sill/overburden ratios (Pollard and Holzhausen, 1979; Fialko, 2001; Malthe-Sørensen et al., 2004; Goulty and Schofield, 2008; Polteau et al., 2008). As long as a notable asymmetric inflation is maintained, a gradual rotation of the propagating edges towards increasing angles relative to the sub-horizontal plane may be expected. The overall elliptic appearances of the Kvívík, the Morskranes and the Sundini sills in map view and the locations of their inferred magmatic sources (Fig. 3.3d; Fig. 3.3e; Fig. 3.3f) suggest that these sills probably

also progressed at uneven/asymmetric rates in the sub-horizontal plane, in addition to inferred upward-curving propagations in the sub-vertical plane (Fig. 3.30b).

As the distance to the Earth's surface from the margins of a sill that propagates at an inclined angle is becoming lesser, a reduction of the total cohesive/necking strength of the remaining overburden must be expected. Also, as the total vertical extent of a magma column is increased a gravity controlled pressure gradient (Δpgz_{magma}) will develop, which for a tholeiitic melt with an average density of 2.65 g/cm^3 will result in differences from bottom to top of ~6.5 and ~13 MPa for melt columns measuring 250 and 500 m respectively. Boiling of magmas with gas exsolution and segregation is commonly associated with the ascent and cooling of melts in the upper crust, and the associated volume increase will generally lead to overpressure in the affected magma chambers (Woods and Cardoso, 1997; Sparks, 2003). Provided that a developing sill system functions as a closed hydraulic system, overpressure from gas exsolution may partly compensate for a gravity-controlled pressure drop as melts ascend towards shallow crustal levels. The process of gas exsolution has clearly been active during margin propagation in some of the sills of the Faroe Islands, as evidenced by mineralized vesicles that make up 15% to 20% of the total intrusion volumes in some of the thinnest parts of sill margins (Fig. 3.18a). Calculations have shown that the exsolution and segregation of gas in basaltic melts with a H_2O content of ~0.3 % result in a pressure increase on top of vertical magma columns measuring 250 and 500 m of ~2.65 and ~5.30 MPa respectively (Woods and Cardoso, 1997). These figures are much smaller than the gravitational pressure drops for similar height differences in vertical magma columns, as shown above. Also, the inclined nature of the upper sections of all sills in question (as opposed to the unrestricted vertical distances encountered in sub-spherical magma chambers) would probably put significant limitations on the formation of any large overpressures from exsolved gases. If necking of strata above propagating sill margins occur at relatively fixed crustal depths, sills initiated at similar depths and expanding by gradual upward curving propagation in radial modes and at broadly similar angles with the horizontal plane should develop roughly similar sizes, where total sills sizes should be expected to increase with increasing depths. The relatively thick elevated NE, SE and E margins of the Kvívík, the Morskranes and the Sundini sills respectively (Fig. 3.3d; Fig. 3.3e; Fig. 3.3f) could not have been accommodated solely by elastic displacement of the host-rocks, but would have required rupture and some uplift of

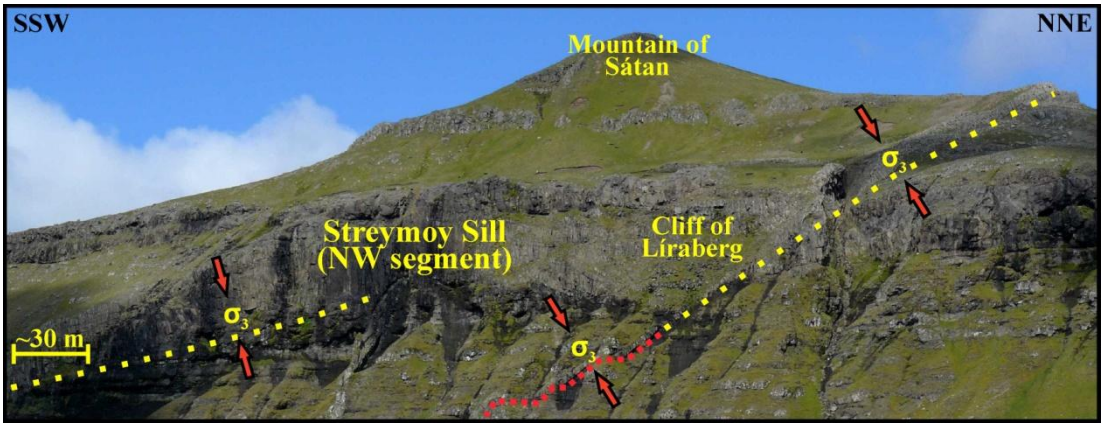

Figure 3.31. Inclined section of the Streymoy Sill displays a noticeable sudden anticlockwise rotation as it climbs from the SSW towards the NNE. The orientation of a feeder dyke/sheet just below the dyke/sill contact is similar to the uppermost section of the Streymoy Sill. Yellow dotted lines indicate lower sill margin and red dotted line indicates trend of feeder dyke/sheet. Red arrows show presumed palaeo orientation of local (and not necessarily regional) least principal stress axes σ_3. See text.

the overlying strata. When failure of a relatively competent and brittle overburden finally occurs on top of a propagating sill margin, as is inferred for the Kvívík, the Morskranes and the Sundini sills, a relatively rapid pressure release, due to the opening up of a previously closed hydraulic system together with a sudden abandonment of cohesive/necking forces to be overcome, may be envisaged. The occurrences of relatively abrupt changes in sill inclinations toward steeper angles with the horizontal plane, observed only at inclined rims in some of the investigated sills (e.g. Fig. 3.31) may signal the occurrences of relatively sudden necking of overburdens during late stages of sill intrusion that in turn resulted in marked shifts of local σ_3 orientations, perhaps in a fashion similar to what has been proposed for the onset of sill climbing inn sedimentary strata (Malthe-Sørensen et al., 2004; Thomson, 2007; Goulty and Schofield, 2008). As the thin dykes/sheet, which fed a part of the inclined margin of the Streymoy Sill that show abrupt inclination changes (Fig. 3.31), display similar strike/dip orientations immediately below their contact and probably also shared local (and not necessarily regional) palaeo σ_3 directions with the rim it once fed, some kind of interaction between feeder and the uppermost parts of this sills may have occurred during their intrusions? Potential scenarios include dyke intrusions triggered by sudden local reorientations/resizing of σ_3 due to wholesale necking of the strata above the propagating sill margins, or perhaps the crustal necking was associated with and triggered by late intrusion of marginal

dykes. However, the very restricted lateral extent of these dykes signal that if they did influence the intrusion styles of any parts of these inclined sill margins, it probably was at insignificant scales.

The pronounced wedge-shaped thickness variations of the Kvívík, the Morskranes and the Sundini sills (Fig. 3.5) show that the main phases of sill inflation preferably took place at the most steeply inclined sill sections at their NE, SE and E margins respectively. Also, the general geometries of these sills suggest that the local σ_3 axes close to these margins had been rotated towards lesser angles with the horizontal plane relative to the local σ_3 axes closer to the thinner parts of the intrusions. The disproportionate inflation and uplifts of overlying strata, which generated the wedge-shaped thickness variations in these sills, would have resulted in slight tilts/rotations of their respective overburdens toward slight inward-directed dips. The asymmetric inflation styles displayed by these three sills are partly in accordance with earlier inferences suggesting that large-scale sill inflation is initiated at the inclined outer margin at one end of the sill in question (Francis, 1982; Chevallier and Woodford, 1999). However, while Francis (1982) as well as Chevallier and Woodford (1999) inferred main magma supplies to their sills from marginal dykes (e.g. Fig. 3.1.a; Fig. 3.1.b), central feeders are interpreted to have acted as major magma sources to the sills from this study, in addition to lesser magma supplies via marginal feeders to the rims of the NW segment of the Streymoy Sill.

The clear division of the large Streymoy and Eysturoy sills into two distinct partly saucer-shaped segments each, together with the close similarities between the general geometries and profiles representing these segments and the general geometry and profiles representing the Kvívík, the Morskranes and the Sundini sills (Fig. 3.5), may suggest similarities in emplacement mechanisms for all of these intrusions albeit they probably represent different evolution stages. The close spatial relationships between these sills, which mostly occur at overlapping crustal levels and in identical host-rocks (Fig. 3.2), further strengthen inferences of a common emplacement mechanism. If each of the Streymoy and the Eysturoy sills indeed formed by merging of two partly saucer-shaped asymmetric sill segments broadly similar to the Kvívík, the Morskranes and the Sundini sills, the cohesion stress σ_c in the host-rocks to be overcome by propagating sill margins would have cancelled out at their zones of merging prior to their solidification if they were broadly contemporaneous. Hence, at this inferred stage of evolution the obstacles for large-scale sill inflations to occur

would perhaps only have included the horizontal stress σ_h (equal to average magmatic pressure P_m of the merged segments) and the lithostatic load of the overburden ($pgz_{overburden}$), thus rendering sill inflation/expansion free to occur until hydrostatic equilibrium was obtained. The ultimate sill thicknesses would depend on a number of factors including the heights and densities of the overburdens as well as the magmatic (over)pressures or the densities and heights of the actual magma column in the open plumbing system (e.g. Goulty, 2005).

3.6.4. Environment of emplacement and host-rocks

At present it has not been possible to constrain the timing and duration of sill intrusion and determine if they are broadly contemporaneous, as no absolute dating is available for any sills or associated dykes. As the sills of the Faroe Islands apparently post-date all sub-vertical dyke systems intersecting the actual area, some of which are interpreted to have been emplaced during various Early Cenozoic tectonic events (Geoffroy et al., 1994), the sill intrusions are probably not linked to any particular stress regime belonging to one of these particular events. Also, the large differences in strike directions between individual feeder dykes as well as between individual sills suggest that, if emplaced broadly contemporaneously, the local magma supplies to these intrusions possessed pressures larger than the largest principal stress σ_1 thus being a governing factor in determining the mode of sill emplacement. Possible links between some of the investigated sills and deep-seated lineaments in adjacent fjords (Ellis et al., 2009) cannot be ruled out completely, but locations and geometries of feeder dykes as well as orientations of numerous protrusions from inclined basal sill sections suggest that magma supplies for many of the sills in question were derived from the interior of the islands where they are exposed at the present time (Fig. 3.3).

Anisotropic behaviour of host-rocks due to contrasting mechanical properties, e.g. at sites containing sub-vertical fracture/dyke zones or sub-horizontal layering, appear to have affected intrusion styles of sills and/or dykes of the Faroe Islands preferably at relatively high stratigraphic levels. Examples of sub-vertically influenced intrusion styles include the whole linear NNE facing inclined margin of the NW segment of the Eysturoy Sill (Fig. 3.3a) and smaller parts of the SE facing inclined margin of the Morskranes Sill (Fig. 3.3f) where intruding melts appear to have been guided along pre-existing fracture/dyke systems. The effect of anisotropy in sub-horizontal layering is particularly evident in one of the feeder dykes to the Streymoy Sill, where

a pronounced ramp-flat geometry point to melt intrusion into layers of different mechanical competences (Fig. 3.14a; Fig. 3.31). Possible effects of sub-horizontal layering in host-rocks that involve the sills themselves include the NW segment of the Streymoy Sill, which flattens out for a short distance as it transects the Sneis Formation as shown at the centre of figures 3.14a and 3.31. Also, the SE segment of the same sill that takes a gentle turn towards a sub-horizontal orientation, which it follows for a distance of around 200 to 250 metres, as it climbs towards the mountain of Núgvan (Centre-right in Fig. 3.6a).

A significant degree of isotropic behaviour in host-rocks at sites of presumed embryonic sill formation at relatively low stratigraphic levels is suggested by the general occurrences of low-angle contacts between basal sill sections and layered host-rocks of the Early Cenozoic Faroe Islands (Fig. 3.6a). Additionally, the common occurrences of dyke to sill transitions and protrusions into homogeneous crystalline host basalts rather than in adjacent sedimentary sequences (e.g. Fig. 3.8; Fig. 3.14d) point to a significant degree of isotropic behaviour of these host-rocks. The inferred differences in intrusion styles according to crustal depths seem to suggest that a large lithostatic load may partly suppress the effect of contrasting mechanical properties in host-rocks thus increasingly leaving them as isotropically homogeneous units with increasing depths.

Sites that represent the lowermost parts of sub-horizontal basal sections of the investigated sills, which arguably represent the embryonic emplacement stages of these intrusions, define a trend in the regional stratigraphy where plotted altitudes representing the lowermost points of individual sills decrease towards the NW or WNW relative to the base of the Enni Formation (Stratigraphic column, Fig. 3.2). This trend is particularly conspicuous when the sills occurring in the main study area are considered as two separate groups, each of which occur on either of the islands of Streymoy (Streymoy and Kvívík sills) and Eysturoy (Morskranes, Eysturoy and Sundini sills) (Fig. 3.2). Similar trends, with basal sill sections occurring at increasing stratigraphic depths towards the NW or WNW, are also displayed by individual segments building up both the Streymoy and the Eysturoy sills (Longitudinal profiles, Fig. 3.5f; Fig. 3.5g). If all the sills were emplaced broadly contemporaneously, such variations could reflect initial sill emplacement at various crustal depths or, if emplaced at roughly similar depths, they may result from systematic thickness variations of the overlying Enni Formation. The palaeo

thickness of this formation is not known for the main area of investigation on the larger islands, but a minimum thickness of ~1100 m is suggested for the Enni Formation in the NE parts of the islands not far from the Svínoy–Fugloy Sill (Jørgensen, 2006). If the current exposed sub-horizontal base of the Svínoy–Fugloy Sill can be taken as a reliable proximate of the palaeo crustal level where a rotation of regional σ_3 from sub-horizontal or inclined orientations to a sub-vertical orientation occurred in the Early Cenozoic lava pile of the Faroe Islands, an ~1100 m thick Enni Formation would initially have been intruded by the embryonic Svínoy-Fugloy Sill at a depth of roughly 1000 m. On the assumption that the other investigated intrusions were also initiated at depths close to 1000 m they may actually provide a record of an Early Cenozoic decrease in thickness of the Enni Formation towards the NW or WNW compared to the central and NE parts of the islands. Future geobarometry calculations may help to constrain this matter. A possible thinning of the palaeo Enni Formation towards the NW and WNW could be due to erosion, but such systematic thickness reduction is also in accordance with previous interpretations suggesting that magma supplies to the final stages of surface magmatism in the Faroe Islands were provided from sources located in the eastern parts of the region (Rasmussen and Noe-Nygaard, 1970; Jørgensen, 2006; Passey and Jolley, 2009).

The above discussion seems to suggest that initial sill intrusion into the Early Cenozoic Faroe Islands were not linked to any particular rock types, i.e. lavas versus sedimentary sequences, within the affected strata. The occurrences of intrusive complexes other than dykes at distinct crustal levels (Stratigraphic column, Fig. 3.2) may indicate distinct magmatic events. The irregular sills intruded into the sedimentary Hvannhagi and Prestfjall formations (~4500 m, Stratigraphic column, Fig. 3.2) were probably intruded at very shallow crustal levels contemporaneously with the lowermost parts of the Malinstindur Formation, as indicated by the common occurrences of non-intrusive contacts between this formation and these irregular sills, i.e. these activities must have occurred prior to the emplacement of the studied sills. Any relationship between the invasive sequences occurring in the Lopra Formation (Lowermost 100 – 500 m, Stratigraphic column, Fig. 3.2) and the studied sills cannot be established as they are separated by a stratigraphic thickness of ~5000 m with volcanic sequences.

3.7. Summary of chapter 3 and concluding remarks

In this chapter it has been demonstrated that the investigated sills display more or less symmetrical saucer-shaped geometries where inner sub-horizontal sill sections gradually curve upwards and outwards toward slightly steeper outer sections without any abrupt changes in inclination angles between inner and outer sections. The Streymoy and Eysturoy sills are clearly composite intrusions, each being built up by two merged individual sill segments, each of which displays geometries and sizes broadly similar to the smaller sills of this study. In spite of the similarities in their general physical appearances the great and uniform thicknesses of the segments making up the Streymoy and Eysturoy sills contrast with those of the much thinner individual or smaller sills, each of which are inflated to relatively large thicknesses at their most elevated margins only and gradually wedge out to near-zero thicknesses towards their opposite ends at lower stratigraphic levels. A number of inclined dykes or sheets have been identified as feeders for various stratigraphic levels of the actual sills, but while the bulk of the total magma volumes were supplied via the lowermost sub-horizontal parts of these sills, the feeders that are attached to inclined sill margins only fed the uppermost 50–100 m of these. Based on field relationships, 3D geometry and the observed systematic thickness trends of the sills in question, a simplified three-stage evolution sequence, occurring during a period with large regional melt production and magmatic pressures, is proposed for these intrusions (Fig. 3.32).

(1) Rotation of local least principal stress axes σ_3 from inclined or sub-horizontal to sub-vertical orientations probably resulted in initial lateral melt injections into the sub-horizontal plane in the lava pile of the Faroe Islands, presumably accommodated by elastic displacement of ambient host-rocks (Fig. 3.30; Fig. 3.32a). It is suggested that different values of *E* on either side of the embryonic sills of the Faroe Islands, within host-rock assemblages that possessed significant degrees of isotropy at vertical scales being affected by the sill intrusions (tens/hundreds of metres), resulted in continuous asymmetrical small-scale inflations/dilations (<3 m thick) behind the propagating margins (Fig. 3.30b; Fig. 3.32a). Inferred rotations of local least principal stress axes σ_3 towards gentler angles with the sub-horizontal plane, resulting from effects associated with the small-scale asymmetrical inflations, arguably generated

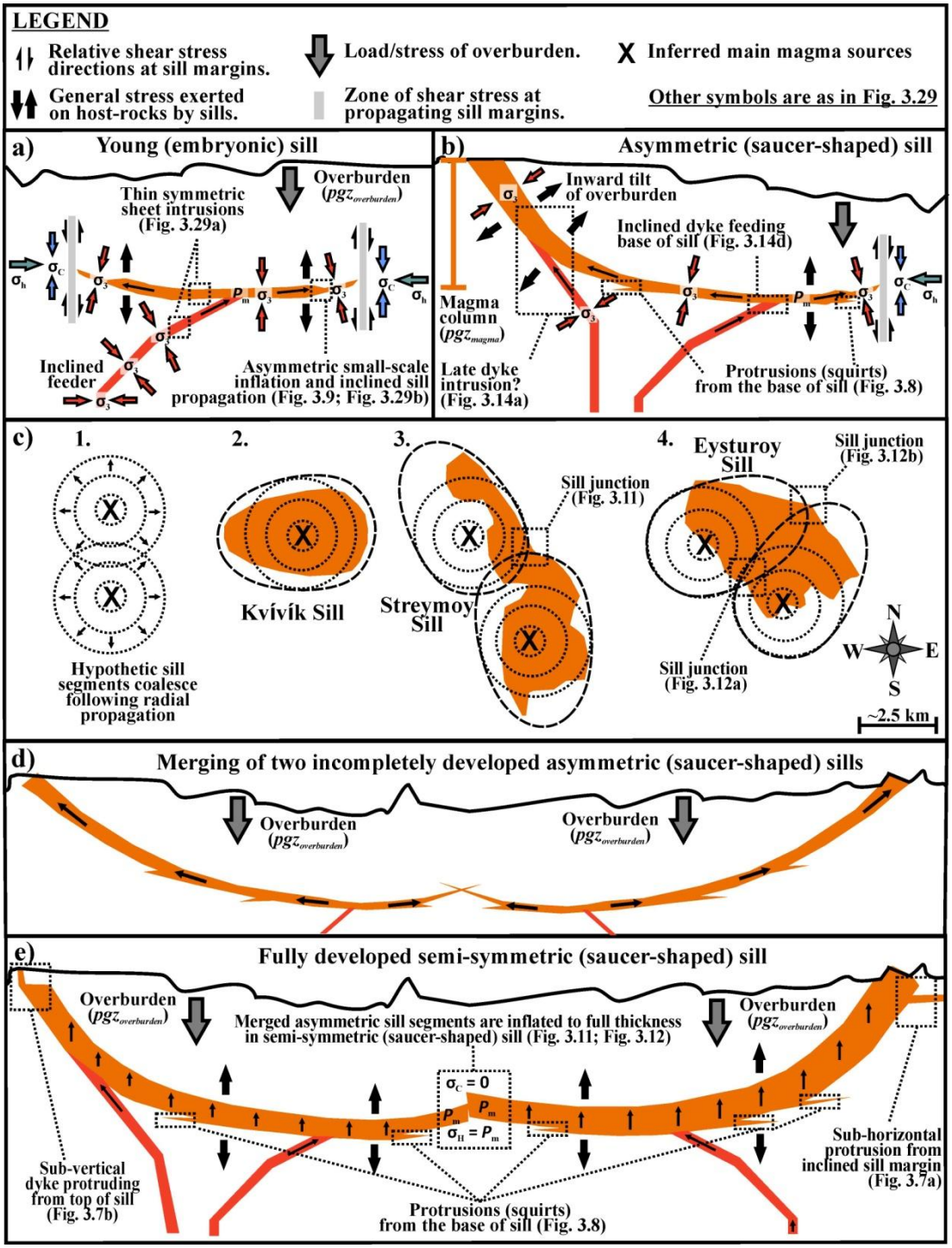

Figure 3.32. Inferred model of sill evolution in the Early Cenozoic Faroe Islands, shown in a few simplified drawings. a) Rotation of regional/local least principal stress axes from sub-horizontal to sub-vertical orientations during periods of igneous activity initiated emplacement of embryonic sills in the sub-horizontal plane. Subsequent small-scale asymmetric inflations (<~3 m thick) behind existing propagation fractures resulted in slightly inclined sill propagation. b) As propagating sills breach the crust atop one end of their propagating margins, local reorientations of least principal stress axes, perhaps in response to sudden pressure changes from wholesale crustal failure, resulted in asymmetric sill inflation and inward tilts of their respective overburdens. The intrusions of a second generation of inclined feeder dykes or sheets that fed the inclined sill margins could have been linked to this

inferred stage of development. c) 1. Sill intrusions initiated from different point sources a few kilometres apart at similar crustal levels (dotted open circles) are bound to coalesce if they experience radial magma propagations. 2. The small individual sills of the Faroe Islands (e.g. Kvívík Sill, orange) most probably experienced radial magma propagations from their main sources (dotted circles and dashed ellipse). 3. and 4. Radial magma propagation from the inferred main sources to the segments of the Streymoy and Eysturoy sills (orange bodies) would have resulted in merging of each segmental pair at some point regardless of directions of maximum magma propagation (dotted circles and dashed ellipses). d) Sill segments at development stages broadly similar to that shown in b) have merged to form a semi-symmetric saucer-shaped sill. e) Large-scale sill inflations, perhaps facilitated by abandonments of cohesion stresses σ_c in host-rocks close to the site of sill merging. The Streymoy and Eysturoy sills supplied melts to sub-horizontal as well as sub-vertical protrusions that potentially fed other adjoining intrusions or surface magmatism. See text.

continuous upward deflections of the young sill margins (Figs 3.13b; Fig. 3. 14a; Fig. 3.30b; Fig. 3.32a; Fig. 3.32b).

(2) Potential rapid gas release from the opening up of previously closed hydraulic systems together with sudden abandonment of cohesive/necking forces within the host-rocks, in response to breaching of overburdens atop one end of propagating sills, are inferred to have resulted in relatively swift local reorientations/reductions of principal stress axes σ_3 acting on the sill margins (Fig. 3.31; Fig. 3.32b). The presumed reorientations/reductions of σ_3 at sill margins probably facilitated inflation preferably at these locations and associated asymmetrical uplifts with associated inward tilts of the respective overburdens (the Kvívík, Morskranes and Sundini sills). A second generation of inclined dykes that fed inclined sill margins locally were most probably intruded at this inferred stage of development (Fig. 3.31; Fig. 3.32b).

(3) Sills at development stages comparable to those inferred for (2) may not be able to produce or sustain magmatic pressures P_m (pgz_{melt}) large enough to overcome the combined stress of their overburdens σ_v ($pgz_{overburden}$), the sub-horizontal stresses σ_h (Equation 5) and the cohesive stress σ_c of the host-rocks with a margin that is sufficiently large so as to ensure continued sill propagation and full-scale inflation at all levels. This could be due to pressure release from melt extrusion onto the Earth's surface before the magma column could reach sufficiently large vertical extent in order to produce/maintain the required magmatic pressure within the plumbing system. Two sills that are initiated ~4.5

and ~3.0 km apart (distances between estimated magma sources to the sill segments of the Streymoy and Eysturoy sills respectively, Fig. 3.3a; Fig. 3.3b) at roughly similar crustal depths and propagate outwards and upwards in a radial fashion are bound to coalesce when the radiuses of both intrusions exceed 1.5 to 2.0 km (Fig. 3.32c1). The elliptic outlines in map view of the smaller sills of the Faroe Islands (Fig. 3.3d; Fig. 3.3e; Fig. 3.3f: Fig. 3.32c2) point to radial melt propagation from their inferred magma sources. If a similar growth style was dominating during emplacement of the sill segments that built up the Streymoy and Eysturoy sills, these could have coalesced at some point regardless of the directions of maximum melt propagation (Fig. 3.32c3; Fig. 3.32c4). It is tentatively suggested that merging of the segments to produce the Streymoy and Eysturoy sills resulted in the cancelling out of the σ_c in their host-rocks around their zones of merging and it is further speculated that this inferred termination of σ_c could have facilitated the uniform large-scale inflations that distinguish these two composite sills from all the thinner individual sills. Merging of sill segments could have occurred prior to complete development of inclined sill margins at the sites of merging or at a later stage. The crosscutting of sill segments in the pronounced class C junction at the elevated NE margin of the Streymoy Sill (Fig. 3.11) could point to partially crystallised magmas in one of the segments during sill propagation and merging at this location or perhaps alternating inflation of each sill segment from magma pulses from different directions.

Chapter Four

4. Petrography, major elements, trace elements and isotopes in basalts from the saucer-shaped sills of the Faroe Islands

4.1. Prelude to chapter four

The ascent of magmas through the Earth's crust presents opportunities for possible assimilation of crustal materials to take place, but the chief potential of basaltic magmatism is that it directly samples the shallow mantle. Also, such magmatism may be able to sample even deeper levels in response to solid-state convection of deep mantle material toward (shallower) sites of basalt formation by means of partial melting (e.g. Hofmann, 1997).

Characteristics/particularities of major and trace elements, including REE, of flood basalts can be used in order to gain information concerning their petrogenetic evolution following the initial melting events. The development of primary magmas may involve crystallisation processes, as well as potential assimilation of crustal material prior to the ultimate ascent/emplacement in the uppermost crust. Key components of such information are sometimes contained within rocks that once formed parts of the active plumbing systems of these provinces such as dykes and sills (e.g. Thompson et al., 2001). These intrusive rocks may represent the only remnants of the final stages of magmatism in the actual province, especially if the youngest onshore/offshore lava flows have been heavily eroded or are difficult to sample in other ways (Jerram et al., 2009).

A number of hypotheses seeking to define possible common sources, e.g. the sub-continental upper mantle versus more deep seated mantle plumes, have been proposed previously in order to explain the geochemical characteristics of the igneous products building up provinces of mainly basaltic compositions such as the NAIP (e.g. Meyer et al., 2007 and references therein). Three main basaltic rock types have been identified throughout the NAIP (Kerr, 1995) and each of these may indicate similarities in source-rock compositions and/or hint to relevant petrogenetic processes that were widespread in this province. These three basalt types can be categorised in terms of their chondrite-normalised REE patterns according to the

following characteristics: type 1 basalts possess relatively low REE concentrations with normalised trends that generally display gentle negative slopes with $(La/Nd)_N$ = ~1 and $(Sm/Yb)_N > 2$; type 2 basalts are MORB-like and possess relatively low REE concentrations with normalised trends that usually display gentle positive slopes with $(La/Nd)_N < 1$ and $(Sm/Yb)_N \leq 1$; type 3 basalts possess relatively high REE concentrations with normalised trends that generally display moderate to steep negative slopes with $(La/Nd)_N = \geq 1$ and $(Sm/Yb)_N >> 2$ (Kerr, 1995). Previous interpretations have suggested that types 1 and 2 basalts formed in response to partial melting of a slightly depleted mantle source at relatively shallow depths, whereas partial melting of a slightly enriched mantle source at greater depths produced type 3 basalts (Kerr, 1995). This same author suggested that relatively high degrees of melting resulted in the formation of types 1 and 2 basalts whereas lower degrees of partial melting were required in order to produce the type 3 basalts that display higher trace element concentrations than the other two basalt types. Apart from being categorised according to their trace element concentrations and/or MgO contents, compositional variations between high-TiO_2 and low-TiO_2 basalts have been utilised previously in order to characterise and distinguish between various units within flood basalt provinces (e.g. Gibson et al., 1995; Peate and Hawkesworth, 1996; Waagstein, 1988, Holm et al., 2001; Søager and Holm, 2011). Differences in TiO_2 contents within basaltic rock suites worldwide have occasionally been interpreted to result from heterogeneous mantle sources (e.g. Xiao et al., 2004) where low-TiO_2 basalts sometimes are inferred to have formed in response to contamination of mantle sources with fluids expelled from subducted crust/sediments (Walker et al., 1990; Ivanov et al., 2008) whereas high-TiO_2 basalts sometimes are assumed to be the result of contamination of mantle sources with small-degree melts (< 10 %) of recycled oceanic crust (Prytulak and Elliot, 2007). High-TiO_2 basalts from W Greenland are thought to have developed from low-TiO_2 basaltic melts by fractional crystallisation of mainly plagioclase and clinopyroxene in periodically replenished, periodically tapped and continuously fractionated magma chambers (Larsen and Pedersen, 2009). These authors proposed that primary melts to relatively low-TiO_2 magmas of W Greenland formed by 16 to 20% melting of a moderately depleted mantle. Early Cenozoic basaltic rocks from E Greenland are thought to have formed by various degrees of partial melting where generation of primary melts to relatively

high-TiO_2 basalts have been interpreted to result from ~4 to ~8% mantle melting (Tegner et al., 1998b; Momme et al., 2006) whereas 19 to 20% mantle melting have been inferred for generation of primary magmas to low-TiO_2 basalts in parts of this region (Momme et al., 2006). Slight compositional differences in mantle sources to these two basalt groups have been suggested earlier (Momme et al., 2006). A broadly similar scenario has been envisaged previously for basaltic rocks of the Faroe Islands, where high-TiO_2 primary magmas are interpreted to have formed by 2.5 to 3.5% mantle melting compared to ~20% melting for primary magmas to low-TiO_2 rocks (Holm et al., 2001). Compositional differences of mantle sources to the high-TiO_2 versus low-TiO_2 basalts of the Faroe Islands have been proposed in previous studies (Holm et al., 2001; Søager and Holm, 2011). The geochemical make-up of silicic basalts, cropping out within relatively restricted parts of the lava pile of the Faroe Islands point to the involvement of crustal materials during ascent of magmas that gave rise to these rocks (Hald and Waagstein, 1983, Holm et al., 2001). Other studies have also pointed to compositional variations of end-member mantle sources as reasons that may explain some of the differences in geochemical compositions of Early Cenozoic basalts encountered in other individual regions of the north Atlantic area such as E Greenland (Fram and Lesher, 1997; Bernstein et al., 2001; Peate and Stecher, 2003) and Iceland (Kitagawa et al., 2008). Earlier works have also proposed the involvements of crustal materials during evolution of Early Cenozoic basaltic melts from E Greenland (Fram and Lesher, 1997; Hanghøj et al., 2003), W Greenland (Larsen and Pedersen, 2009) and NW Britain (Font et al., 2008). Melting at successively shallower mantle depths has been invoked earlier in order to explain increased melt percentages during basalt formation in other contemporaneous parts of the NAIP such as the NW parts of the British Isles (Kerr, 1994). As previous studies have indicated a trans-Atlantic correlation between Early Cenozoic volcanic successions of the Faroe Islands and E Greenland with matching basaltic compositions and evolution patterns with time (Larsen et al., 1999b; Søager and Holm, 2009), similarities in their petrogenetic processes, as proposed for these two regions in earlier studies, are not unexpected.

Potential uncertainties with respect to petrogenetic histories of basaltic rock suites, as interpreted from major/trace element compositions, may be clarified and constrained by careful interpretations of isotopic compositions of the actual basalts. In addition to the frequent use of trace element ratios to detect particular mantle or crustal

reservoirs (e.g. Rollinson, 1998), geological interpretations based on isotopic ratios of the elements Sr ($^{87}Sr/^{86}Sr$), Nd ($^{143}Nd/^{144}Nd$) and Pb ($^{206}Pb/^{204}Pb$, $^{207}Pb/^{204}Pb$, $^{208}Pb/^{204}Pb$) are commonly used for investigations of both felsic and basic rock suites (e.g. Faure, 1986, 2001). These isotopic ratios are useful tools if one attempts to identify/quantify potential contributions to actual rock samples from specific end-member mantle reservoirs and/or for detection of potential crustal components in mantle-derived melts, i.e. isotopic differences/characteristics may help to discriminate between relevant events that have taken place in the source region during earlier igneous events or they may indicate the actions of specific syn-magmatic processes. Also, details of crustal assimilation processes, as recorded in magma compositions, can themselves provide important information and be used to track the temporal evolution of magmatic plumbing systems during changes in tectonic environments and igneous activity within the actual flood basalt province (e.g. Peate et al., 2008).

Distinct global isotopic mantle reservoirs commonly considered for geological interpretations include primitive upper mantle (PUM) or the bulk silicate Earth (BSE), which plot at zero $\in$Sr and $\in$Nd values in $^{87}Sr/^{86}Sr$ versus $^{143}Nd/^{144}Nd$ diagrams, depleted MORB mantle reservoir (DMM), in addition to three enriched (HIMU, EMI and EMII) mantle reservoirs (Zindler and Hart, 1986; Hart, 1988; Hofmann, 1997). Here $\in$Sr and $\in$Nd notations refer to presumed uniform Sr and Nd isotopic reservoirs with present day $^{87}Sr/^{86}Sr$ and $^{143}Nd/^{144}Nd$ values of 0.7045 and 0.512638 respectively. These presumed $\in$Sr and $\in$Nd reservoirs can then be age corrected back to desired ages (Ma) using decay constants relevant for the generation of radiogenic ^{87}Sr and ^{143}Nd respectively (e.g. Faure, 1986, 2001). Mantle-derived melts that have interacted extensively with continental materials during their ascent are expected to have had their isotopic compositions modified significantly, as most rocks of the continental crust are likely to have isotopic and other elemental compositions that are markedly different when compared to mantle-derived magmas (Peate et al., 2008). Here the general rule is that $^{87}Sr/^{86}Sr$ ratios increase and $^{143}Nd/^{144}Nd$ ratios decrease with increasing crustal contamination, although an anticipated decrease in $^{143}Nd/^{144}Nd$ ratios with increasing crustal contamination is expected to be more prevalent for older material originating in the lower crust compared to similar amounts of contamination with younger material originating in

the upper crust (Rollinson, 1998). Isotopic enrichment from crustal contamination can occur in response to bulk mixing or mixing with interstitial liquids (Foland et al., 2000), and continued use of an existing magma conduit system has previously been interpreted to lead to a progressive decrease in the extent of assimilation, while a shift in the location of feeder systems to new conduits in the crust has been suggested to result in a sudden increase in the extent of assimilation (Peate et al., 2008).

Numerous individual studies on basaltic rocks occurring within regions of the NAIP have hinted to the presence of several mantle sources possessing distinct isotopic compositions. Three isotopically distinct end-member mantle sources have been identified for the Neogene magmatism in Iceland, where geochemically/isotopically enriched basalts were produced during periods with high magma productivity compared to extrusion of magmas with relatively depleted isotopic signatures during periods of lower melt productivity (Kitagawa et al., 2008). The inferred asthenospheric mantle sources to Early Cenozoic basalts of W Greenland dominantly possessed MORB-like isotopic signatures with an additional less depleted isotopic component comparable to Iceland-type sources, while an additional incompatible-element enriched mantle component is inferred to have supplied melts to other parts of the actual region (Larsen and Pedersen, 2009). Peate and Stecher (2003) suggested magma tapping from sources that possessed a broad isotopic range, comparable in isotopic compositions to recent Icelandic basalts, during formation of Cenozoic E Greenland basalts, while other authors more specifically inferred magma supplies from an isotopically depleted sub-continental lithospheric source in addition to an Iceland-type source (Hanghøj et al., 2003). Based on examples from the British Tertiary Igneous Province (BTIP) and SE Greenland, Ellam and Stuart (2000) argued in favour of a common primitive end-member isotopic mantle source, the North Atlantic end-member source (NAEM, $^{207}Pb/^{204}Pb$ ~15.4, $^{208}Pb/^{204}Pb$ ~37.4), the melts from which ultimately evolved by interaction with material originating in the lithosphere to the isotopic compositions of basalts found in both Iceland and the Early Cenozoic BTIP. The $^{206}Pb/^{204}Pb$ and $^{207}Pb/^{204}Pb$ ratios of NAEM are broadly similar to the depleted MORB mantle (DMM A) of Zindler and Hart (1986). Comparable results were obtained in the course of a contemporaneous isotope study on the basalts of the Shiant Isles Main Sill, Scotland (Foland et al., 2000). An earlier study has suggested that melt supplies from a Faroese main mantle plume component with relatively depleted isotopic signatures resulted in the generation of the bulk of

the Early Cenozoic high-TiO_2 basalts of this region while a mixture of this main component and a radiogenic mantle plume component gave rise to other local high-TiO_2 magnesian basalts being LREE-enriched and displaying elevated $^{206}Pb/^{204}Pb$ ratios (Holm et al., 2001). An origin by partial melting of another more depleted isotopic source contained within the same mantle plume has been invoked previously in order to explain the moderate volumes of low-TiO_2 basalts encountered in this area (Holm et al., 2001). A broadly similar scenario, involving partial melting at relatively great depths of a plume source being relatively enriched with respect to its isotopic compositions to produce high-TiO_2 basalts and melting at shallower levels of an isotopically depleted (NAEM-like) source, which was contained within the same mantle plume, to generate the low-TiO_2 basalts of the Faroe Islands has been envisaged in a recent study (Søager and Holm, 2011). However, still other authors have advocated in favour of melting of an isotopically depleted asthenospheric source to produce LREE depleted (low-TiO_2) basalts of this region while associated LREE-enriched (high-TiO_2) basalts have tentatively been interpreted to have formed by melting of a likewise isotopically depleted source within the sub-continental lithosphere (Gariépy et al., 1983).

In accordance with some of the geochemical studies mentioned above, several isotopic studies on the main regions making up the NAIP (excluding Iceland) suggest variable degrees of isotopic contamination with crustal lithologies of various compositions. With respect to the Faroe Islands, the occurrences of substantial enrichments in isotopic signatures of silicic lavas have previously been explained in terms of contamination with Lewisian-type amphibolite facies gneisses (Gariépy et al., 1983; Holm et al., 2001). While Gariépy et al. (1983) interpreted the occurrences of moderate isotopic variations in non-silicic basalts of the Faroe Islands to have developed in response to mild crustal contamination, Holm et al. (2001) suggested that slight isotopic variations in high-TiO_2 basalts from this region most likely reflected isotope compositions inherited from their mantle sources.

The saucer-shaped sills that crop out within the Faroe Islands Basalt Group (FIBG), being mapped in detail in the course of this study (chapter 3), provide an ideal opportunity to investigate key geochemical variations of late stage magma types aiming at a better understanding of the nature of mantle sources and the extent of melting in a key area of the NAIP where no sub-basaltic sequences are exposed. In this thesis/chapter, new petrographic, geochemical and isotopic data for seven

saucer-shaped sills of basaltic compositions that crop out in the lava pile of the Faroe Islands (Fig. 3.2) are presented. Intrusive relationships suggest that they were the latest manifestation of igneous activity of any significant scale in that particular area (Rasmussen and Noe-Nygaard, 1970; Hald and Waagstein, 1991; Passey and Jolley, 2009). The aim is to use major/trace elements including REE as well as relevant isotopes in order to link these intrusions to potential mantle sources and potential crustal contaminants in order to detect/quantify the nature of relevant rock-forming processes that contributed to formation of the magmas that ultimately gave rise to the actual sills.

This chapter starts with a brief description of rock sampling including site maps (4.2). In the petrography section (4.3) each of the investigated sills are briefly discussed with the aid of representative photomicrographs. The geochemistry section (4.4) starts with an introduction of the geochemistry of lavas/dykes within the actual region as presented in earlier studies and then introduces compositions of major elements and trace elements including the REE of intrusions from this study, using tables in addition to variation diagrams where individual sills are compared/contrasted. The results of the isotope analyses as well as various calculations such as age-corrected isotope ratios are presented in table format (4.5). Ratio – ratio plots are presented for measured and age-corrected lead isotopes from this and previous studies and measured ratios are contrasted against isotopes from neighbouring basaltic regions (4.5.1.). Sr and Nd isotopes from this and earlier studies are briefly presented in ratio-ratio plots at different scales (4.5.2.). Pb isotope ratios are contrasted against Sr and Nd isotope ratios (4.5.3.). The discussion section (4.6) is divided into sub-sections dealing with: element mobility (4.6.1.), geochemical constraints on potential crustal contamination (4.6.2.), isotopic constraints on potential crustal contamination (4.6.3.), partial melting (4.6.4.), fractional crystallisation (4.6.5.), constraining depths of formation (4.6.6.), geochemical constraints on potential mantle sources (4.6.7.) and isotopic constraints on potential mantle sources (4.6.8.). Summary and concluding remarks (4.7) based on isotopes (4.7.1.) and geochemistry (4.7.2.).

4.2. Rock sampling

Following careful inspection of collected rock samples a total of 44 specimen representing seven sills and four feeder dykes, which supplied melts to two of the

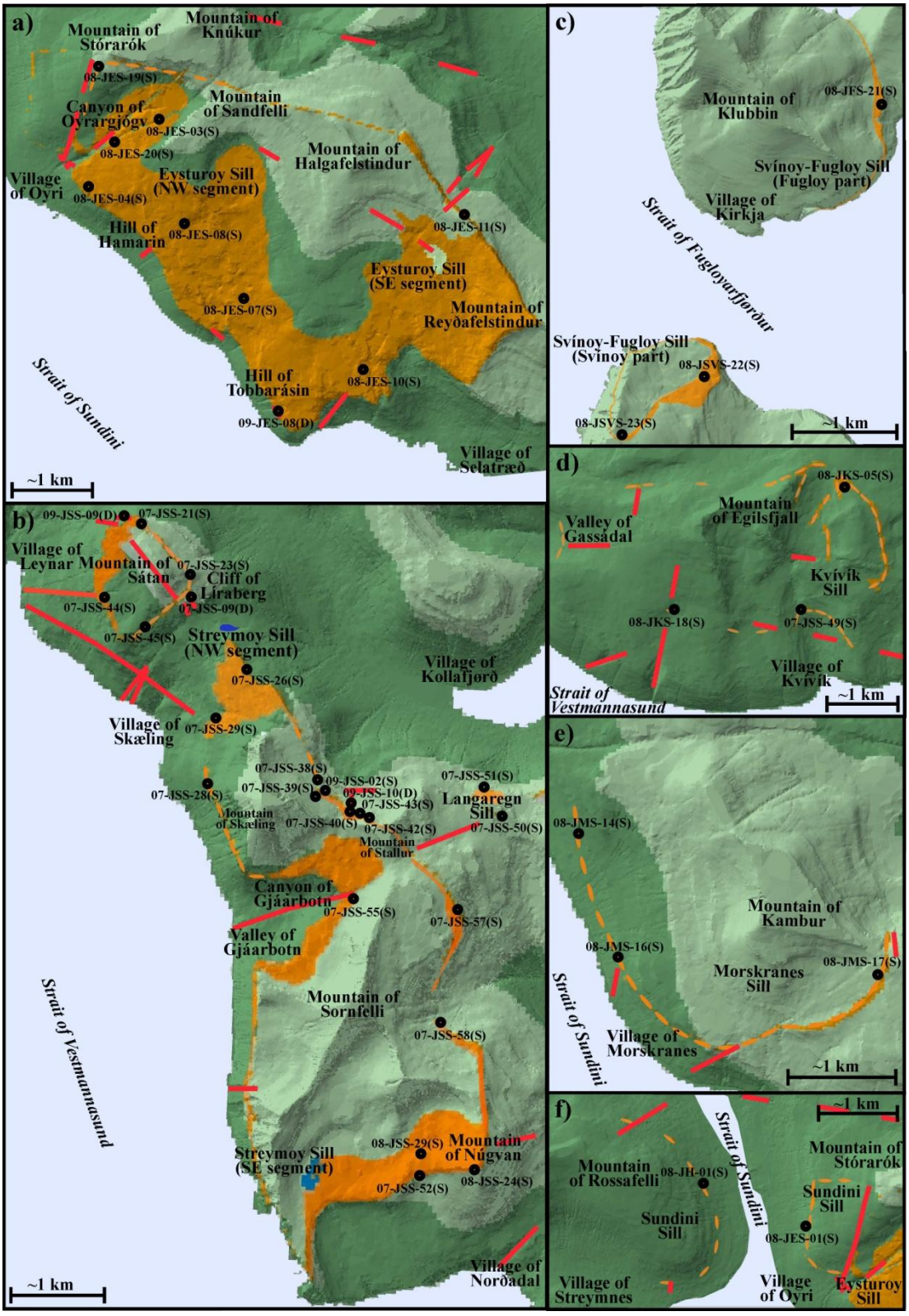

Figure 4.1. Localities of rock samples accepted for use in this study are indicated by black circles labelled with sample designations. (S) = sill sample; (D) = dyke sample.

sills, were selected for use in this study (Fig. 4.1). Due to weathering and intense fracturing in many parts of the investigated sills (e.g. sub-section 3.5.2.), a relatively

large proportion of collected rock samples have been discarded, particularly from those parts of the Eysturoy Sill that have experienced more intense chemical weathering relative to the other sills.

The samples were crushed to fine gravel using standard techniques and subsequently ground to fine powder using agate ball mills at the Department of Earth Sciences at Durham University.

Analyses of major elements and some selected trace elements (44 samples, Table 4.2) were carried out at the Open University in Milton Keynes, UK. Analyses of trace elements including the REE (14 samples, Table 4.3) were done at Durham University. Overviews of analytical techniques employed during the analyses of major elements as well as trace elements are outlined in appendices 2 and 3 respectively. Also, a detailed description of the techniques utilised in the preparation of samples for ICP–MS analyses at Durham University is given in Ottley et al. (2003) and Thompson et al. (2005). Isotopic analyses were performed on all sills from this study (8 samples, Table 4.4). Apart for the sample 08-JMS-14, these specimens are also included in the trace element analyses shown in Table 4.3. The analyses involved measurements of isotope ratios of the elements: Sr, Nd and Pb, i.e. $^{87}Sr/^{86}Sr$, $^{143}Nd/^{144}Nd$, $^{206}Pb/^{204}Pb$, $^{207}Pb/^{204}Pb$ and $^{208}Pb/^{204}Pb$ ratios. The isotope analyses were carried out at Durham University. Analytical techniques and the methods employed in calculations of isotopic ratios ($^{87}Rb/^{86}Sr$ and $^{147}Sm/^{144}Nd$) as well as age correction of measured ratios are outlined in appendix 4.

4.3. Petrography

Variations in textures and petrographic characteristics between some of the seven sills that are included in this study, as demonstrated under the microscope, may reflect some variations in their crystallisation sequences and cooling histories, but do not necessarily reflect significant geochemical variations of their mantle sources.

4.3.1. The Streymoy and Kvívík sills

Intergranular plagioclase constitute ~35 % of most samples from these sills and occur as 0.07 – 0.75 mm randomly oriented subhedral laths and 0.75 – 1 mm equant anhedral grains (Fig. 4.2a; Fig. 4.2d). Additional plagioclases constituting perhaps 15 – 20 % of the total rock volume occur as scattered 1.5 to 3 mm subhedral and often chemically zoned phenocrysts, which commonly contain minute melt inclusions (Fig.

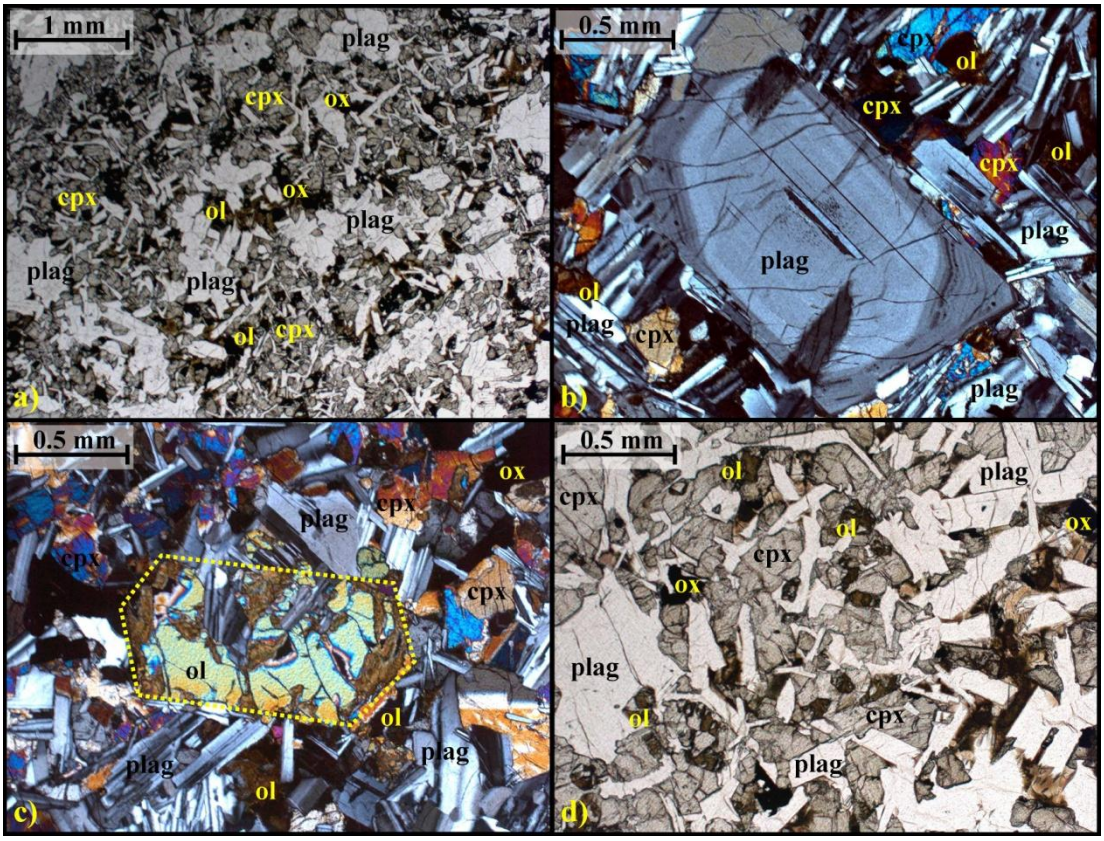

Figure 4.2. Photomicrographs representative of the Streymoy and Kvívík sills. a) Image under plane-polarised light displaying general distribution of most common minerals. b) Image under crossed-polarised light showing chemically zoned plagioclase phenocryst. c) Image under crossed-polarised light showing partially resorbed olivine phenocryst (outlined by yellow dotted line). d) Image under plane-polarised light showing distribution of tiny partially resorbed olivines. cpx = clinopyroxene; ol = olivine; ox = oxide; plag = plagioclase.

4.2b). Intergranular anhedral equant 0.07 – 0.75 mm grains of clinopyroxene count for ~40 % of these rocks (Fig. 4.2a). Randomly strewn <0.25 mm anhedral equant olivine grains that are partly altered to phyllosilicates (partly resorbed = "cracked-eggs" appearance) make up 2 – 6 % of the volumes of these rocks joined by <3 % of oxide grains of roughly similar sizes (Fig. 4.2d). A few larger 0.5 – 1 mm partially resorbed olivine grains constitute <0.5 % of these sills (Fig. 4.2c).

4.3.2. The Eysturoy and Sundini sills

Randomly oriented subhedral lath-shaped 0.07 – 1 mm subhedral plagioclase grains make up 35 – 40 % of the Eysturoy and Sundini sills and anhedral to subhedral 0.1 – 0.75 mm equant grains of clinopyroxene constitute 45 – 50 % of samples from both of these sills (Fig. 4.3a; Fig. 4.3d). The clinopyroxene and plagioclase may occur as

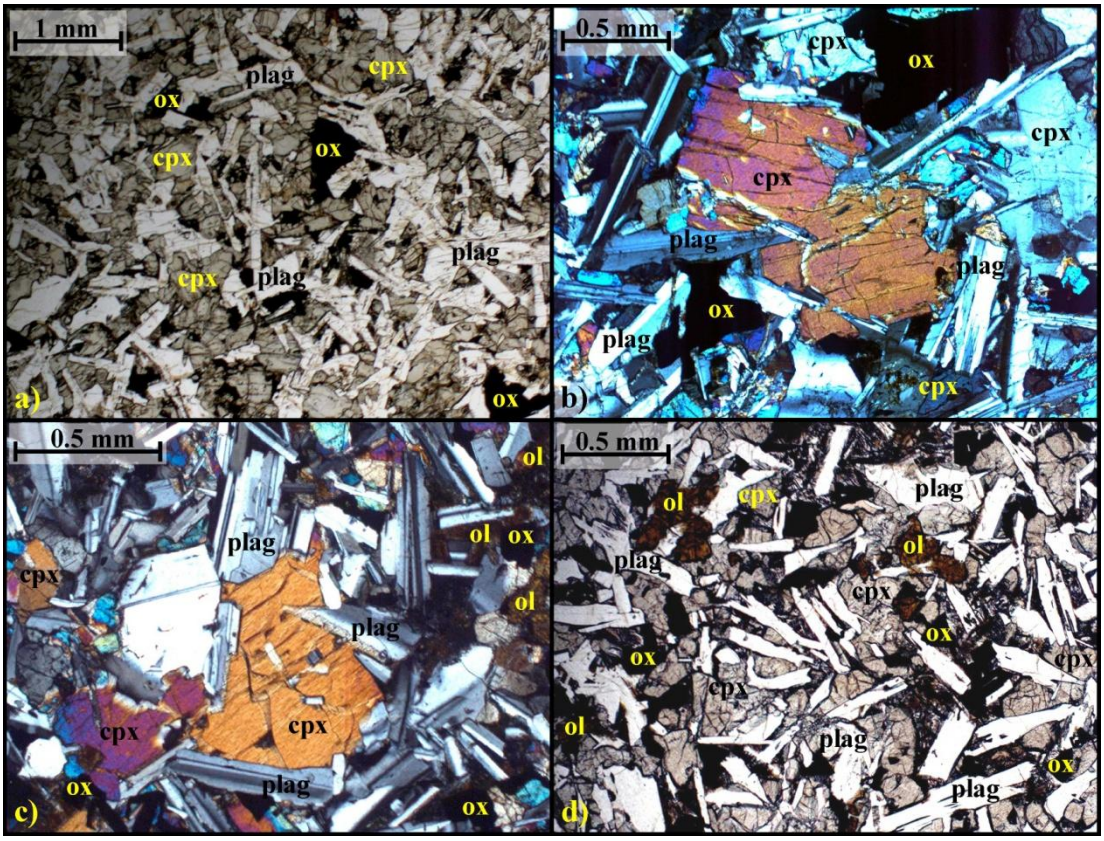

Figure 4.3. Photomicrographs representative of the Eysturoy and Sundini sills. a) Image under plane-polarised light displaying general distribution of three of the most common minerals. b) Image under crossed-polarised light showing subophitic texture. c) Broadly similar to b, but also showing pseudomorphed olivine grains. d) Image under plane-polarised light showing distribution of most common minerals including pseudomorphed olivines. Abbreviations are as in Fig. 4.2.

intergranular grains or they display subophitic textures where pyroxene grains partly enclose smaller laths of plagioclase (Fig. 4.3b; Fig. 43c). Scattered <0.25 mm olivine grains constitute 4 – 6 % of these sills and, in contrast to olivines from the Streymoy and Kvívík sills, these appear to have been entirely pseudomorphed (Fig. 4.3c; Fig. 4.3d). Anhedral to subhedral oxide grains measuring 0.05 – 0.5 mm count for 4 – 6 % of samples from these sills (Fig. 4.3a; Fig. 4.3d).

4.3.3. The Svínoy-Fugloy Sill

Samples of the Svínoy-Fugloy Sill display ophitic to subophitic textures where laths of subhedral 0.05 – 0.75 mm plagioclase grains, amounting to 35 – 40 % of total rock volume, are poikilitically enclosed by larger 0.35 – 2 mm anhedral equant clinopyroxene grains that make up 45 – 50 % of these rocks (Fig. 4.4a; Fig. 4.4b). Partly resorbed ("cracked-eggs") or entirely pseudomorphed anhedral 0.05 – 0.35

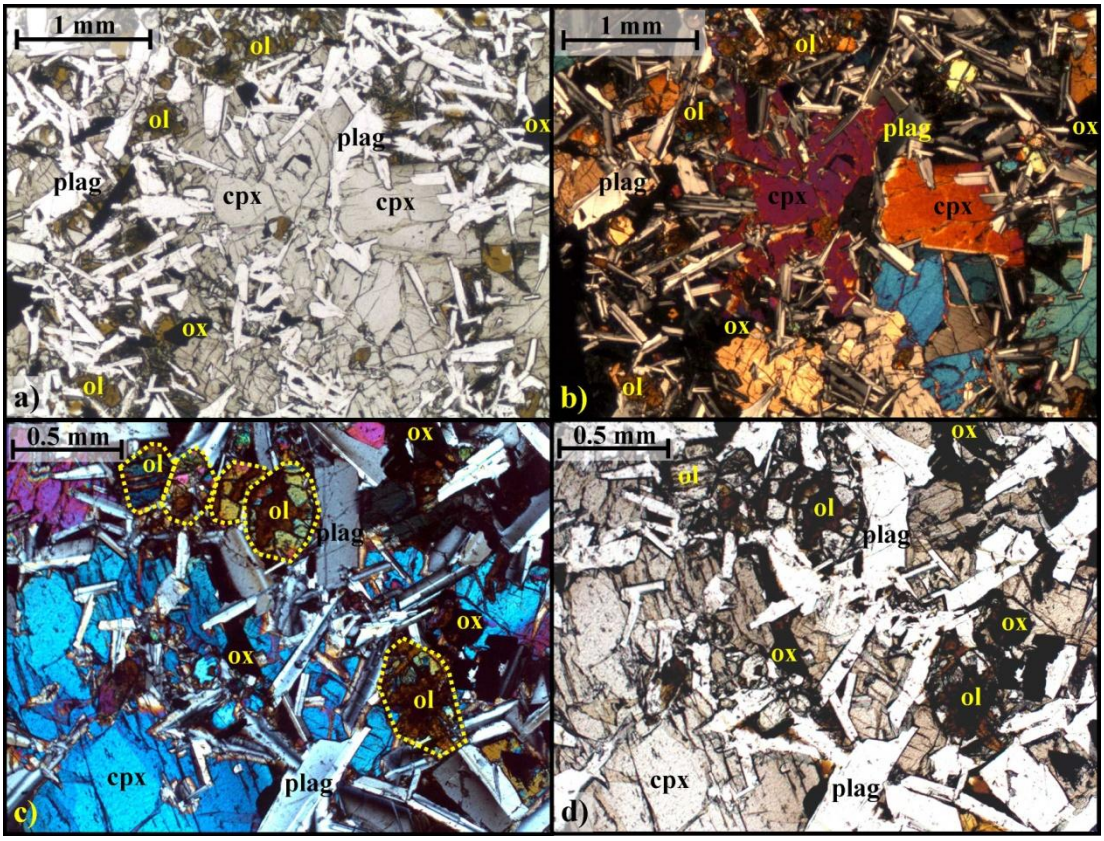

Figure 4.4. Photomicrographs representative of the Svínoy-Fugloy Sill. a) Image under plane-polarised light showing ophitic to subophitic texture and general distribution of the most common minerals of this sill. b) Same as a, but under crossed-polarised light. c) Some partly resorbed olivines are outlined by yellow dotted lines. d) Same as c, but under plane-polarised light. Abbreviations are as in Fig. 4.2.

mm olivine grains in addition to oxides of similar grain sizes constitute 5 – 10 % of the Svínoy-Fugloy Sill each (Fig. 4.4a; Fig. 4.4b; Fig. 4.4c; Fig. 4.4d). These minor mineral phases are commonly relatively concentrated at contacts between individual clinopyroxene phenocrysts.

4.3.4. The Morskranes Sill

The Morskranes Sill is broadly similar to the Svínoy-Fugloy Sill with respect to most parts of the petrography (Fig. 4.5a), but it has a slightly larger content of olivines and oxides. Parts of the Morskranes Sill contain 5 – 10 % of a mineral phase that has not been encountered in any of the other sills from this study. The geochemistry of this mineral phase has not been positively identified, as no relevant microprobe analyses are available. However, incompletely developed twinning (according to the albite and pericline laws) in some of these mineral grains may point to a (potassium-

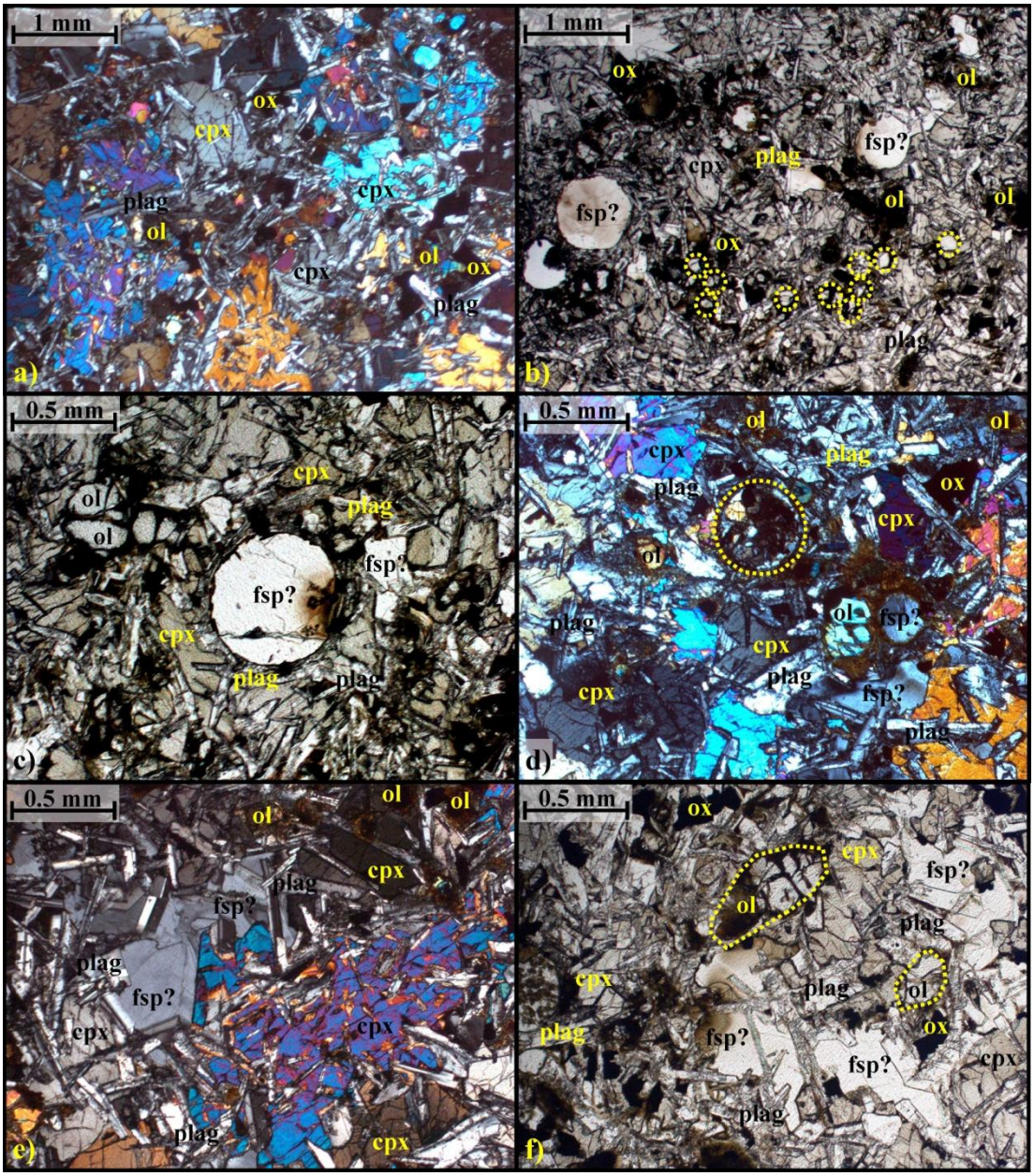

Figure 4.5. Photomicrographs representative of the Morskranes Sill. a) Ophitic texture under crossed-polarised light with clinopyroxene poikilitically enclosing smaller laths/needles of plagioclase. b) Image under plane-polarised light showing scattered mostly sub-spherical whitish grains of unknown geochemical compositions (feldspars/zeolites?) and olivines (small specimen outlined by yellow dotted circles) in ophitic sill material. c) Image under plane-polarised light showing clinopyroxene poikilitically enclosing laths of plagioclases that in turn are wrapped around a large sub-spherical grain (feldspar?). d) Image under crossed-polarised light showing the remnants of a spherical grain (enclosed by yellow dotted circle) almost entirely replaced by clinopyroxene, plagioclase and phyllosilicates. The centre-right of image shows alteration of olivine and presumed feldspar to brown phyllosilicates. e) Image under crossed-polarised light showing laths of plagioclase being poicilitically enclosed by clinopyroxene and a presumed low-temperature variety of potassium-bearing feldspar. f) Image under plane-polarised light displaying a scenario broadly similar to that of e, but with additional olivines (dotted outlines). fsp? = unknown mineral. Other abbreviations are as in Fig. 4.2.

bearing?) feldspathic composition. This mineral phase may occur as <0.7 mm sub-spherical grains (Fig. 4.5b; Fig. 4.5c) or as <1 mm oikocrysts that partially enclose laths of plagioclase and the odd clinopyroxene (Fig. 4.5e; Fig. 4.5f). Their poikilitic nature suggests that some of these mineral grains were among the latest phases to solidify. The wrapping of plagioclase laths around some sub-spherical specimen of this mineral (Fig. 4.5c) and the apparent replacement of others by pyroxene, plagioclase and phyllosilicates (Fig. 4.5d) could suggest early crystallisation or perhaps even an exotic origin of some of the sub-spherical varieties of these minerals. An origin of these mineral phases by solidification from tiny pockets of immiscible liquids or from secondary processes such as vesicle infills remains an alternative explanation.

4.3.5. The Langaregn Sill

Subhedral <5 mm plagioclase phenocrysts with partially resorbed margins, set in a fine-grained matrix, make up <10 % of this sill (Fig. 4.6b; Fig. 4.6c). <0.5 % of partly resorbed olivine microphenocrysts (0.15 – 0.7) mm commonly occur within these phenocrysts (Fig. 4.6b; Fig. 4.6c). The matrix is made up of intergranular (0.02

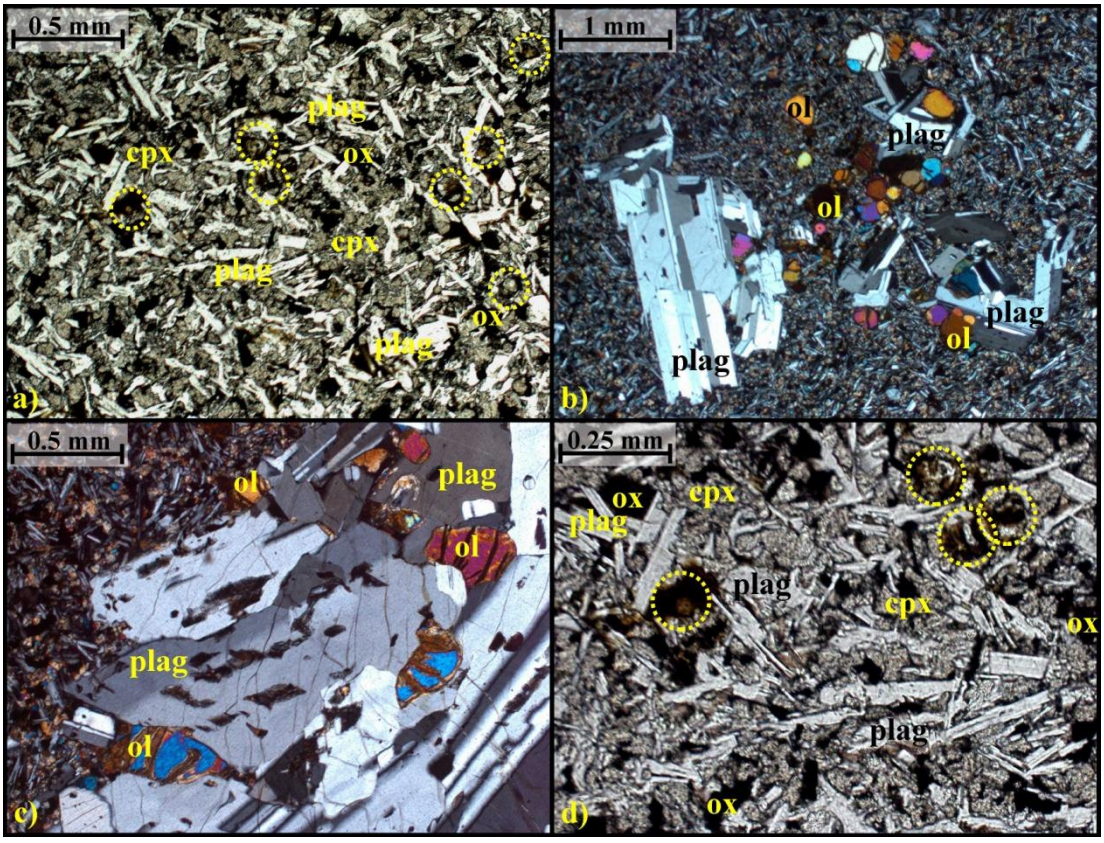

Figure 4.6. (Previous page). Photomicrographs representative of the Langaregn Sill. a) Image under plane-polarised light showing general distribution of the most common minerals that make up the matrix of this sill (olivines are enclosed yellow dotted circles). b) Image under crossed-polarised light showing subhedral slightly resorbed plagioclase phenocrysts and sub-spherical brightly coloured olivine microphenocrysts set in a fine grained matrix of composition as in a. c) Image under crossed-polarised light showing a closer view of a broadly similar scenario as in b, but with larger an differently shaped olivine microphenocrysts. d) Image under plane-polarised light showing a closer view of matrix minerals as in a (olivines enclosed by yellow dotted circles). Abbreviations are as in Fig. 4.2.

– 0.35 mm) subhedral randomly oriented plagioclase laths making up 35 – 40 % of these rocks and anhedral equant clinopyroxenes (0.02 – 0.35 mm) constituting 45 – 50 % of total rock volume (Fig. 4.6a; Fig. 4.6d). Scattered (<0.12 mm) grains of ("cracked-eggs") olivine in the matrix count for <5 % and oxides measuring <0.2 mm count for 3 – 6 % of total volume of the Langaregn Sill (Fig. 4.6a; Fig. 4.6d).

4.3.6. Feeder dykes to the Streymoy Sill

The feeders to the Streymoy Sill generally display similar proportions/volumes of plagioclase (micro) phenocrysts when compared to the Streymoy and Kvívík sills, i.e. around 15 – 20 %. These phenocrysts are set in basaltic glasses immediately at dyke – host rock contacts together with the odd clinopyroxene grains (Fig. 4.7a; Fig. 4.7d), but at distances greater than 1 – 2 cm from the dyke contacts these glasses gradually begin to be replaced by a very fine grained matrix consisting mainly of plagioclase and clinopyroxene (Fig. 4.7b; Fig. 4.7c). It is conspicuous that plagioclase phenocrysts generally are euhedral to subhedral and completely fresh when set in a glassy substance close to dyke contacts (Fig. 4.7a; Fig. 4.7d), but are subhedral and partly resorbed when set in a matrix of both glass and very fine grained plagioclases and clinopyroxenes only centimetres from the dyke contacts (Fig. 4.7b: Fig. 4.7c). On a few occasions plagioclase (micro) phenocrysts set in glassy basalt of the investigated feeder dykes have acted as nucleus to crystallisation of fine grained clinopyroxenes (Fig. 4.7d). The overall impression obtained from the petrography of the investigated feeder dykes is that plagioclase was a dominating early crystallisation phase and that these crystals subsequently reacted with surrounding melts to produce other fine grained plagioclases and clinopyroxenes. Reaction of Ca-rich plagioclases with surrounding basaltic melts to generate more

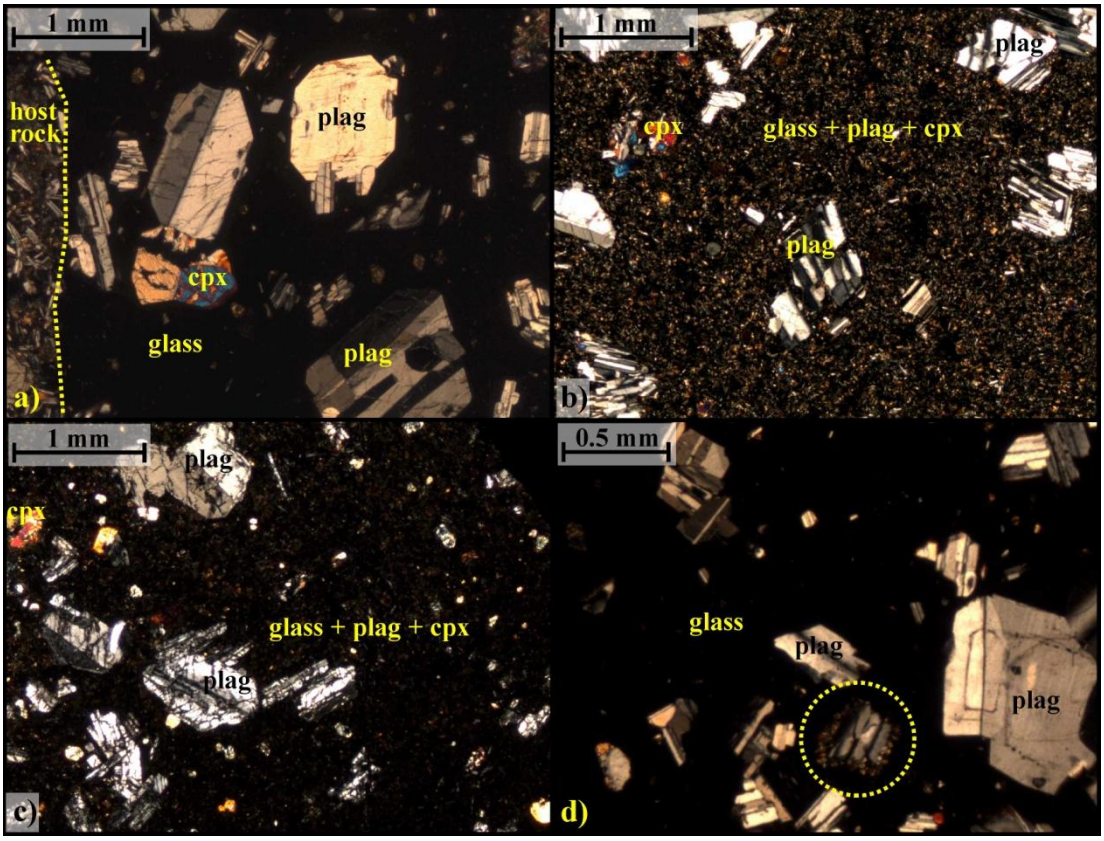

Figure 4.7. Photomicrographs under crossed-polarised light that are representative of feeder dykes to the Streymoy Sill. a) Euhedral completely fresh grains of plagioclase and the odd clinopyroxene set in basaltic glass immediately at dyke contact (yellow dotted line). b) Slightly resorbed plagioclase grains set in a fine grained matrix of glass, plagioclase and clinopyroxene ≥ 2 cm from the dyke contact. c) Broadly similar to b, but with the larger plagioclase grains being slightly more altered/resorbed. d) Similar scenario as in a, but also showing an individual plagioclase grain acting as a nucleus for the growth of tiny clinopyroxene crystals (enclosed by yellow dotted circle). Abbreviations as in Fig. 4.2.

Table 4.1. Brief summary of the petrography that characterise the sills of the Faroe Islands.

Sills, Faroe Islands	Ol	Cpx	Plag	Ox	Texture
Streymoy Sill	< 6	~ 40	50 – 55	<3	Feldspar-phyric
Kvívík Sill	< 6	~ 40	50 – 55	< 3	Feldspar-phyric
Langaregn Sill	< 5	~ 45	45 – 50	< 6	Feldspar- and olivine-phyric
Eysturoy Sill	< 6	~ 45	40 – 45	< 6	Intergranular + Cpx oikocrysts
Sundini Sill	< 6	~ 45	40 – 45	< 6	Intergranular + Cpx oikocrysts
Svínoy-Fugloy Sill	< 10	~ 45	35 – 40	< 10	Ophitic
Morskranes Sill	< 10	~ 45	35 – 40	< 10	Ophitic

Mineral abbreviations are as in Fig. 4.2.

Na-rich plagioclases in addition to clinopyroxenes upon cooling would be in accordance Bowen's reaction series. However, as no microprobe analyses are available on minerals from any samples used in this study, it has not been possible to document potential compositional differences between e.g. plagioclase phenocrysts versus associated fine grained specimens of this mineral. Earlier studies on basalts of the Faroe Islands have suggested olivine compositions of Fo_{86-88} in low-TiO_2 basalts and Fo_{72-73} in high-TiO_2 basalts whereas An_{64-70} has been indicated for plagioclases from both these rock types (Holm et al., 2001).

A brief summary of the petrography that characterise the sills of the Faroe Islands is given in Table 4.1.

4.4. Geochemistry

4.4.1. Dykes and lavas of the Faroe Islands

Earlier studies on the geochemical composition of the Faroe Islands have shown that the basalts building up this lava pile and associated dyke systems are all of tholeiitic composition with MgO contents ranging from ~4.5 to ~23.0 wt% and TiO_2 contents ranging from ~0.6 to ~4.0 wt% (Waagstein, 1988; Holm et al., 2001; Søager and Holm, 2009, 2011). However, the bulk of analysed samples from the Faroe Islands display MgO 7 to 9 wt% (e.g. Hald and Waagstein, 1984; Holm et al., 2001; Søager and Holm, 2011). A few lava flows in the uppermost parts of the Malinstindur Formation (Stratigraphy explained in sub-section 2.3; Fig. 2.3; Fig. 3.2) display anomalously high SiO_2 contents of ~54.0 wt% (Hald and Waagstein, 1983). Both MgO and TiO_2 contents commonly vary between individual lava flows within basalts of this region irrespective of stratigraphic levels (e.g. Hald and Waagstein, 1984; Søager and Holm, 2009, 2011). The observed differences of these two major elements in addition to common occurrences of up-section variations of Y and Zr concentrations in basalts of the Beinisvørð Formation (Stratigraphy explained in sub-section 2.3; Fig. 2.3; Fig. 3.2) led Hald and Waagstein (1984) to suggest that magmas were supplied from at least two independent volcanic systems during extrusion of the lava flows building up this formation. Basalts from this region have commonly been grouped according to their REE compositions or their titanium contents, i.e. high-TiO_2 versus low-TiO_2 rocks, during previous studies (Gariépy et al., 1983; Waagstein, 1988; Hald and Waagstein, 1991; Holm et al., 2001; Søager and Holm, 2009, 2011). Relatively high-TiO_2 lavas make up most of the volume in the

lowermost ~5.5 km of the lava pile whereas low-TiO_2 lavas are becoming increasingly common in the remaining upper parts (e.g. Hald and Waagstein, 1984; Passey and Jolley, 2009; Søager and Holm, 2011), but the overall geochemical compositions of dykes/lavas of the Faroe Islands suggest that both these titanium groups were emplaced throughout the final stages of magmatism within this region as well (Hald and Waagstein, 1991). Increased TiO_2 contents of dykes from this area are generally linked to a clockwise rotation of their REE trends towards steeper negative slopes. Low-TiO_2 dykes (0.75 – 1.75 wt% TiO_2) from this area display flat or MORB-like depleted trends of $(La/Sm)_N$ = 0.4 – 1.2 and $(Sm/Yb)_N$ = 0.5 – 1.15; intermediate-TiO_2 dykes (1.45 – 2.45 wt% TiO_2) display $(La/Sm)_N$ = 1.0 – 1.6 and $(Sm/Yb)_N$ = 1.35 – 2.35 whereas high-TiO_2 dykes (2.6 – 3.8 wt% TiO_2) display $(La/Sm)_N$ = 1.25 – 1.75 and $(Sm/Yb)_N$ = 1.95 – 2.65 (Holm et al., 2001). Of the basalts occurring above sea level, lava flows of the Beinisvørð and Malinstindur formations are LREE enriched ($(La/Yb)_N$ = 1.4 – 3.3) with a relatively wide range in overall REE concentrations, whereas many parts of the Enni Formation display depleted MORB-like LREE trends ($(La/Yb)_N$ = 0.45 – 0.62) while other parts display REE trends that are comparable to those of the Beinisvørð and Malinstindur formations (Gariépy et al., 1983).

An earlier comprehensive study has suggested that high-TiO_2 basalts of this region formed by 2.5 to 3.5% mantle melting compared to ~20% melting to produce local low-TiO_2 basalts (Holm et al., 2001). However, while Holm et al. (2001) in addition to Søager and Holm (2011) proposed depleted and more enriched sources to low-TiO_2 and high-TiO_2 basalts respectively, both sources originating within a deep-seated mantle plume (the Iceland Plume), Gariépy et al. (1983) tentatively suggested the sub-continental lithospheric mantle (SCLM) as the source of LREE enriched basalts of the Faroe Islands and hence also the source of the bulk of the basalt volumes encountered in the actual region. Gariépy et al. (1983) further suggested that LREE enriched and LREE depleted basalts formed in response to melting of two distinct, but depleted, mantle sources. While fractionation of mainly olivine is the mechanism preferably inferred to explain the compositional gap between primary magnesian basic magmas and more evolved basaltic melts (e.g. Yaxley, 2000), the observed variations within the low-TiO_2 dykes of the Faroe Islands have previously been explained by low-pressure fractional crystallisation of olivine ± plagioclase ±

clinopyroxene (Hald and Waagstein, 1991) whereas the observed variations amongst high-TiO_2 lavas of the Beinisvørð Formation have been explained previously in terms of high-pressure fractional crystallisation of plagioclase + clinopyroxene + garnet (Bernstein, 1994).

This first detailed study on geochemistry of seven sills occurring in the upper parts of the Malinstindur Formation, the Sneis Formation and the lower parts of the Enni Formation (Fig. 4.1) shows that these intrusions can be categorised into three groups with well-defined major and trace element characteristics (Table 4.2; Table 4.3).

4.4.2. Major elements

Altogether the sills of the Faroe Islands display SiO_2 contents ranging from 47.5 to 50.5% and total $Na_2O + K_2O$ contents ranging from 1.9 to 2.9% i.e. in a silica versus total alkalis diagram (Rickwood 1989; Rollinson 1998) they can be classified as subalkaline or tholeiite series basalts (Table 4.2; Fig. 4.8a). In a ternary Fe_{tot} + Ti – Al – Mg classification diagram (Rickwood 1989; Rollinson 1998), where cation percentages have been recalculated to 100%, the sill data straddle the margins of fields representing three main basalt types (Fig. 4.8b). More specifically the

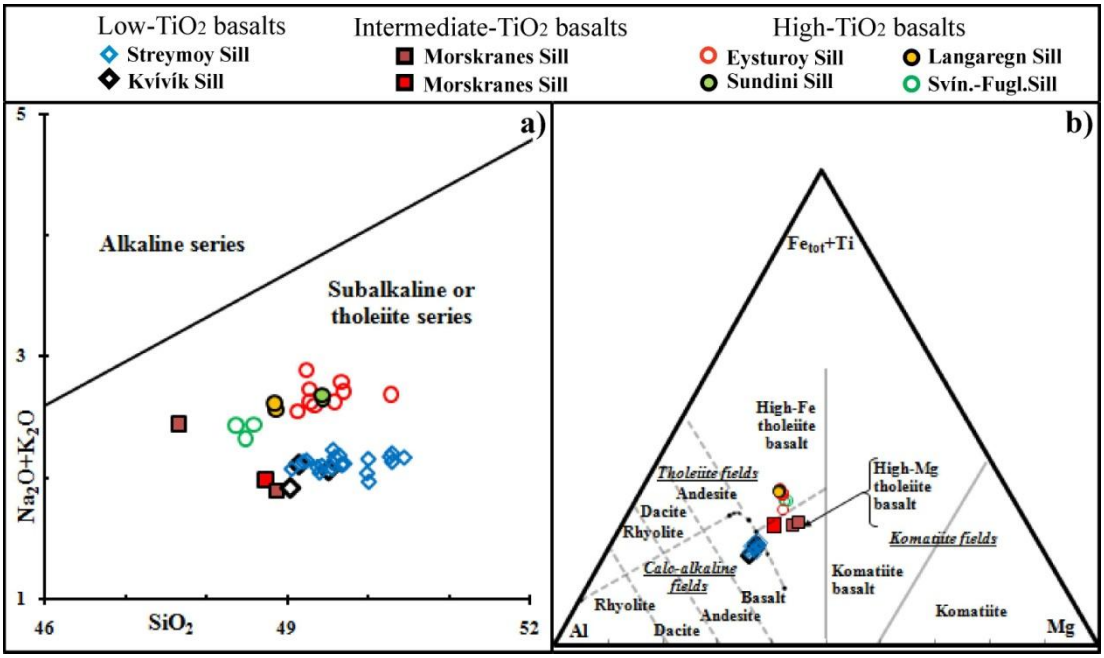

Figure 4.8. a) The investigated sills all plot in the subalkaline/tholeiite field in a SiO_2 versus total $Na_2O + K_2O$ diagram. The line defining the alkaline and the subalkaline/tholeiite fields is from MacDonald (1968). b) The sills plot in three fields in a Fe_{tot} – Al – Mg cation diagram of Rickwood (1989) and Rollinson (1998). See text.

Table 4.2. Whole rock XRF data on major and trace elements from the sills of the Faroe Islands analysed on glass discs and pressed powder pellets respectively.

	Streymoy Sill														
Sample	**09-JSS-02**	**07-JSS-21**	**07-JSS-23**	**08-JSS-24**	**07-JSS-26**	**07-JSS-28**	**07-JSS-29**	**08-JSS-29**	***07-JSS-38***	**07-JSS-39**	**07-JSS-40**	**07-JSS-42**	**07-JSS-43**	**07-JSS-44**	**07-JSS-45**
Wt. %	Sill	Sill	Sill	Sill	Sill	Sill	Sill	Sill	***Sill***	Sill	Sill	Sill	Sill	Sill	Sill
SiO_2	49.05	49.58	49.55	50.00	49.64	49.19	49.23	49.55	***47.80***	49.70	49.42	49.37	49.67	50.29	50.44
TiO_2	0.76	0.76	0.75	0.80	0.79	0.76	0.78	0.78	***1.13***	0.78	0.73	0.76	0.76	0.77	0.82
Al_2O_3	17.04	16.90	17.75	16.90	16.61	17.00	17.15	16.51	***14.76***	16.68	17.55	16.71	17.41	17.45	17.03
Fe_2O_3	9.91	10.13	9.68	10.25	10.35	9.99	10.06	10.34	***12.05***	10.27	9.65	10.27	9.93	10.01	10.34
MnO	0.16	0.16	0.16	0.16	0.17	0.16	0.16	0.17	***0.19***	0.17	0.16	0.16	0.16	0.16	0.17
MgO	6.74	6.92	6.56	7.03	6.93	6.73	6.76	6.92	***8.46***	6.94	6.74	6.86	6.83	6.83	6.92
CaO	12.98	13.07	13.40	13.18	13.01	13.08	13.07	13.11	***12.96***	13.09	13.31	13.22	13.40	13.25	13.13
Na_2O	1.88	1.96	1.87	1.95	1.96	1.92	1.93	1.92	***1.89***	1.93	1.91	1.91	1.91	1.93	1.95
K_2O	0.20	0.21	0.21	0.21	0.22	0.21	0.22	0.21	***0.06***	0.19	0.20	0.19	0.20	0.20	0.22
P_2O_5	0.08	0.08	0.08	0.08	0.08	0.08	0.08	0.08	***0.09***	0.08	0.07	0.07	0.08	0.08	0.08
[a]LOI	0.14	0.33	0.45	0.11	0.19	0.28	0.27	0.19	***0.43***	0.11	0.18	0.23	0.32	0.26	0.46
Total	98.92	100.11	100.46	100.67	99.95	99.40	99.71	99.77	***99.81***	99.95	99.91	99.73	100.67	101.24	101.58
ppm															
Sr	197	199	205	195	199	196	196	190	***113***	197	203	180	198	193	189
Y	16	18	16	18	18	17	18	18	***27***	18	16	18	17	17	18
Zr	50	50	49	49	52	49	51	51	***58***	52	46	46	47	48	50
Ba	64	66	63	67	75	66	66	64	***25***	69	65	54	63	57	59
Sc	36	37	35	43	39	34	40	38	***46***	39	36	37	36	38	37
V	242	228	229	251	247	228	250	252	***298***	254	228	248	218	247	244
Cr	181	176	166	200	184	170	182	179	***359***	176	183	174	175	181	178
Ni	80	78	73	86	81	78	76	77	***132***	79	74	79	85	86	81
Cu	118	110	114	114	122	113	113	106	***137***	118	107	127	114	114	122
Zn	56	56	53	60	60	54	58	58	***74***	60	55	60	52	59	59
Y/TiO_2	21.67	24.03	21.73	22.41	22.81	22.65	23.31	23.74	***23.77***	22.59	22.25	23.31	22.72	21.39	21.46

Table 4.2. (continued)

	Streymoy Sill							Kvívík Sill			Langaregn Sill		Sundini Sill		[b]Ey. S.
Sample	**07-JSS-52**	**07-JSS-55**	**07-JSS-57**	**07-JSS-58**	**07-JSS-09**	**09-JSS-09**	**09-JSS-10**	**08-JKS-05**	**08-JKS-18**	**07-JSS-49**	**07-JSS-50**	**07-JSS-51**	**08-JES-01**	**09-JH-01**	**08-JES-03**
Wt. %	Sill	Sill	Sill	Sill	F.Dyke	F.Dyke	F.Dyke	Sill	Sill	Sill	Sill	Sill	Sill	Sill	Sill
SiO_2	50.29	50.27	49.56	49.67	49.39	50.00	49.98	49.15	49.04	49.51	48.86	48.84	49.44	49.43	50.28
TiO_2	0.82	0.75	0.80	0.71	0.79	0.81	0.79	0.79	0.76	0.76	2.58	2.51	2.12	2.19	2.07
Al_2O_3	16.95	17.72	16.90	17.82	16.50	17.02	17.11	16.74	16.85	17.16	13.80	13.81	13.43	13.40	13.54
Fe_2O_3	10.42	9.68	10.37	9.53	10.57	10.41	10.36	10.47	10.20	10.11	14.97	14.79	15.16	14.92	14.60
MnO	0.17	0.16	0.17	0.15	0.17	0.17	0.17	0.17	0.17	0.17	0.21	0.22	0.21	0.22	0.21
MgO	6.86	7.21	6.70	6.79	6.63	6.75	6.65	6.60	6.68	6.81	6.47	6.35	6.32	6.16	6.47
CaO	13.22	13.35	12.86	13.50	13.31	13.38	13.27	13.07	13.46	13.42	10.80	10.76	11.01	10.85	11.15
Na_2O	2.00	1.96	2.00	1.91	1.91	1.88	1.86	1.91	1.82	1.89	2.36	2.36	2.34	2.38	2.36
K_2O	0.20	0.22	0.23	0.20	0.14	0.09	0.18	0.20	0.10	0.18	0.20	0.25	0.31	0.30	0.33
P_2O_5	0.09	0.08	0.09	0.08	0.07	0.08	0.08	0.08	0.07	0.07	0.24	0.24	0.21	0.23	0.21
[a]LOI	0.14	0.39	0.17	0.20	0.36	0.28	0.17	0.27	0.50	0.24	0.01	-0.23	-0.12	-0.29	0.07
Total	101.17	101.78	99.86	100.57	99.84	100.88	100.62	99.46	99.64	100.31	100.51	99.90	100.45	99.79	101.29
ppm															
Sr	198	195	202	200	176	181	181	185	180	178	255	253	170	176	169
Y	19	17	19	16	19	18	18	18	18	18	34	34	38	38	37
Zr	53	47	52	46	48	51	50	50	46	47	166	164	139	145	132
Ba	72	65	74	64	55	34	55	55	43	60	73	66	89	91	90
Sc	38	34	36	33	43	39	37	39	39	37	41	39	48	41	47
V	244	217	236	214	252	250	254	260	252	238	378	392	419	433	422
Cr	168	189	159	178	171	162	166	154	170	162	148	140	59	52	65
Ni	74	81	75	74	80	83	80	79	79	77	94	94	68	63	64
Cu	115	106	117	99	131	133	128	129	127	121	192	216	253	264	228
Zn	59	53	57	52	65	64	61	60	62	56	104	106	97	100	94
Y/TiO_2	22.57	22.82	23.57	23.02	23.82	22.61	22.19	23.15	23.94	24.05	13.00	13.53	17.69	17.20	17.71

Table 4.2. (continued)

	Eysturoy Sill								Morskranes Sill			Svínoy-Fugloy Sill		
Sample	**08-JES-04**	**08-JES-07**	**08-JES-08**	**08-JES-10**	**08-JES-11**	**08-JES-19**	**08-JES-20**	**09-JES-08**	**08-JMS-14**	**08-JMS-16**	**08-JMS-17**	**08-JFS-21**	**08-JSVS-22**	**08-JSVS-23**
Wt. %	Sill	Sill	Sill	Sill	Sill	Sill	Sill	F.Dyke	Sill	Sill	Sill	Sill	Sill	Sill
SiO_2	49.67	49.27	49.69	49.23	49.59	49.33	49.28	49.13	48.73	48.87	47.65	48.37	48.49	48.58
TiO_2	2.11	1.97	2.09	2.06	2.01	2.13	2.06	2.16	1.20	1.20	1.21	2.09	2.10	2.10
Al_2O_3	13.47	13.26	13.22	13.41	13.39	13.31	13.34	13.54	15.19	14.48	13.83	13.89	13.54	13.86
Fe_2O_3	14.99	14.62	14.94	13.48	14.94	14.69	15.13	14.89	14.85	12.33	12.66	12.83	14.37	14.22
MnO	0.22	0.21	0.22	0.22	0.22	0.22	0.22	0.22	0.21	0.20	0.21	0.21	0.21	0.20
MgO	6.25	6.23	6.18	6.26	6.55	6.22	6.46	6.26	7.06	8.09	8.22	7.00	7.07	6.95
CaO	10.91	10.87	10.83	10.75	11.19	11.07	11.16	11.10	13.26	12.86	11.86	11.74	11.66	11.77
Na_2O	2.45	2.37	2.39	2.32	2.33	2.34	2.32	2.32	1.95	1.86	1.68	2.26	2.18	2.26
K_2O	0.34	0.36	0.32	0.57	0.30	0.26	0.31	0.23	0.04	0.03	0.79	0.17	0.15	0.18
P_2O_5	0.22	0.22	0.22	0.21	0.20	0.22	0.21	0.22	0.10	0.10	0.10	0.19	0.19	0.19
[a]LOI	0.06	0.07	-0.10	0.07	0.09	-0.09	-0.15	-0.17	0.64	0.61	2.01	-0.22	0.00	-0.22
Total	100.67	99.44	100.01	100.65	100.04	100.56	100.15	100.10	99.85	100.70	100.95	100.39	100.08	99.80
ppm														
Sr	174	167	170	168	171	174	170	175	88	86	94	215	213	214
Y	37	37	38	36	35	36	36	37	29	27	29	29	28	29
Zr	138	139	141	135	125	141	134	142	63	61	62	124	117	126
Ba	88	88	96	101	95	84	90	79	19	18	25	56	64	63
Sc	43	44	43	44	44	45	45	45	49	44	45	39	39	38
V	426	419	426	427	413	432	418	425	350	326	349	352	359	371
Cr	59	63	60	66	66	62	72	58	361	344	352	215	237	228
Ni	58	64	61	61	60	64	63	66	119	109	112	100	118	101
Cu	236	243	236	221	208	257	219	250	173	157	132	194	203	210
Zn	93	98	101	95	91	101	95	95	83	77	77	89	92	93
Y/TiO_2	17.46	18.89	18.04	17.61	17.28	17.08	17.25	17.11	23.70	22.73	23.67	14.00	13.28	13.93

Major elements are indicated in weight percent and trace elements are indicated in parts per million. All iron given as Fe_2O_3. Sample 07-JSS-38 (in bold Italic) represents weathered basalt. The abbreviation F. Dyke indicate feeder dyke. [a]LOI indicate loss on ignition. [b]Ey.S. indicates the Eysturoy Sill. Sample 07-JSS-38 in bold italic represents rocks that show clear signs of weathering. Control analyses of major elements using the standards WS-E and G94 and using the standards BHVO-1, QLO-1, DNC-1 and W-2 for trace elements during XRF analyses are shown in tables labelled Appendix 2.1. and Appendix 2.2. respectively in appendix 2. Error bars representing obtained values of St. Dev. for the actual standards would be smaller than the symbols used to plot major/trace element compositions in relevant diagrams.

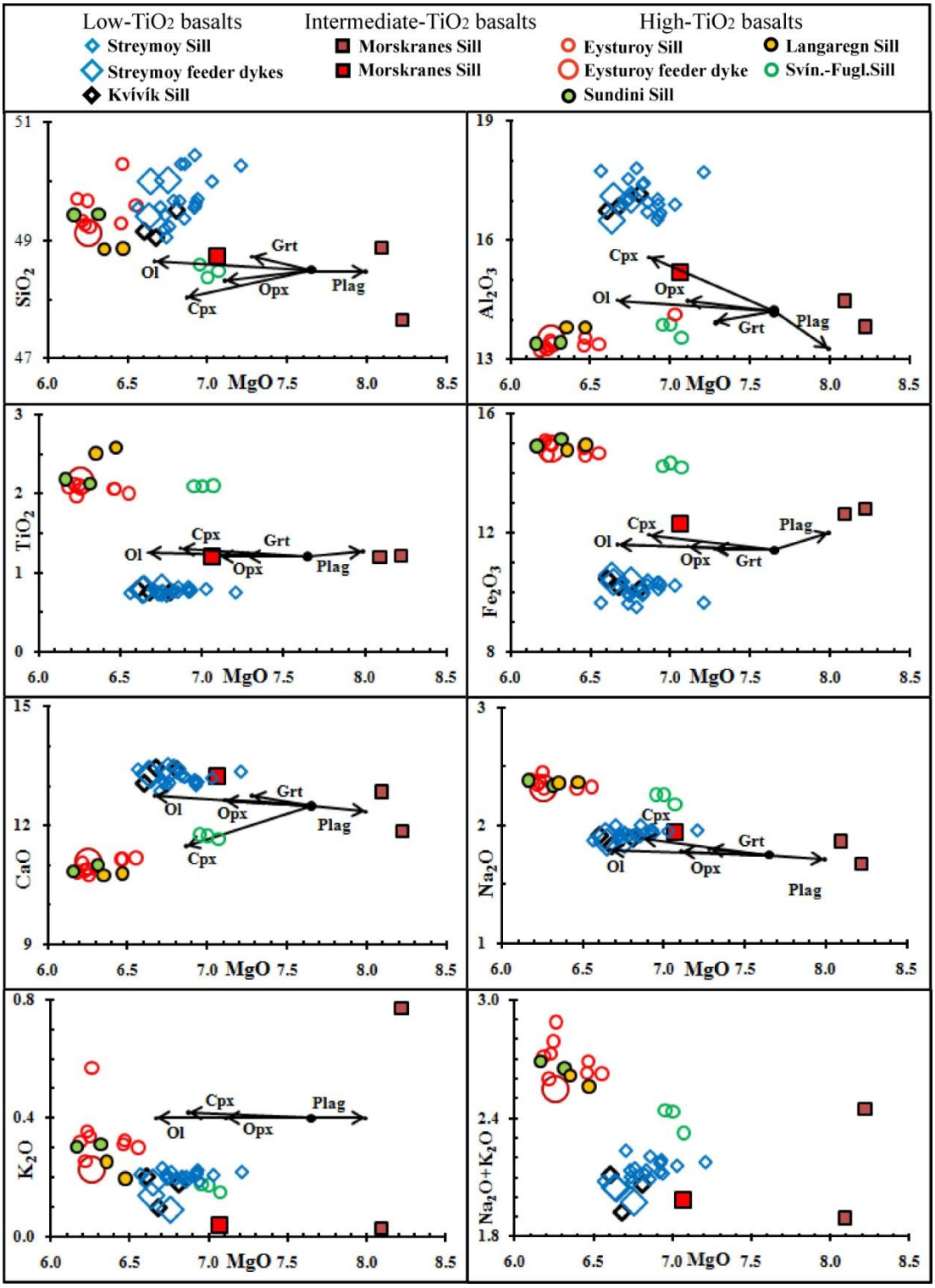

Figure 4.9. Bivariate plots of MgO versus the other major element oxides from Table 4.2. Vectors indicate calculated crystallisation trends (wt%). Ol = olivine (2 wt%); Opx = orthopyroxene (2 wt%); Cpx = clinopyroxene (10 wt%); Plag = plagioclase (5 wt%); Grt = garnet (3 wt%). Major element compositions used in the vector mass-balance calculations are from the compilation of Deer et al. (1992), where Ol = Table 1, sample 1; Grt = table 6, sample 1; Opx = table 18, sample 1; Cpx = table 18, sample 8; Plag = table 38, sample 6. The starting (parent) composition of the calculated vectors does not represent any specific sample, but resembles the average of the Morskranes Sill. See text.

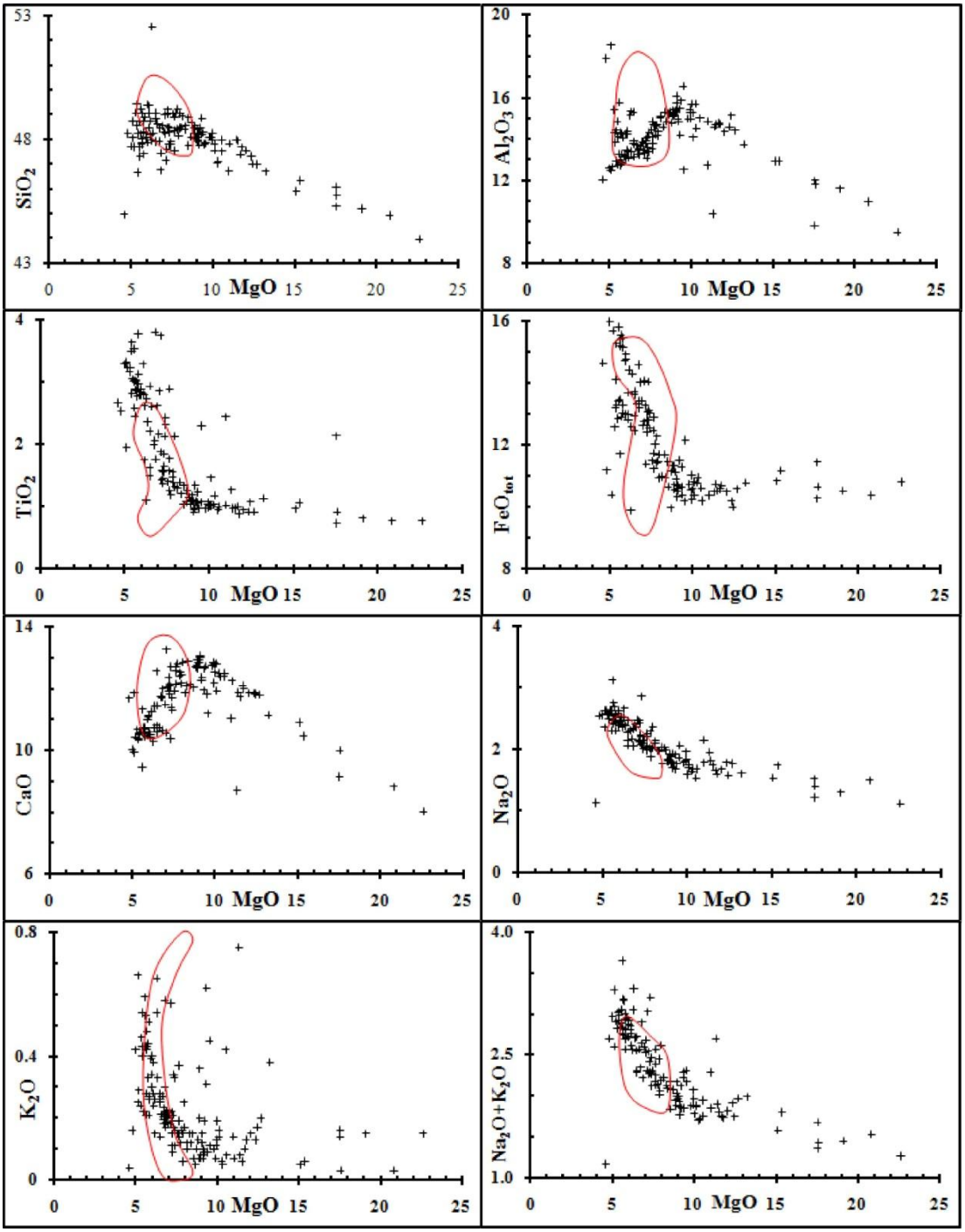

Figure 4.10. The compositional spectrum of the investigated sills (enclosed by red outlines) is contrasted against data representative of lava flows and dykes of the Faroe Islands (black crosses) in bivariate plots of MgO versus other major element oxides. Data on lavas and dykes are from: Hald and Waagstein (1984, 1991); Holm et al. (2001); Søager and Holm (2009, 2011). In the MgO versus FeO_{tot} diagram, total iron for the sills (Given as Fe_2O_3, Table 4.2) is contrasted against total iron (Expressed as raw wt% = FeO + Fe_2O_3) from the literature. See text.

Eysturoy, Langaregn, Sundini and Svínoy-Fugloy sills plot in the high-Fe tholeiite basalt field; the Morskranes Sill plots in the high-Mg tholeiite basalt field while the

Kvívík and Streymoy sills plot in the calc-alkaline basalt field (Fig. 4.8b). The total range in MgO for all the sills combined is 6.15 – 8.25, but overlaps in MgO concentrations for individual sills are of common occurrences (Table 4.2; Fig. 4.9).

Bivariate plots of MgO versus the other major oxides from Table 4.2 show that apart from the SiO_2 and K_2O plots, which display considerable spread and overlaps between individual intrusions, the sills in question can be grouped into three main categories (Fig. 4.9). The Kvívík and Streymoy sills are relatively enriched in Al_2O_3 and CaO and the Eysturoy, Langaregn, Sundini and the Svínoy-Fugloy sills are relatively enriched in Na_2O, TiO_2 and Fe_2O_3 whereas samples representing the Morskranes Sill generally plot in between these two groups (Fig. 4.9).

Most of the geochemical range displayed by the investigated intrusions falls within the compositional range of lavas/dykes of the Faroe Islands as determined during previous studies, but some sills (especially the Streymoy and Kvívík sills) also display higher concentrations of SiO_2 and Al_2O_3 and lower concentrations of TiO_2 and Fe_2O_3 when compared to most of the lavas/dykes that possess MgO compositions comparable to the sills (Fig. 4.10).

4.4.3. Trace elements

The concentrations of trace elements such as Sr, Ba, Zr and Y from individual sills of this study (Table 4.3.) define groups that being slightly different from those of Fig. 4.9 (particularly the Svínoy-Fugloy Sill) when plotted against MgO (Fig. 4.11a, b, c, d). These trace elements define tight clusters for individual sills in Sr versus Ba and Y versus Zr plots (Fig. 4.11e, f). The concentrations of these 4 trace elements in each of the pairs of Streymoy/Kvívík sills and the Eysturoy/Sundini sills respectively plot in identical clusters on all bivariate diagrams shown in Fig. 4.11.

Trace-element data from Table 4.3 normalised to primordial mantle values and plotted in order of increasing (MORB source) compatibility from left to right in a spider diagram (Fig. 4.12a) define three main trends being in accordance with the three basalt groups shown in the classification diagram in Fig. 4.8b and the High, intermediate and low-TiO_2 groups of Fig. 4.9. Apart from strong enrichments in Rb and K, the high-Mg (intermediate-TiO_2) tholeiite Morskranes Sill displays a gradual and smooth depletion in trace elements from right to left in Fig.4.12a. Variations in Ba, Rb, Th and K within individual intrusions are particularly evident in the Eysturoy Sill (Fig. 4.12b). Apart from slight negative P anomalies, both of the two main sill

Table 4.3. Whole rock ICP-MS data on trace elements from the sills of the Faroe Islands.

	[a]Str. S.				[b]Kv. S.	[c]Lr. S.	[d]Su. S.	[e]Ey. S.				[f]Mn. S.	[g]Sv.-Fu. S.	
Ppm	**07-JSS-26**	**07-JSS-40**	**07-JSS-52**	**07-JSS-09**	**07-JSS-49**	**07-JSS-50**	**08-JES-01**	**08-JES-08**	**08-JES-10**	**08-JES-11**	**08-JES-19**	**08-JMS-17**	**08-JFS-21**	**08-JSVS-22**
Rb	3.81	3.45	1.98	1.42	3.00	3.40	6.71	7.03	10.34	7.14	4.83	24.04	3.50	3.19
Sr	208	215	204	186	185	260	176	176	174	174	180	97.9	220	217
Y	18.8	17.1	18.7	19.4	18.2	34.9	38.9	39.8	38.9	36.6	39.1	29.9	31.2	29.1
Zr	50.8	46.3	50.9	47.4	45.2	173	144	147	142	135	147	61.7	132	123
Nb	2.87	2.61	2.81	2.65	2.47	13.98	11.89	11.81	11.57	10.85	11.73	1.54	11.05	10.47
Ba	59.3	53.8	62.8	47.7	44.9	64.9	77.4	84.4	87.0	76.4	74.0	15.8	47.1	49.4
La	4.24	3.62	4.24	3.50	3.28	11.37	10.37	10.87	10.48	9.38	10.61	2.65	8.76	8.47
Ce	10.28	8.74	10.20	8.55	8.04	29.7	25.7	26.8	26.2	23.2	26.1	6.54	22.4	21.6
Pr	1.60	1.36	1.57	1.34	1.28	4.80	3.99	4.13	4.01	3.60	4.05	1.11	3.59	3.43
Nd	7.40	6.39	7.39	6.48	6.09	22.76	18.80	19.47	18.83	17.34	19.03	6.67	17.22	16.53
Sm	2.04	1.78	2.03	1.86	1.79	6.00	4.98	5.22	5.03	4.63	5.07	2.57	4.61	4.50
Eu	0.757	0.663	0.744	0.719	0.674	1.973	1.642	1.702	1.667	1.545	1.668	1.004	1.532	1.507
Gd	2.57	2.25	2.65	2.57	2.41	7.03	6.14	6.38	6.17	5.63	6.17	4.39	5.45	5.30
Tb	0.457	0.403	0.484	0.464	0.440	1.10	1.02	1.07	1.03	0.945	1.055	0.787	0.900	0.876
Dy	2.84	2.46	2.95	2.93	2.77	6.11	6.15	6.31	6.24	5.70	6.16	4.83	5.15	4.88
Ho	0.634	0.540	0.647	0.654	0.604	1.20	1.28	1.33	1.30	1.18	1.30	1.06	1.04	0.988
Er	1.79	1.54	1.86	1.82	1.80	3.08	3.53	3.68	3.57	3.24	3.51	2.95	2.74	2.64
Yb	1.79	1.56	1.87	1.92	1.75	2.70	3.37	3.45	3.39	3.13	3.39	2.90	2.49	2.36
Lu	0.294	0.254	0.307	0.315	0.294	0.422	0.557	0.554	0.547	0.499	0.550	0.475	0.395	0.380
Hf	1.34	1.17	1.40	1.25	1.21	4.37	3.56	3.67	3.53	3.30	3.63	1.81	3.31	3.07
Ta	0.177	0.150	0.180	0.160	0.158	0.869	0.696	0.707	0.699	0.625	0.697	0.105	0.667	0.636
Pb	0.770	0.730	0.844	0.731	0.681	1.09	1.20	1.23	1.23	1.26	1.22	0.336	0.845	0.900
Th	0.525	0.439	0.526	0.421	0.374	0.854	0.961	0.993	0.949	0.854	0.944	0.171	0.692	0.661
U	0.140	0.127	0.138	0.112	0.111	0.262	0.287	0.287	0.285	0.252	0.284	0.050	0.216	0.208
[h]$(Ce/Sm)_N$	1.19	1.15	1.18	1.08	1.05	1.16	1.21	1.20	1.22	1.17	1.21	0.60	1.14	1.13
[h]$(Sm/Yb)_N$	1.23	1.24	1.18	1.05	1.11	2.41	1.60	1.64	1.61	1.60	1.62	0.96	2.00	2.06
Nb/Ta	16.21	17.37	15.63	16.53	15.61	16.09	17.09	16.70	16.55	17.36	16.84	14.70	16.57	16.47

Trace element concentrations are indicated in parts per million. [a]Str.S. = Streymoy Sill; [b]Kv.S. = Kvívík Sill; [c]Lr.S. = Langaregn Sill; [d]Su.S. = Sundini Sill; [e]Ey.S. = Eysturoy Sill; [f]Mn.S. = Morskranes Sill; [g]Sv.-Fu.S. = Svínoy-Fugloy Sill. [h]Normalising chondrite values from Nakamura (1974). Control analyses of trace elements using the standards NBS688, BHVO-1, W-2 and AGV1 during the ICP-MS analyses are shown in table labelled Appendix 3.1. in appendix 3. Error bars representing the obtained values of St. Dev. for the actual standards would be smaller than the symbols used to plot trace element compositions in relevant diagrams.

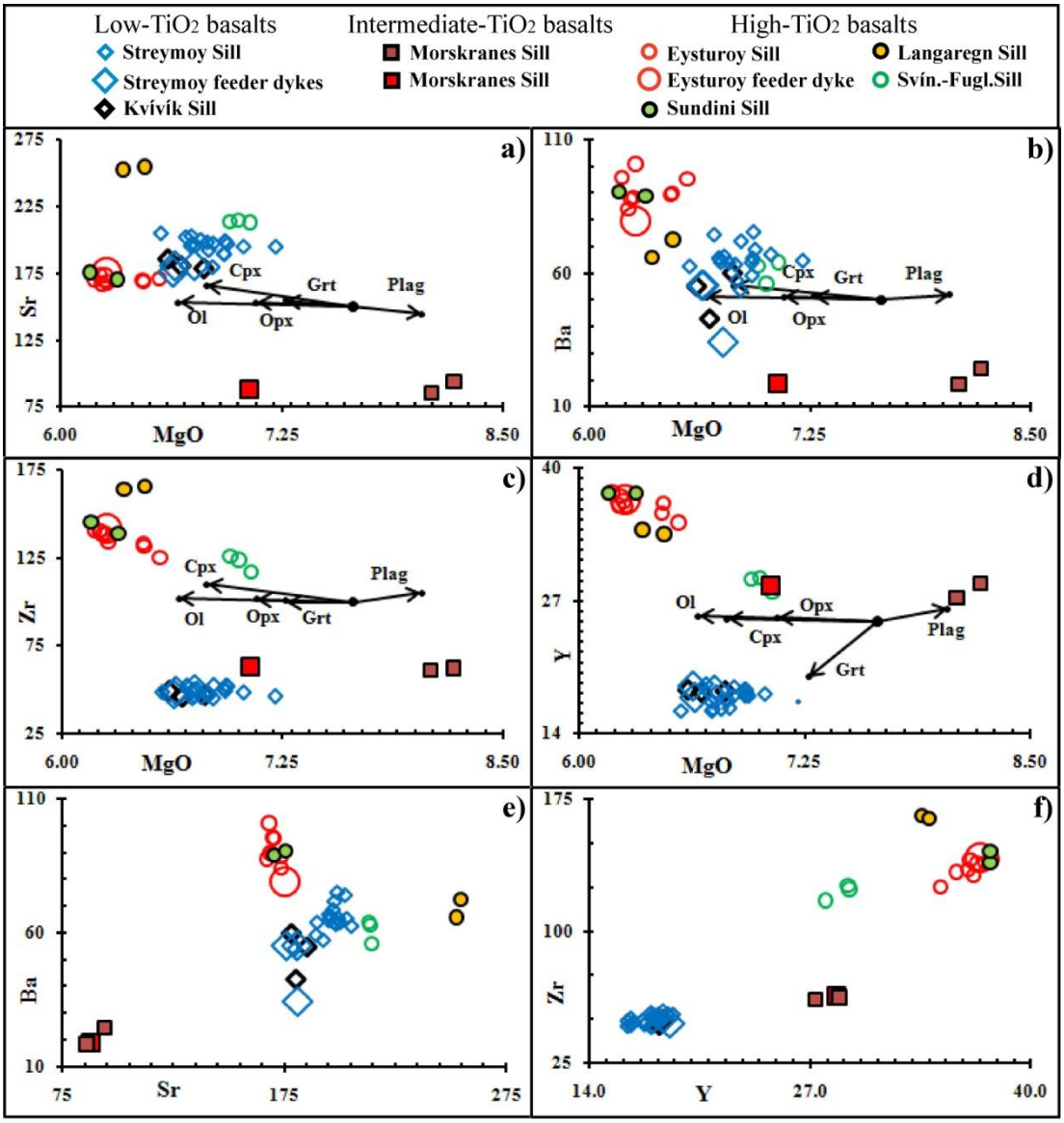

Figure 4.11. Bivariate plots involving Sr, Ba, Zr and Y from sills of the Faroe Islands. The plotted clusters are broadly similar to the inferred groups from Fig. 4.9, i.e. low, intermediate and high-TiO_2 groups. Percentages in calculated fractionation vectors (see equation 9 below) are as in Fig. 4.9 and start (parent) composition does not represent any specific sample, but is chosen at random. See text.

groups display separate well-defined relatively flat sub-parallel trends in most of their trace elements, but the high-TiO_2 sills display negative Sr anomalies and the low-TiO_2 sills display positive Sr anomalies (Fig. 4.12). The high-TiO_2 Eysturoy and Sundini sills display stronger Sr depletion relative to the Langaregn and Svínoy-Fugloy sills, but the two latter display stronger depletion in Ba, Rb, Th and K (Fig. 4.12b; Fig. 4.12c). Perhaps less conspicuous are moderately positive Nb and Ta anomalies in the Langaregn and Svínoy-Fugloy sills and moderately negative Nb and Ta anomalies in the Streymoy and Kvívík sills (Fig. 4.12a; Fig. 4.12c; Fg. 4.12d).

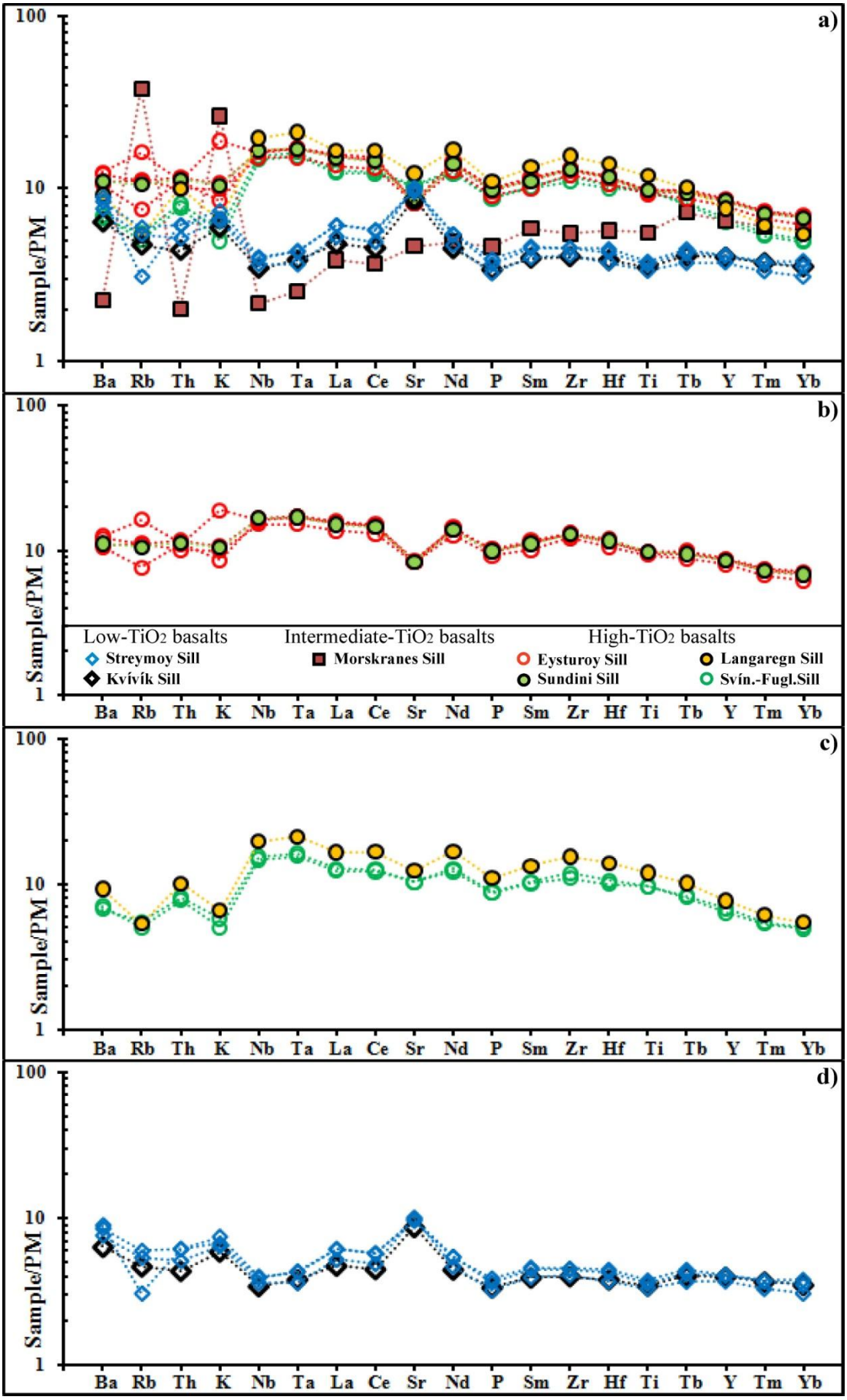
a)
b)
c)
d)
100
10
1
Sample/PM
Ba Rb Th K Nb Ta La Ce Sr Nd P Sm Zr Hf Ti Tb Y Tm Yb
Low-TiO2 basalts
Intermediate-TiO2 basalts
High-TiO2 basalts
Streymoy Sill
Kvívík Sill
Morskranes Sill
Eysturoy Sill
Sundini Sill
Langaregn Sill
Svín.-Fugl.Sill

Figure 4.12. (Previous page**)**. Trace elements normalised to primitive mantle composition (PM) of Sun and McDonough (1989). a) The investigated sills define three main trends with the incompatible element depleted Morskranes Sill being characterised by strong Rb and K enrichments. b) Most samples of the the Eysturoy and Sundini sills display negative P, Sr, K, Th, Rb and Ba anomalies. c) The Langaregn and Svínoy sills display negative anomalies for the same elements as in b, but also display moderately positive Ta and Nb anomalies. d) The Streymoy and Kvívík sills display positive Sr anomalies and moderately negative P, Ta and Nb anomalies. y axes are in log scales. See text.

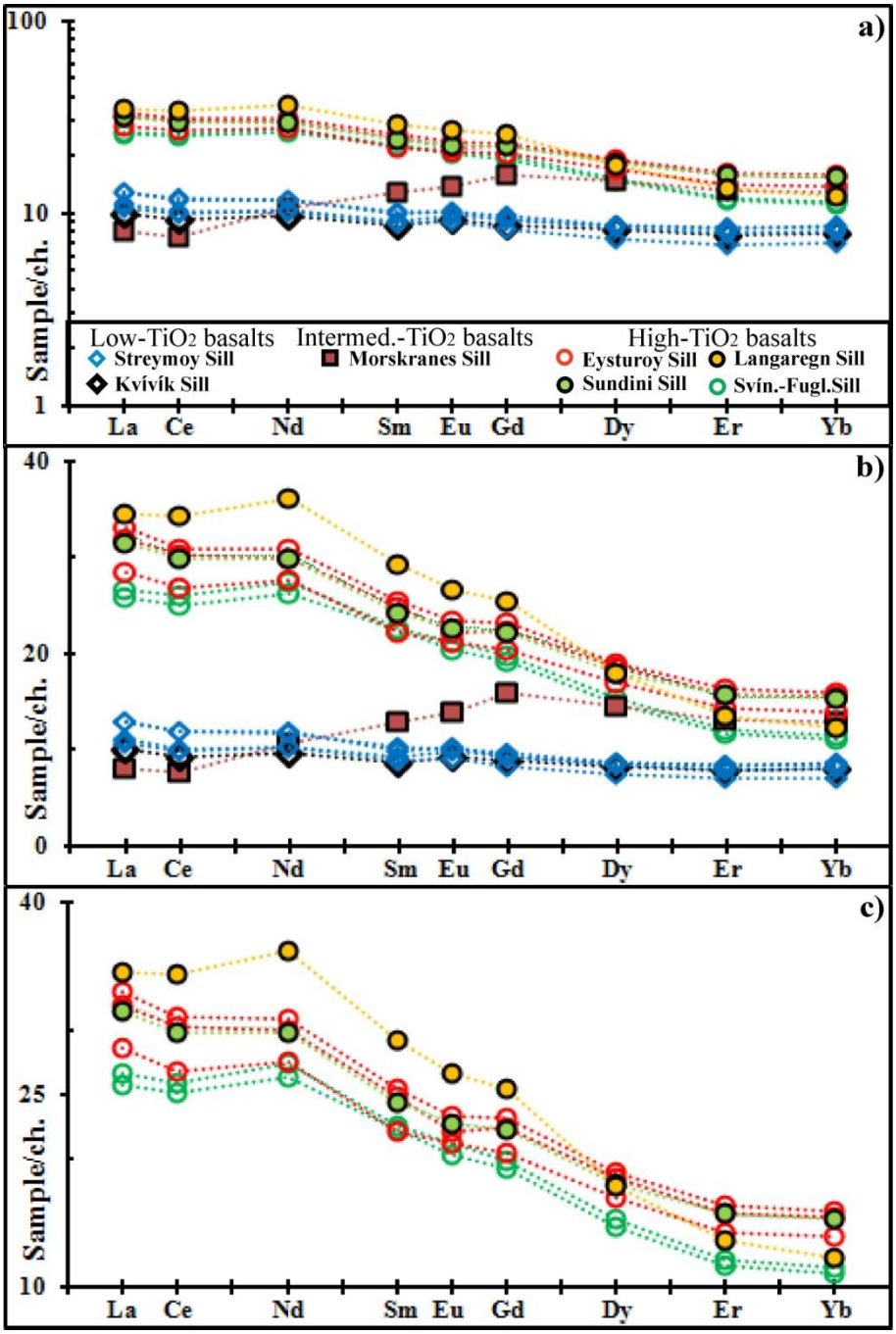

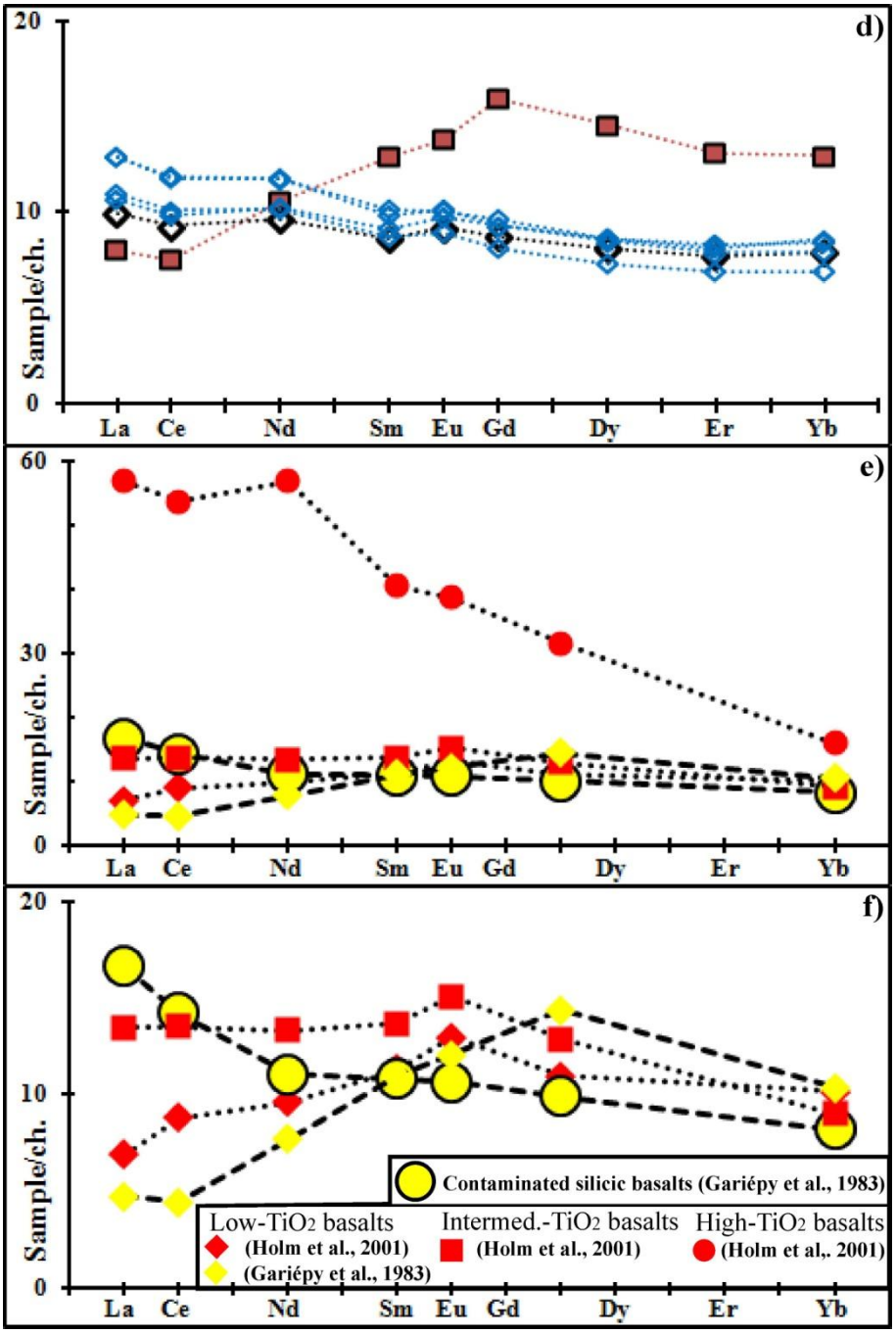

Figure 4.13. (Previous and current pages). REE concentrations of sills from this study and selected local literature basalts normalised to chondrite values of Nakamura (1974). a) The sills can be grouped into three main categories according to their REE compositions. b) Same as in a, but with linear scale on the y axis. c) The Langaregn Sill displays steeper HREE trend compared to the rest of the LREE enriched sill samples in this linear plot. d) The Streymoy and Kvívík sills display relatively flat REE trends whereas the Morskranes Sill is depleted with respect to its LREE concentration as shown in this linear plot. e) Linear plot of local basalts from the literature for comparison, including a very high-TiO_2/LREE specimen. f) A silicic basalt sample shows clear enrichment with respect to its LREE, while low-TiO2 local basalt samples are LREE depleted in this linear plot. Note differences in scales at y axes. See text.

4.4.4. REE

Chondrite-normalised REE data from Table 4.3 representing sill samples of the Faroe Islands display three distinct and well defined trends (Fig. 4.13a, Fig. 4.13b), which correspond to basalt types 1, 2 and 3 reported for most regions of the NAIP previously (Kerr, 1995). The sills that define each of these three REE trends correspond to each of the three groups of Fig. 4.8b and Fig. 4.9 and the categories/trends from Fig. 4.12. The Morskranes Sill is depleted in the LREE, but displays a relatively flat HREE trend (Fig 4.13d). Both of the other two groups display relatively uniform flat LREE trends with $(Ce/Sm)_N$ ratios ranging from 1.05 to 1.23 (Fig 4.13c; Fig. 4.13d). Samples of the low-Ti group display relatively flat HREE trends with $(Sm/Yb)_N$ ratios ranging from 1.05 to 1.24 (Fig. 4.13d) compared to more steeply sloping trends for the same elements belonging to the high-Ti group with $(Sm/Yb)_N$ ratios ranging from 1.6 to 2.1 (Fig. 4.13c). It is noteworthy that the Langaregn Sill has a steeper HREE slope than any other sill from this study (Fig. 4.13c).

4.5. Isotopes

4.5.1. Lead isotopes

Apart from the Kvívík Sill, all of the saucer-shaped sills from this study are represented by the samples analysed for $^{206}Pb/^{204}Pb$, $^{207}Pb/^{204}Pb$ and $^{208}Pb/^{204}Pb$ isotope ratios (Table 4.4; Fig. 4.14). The measured lead isotope ratios (Fig. 5.1a, b, c) and the ratios being corrected/adjusted back to 54 Ma (Fig. 4.14a*, b*, c*) display broadly similar configurations and define positive slopes (Apart from one sample of the Morskranes Sill where no Pb, Th and U are available). Although the sills from this study display moderate spread in measured/age-corrected lead isotope ratios and also show overlapping values for some samples, they can be grouped into two main categories according to their $^{206}Pb/^{204}Pb$ ratios (Fig. 4.14. Fig. 4.15a; Fig 4.15b). The group defined by the Morskranes Sill exhibits $^{206}Pb/^{204}Pb$ ratios in the range from 18.2442 to 18.2501 compared to $^{206/204}Pb$ ratios of 18.0436 to 18.4444 for the other category defined by the rest of the investigated sills (Table 4.4; Fig. 4.14).

Only measured lead isotope ratios are shown in Table 4.4 and used in the comparisons/calculations below, as there are relatively limited differences between measured and age-corrected lead isotope ratios for both sills and basement samples. For instance, the maximum deviations of Pb isotopic ratios associated with age

Table 4.4. Whole rock isotope data on sill samples (MC-ICP-MS) and selected lavas/dykes of the Faroe Islands and selected basement samples from neighbouring regions.

Samples	$^{206/204}$Pb	$^{207/204}$Pb	$^{208/204}$Pb	Pb	Rb	Sr	$^{87/86}$Sr (0)	^{87}Rb/^{86}Sr	$^{87/86}$Sr (t)	$\epsilon^{(t)}_{UR}$ (Sr)	Sm	Nd	$^{143/144}$Nd (0)	^{147}Sm/^{144}Nd	$^{143/144}$Nd (t)	$\epsilon^{(t)}_{CHUR}$ (Nd)
08-JSVS-22	[a]18.3736	[b]15.4482	[c]38.2266	0.85	3.19	217.10	[d]0.703306	[f]0.060346	0.703260	-16.718	4.52	16.53	[e]0.512987	[g]0.211594	0.512912	6.706
07-JSS-49	-----	-----	-----	-----	3.00	185.08	[d]0.703255	[f]0.066592	0.703204	-17.510	1.76	6.09	[e]0.513032	[g]0.223383	0.512953	7.503
07-JSS-50	[a]18.2326	[b]15.4246	[c]38.1692	1.08	3.40	259.63	[d]0.703266	[f]0.053838	0.703225	-17.215	5.93	22.76	[e]0.512999	[g]0.201413	0.512928	7.010
07-JSS-52	[a]18.4444	[b]15.4756	[c]38.2700	0.85	1.98	203.59	[d]0.703313	[f]0.039892	0.703282	-16.396	2.06	7.39	[e]0.513023	[g]0.215840	0.512947	7.379
08-JES-10	[a]18.2501	[b]15.4493	[c]38.1765	1.28	10.34	174.13	[d]0.703380	[f]0.244165	0.703193	-17.669	5.02	18.83	[e]0.512983	[g]0.206201	0.512910	6.665
08-JES-01	[a]18.2442	[b]15.4493	[c]38.1727	1.19	6.71	176.03	[d]0.703308	[f]0.156658	0.703188	-17.738	4.93	18.80	[e]0.512986	[g]0.202623	0.512914	6.749
08-JMS-17	[a]17.9505	[b]15.4086	[c]37.9737	0.32	24.04	97.92	[d]0.703693	[f]1.008897	0.702919	-21.553	2.62	6.67	[e]0.513073	[g]0.303742	0.512966	7.749
08-JMS-14	[a]17.9131	[b]15.4536	[c]37.8876	-----	2.70	86.00	[d]0.702895	[f]0.129173	0.702796	-23.302	1.80	4.45	[e]0.513086	[g]0.312780	0.512976	7.940
K-11	*17.9830*	*15.4140*	*37.6010*	-----	*2.50*	*94.00*	-----	-----	[h]*0.702660*	-----	-----	-----	-----	-----	[h]*0.513071*	-----
K-1	*16.1000*	*15.1840*	*39.8250*	-----	*3.90*	*131.00*	-----	-----	-----	-----	-----	-----	-----	-----	-----	-----
Sv-12	*17.8920*	*15.3770*	*37.6490*	-----	*2.90*	*72.00*	*0.702780*	*0.119900*	*0.702688*	*-24.833*	*1.49*	*4.09*	*0.513151*	*0.221000*	*0.513073*	*9.841*
Str-188	*18.3570*	*15.4940*	*38.0150*	-----	*1.90*	*176.00*	*0.703000*	*0.031600*	*0.702976*	*-20.749*	*2.77*	*8.38*	*0.513062*	*0.201000*	*0.512991*	*8.242*
Va-20	*18.2310*	*15.4420*	*38.0990*	-----	*13.00*	*327.00*	*0.703388*	*0.142000*	*0.703279*	*-16.443*	*8.19*	*35.80*	*0.513023*	*0.171000*	*0.512963*	*7.688*
X14	*16.2330*	*15.0930*	*37.3660*	-----	*17.00*	*193.00*	-----	-----	[i]*0.709990*	[i]*75.900*	-----	-----	-----	-----	[i]*0.512070*	[i]*-9.7*
X16	*17.1720*	*15.3140*	*39.6650*	-----	*12.00*	*179.00*	-----	-----	[i]*0.716260*	[i]*164.900*	-----	-----	-----	-----	[i]*0.511760*	[i]*-15.7*
69A	*15.2750*	*14.9060*	*36.6590*	-----	*15.00*	*243.00*	-----	-----	-----	-----	-----	-----	-----	-----	-----	-----
Lewis.Ampbh.	14.5000	14.8000	38.2000	12.00	-----	493.00	-----	-----	[h]0.717000	-----	-----	25.00	-----	-----	[h]0.510600	-----
Lewis.Gran.	14.5000	14.8000	34.1000	5.00	-----	387.00	-----	-----	[h]0.703000	-----	-----	25.00	-----	-----	[h]0.510600	-----
SMZ-AMG-01	-----	-----	-----	-----	18.70	349.00	-----	-----	[h]0.717000	-----	14.90	71.50	-----	-----	[h]0.511350	-----
P42	14.5900	14.8450	35.4090	13.49	101.00	541.00	0.723478	0.747784	0.722904	262.152	3.94	23.08	0.510588	0.132521	0.510541	-39.552
A	16.5980	15.3750	35.7900	25.00	116.00	309.00	0.729330	1.097800	0.728488	341.414	12.13	68.69	0.511828	0.118800	0.511737	-14.639
B	16.7420	15.4180	35.9840	17.00	34.00	428.00	0.708320	0.246200	0.708131	52.435	29.59	127.08	0.512118	0.148000	0.512066	-9.809
E	21.7990	15.8800	39.1010	19.00	160.00	51.00	0.914010	9.024800	0.907087	2876.760	4.18	30.45	0.511524	0.091800	0.511454	-20.167
KS60/KS19A	20.4670	15.8410	60.4680	12.66	38.00	250.l00	0.726550	0.416500	0.726231	309.369	1.76	40.00	-----	-----	[j]0.510700	-----
229632	13.9620	14.7420	33.6930	[k]25.00	19.00	553.00	0.705200	0.100000	0.705123	9.737	1.56	10.88	0.510724	0.092100	0.510691	-36.621
229642	16.7400	15.5890	35.4950	[k]25.00	33.00	460.00	0.713090	0.210000	0.712929	120.543	6.56	43.13	0.510600	0.092100	0.510567	-39.040
229661	13.7150	14.6510	33.2400	[k]25.00	11.00	598.00	0.703560	0.055000	0.703518	-13.054	0.74	6.01	0.510463	0.092100	0.510430	-41.713

Numbers displayed in rows 1 to 8 indicate data from this study, numbers in rows 9 to 16 indicate data from earlier studies on selected dykes/lavas of the Faroe Islands (Gariépy et al., 1983; Holm et al., 2001) and numbers in rows 17 to 28 indicate data on basement samples from NW Britain, Rockall Plateau and E Greenland (Sample identifications given in figures below). Unless otherwise stated, (t) refer to age correction back to 54 Ma for data on the actual column. [a]2SE range from 0.0013 to 0.0053, [b]2SE range from 0.0015 to 0.0051, [c]2SE range from 0.0049 to 0.0190, [d]2SE range from 0.000004 to 0.000023, [e]2SE range from 0.000006 to 0.000014, [f]calculated ratios (see appendix 4 for methods), [g]calculated ratios (see appendix 4 for methods), [h]age corrected to 60 Ma, [i]age corrected to 56 Ma, [j]interpolated ratio based on average E Greenland data, [k]interpolated from average E Greenland data. Rb, Sm and Nd concentrations for sample 08-JMS-14 are interpolated from published samples with identical compositions of other trace elements (Gariépy et al., 1983). Decay constants used in the calculated age corrections are recommended by the IUGS and are: $^{87}Rb \rightarrow {}^{87}Sr = 1.42\times10^{-11}$ yr^{-1} (Steiger and Jäger, 1977) and $^{147}Sm \rightarrow {}^{143}Nd = 6.54\times10^{-12}$ yr^{-1} (Lugmair and Marti, 1978). Control analyses of isotope ratios using the standards NBS 981, NBS 987 and J&M during MC-ICP-MS analyses are shown in table labelled Appendix 4.1. in appendix 4. Error bars for analysed sill samples are shown in Fig. 4.14a-c and Fig. 4.16a.

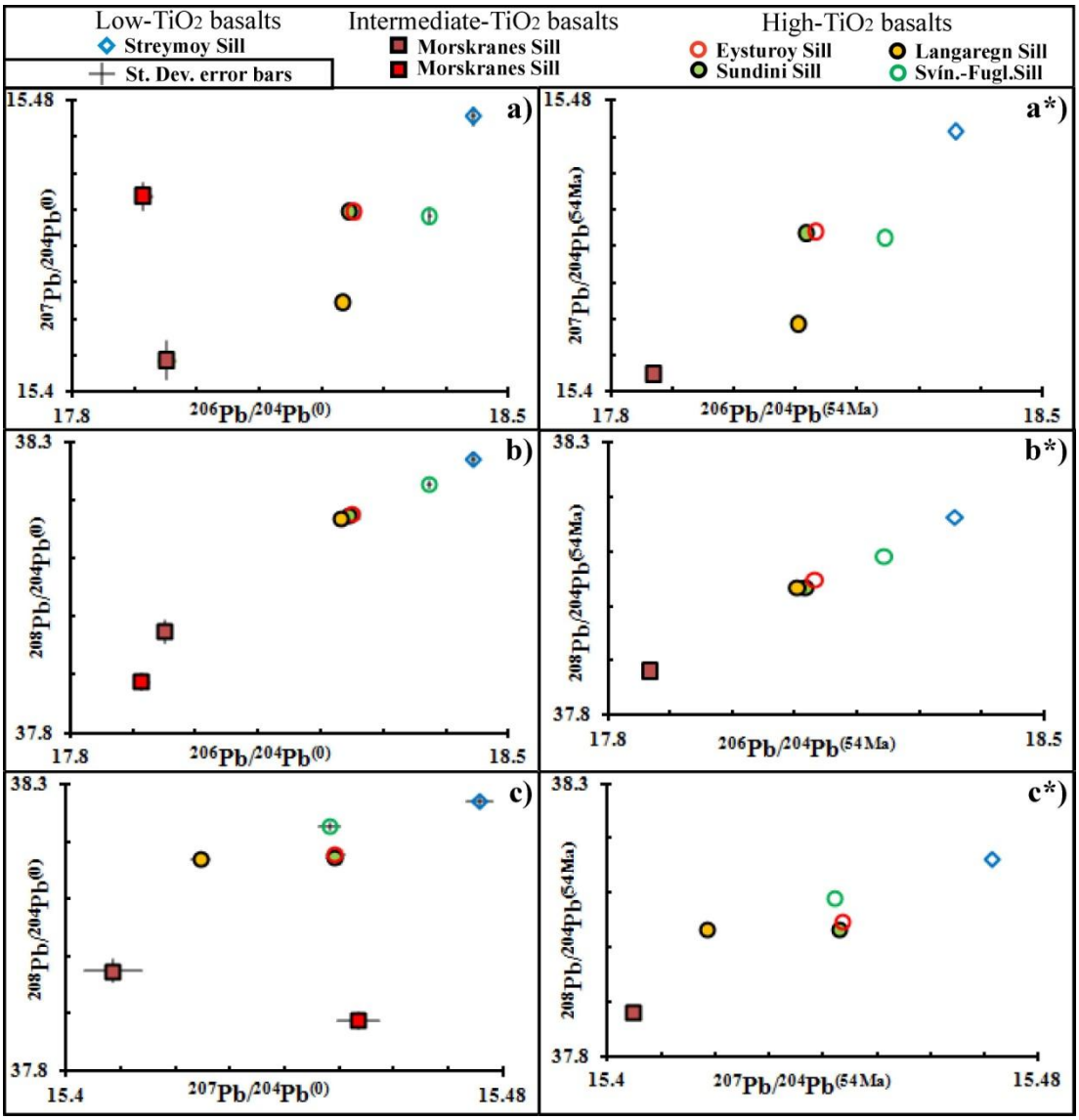

Figure 4.14. Measured isotope ratios in a), b) and c) (Table 4.4) show configurations similar to those of the same samples being age-corrected back to 54 Ma, as shown in a*), b*) and c*) and using decay constants as recommended by the IUGS where: $^{238}U \rightarrow ^{206}Pb$ = 1.55125×10^{-10} yr^{-1}, $^{235}U \rightarrow ^{207}Pb$ = 9.8485×10^{-10} yr^{-1} and $^{232}Th \rightarrow ^{208}Pb$ = 4.9475×10^{-11} yr^{-1} (Steiger and Jäger, 1977). Measured and age-corrected isotope ratios display broadly linear trends that define positive slopes in diagrams a) to c*) apart for one sample of the Morskranes Sill, the isotope ratios of which are relatively enriched in $^{207}Pb/^{204}Pb$. Samples of the Morskranes Sill are relatively depleted in $^{206}Pb/^{204}Pb$ and $^{208}Pb/^{204}Pb$ ratios. Pb ratios of the Svínoy-Fugloy and Langaregn sills vary relative to those of the others. Measured St. Dev. values (Table 4.4) are indicated by shaded grey error bars in a), b) and c). See text.

corrections back to 54 Ma of the basalt sills in question are: $^{206}Pb/^{204}Pb$ = -0.13; $^{207}Pb/^{204}Pb$ = -0.006 and $^{208}Pb/^{204}Pb$ = -0.14, compared to maximum deviations for similar age corrections of a typical felsic basement sample (e.g. P42 of Kerr et al.,

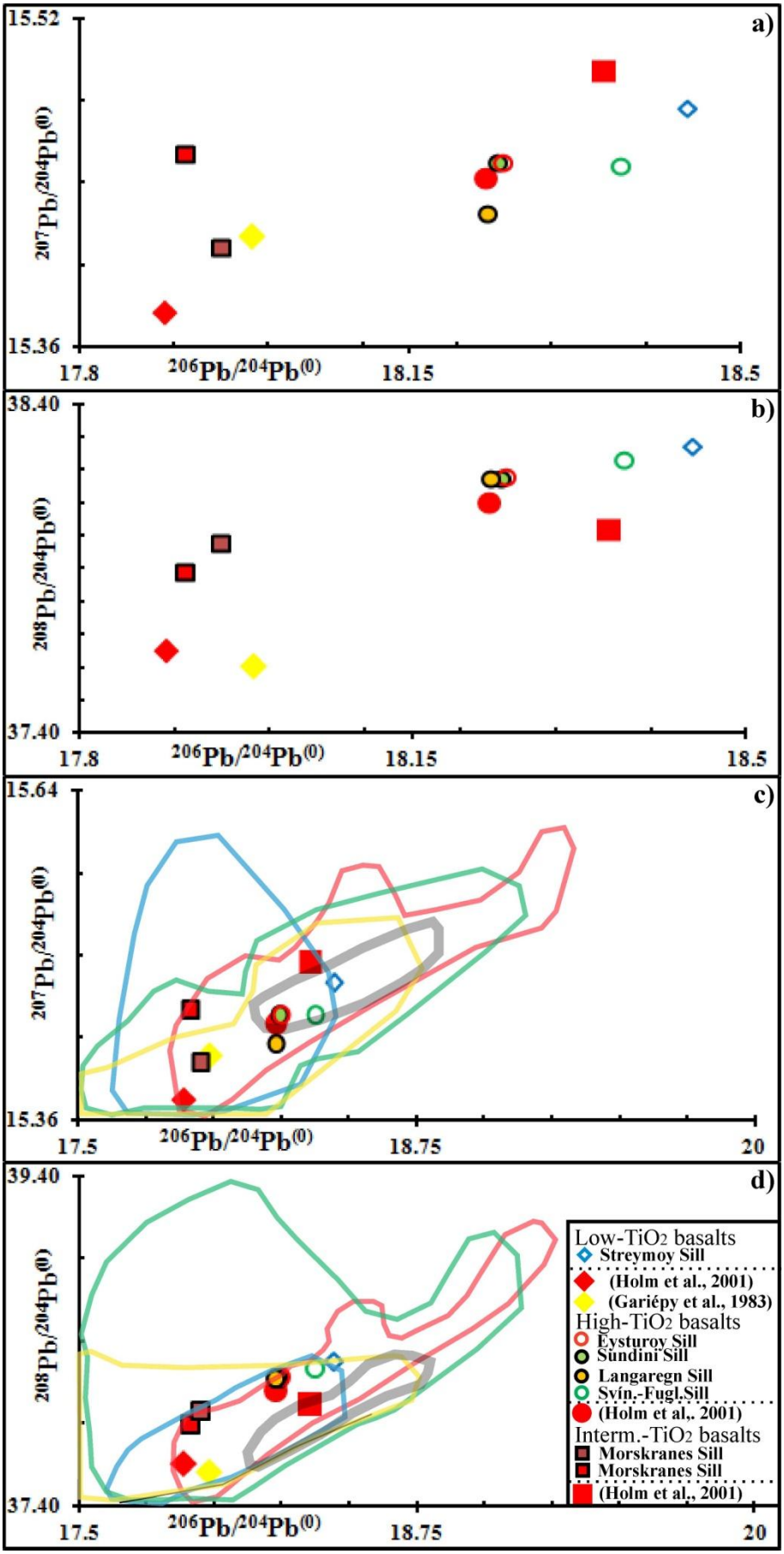
a)
15.52
15.36
17.8
18.15
18.5
$^{207}Pb/^{204}Pb^{(0)}$
$^{206}Pb/^{204}Pb^{(0)}$
b)
38.40
37.40
17.8
18.15
18.5
$^{208}Pb/^{204}Pb^{(0)}$
$^{206}Pb/^{204}Pb^{(0)}$
c)
15.64
15.36
17.5
18.75
20
$^{207}Pb/^{204}Pb^{(0)}$
$^{206}Pb/^{204}Pb^{(0)}$
d)
39.40
37.40
17.5
18.75
20
$^{208}Pb/^{204}Pb^{(0)}$
$^{206}Pb/^{204}Pb^{(0)}$
Low-TiO2 basalts
Streymoy Sill
(Holm et al., 2001)
(Gariépy et al., 1983)
High-TiO2 basalts
Eysturoy Sill
Sundini Sill
Langaregn Sill
Svín,-Fugl.Sill
(Holm et al,. 2001)
Interm.-TiO2 basalts
Morskranes Sill
Morskranes Sill
(Holm et al,. 2001)

Figure 4.15. (Previous page). a) and b) Same as in Fig. 4.14a and Fig. 4.14b but with selected dyke/lava samples from the Faroe Islands published earlier (red and yellow symbols). c) and d). Fields representing isotopic data from Iceland (red outlines) are from Thirlwall et al. (2004) and the compilation of Kitagava et al. (2008). Field representing isotopic data from E Greenland (green outlines) are from Hanghøj et al. (2003); Peate and Stecher (2003) and the compilation of Peate et al. (2008). Fields representing isotopic data from W Greenland (blue outlines) are from Larsen and Pedersen (2009). Fields representing isotopic data from previous studies of the Faroe Islands (yellow outlines) are from Gariépy et al. (1983), Holm et al. (2001) and Søager and Holm (2011). Fields representing isotopic data from the Reykjanes Ridge MORB (grey outlines) are from Mertz and Haase (1997). Sample data are from Table 4.4. See text.

1995) are: $^{206}Pb/^{204}Pb$ = -0.01; $^{207}Pb/^{204}Pb$ = -0.001 and $^{208}Pb/^{204}Pb$ = -0.14). Also, all the Pb isotope data published previously on basalts from the Faroe Islands and on most basalts from other parts of the NAIP, in addition to the vast majority of basement samples from neighbouring regions such as the NW British Isles, the Rockall Plateau and E Greenland are only given as measured values and mostly lack data on one or more of elements such as Pb, Th and U.

Representative Pb isotope data from dykes and lava flows of the Faroe Islands that have been published earlier define trends that are broadly similar to those of the investigated sill samples and can be grouped into the same two categories. Compared to the relative stable configurations of most samples in Fig. 4.15a and Fig. 4.15b, one sample of the Morskranes Sill in addition to the yellow rhombus and the red square covary and occupy different positions in each of these two diagrams.

The Pb isotope ratios of individual basalt samples from the Faroe Islands being used in this study (Sills and selected lavas/dykes) all fall within the compositional range of published E Greenland and W Greenland data and many are also encompassed within the fields for published Icelandic data (Fig. 4.15c; Fig. 4.15d). However, the sill samples of the Faroe Islands generally display higher $^{208}Pb/^{204}Pb$ ratios relative to basalts from Iceland, including MORB samples from the Reykjanes Ridge (Fig. 4.15d). Otherwise, only sill samples that are relatively enriched with respect to their Sr and Nd isotopes (Fig. 4.16a) fall within the range defined by $^{206}Pb/^{204}Pb$ versus $^{207}Pb/^{204}Pb$ ratios of MORB samples from the Reykjanes Ridge (Fig. 4.15c).

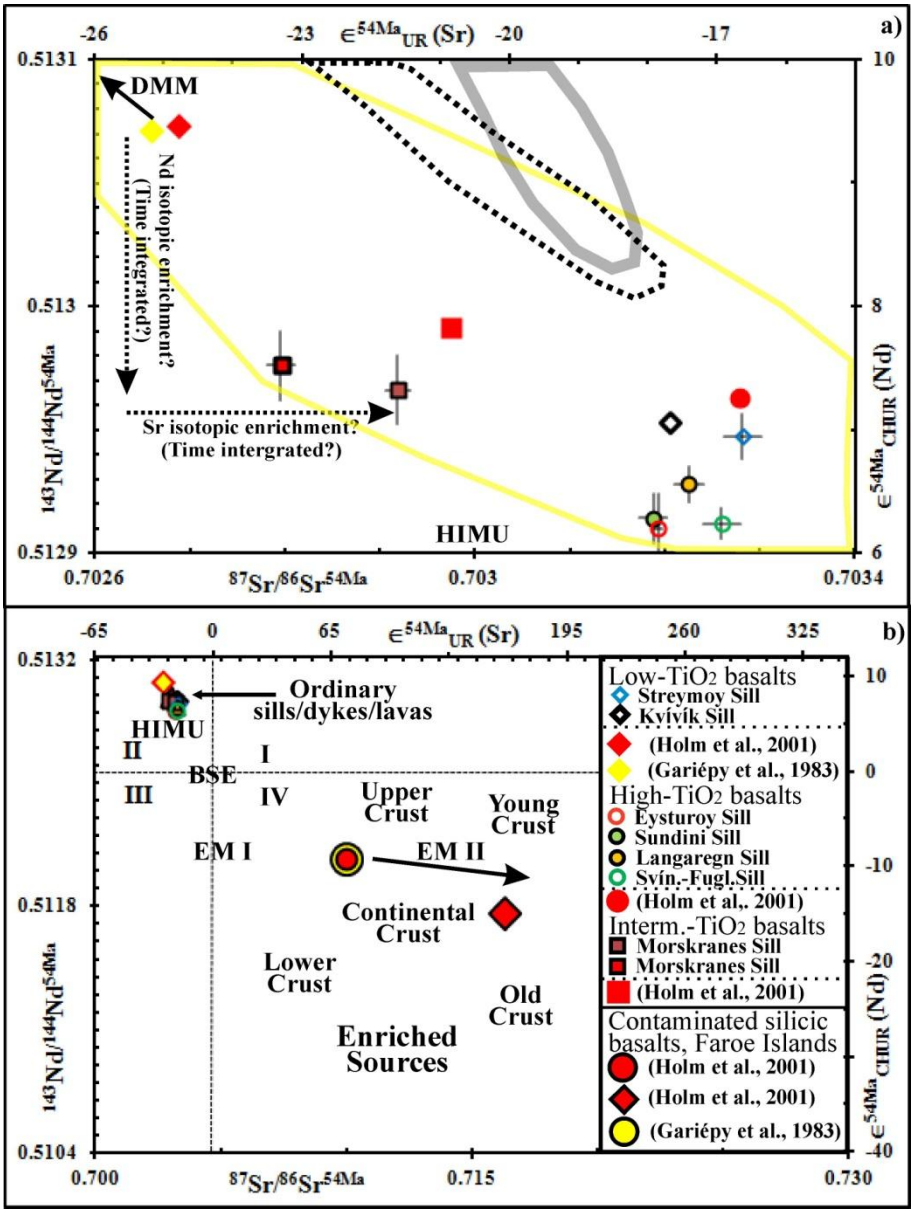

Figure 4.16. a) Age-corrected Sr versus Nd isotopic ratios representing sills and selected dykes/lavas of the Faroe Islands define a negative slope with samples apparently being concentrated in three clusters. Potential isotopic enrichments of depleted samples of the Morskranes Sill due to potential contamination with crustal material or in response to time-integrated enrichments (e.g. Anderson, 1982) are shown by dotted arrows. Yellow outline = field of other basalts of the Faroe Islands (Holm et al., 2001). Grey outline shows parts of the isotopic composition of Reykjanes Ridge MORB (Mertz and Haase, 1997). Dotted outline indicates parts of Theistareykir, Iceland (Stracke et al., 2003). b) Basalts from a) plot in II quadrant of a Sr versus Nd isotopic diagram while contaminated/silicic lava samples of the Faroe Islands plot in the IV quadrant, indicating the involvement of continental crustal material in the contamination process. Distribution of crustal material in the IV quadrant is from DePaolo and Wasserburg (1979). DMM, HIMU, BSE, EM I and EM II compositions are from Zindler and Hart (1986) and Hart (1988). Measured St. Dev. (Table 4.4) is indicated by shaded grey error bars in a). See text.

4.5.2. Sr and Nd isotopes

Representative samples from all sills of this study are analysed for Sr and Nd isotopes (Table 4.4). Relative to bulk silicate Earth (BSE), the Sr and Nd isotopic composition of the investigated sills define $\in^{54Ma}_{UR}$(Sr) values ranging from -6.40 to -23.30 and $\in^{54Ma}_{CHUR}$(Nd) values in the range from 6.67 to 7.94 (Table 4.4; Fig. 4.16). The sill samples from this study and some (supposed) uncontaminated dykes and lava flows from the literature define a broad linear negative slope that is roughly similar to trends representing the mantle array in a $^{87}Sr/^{86}Sr$ versus $^{143}Nd/^{144}Nd$ diagram (Fig. 4.16a). Combined, the sills themselves define two clusters (Morskranes Sill versus all the other sills) similar to those inferred for the Pb isotopes (Fig. 4.16a; Fig. 4 14). Three samples from silica-rich lava flows of the Faroe Islands that have been dealt with in earlier isotopic studies (Gariépy et al. 1983; Holm et al. 2001) all plot in the IV quadrant in a $^{87}Sr/^{86}Sr$ versus $^{143}Nd/^{144}Nd$ diagram (Fig. 4.16b), i.e. indicating significant degrees of crustal involvement.

Basalts of the Faroe Islands being affected by Sr and Nd isotopic contamination to any significant degrees are also relatively enriched with respect to SiO_2 compared to

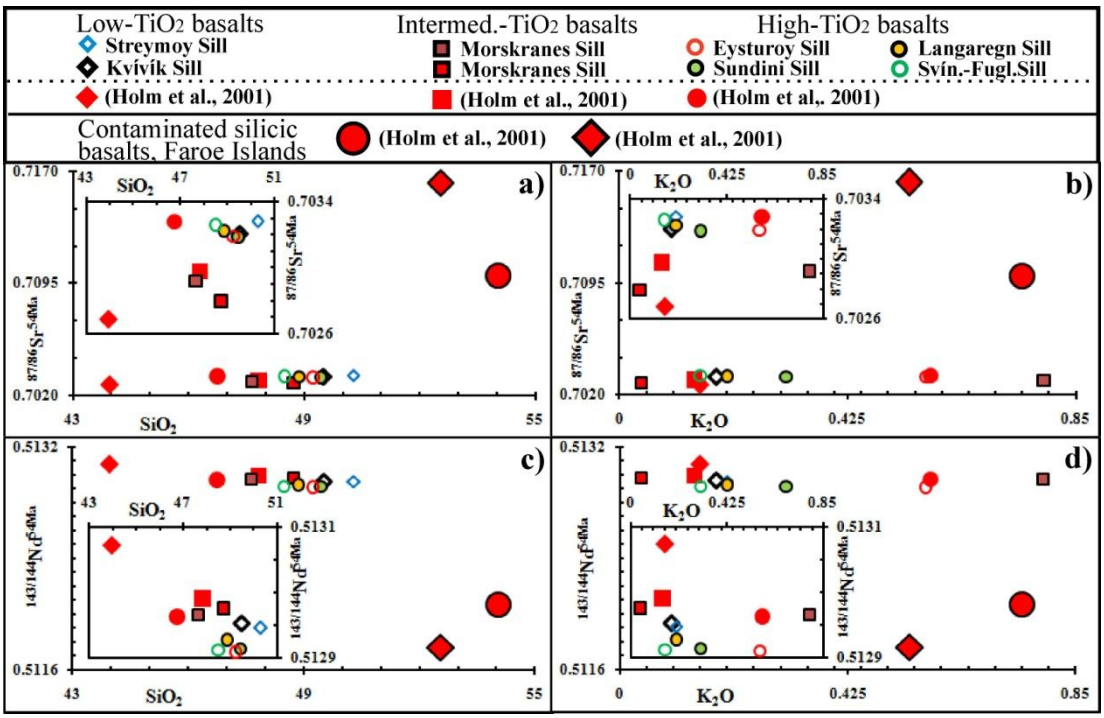

Figure 4.17. a) SiO_2 versus age-corrected Sr isotopes of sills and other selected basalts of the Faroe Islands. b) K_2O versus age-corrected Sr isotopes of sills and other selected basalts. c) SiO_2 versus age-corrected Nd isotopes of sills and other selected basalts of the Faroe Islands. d) K_2O versus age-corrected Nd isotopes of sills and other selected basalts. See text.

other less contaminated samples originating within the same area (Fig. 4.17a; Fig. 4.17c). The same is partly true for the K_2O content of these contaminated samples, but comparable K_2O enrichment of other basalt samples, which do not display clear signs of considerable isotopic contamination, are sometimes encountered as well (Fig. 4.17b; Fig. 4.17d). This is particularly true for the sample 08-JMS-17 of the Morskranes Sill (Brown square); which is more enriched in K_2O than any other basalt sample that has been encountered hitherto in the Faroe Islands.

Magmas being significantly enriched in K_2O (and Rb) may be the result of very small degrees of partial melting or they may represent the latest stages of melt evolution in consequence to their incompatible nature in silicate melts (e.g. Rollinson, 1998). However, as the other investigated samples from this relatively small sill are depleted with respect to K_2O and do not display any abnormal concentrations in other major elements (Table 4.2; Fig. 4.9), it is hard to envisage that they too could have been affected by any significant degrees of magma evolution. Also, if selective K_2O enrichment occurred in response to e.g. immiscibility or other late-stage melt processes, one would have expected that major elements such as SiO_2 or Na_2O in addition to incompatible trace elements other than Rb (e.g. Ba, Sr, Th etc.) would have been affected to some degree as well during potential magma evolution. Alternative explanations of K_2O (and Rb) enrichment in the sample 08-JMS-17 could be selective assimilation of K_2O/Rb – rich material with relatively short residence time, which resulted in moderate modifications of initial Sr and Nd isotopic compositions in the affected rocks (e.g. as indicated by dotted arrows in Fig. 4.16a), or the addition of K_2O/Rb could result from post-magmatic crystallisation of secondary minerals that scavenged these elements from other weathered basalts. However, as the sample 08-JMS-17 appears to be completely fresh without the faintest signs of microscopic joints, this latter option cannot be stated with any degree of certainty. Relative to samples showing obvious signs of contamination with crustal material, most ordinary basalts of the Faroe Islands display flat trends in plots of SiO_2 and K_2O versus Sr and Nd isotopes (Fig. 4.17). More detailed views of plots representing these ordinary basalts show scattered distributions in K_2O versus $^{87}Sr/^{86}Sr$ and K_2O versus $^{143}Nd/^{144}Nd$ diagrams (insets in Fig. 4.17b, Fig. 4.17d), but with a broad positive trend in the SiO_2 versus $^{87}Sr/^{86}Sr$ diagram (inset in Fig. 4.17a) and a broadly equivalent negative trend in the SiO_2 versus $^{143}Nd/^{144}Nd$ diagram (inset in Fig. 4.17c).

Hence, it appear as if the more evolved basalts of the Faroe Islands, i.e. specimens displaying slight relative enrichments in silica, in many cases also display slight relative enrichments in their Sr and Nd isotopic compositions.

4.5.3. Combined isotopes

Comparisons between different types of isotopes of the Faroe Islands, involving plots of measured Pb isotopes contrasted against age-corrected Sr and Nd isotopes, yield positive slopes for Pb versus Sr isotope ratios and Pb versus Nd isotope ratios define broadly equivalent negative slopes (Fig. 4.18). It is noteworthy that plots involving $^{208}Pb/^{204}Pb$ ratios (Fig. 4.18e; Fig. 4.18f) display well-defined linear slopes compared

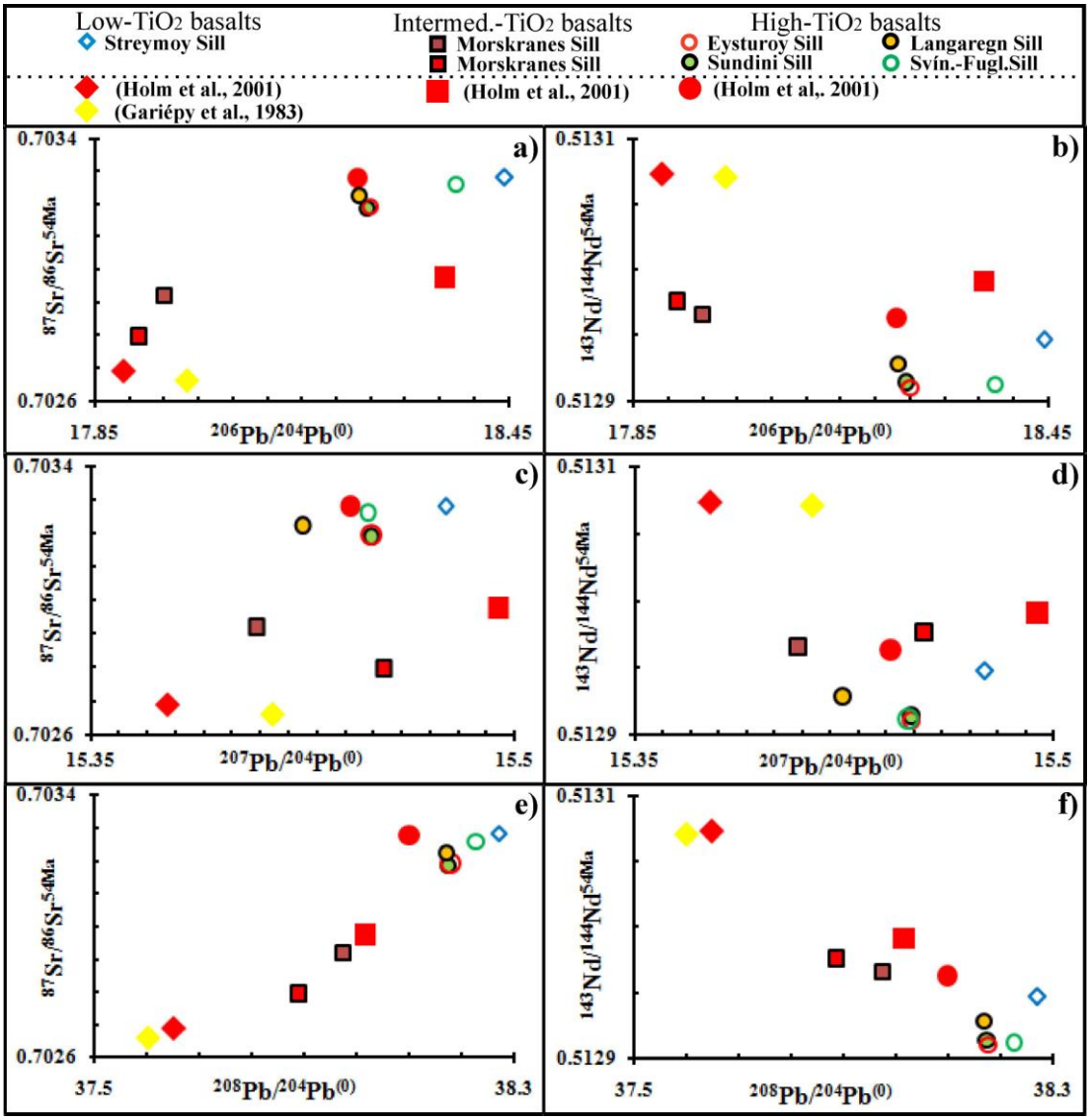

Figure 4.18. The plots show measured Pb isotope ratios versus age-corrected Sr and Nd isotopic ratios. See text.

to more scattered trends in the other diagrams displayed in Fig. 4.18. The fact that samples representing the Morskranes Sill (brown square and rhombus) plot amongst the most depleted basalts (red and yellow rhombuses) in Fig. 4.18a, define their own field in Fig. 4.18b, plot in-between depleted and more enriched basalts in Fig. 4.18c and Fig. 4.18e and plot amongst relatively enriched basalts in Fig. 4.18d as well as in Fig. 4.18f may suggest that the primary melts that ultimately gave rise to this sill were exposed to various degrees of isotopic influence.

4.6 Discussion

4.6.1. Element mobility

The reliability of geochemical data as petrogenetic indicators should be evaluated carefully, as post-magmatic mobilisation of major and/or trace elements and potential mineral break-down or recrystallisation at the whole-rock scale may affect igneous rocks under a variety of hydrothermal conditions (e.g. Rollinson, 1998). The major elements Si, Mg and K in addition to the large ion lithophile elements (LILE) may be mobilised by low-grade metamorphism/weathering (Wood et al., 1976; Higgins et al., 1985) whereas hydrothermal activity associated with moderate metamorphism has the potential of mobilising Si, Mg, Ca, Fe, Na, K and Mn as well as the LILE and perhaps some of the LREE (Ordóñez-Calderón et al., 2008). Trace elements such as the high field strength elements (HFSE) Th, Nb, Ta, Zr, Y and Ti are commonly considered to remain relatively unaffected during moderate metamorphic events (Wood et al., 1976; Ordóñez-Calderón et al., 2008).

In the Faroe Islands various degrees of weathering and/or or low-grade metamorphism have affected parts of the sills in question. The most common manifestation of element mobilisation in the investigated intrusions are the partial alteration (deuteric?) of minute olivine grains to phyllosilicates at the microscopic scale, but visually there is nothing in these samples that indicate element transport for distances greater than fractions of millimetres (Fig. 4.2 to Fig. 4.6). Hints of element mobilisation at scales of hand specimen and on microscopic scales are sometimes encountered in samples having experienced fracturing (Not used for geochemical interpretations), where thin (<0.5 mm wide) joints commonly display a greenish coating of low-temperature minerals derived from hydrothermal solutions. Comparison of geochemical compositions between rocks showing clear signs of element mobilisation in hand specimen (sample 07–JSS–38, shown in bold italic in

Table 4.2) and an apparently fresh and intact rock specimen (sample 09–JSS–02, Table 4.2), being collected ~100 metres apart, strongly suggest geochemical modification at the whole-rock scale for the first sample, which has resulted in relative depletion in Si, Al, K, Sr and Ba and relative enrichment in Mg, Fe, Ti and Y. Relative enrichment in e.g. Ti and Y may in this case well reflect relative stability of minerals such as oxides and/or clinopyroxene during the weathering process. Only samples showing a relatively high degree of geochemical correlation in most elements within each sill/region have been accepted for use in this study and all samples displaying signs of fracturing or element mobilisation at the whole-rock scale have been discarded.

4.6.2. Trace element constraints on potential crustal contamination

Apart from enrichments in some of the most incompatible elements, the trace element concentrations of the Morskranes Sill are virtually identical to those of N-MORB (Fig. 4.19a). In the other sills, compatible trace element concentrations of the low-TiO_2 sills and incompatible element concentrations of many of the high-TiO_2 sills resemble those reported for E-MORB (Fig. 4.19a). While negative Rb and K anomalies encountered in some sill samples could reflect geochemical characteristics inherited from their mantle sources, the clear positive anomalies in these two elements that are encountered in some of the investigated specimens (particularly sample 08-JMS-17) could in theory point to selective enrichment/contamination. Potential candidates that could have acted as enrichment sources include material from the upper crust (e.g. Fig. 4.14a) or perhaps metasomatic fluids containing elements leached from other adjacent basalts could be to blame (i.e. vesicle infillings). Comparison between presumed contaminated sill samples and various basement samples from neighbouring regions (Fig. 4.19b) indicates that a number of basement specimens have the potential to act as possible K and Rb contaminants.

The incorporation of crustal material into magmas en-route to the upper crust is commonly interpreted to result either from bulk assimilation with concomitant fractional crystallisation and/or from partial/net assimilation of fusible felsic material (Thompson et al., 1983; Kerr et al., 1995; Font et al., 2008). In the first case the mechanism involves heating of wallrocks in response to crystallisation from a near-stationary melt in a sub-spherical magma chamber (DePaolo, 1981) whereas turbulent flows of very hot magmas in dyke swarms are thought to provide the means

of heat for partial melting of wall-rocks in the latter case (Huppert and Sparks, 1985). The lack of any microprobe data on grains of unknown compositions, being encountered in the Morskranes Sill, is a substantial obstacle to correct interpretation with respect to their origin. If some of them do indeed represent assimilated material,

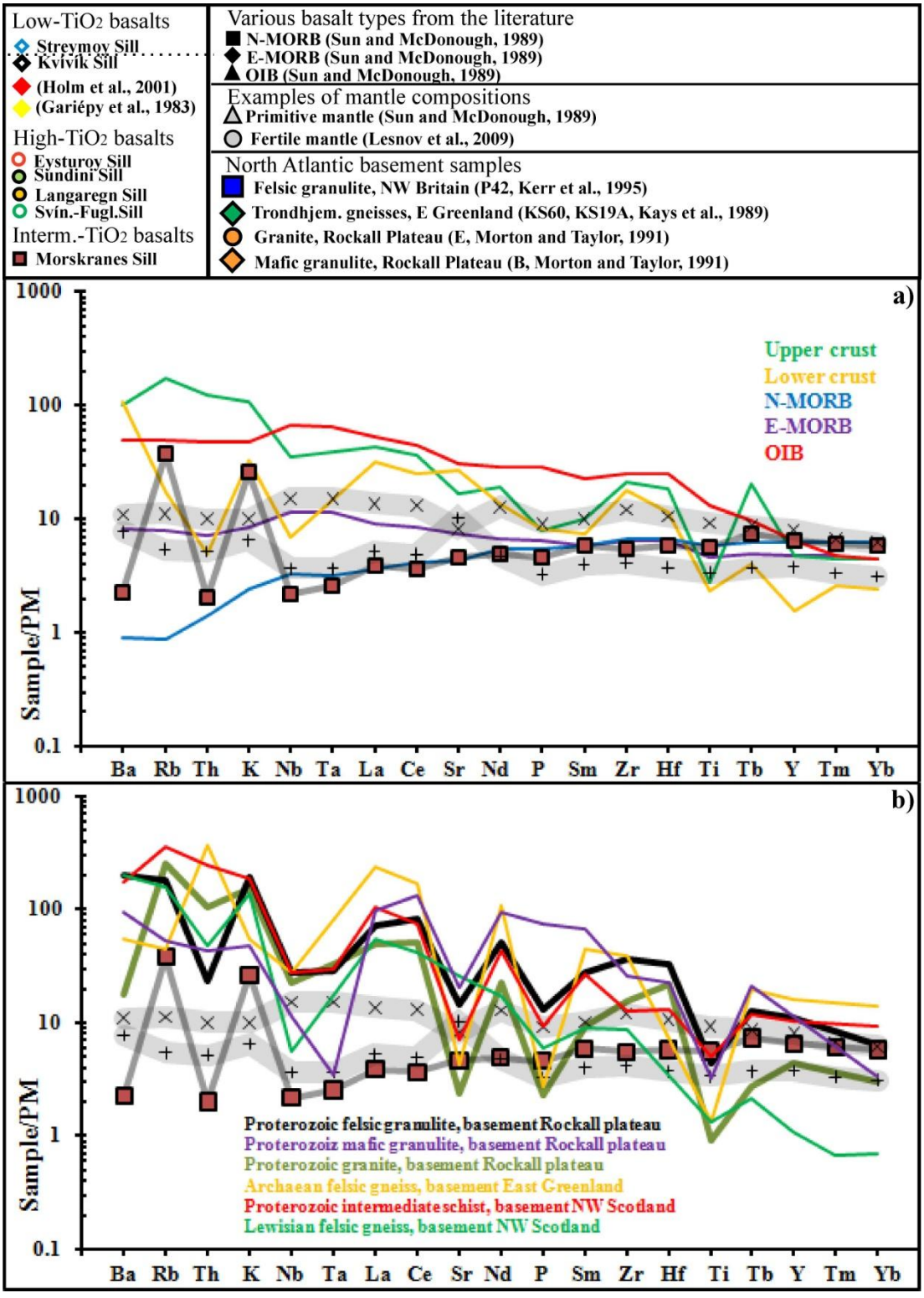

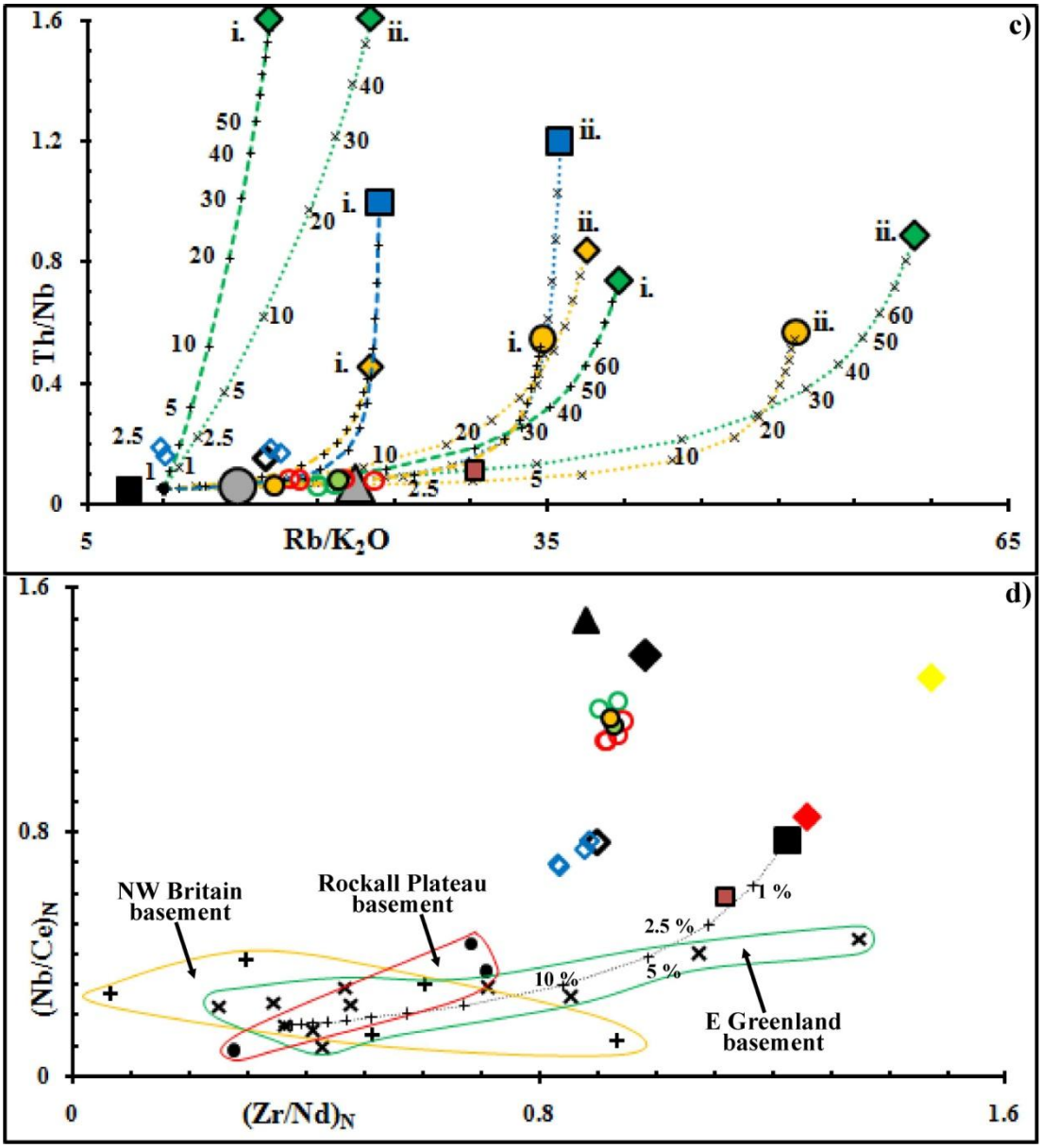

Figure 4.19. a) Trace element concentrations, normalised to primitive mantle values (Sun and McDonough, 1989), from representative samples of the sills of the Faroe Islands are contrasted against published examples of well known rock types. OIB, E-MORB and N-MORB concentrations are from Sun and McDonough (1989) whereas elemental concentrations from the upper and lower crust are from the compilation of Rollinson (1998). Upper and lower thick grey shaded lines represent high-TiO_2 and low-TiO_2 sills from this study respectively. Thinner grey shaded line indicates the Morskranes Sill (08-JMS-17). b) Representative sill samples are compared with basement samples from neighbouring regions. c) Two-component mixing between lowest common sill ratios (Rb/K_2O = 10 and Th/Nb = 0.05) and some of the basement samples that are indicated in 4.19b. Mixing hyperbolas labelled i. and ii. represent bulk assimilation and assimilation from 15% partial melts respectively. Partition coefficients used in partial melting calculations are from Table 4.5 (For rocks of intermediate/felsic compositions). Markers on hyperbolas indicate 1, 2.5, 5, 10, 20, 30 (and so forth) % basement contribution to the mixing. d) The Zr/Nd versus Nd/Ce ratios of the Morskranes Sill normalised to primitive mantle values could be recreated if N-MORB-like material was contaminated

with around 1% basement material comparable in composition to the average of basements from all regions of the N Atlantic. E Greenland basement from: Kays et al. (1989); Kalsbeek (1995); Thrane (2002). NW Britain basement from: Weaver and Tarney (1980); Thompson et al. (1986); Kerr et al. (1995); Meyer et al. (2009). Rockall Plateau basement from: Morton and Taylor (1991). (Results from modelling in Fig. 4.19c are shown in appendix 5.1). See text.

the common occurrences of sub-spherical specimen of these mineral grains could in theory point to mechanical abrasion, i.e. they could have been incorporated mechanically by bulk assimilation as discussed by DePaolo (1981). However, it may be hard to envisage that broadly sub-spherical forms of individual grains in e.g. dismembered sandstones or granulitic material would retain their original shapes when heated close to their solidus during assimilation. The common occurrences of plagioclase laths being wrapped around sub-spherical specimen of these minerals (e.g. Fig. 4.5c) seems to suggest that the plagioclases must have crystallised prior to a possible assimilation event. However, a scenario with vesicle expansion in partially molten magmas that oriented crystallised plagioclase laths is perhaps a more likely explanation of this phenomenon. If the poikilitic minerals of presumed feldspathic compositions encountered in the Morskranes Sill originate from wallrock assimilation, they could have been incorporated as tiny melt batches or the melting may have occurred subsequent to assimilation. Alternatively, these minerals may be of secondary origin (zeolites?) or they could represent late stage crystallisation phases from the basaltic magmas that gave rise to this sill.

As comparisons between data from representative sill samples and published data from basement material originating in E Greenland, NW Britain and the Rockall Plateau suggest that potential contamination was selective and primarily involved the incompatible elements K and Rb (Fig. 4.14b), a Rb/K_2O versus Th/Nb ratio diagram is utilised in an attempt to identify/quantify potential contamination (Fig. 4.19c). Due to similarities in their bulk partition coefficients, ratios of these elements are relatively insensitive to fractionation of plagioclase, olivine and clinopyroxene from basaltic melts and to partial melting in a peridotitic mantle. However, as the low field strength elements K and Rb may be mobilised by post-magmatic processes, calculations involving these elements should be interpreted with caution.

Calculations of two-component mixing between the lowest common ratios representing all the sills ($Rb/K_2O = 10$ and $Th/Nb = 0.05$) and the published data

from basement material have been carried out using the expression (Faure, 1986):

$$R_M = (R_A X_A f + R_B X_B (1 - f)) / (X_A f + X_B (1 - f)) \quad (7)$$

where R_M is the element ratio in a mixture of components A and B, R_A and R_B are the element ratios in A and B, X_A and X_B are the element concentrations in A and B and f is the weight fraction of A. Two sets of calculated mixing hyperbolas representing bulk assimilation and assimilation of melts extracted from ~15 % partial melts from the same basement samples are labelled i. and ii. respectively in Fig. 4.19c. Partial melting calculations of the basement samples were carried out assuming low and broadly similar Kd's of residual minerals and modal melting that leaved anhydrous residues (pyroxenes + plagioclase + quartz) using the expression (Rollinson, 1998):

$$C_L / C_0 = 1 / (D_{RS} + F(1 - D_{RS})) \quad (8)$$

where C_L is the wt% of a trace element in the produced liquid, C_0 is the wt% of a trace element in the original unmelted solid, D_{RS} is the bulk distribution coefficient of the residual solids and F is the weight fraction of melt produced in partial melting. Clearly, potential residual phases such as biotite (strongly partitioning K and Rb) or zircon (strongly partitioning Th and Nb) would affect the outcome of partial melting calculations according to potential differences in the partitioning of the elements making up the pairs Rb/K_2O and Th/Nb. However, as the modelling in Fig. 4.19c is merely an attempt to demonstrate the differences between bulk and partial/net assimilation of crustal material, modelled results should be interpreted with caution. As a result of the much larger concentrations of trace elements in the partial melts compared to the original unmelted basement rocks, only around ~2% assimilation of the 15% partial melt is required to match ~10% of bulk assimilation (Fig. 4.19c). In theory, crustal samples with geochemical compositions found in any of the regions NW Britain; Rockall Plateau and E Greenland could have contributed as contaminants, if an initial magma with a composition comparable to that of N-MORB is considered (Fig. 4.19c). In the case of the Morskranes Sill, ~15% of bulk assimilation of either granites or gneisses could explain the Rb/K_2O and Th/Nb ratios of this intrusion, whereas perhaps only ~3% of net contamination (with ~15% melts) of these same potential contamination sources are required to obtain the same results (Fig. 4.19c). As high field strength elements are not easily affected by post-magmatic processes, plots of the actual sill samples and relevant basement samples in a

Table 4.5. Partition coefficients used in calculations of batch-melting and fractional crystallisation.

	Ol	Opx	Opx	Cpx	Plag	Plag	Grt	Sp	Qtz
Sr	[a] 0.0050	[b] 0.0037	-	0.060	[c] 1.715	-	0.012	-	-
Nb	[a] 0.0005	[b] 0.0023	[g]0.800	0.005	[c] 0.029	[g]0.060	0.020	-	[e] 0.015
Th	[a] 0.0015	[b] 0.0010	[g]0.130	0.030	[c] 0.173	[g]0.048	[d] 0.010	-	[g]0.009
Ta	[e] 0.0010	[b] 0.0070	-	0.013	[c] 0.042	-	0.060	-	-
K	0.0068	0.0140	[g]0.002	0.038	0.170	[g]0.263	0.015	-	[g]0.013
Ti	0.0200	0.1000	-	0.400	0.040	-	0.300	-	-
Rb	0.0098	0.0220	[g]0.003	0.031	0.071	[g]0.048	0.042	-	[g]0.041
Ba	0.0099	0.0130	-	0.026	0.230	-	0.023	-	-
Zr	0.0120	0.1800	-	0.100	0.048	-	0.650	-	-
Y	0.0100	0.1800	-	0.900	0.030	-	9.000	-	-
La	[f] 0.0074	[f] 0.0100	-	[f] 0.056	[f] 0.180	-	0.001	2.25	-
Ce	0.0069	0.0200	-	0.092	0.120	-	0.007	2.15	-
Nd	0.0066	0.0300	-	0.230	0.081	-	0.026	2.00	-
Sm	0.0066	0.0500	-	0.500	0.067	-	0.290	1.65	-
Eu	0.0068	0.0500	-	0.474	0.340	-	0.243	1.05	-
Gd	0.0077	0.0900	-	0.556	0.063	-	0.680	-	-
Dy	0.0096	0.1500	-	0.582	0.055	-	1.940	-	-
Er	0.0110	0.2300	-	0.583	0.063	-	4.700	-	-
Yb	0.0140	0.3400	-	0.620	0.067	-	11.500	1.35	-

Unless otherwise stated, the partition coefficients for the different minerals are for melts of basaltic composition from Table 4.1 in the compilation of Rollinson (1998). [a]Partition coefficients (basalts) from Fig. 15C of Bédard (2005). [b]Partition coefficients (basalts) from Table 3 of Frei et al. (2009). [c]Partition coefficients (basalts) from Table 5 of Aigner-Torres et al. (2007). [d]Partition coefficient (basalts) from Table 1 of Berlo et al. (2004). [e]Interpolated values. [f]Extrapolated values. [g]Partition coefficients for felsic rocks from Table 4.3 in the compilation of Rollinson (1998). Qtz = quartz and Sp = spinel, the other mineral abbreviations are as in Fig. 4.9.

$(Zr/Nd)_N$ versus $(Nb/Ce)_N$ diagram may yield additional and perhaps more reliable information with respect to potential crustal contamination (Fig. 4.19d). If the initial mantle derived melts of the Morskranes Sill had trace element compositions comparable to those of N-MORB or other local depleted basalts (red circle), around 1.5% bulk assimilation of a basement contaminant possessing a composition roughly similar to the average of selected N Atlantic basement samples could explain the ratios of these trace elements within this sill (Fig. 4.19d). If potential contamination involved partial/net assimilation of material derived by ~15% melting of fusible crustal material instead, less than 0.5% assimilation would be required, as these (low-degree) melts would be enriched in the actual trace elements (e.g. Fig. 4.19c).

4.6.3. Isotopic constraints on potential crustal contaminants

It has been firmly established earlier that the enriched isotopic signatures of silicic basalts from the Enni Formation of the Faroe Islands originate from substantial

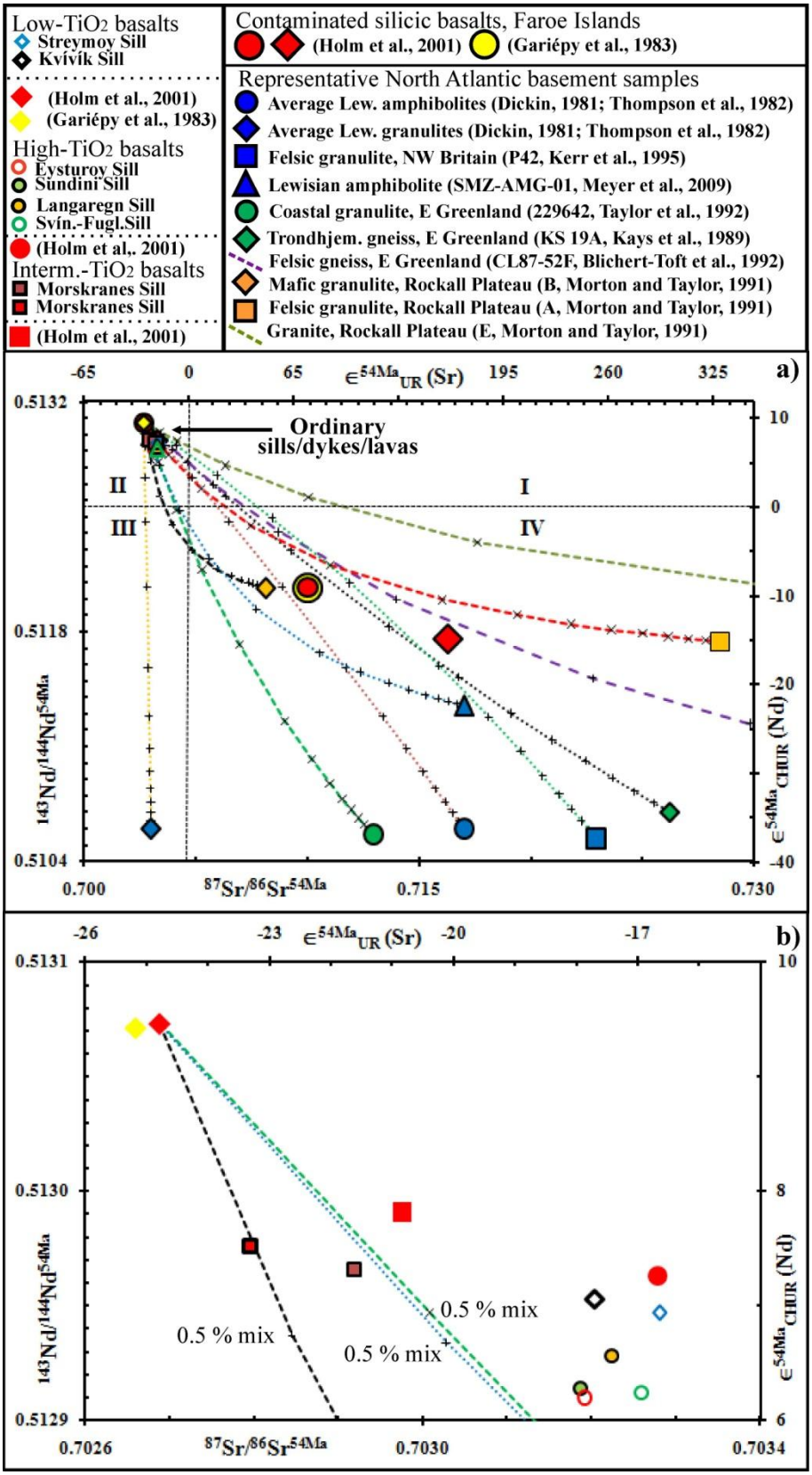

Figure 4.20. a) Two-component mixing calculated for contamination of an Early Cenozoic depleted basalt sample of the Faroe Islands with Proterozoic/Archean crustal basement samples from the North Atlantic. Crosses on dotted/dashed lines indicate 0.5, 1.0, 2.5, 5.0, 10.0, 20.0, 30.0.....90.0 % mixing of basalts with basement samples. b) Closer view of II quadrant from a). See text.

contamination with crustal material (Gariépy et al., 1983; Hald and Waagstein, 1983; Holm et al., 2001). Previous studies have suggested that basement material comparable in composition to Lewisian amhibolites best fit the observed isotopic characteristics of these lavas (Gariépy et al., 1983; Holm et al., 2001). Two-component mixing calculations (equation 7) involving representative Proterozoic/Archean basement samples/compositions from NW Britain, the Rockall Plateau and from E Greenland mixed with a depleted basalt sample utilised in this study and using age corrected $^{87}Sr/^{86}Sr$ versus $^{143}Nd/^{144}Nd$ ratios seem to suggest that a number of contamination sources have the potential to shift the compositions of these isotopes from those displayed by ordinary local basalts (i.e. not significantly contaminated) to those observed for the contaminated silicic basalts (Fig. 4.20). Of these basement samples, mixing lines from Lewisian amphibolite, felsic granulite from NW Britain, trondhjemitic gneiss from E Greenland, felsic gneiss from E Greenland and felsic granulite from the Rockall plateau most closely approach the plotted positions that represent the contaminated silicic basalts in Fig. 4.20a. In general, contribution of 10 to 20% of these basement samples can explain the isotopic range displayed by the silicic basalts plotting in the IV quadrant (Fig. 4.20a). If the LREE depleted samples from the Morskranes Sill initially possessed Nd isotopic composition comparable to those of other depleted basalts of the Faroe Islands (Red and yellow rhombuses), less than 0.5% contributions from contamination sources possessing isotopic compositions broadly similar to e.g. Lewisian amphibolites, coastal granulites from E Greenland or mafic granulites from the Rockall Plateau could account for the potential enrichments in the $^{143}Nd/^{144}Nd$ ratios of these samples (Fig. 4.20a; Fig. 4.20b). The enrichment in $^{87}Sr/^{86}Sr$ ratio of sample 08-JMS-17 relative to that of sample 08-JMS-14 (both samples belonging to the small Morskranes Sill, Table 4.4; Fig. 4.16a; Fig. 4.20b) may be an argument in favour of some Rb (and K) enrichment of the former sample perhaps from a felsic basement source (e.g. with $^{87}Sr/^{86}Sr$ ratios comparable to felsic gneiss/granulite or granite from E Greenland and/or the Rockall Plateau as shown in Fig. 4.20) upon ascent of the actual magmas, as might be indicated by petrographic observations (e.g. Fig. 4.5) and trace element characteristics (e.g. Fig. 4.12; 4.19). If the variations in Sr and Nd isotopic compositions within the more enriched sills (High-TiO_2 and low-TiO_2 sills) originated only from contamination with basement sources comparable to e.g. felsic rocks from E Greenland and/or the Rockall Plateau, less than 0.25%

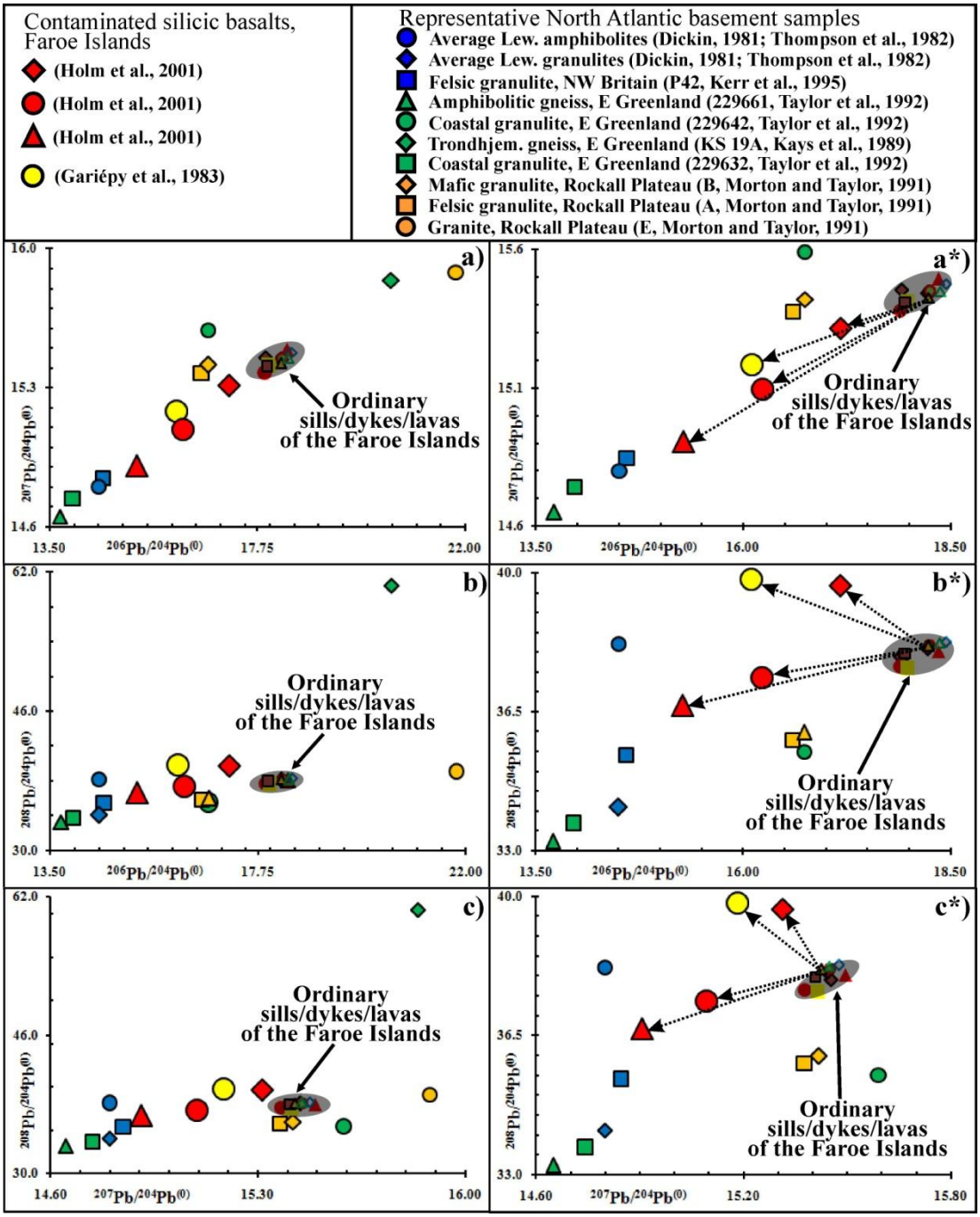

Figure 4.21. The Pb isotope ratios (measured) in the diagrams show potential relationships between various basalt samples of the Faroe Islands and Proterozoic/Archaean basement samples from the North Atlantic area. The notation "ordinary sills/dykes/lavas" refer to basalts that do not appear to be significantly contaminated. Enlarged views of the diagrams to the left (a, b and c) are shown in the diagrams to the right (a*, b* and c*). Dotted arrows indicate directions from ordinary basalts of the Faroe Islands toward the contaminated silicic basalt samples, i.e. toward potential contaminants as well, as mixing of Pb isotope ratios between any samples will always be defined by straight lines on these diagrams. Arrows in b*) and c*) strongly suggest two distinct contamination sources. See text.

contributions from these would be required in order to explain the observed isotopic range (Fig. 4.20b).

Comparisons between Pb isotopic compositions of relevant basement samples and basalt samples of the Faroe Islands yield a slightly more nuanced picture of potential crustal contamination processes when compared to the Sr and Nd isotopes. At a first glance, it appears as if basement samples from E Greenland and NW Britain best explain the shift in Pb isotope ratios of contaminated silicic basalts of the Faroe Islands (large red and yellow symbols) relative to the ordinary basalts (rocks that do not appear to be significantly contaminated) from this region (Fig. 4.21a; Fig. 4.21c; Fig. 4.21e). As two-component mixing between ordinary tholeiitic basalts and basement samples will produce straight mixing lines in Pb isotopic ratio diagrams, a more detailed inspection of relevant/potential contaminants suggests that none of the plotted basement samples from NW Britain or a combination of these can produce the whole span displayed by the contaminated basalts when mixed with ordinary basalts of the actual region due to their relatively low $^{208}Pb/^{204}Pb$ ratios (e.g. dotted arrows, Fig. 4.21b; Fig. 4.21d and Fig. 4.21f). However, most features of the contaminated samples could be explained, if the assimilated crustal material possessed Pb isotopic composition(s) close to average values of the selected E Greenland samples (Fig. 4.21). If the actual contaminants indeed possessed Pb compositions comparable to the average of the E Greenland samples, contributions from materials with Pb isotopic compositions comparable to that of the high $^{208}Pb/^{204}Pb$ basement specimen (green rhombus, Fig. 4.21) would have been an important factor in explaining the relatively high $^{208}Pb/^{204}Pb$ ratios of some of the contaminated samples (yellow circle and red rhombus, Fig. 4.21c; Fig. 4.21d; Fig. 4.21e; Fig. 4.21f). Also, some isotopic contribution from the relatively high $^{207}Pb/^{204}Pb$ sample (green circle, Fig. 4.21) could explain relatively high ratios of these isotopes in some of the contaminated basalts (yellow circle, Fig. 4.21a, Fig. 4.21b). A closer comparison/investigation of potential relationships between the Pb isotopic compositions of sills as well as selected lavas/dykes of the Faroe Islands and various basement samples from the North Atlantic area indicates that variations in Pb isotopic ratios of one sill sample in particular (red square with black outline), contrary to most of the other plotted ordinary basalts, covary with a basement sample from E Greenland (green circle, dashed arrows) and (but perhaps less likely) to two basement samples from the Rockall Plateau (Fig. 4.21; Fig. 4.22). Attempts to

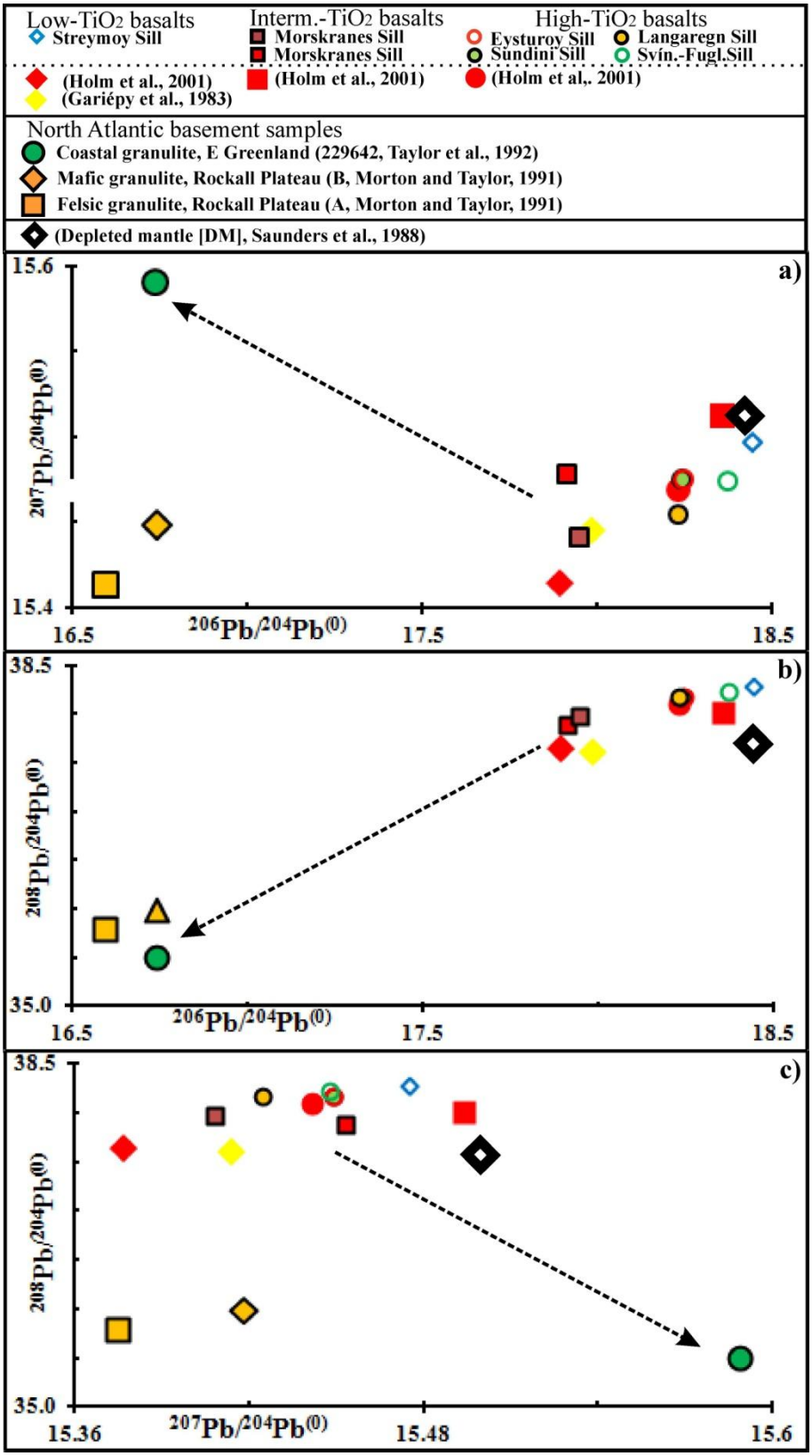

Figure 4.22. A sample from the Morskranes Sill vary relative to the other sill samples in Pb isotope ratio diagrams. Potential crustal contaminants include basement samples from the Rockall Plateau and a basement sample from E Greenland. Genetic links to DM could be an alternative explanation. Dashed arrows suggest directions to potential contaminants. See text.

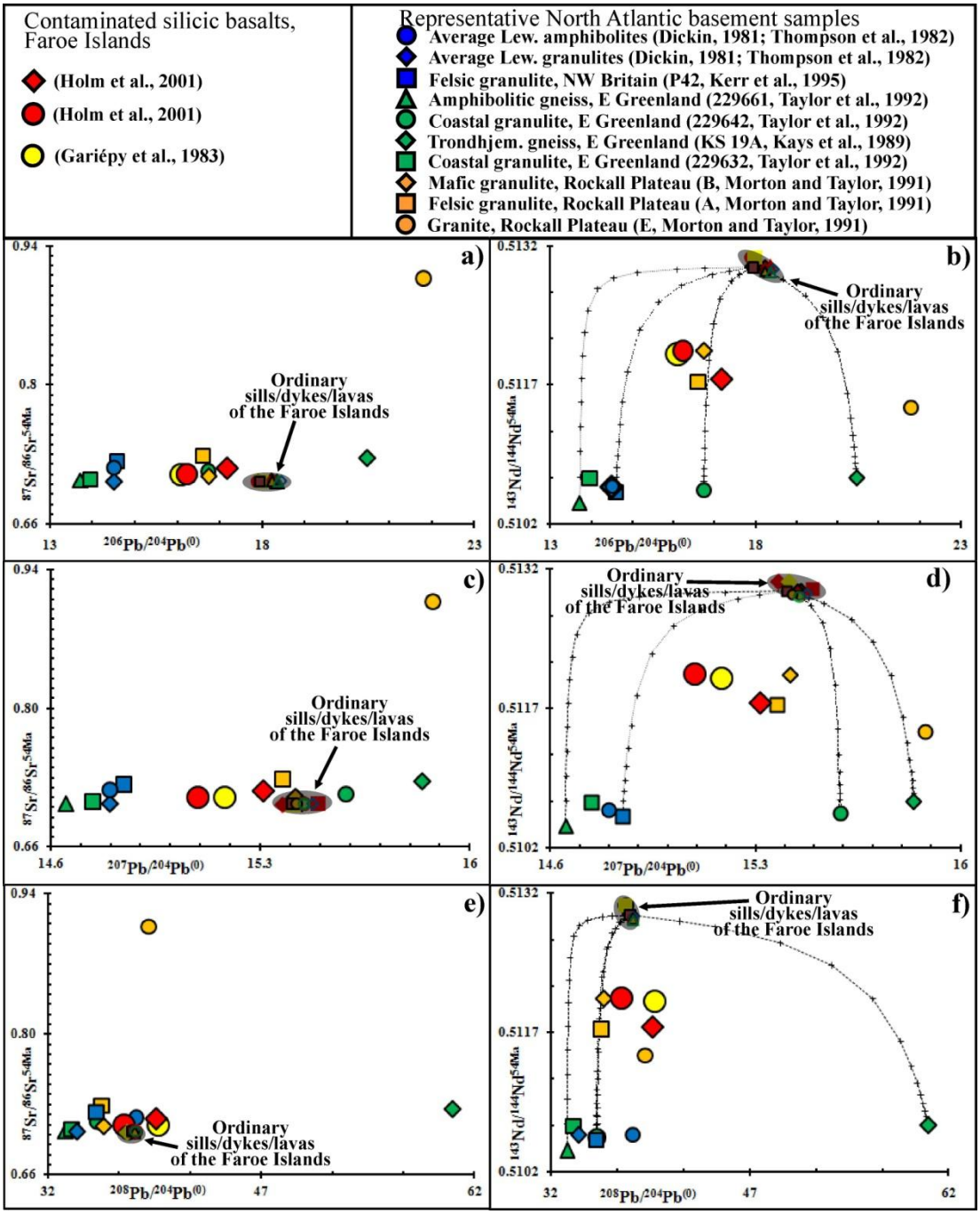

Figure 4.23. (Previous page) a), c) and e) Age-corrected $^{87}Sr/^{86}Sr$ ratios versus measured $^{206}Pb/^{204}Pb$, $^{207}Pb/^{204}Pb$ and $^{208}Pb/^{204}Pb$ ratios. b), d) and f) Age-corrected $^{143}Nd/^{144}Nd$ ratios versus measured $^{206}Pb/^{204}Pb$, $^{207}Pb/^{204}Pb$ and $^{208}Pb/^{204}Pb$ ratios and modelled mixing lines (at 10% intervals from basement samples). See text.

quantify any potential Pb contamination of this sample with the actual E Greenland basement sample have not been done (Fig. 4.22), but two-component mixing calculations involving $^{87}Sr/^{86}Sr$ and $^{143}Nd/^{144}Nd$ ratios strongly suggest that less than 0.5% contribution from this potential contaminant to more depleted basalts used in

this study would be required in order to explain such moderate isotopic variations (Fig. 4.20b). It is clear that one dyke sample (red square) covary closely with Atlantic depleted mantle (Fig. 4.22). Likewise, it is possible that the variations in Pb isotopes of the actual sill sample (red square with black outline) relative to the other sill samples could result from a particular link with a DM source instead of contamination with ancient basement material from E Greenland, although the latter option best explain the observed variations with respect to all Pb isotopes in question (Fig. 4.22).

Comparisons and mixing calculations (equation 7) between ordinary sill/dyke/lava samples and basement samples using age-corrected $^{87}Sr/^{86}Sr$ and $^{143}Nd/^{144}Nd$ ratios versus measured $^{206}Pb/^{204}Pb$, $^{207}Pb/^{204}Pb$ and $^{208}Pb/^{204}Pb$ ratios (Fig. 4.23) seem to support earlier inferences (e.g. Fig. 4.21) suggesting that involvement of crustal material comparable in isotopic composition to the average of the plotted E Greenland basement samples best explain the isotopic characteristics of some of the contaminated silicic basalts (particularly the yellow circle and red rhombus, Fig. 4.23). The apparent requirement for a basement component that is particularly enriched with respect to its Pb isotopes is well illustrated in Fig. 4.23b; Fig. 4.23e and Fig. 4.23f, where some contribution from a source comparable in isotopic composition to the sample represented by the green rhombus seems to be needed in order to explain high $^{206}Pb/^{204}Pb$ and $^{208}Pb/^{204}Pb$ ratios of some of the silicic basalts (particularly the yellow circle and red rhombus). Contamination of ordinary basalts of the Faroe Islands with material possessing isotopic composition comparable to a combination of basement samples from NW Britain could in theory explain the observed $^{87}Sr/^{86}Sr$ versus $^{206/204}Pb$ and $^{87}Sr/^{86}Sr$ versus $^{207}Pb/^{204}Pb$ ratios of all the contaminated basalts (Fig. 4.23a; Fig. 4.23c), but fail to account for the whole range in Pb isotopes of the silicic basalts in the other diagrams shown in Fig. 4.23. The calculated mixing lines between basement specimen from both E Greenland and NW Britain and ordinary (presumably uncontaminated) basalts from the actual region suggest contamination percentages in the range from 10 to 20%. Neither individual basement samples from the Rockall Plateau nor a combination of these can reproduce the isotopic compositions of the actual contaminated basalts upon mixing with ordinary basalts of the Faroe Islands (Fig. 4.23).

4.6.4. Partial melting

Although major elements may be useful in determining which processes led to compositional variations within individual basalt groups, the compositions of these elements alone are not likely to provide reliable evidences of all aspects of the petrogenetic processes that led to the formation of the investigated sills. In attempts to constrain degrees of partial melting and geochemical compositions of the primary melts that gave rise to the basalts of the Faroe Islands, batch melting modelling/calculations (equation 8) have been carried out using REE compositions from a wide array of relevant mantle sources and assuming residual mineral assemblages broadly similar to those commonly encountered during experimental melting of mantle lithologies to produce basaltic liquids (e.g. Gudfinnson and Presnall 1996; Kogiso et al. 1998). *Potential corrections of melting percentages from the partial melting modelling/calculations that may be relevant due to potential fractional crystallisation effects are dealt with in the fractional crystallisation sub-section below.* In the batch melting calculations used in this chapter it is assumed that the produced melts were in perfect equilibrium with the actual source region prior to their uninterrupted ascent as a closed system to distinct crystallisation chambers at shallower depths, while the real situation would probably have been one in which the melts migrated at finite rates and continuously interacted with the matrixes they passed through (e.g. Richter, 1986). However, earlier testing of simple batch melting scenarios (equation 8) against more real and complex melting/extraction/interaction processes have demonstrated that batch melting calculations involving trace elements do indeed provide reliable indications on actual degrees of partial mantle mantle melting in most cases (Richter, 1986).

Out of several potential mantle sources, partial melting of mantle sources with trace element compositions comparable to fertile spinel lherzolites from the sub-continental lithospheric mantle (SCLM), as reported by Lesnov et al. (2009), could explain much of the compositions of sills and lava flows displaying negative REE slopes (Fig. 4.24a). The calculations (Fig. 4.24a) suggest that the entire span in REE concentrations of these basalts can be recreated by ~4.5 to ~25% partial melting of a fertile spinel lherzolite, where samples displaying low REE concentrations (low-TiO_2 sills) can be linked to moderate/large degrees of melting (20 – 24%) in contrast to high REE samples (high-TiO_2 sills) that can be associated with lower degrees of melting (7 – 8%). Residual mineral assemblages used in the calculations shown in

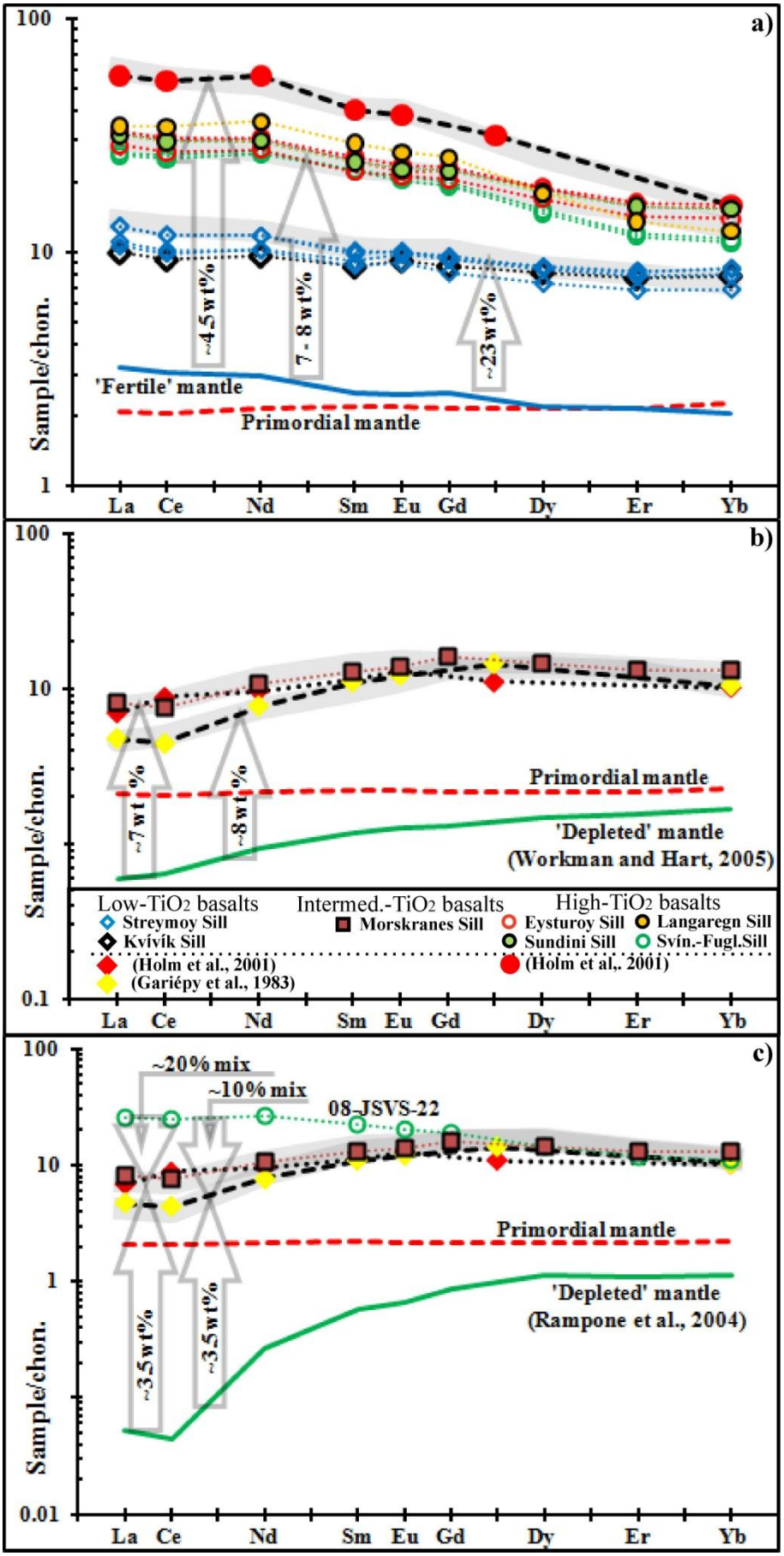
a)
100
10
1
Sample/chon.
~4.5wt%
7 - 8 wt%
~23wt%
'Fertile' mantle
Primordial mantle
La Ce Nd Sm Eu Gd Dy Er Yb
b)
100
10
0.1
Sample/chon.
~7wt%
~8wt%
Primordial mantle
'Depleted' mantle
(Workman and Hart, 2005)
Low-TiO2 basalts
Streymoy Sill
Kvívík Sill
(Holm et al., 2001)
(Gariépy et al., 1983)
Intermed.-TiO2 basalts
Morskranes Sill
High-TiO2 basalts
Eysturoy Sill
Sundini Sill
(Holm et al., 2001)
Langaregn Sill
Svín.-Fugl.Sill
La Ce Nd Sm Eu Gd Dy Er Yb
c)
100
10
1
0.01
Sample/chon.
~20% mix
~10% mix
08-JSVS-22
~3.5wt%
~3.5wt%
Primordial mantle
'Depleted' mantle
(Rampone et al., 2004)
La Ce Nd Sm Eu Gd Dy Er Yb

Figure 4.24. (Previous page). a) Compositions of most LREE enriched sills and lava flows (from Fig. 4.13) can be reproduced by 4.5 – 23% partial melting of a moderately fertile mantle of composition comparable to those reported by Lesnov et al. (2009) leaving residual assemblages of olivine + orthopyroxene ± clinopyroxene ± spinel ± garnet. (Results from modelling are shown in appendix 5.2). b) Compositions of LREE depleted sill and lava flow (from Fig. 4.13) can be recreated by 7 to 8% partial melting of a depleted spinel lherzolite of composition similar to the average values of depleted morb mantle (DMM) as reported by Workman and Hart (2005). (Results from modelling are shown in appendix 5.3). c) Alternatively, 3.5% partial melts originating from a depleted mantle, of composition similar to that reported by Rampone et al. (2004), mixed with 10 – 20% melts of compositions broadly similar to sample 08-JSVS-22 (open green circles) could potentially explain the depleted trends of some basalts of the Faroe Islands. Figures in open arrows indicate melt percentages and thick grey shaded lines indicate the calculated REE trends. Residual assemblages = olivine + orthopyroxene ± clinopyroxene. Partition coefficients (for mafic melts) used in the calculations are shown in Table 4.5. Dashed red line(s) = primordial mantle (Sun and McDonough, 1989); full blue line = fertile mantle (Lesnov et al., 2009); full green line(s) = depleted mantle (Workman and Hart, 2005; Rampone et al., 2004). Normalising values are as in Fig. 4.13. (Results from modelling are shown in appendix 5.4). See text.

Fig. 4.24a includes various combinations of the minerals: Olivine (75 – 85%) + orthopyroxene (15 – 25%) ± clinopyroxene (< 8%) ± spinel (< 2%) ± garnet (< 1%). Hence, the range in relative mineral abundances in these modelled residues are positioned well within the limits commonly encountered in naturally occurring peridotites (e.g. Obata and Morten, 1987; Choi and Kwon, 2005). Although trace amounts of garnet can be accommodated in the residue for a few of the modelled samples especially for the Langaregn Sill and samples of very high-TiO_2 lavas, these calculations also suggest that it is equally possible that olivine and pyroxenes were the only residual phases following partial melting to produce most of the investigated sills. As experimental melting of peridotites/pyrolites suggest residual garnets only at pressures higher than 2.6 to 3.0 GPa (Kushiro 1996; Robinson and Wood 1998; Kogiso et al. 1998), the modelling seem to suggest that most of the primary melts that gave rise to the basalts shown in Fig. 4.24a probably formed at ≤ 2.6 GPa i.e. within the spinel lherzolite stability field, but with some samples perhaps also straddling the lower limits of the garnet stability field.

The compositions of some of the LREE-depleted sills and lava flows of the Faroe Islands can be explained by moderate degrees (7 to 8%) partial melting of a depleted source (Fig. 4.24b) having composition broadly similar to the average values of

depleted MORB mantle (DMM) as reported by Workman and Hart (2005). Alternatively, these LREE-depleted basalts could have been generated by low degree (~3.5%) partial melting of a depleted source having a composition broadly similar to a spinel lherzolite recovered from an abyssal peridotite (Rampone et al. 2004), which left residues broadly similar to those produced by melting of the fertile lherzolites (Fig. 4.24c). However, the incorporation of some additional LREE-enriched material would have been required in order to compensate for a slight deficiency of these elements in the modelled melts. LREE-enriched crustal rocks could perhaps have acted as secondary sources to such potential melts, but ~10 to ~20% hybridisation with mantle-derived melts of compositions broadly similar to the high-TiO_2 sills (e.g. 08-JSVS-22) could also explain parts of the observed REE trends (Fig. 4.24c).

The relationships between the sills of the Faroe Islands and their inferred fertile versus depleted end-member sources are perhaps better illustrated in a $(Yb)_N$ versus $(Ce/Sm)_N$ binary diagram, where various degrees of melting of fertile and depleted sources are calculated for various residual assemblages and compared with sill and other basalt samples (Fig. 4.25). The modelled melting curves define distinct trends for individual residual mineral assemblages where the calculations suggest generation of the high-TiO_2 sills by low/moderate degrees melting of fertile mantle rocks compared to moderate/high degree melting of similar source rocks for the low-TiO_2 rocks (Fig. 4.25). Various degrees of melting of depleted mantle sources can generate the $(Ce/Sm)_N$ and $(Yb)_N$ variations observed in the LREE-depleted basalts (Fig. 4.25). However, all modelled melts from the most strongly depleted mantle material (Large grey rhombus) become exhausted with respect to $(Ce/Sm)_N$ ratios before the desired concentrations are encountered for melt percentages >1%, irrespective of the chosen residual mineral assemblages. Two-component mixing calculations (equation 7) involving $(Ce/Sm)_N$ ratios suggest that the differences between low-degree partial melts from the most depleted mantle source (large grey rhombus) and $(Ce/Sm)_N$ ratios representing the LREE-depleted samples from Fig. 4.13 can be matched by the addition of 5 to 20% melts of compositions similar to the high-TiO_2 sample 08-JSVS-22 (Fig. 4.25). In theory, infinitesimal melt percentages from melting of the strongly depleted mantle (Large grey rhombus) with garnet present in the residue could reach $(Ce/Sm)_N$ ratios comparable to the LREE-depleted basalts, but it is open to discussion whether this scenario would be realistic.

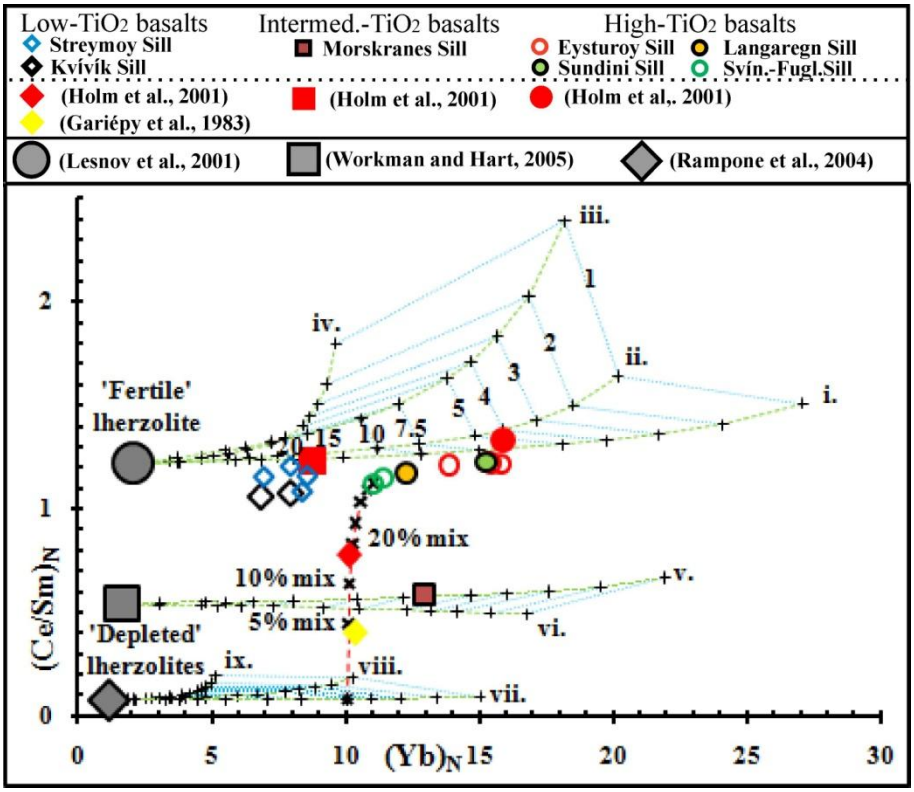

Figure 4.25. Partial melting calculations of a moderately fertile mantle (Large grey circle, Lesnov et al., 2009) versus a moderately depleted mantle (Large grey square, Workman and Hart, 2005) and a more strongly depleted mantle (Large grey rhombus, Rampone et al., 2004). Residual mineralogies used in calculations: Trend i. = 84% Ol + 16% Opx; trend ii. = 76% Ol + 24% Opx; trend iii. = 76% Ol + 20% Opx + 4% Cpx; trend iv. = 76% Ol + 23% Opx + 1% Grt; trend v. = 84% Ol + 16 Opx; trend vi. = 83% Ol + 15% Opx + 2% Sp; trend vii. = 84% Ol + 16% Opx; trend viii. = 80% Ol + 12% Opx + 8% Cpx; trend ix. = 80% Ol + 11% Opx + 8% Cpx + 1% Grt. Mineral abbreviations are as in Fig. 4.9 and Table 4.4. Melt percentages (numbers at blue dotted lines) increase from right to left. Melting intervals for depleted mantle (not labelled) are similar to those calculated for the fertile mantle. Mixing with ~5 to ~20% melts comparable in composition to high-TiO_2 sills from this study (red dashed line with black crosses) may be required in order to reproduce the LREE-depleted basalts from Fig. 4.13 (yellow/red rhombuses and brown square) if these initially resulted from low-degree melting of mantle material comparable in composition to the strongly depleted mantle reported by Rampone et al. (2004). Normalising chondrite values as in Fig. 4.13. Partition coefficients (mafic melts) used in the calculations are shown in Table 4.5. (Results from modelling are shown in appendix 5.5.i to 5.5.ix). See text.

Testing of the results from the REE modelling by means of plots where Zr concentrations are contrasted against Y/TiO_2 ratios support the inferences regarding formation of most sills by various degrees of melting of fertile mantle material (Fig.4.26). The observed variations in Y/TiO_2 ratios at relatively constant Zr concentrations within the high-TiO_2 sill group could result from a relative depletion

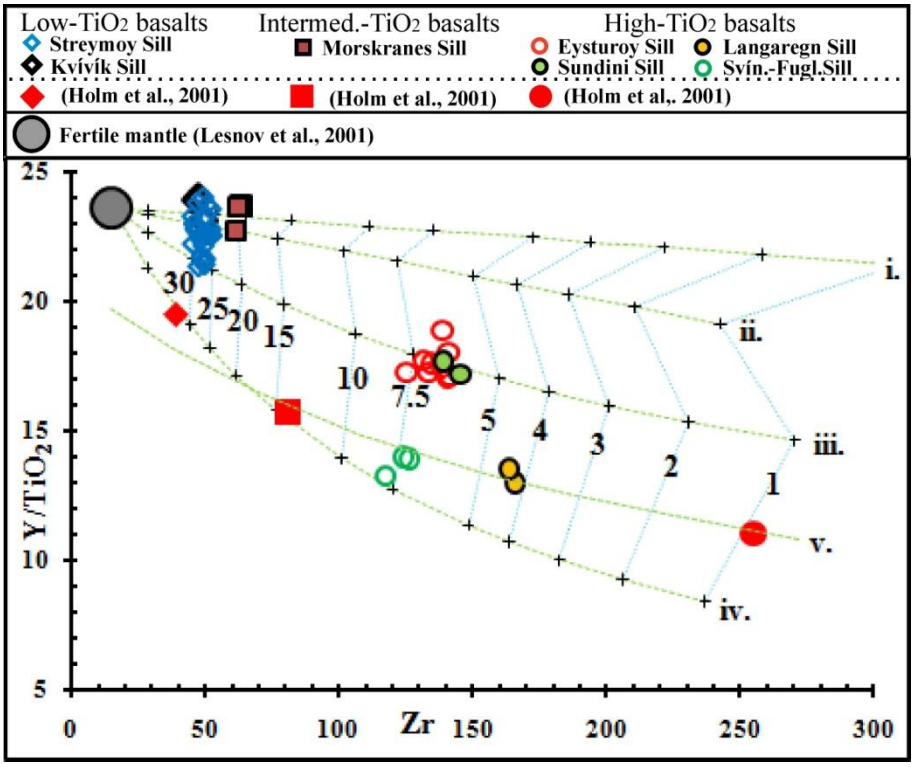

Figure 4.26. Partial melting of a fertile mantle (Large grey circle). Residual mineralogies used in the calculations are: Trend i. = 84% Ol + 16% Opx; trend ii. = 76% Ol + 24% Opx; trend iii. = 76% Ol + 16% Opx + 8% Cpx and trend iv. = 76% Ol + 19% Opx + 4% Cpx + 1% Grt. Trend v. is similar to trend iii, but is based on a lower Y/TiO_2 ratio in the source material. Mineral abbreviations are as in Fig. 4.9. Partition coefficients are shown in Table 4.5. Calculated melt percentages (numbers at blue dotted lines) increase from right to left. (Results from modelling are shown in appendix 5.6.i to 5.6.iv). See text.

of Y, which again could be indicative of residual garnet following partial mantle melting or the involvement of garnet during fractional crystallisation. In the case of the Langaregn Sill, the low Y/TiO_2 ratios shown in Fig. 4.26 could be related to the relatively pronounced HREE depletion observed for this sill (Fig. 4.13c). Alternatively, the variations in Y/TiO_2 ratios displayed by some of the sill/lava samples from the Faroe Islands could reflect partial melting along two distinct sub-parallel trends (i.e. along melting curves iii. and v. in Fig. 4.26) due to slight differences in Y/TiO_2 ratios of their respective mantle sources.

The pronounced negative/positive Sr anomalies and weak negative/positive Eu anomalies, best observed in the Eysturoy and Sundini sills versus the Streymoy and Kvívík sills (Fig. 4.12 and Fig. 4.13 respectively), suggest the involvement of plagioclase at some point during their magmatic evolution. Calculations (not shown) indicate that even very small volumes of residual plagioclase (< 5%) during partial

melting of fertile lherzolitic source rocks will produce conspicuous negative Eu anomalies in normalised diagrams, which is at odds with the trends observed in Fig. 4.13. Also, the overall tholeiitic nature of the sills in question seems to suggest primary magma formation by partial melting outside the plagioclase stability field, in accordance with results from experimentally produced basalts (e.g. Kushiro 1996; 2001). Alternatively, the observed Sr and Eu anomalies (Fig. 4.12; Fig. 4.13) could be primary features resulting from partial melting of plagioclase-free sources possessing "ghost" plagioclase signatures inherited from earlier geologic events, as proposed for basaltic rocks from Hawaii (e.g. Sobolev et al., 2000). However, such "ghost" signatures would require the involvement of substantial proportions of subducted/recycled crustal material during mantle melting (Sobolev et al., 2000) and the overall low Pb isotopic ratios in sills from this study (Table 4.4, Fig. 4.14) are not in accordance with typical (higher) Pb isotopic ratios encountered in basalts thought to result from melting of mantle sources contaminated with recycled oceanic crust, i.e. containing clear HIMU signatures as demonstrated in the compilation of Rollinson (1998) and in the recent study of Day et al. (2010).

Although the observed relative abundances of most major elements in high-TiO_2 versus low-TiO_2 sills seem to support the trace element modelling suggesting formation of these two main sill groups by different degrees of melting, the higher Al_2O_3 and lower Fe_2O_3 contents in the low-TiO_2 Streymoy and Kvívík sills relative to those of the high-TiO_2 Eysturoy and Sundini sills (Fig. 4.9) seem to be at odds with high or moderately high degrees of melting during formation of the low-TiO_2 sills compared to low degrees of melting during formation of the high-TiO_2 sills, as relative abundances of Al_2O_3 and FeO_{tot} in experimentally produced basalts are expected to decrease and increase respectively during increased degrees of melting (Table 1.1; Fig.1.5).

Hence, an additional mechanism seems to be required in order to fully explain this apparent inconsistency in Al_2O_3 and Fe_2O_3 compositions measured for the high-TiO_2 Eysturoy and Sundini sills versus those measured for the low-TiO_2 Streymoy and Kvívík sills (Fig. 4.9) as well as the common occurrences of Sr and Eu anomalies within these sills (Fig. 4.12; Fig. 4.13).

4.6.5. Fractional crystallisation

The geochemical spread observed in flood basalts might reflect differences in e.g. percentages of mantle melting, but fractional crystallisation too has a significant potential to modify geochemical compositions of basaltic melts and MgO-rich primary basaltic magmas typically evolve to other less magnesian basalt varieties by olivine fractionation (Hald and Waagstein, 1991; Yaxley, 2000). In order to investigate to what degree fractional crystallisation processes affected trace element compositions of the investigated sills, calculations/modelling have been carried out using the expression for Rayleigh fractionation (Rollinson, 1998):

$$C_L / C_0 = F^{(D-1)} \quad (9)$$

where C_L is the wt% of a trace element in the residual liquid, C_0 is the wt% of a trace element in the parental liquid, D is the bulk distribution coefficient of the fractionating assemblage during crystal fractionation and F is the fraction of remaining melt. Rayleigh fractionation infers effective removal of newly formed crystals from residual melts without significant incorporation of new material from external sources i.e. wallrock assimilation or additional magma injection. Earlier studies have pointed to potential evolution of magmas by complex periodical replenishment/tapping/fractionation (RTF) processes (O'Hara and Mathews, 1981). However, while Larsen and Pedersen (2009) suggested that Early Cenozoic high-TiO_2 basalts from W Greenland evolved by RTF processes from contemporary low-TiO_2 basaltic melts, based on his study of trace element compositions of flood basalt sequences within the Deccan Traps Cox (1988) came to the conclusion that there was no proof to suggest that continental flood basalts (CFB) should evolve via RTF processes.

Plots representing Sr/Nb versus Eu/Eu* (Chondrite normalised) ratios of the sills from this study support inferences suggesting the involvement of plagioclase during evolution of these intrusions (Fig. 4.27). If normalised Eu/Eu* ratios of ~1 are used as estimates of basaltic melts that are unaffected by the activity of plagioclase, both fractionation and accumulation of this mineral seem to be required in order to explain the entire range in Eu/Eu* ratios defined by these sills (Fig. 4.27). Calculations of plagioclase fractionation and accumulation (Equation 9) from the average Sr/Nb versus Eu/Eu* ratios between the high-TiO_2 sample 08-JES-11 and the low-TiO_2 sample 07-JSS-52 (i.e. ~45 versus ~1) suggest that 20 to 25 wt% plagioclase

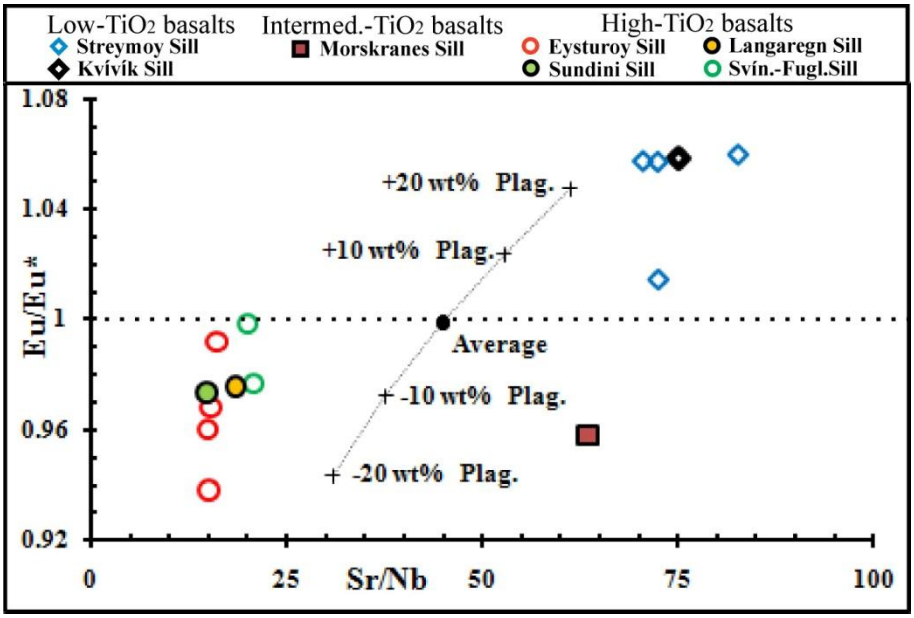

Figure 4.27. The plots of high-TiO_2 versus low-TiO_2 sill in a Sr/Nb versus Eu/Eu* (Normalised to chondrite values of Nakamura, 1974) ratio diagram seem to suggest both plagioclase fractionation and accumulation respectively. The starting ratios (~45 versus ~1) for the modelling represents a broad average between the two samples of the Eysturoy and Streymoy sills respectively that most closely approach an Eu/Eu* ratio of 1. Partition coefficients used in calculations are shown in Table 4.5. (Results from the modelling are shown in appendix 5.7). See text.

fractionation and accumulation from these starting ratios would be required to cover the span in Eu/Eu* ratios displayed by the high-TiO_2 and the low-TiO_2 sills respectively (Fig. 4.27). However, 20 to 25 wt% of fractionated/accumulated plagioclase using the partition coefficients for basaltic melts shown in Table 4.5 fail to reproduce the observed span in Sr/Nb ratios of high-TiO_2 versus low-TiO_2 sills (Fig. 4.27), suggesting that either different degrees of partial melting (as suggested previously) and/or differences in the concentrations of these two elements in the respective mantle sources to these two sill groups generated the observed gap in their Sr/Nb ratios. Clearly, the Morskranes Sill does not fit in with the other sills, probably because it is derived from quite different source material as suggested earlier.

The weak negative Eu anomalies of chondrite normalised REE samples representing the high-TiO_2 intrusions of this study (Fig. 4.13) can be reproduced by ~20 wt% fractional crystallisation of plagioclase from parental melts that display smooth REE trends (Fig. 4.28), while moderate/large degrees (15 to 20 wt%) of olivine or clinopyroxene fractionation from basaltic liquids (not shown) would not result in any noticeable Eu anomalies. Around 20 wt% plagioclase fractionation from liquids

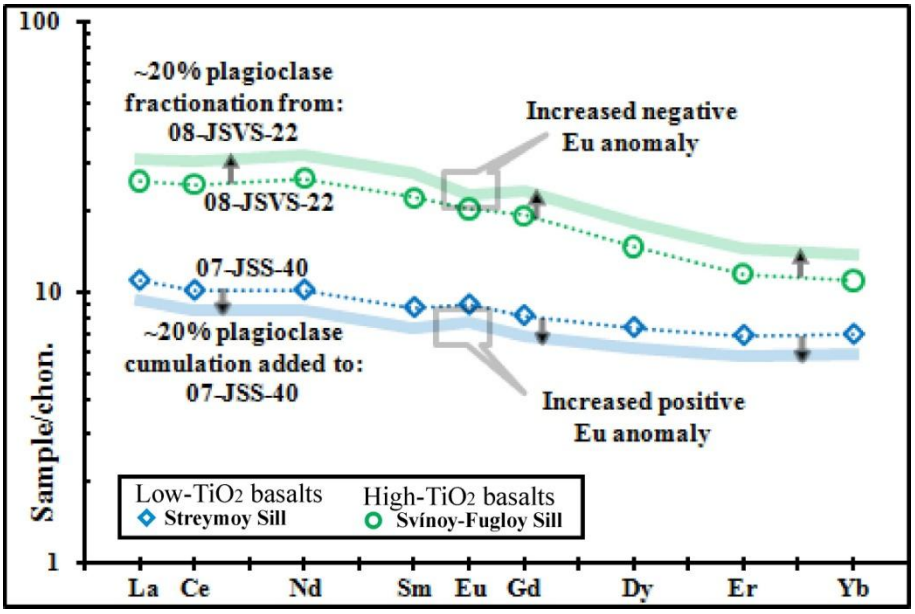

Figure 4.28. Plagioclase fractionation (~20 wt%) from a high-TiO_2 basaltic liquid would result in an overall increase in REE concentrations and a weak negative Eu anomaly in the residual melts (Bold green semi-transparent line). Net plagioclase accumulation (~20 wt%) from an external source into a low-TiO_2 basaltic liquid would result in an overall decrease in REE concentrations and a weak positive Eu anomaly in the cumulate-bearing melts (Bold blue semi-transparent line). Normalising values are as in Fig. 4.13. Partition coefficients are shown in Table 4.5. (Results from modelling are shown in appendix 5.8). See text.

REE compositions broadly similar to those of high-TiO_2 sills like the sample 08-JSVS-22 would generate an overall increase in their REE sample/chondrite ratios of 6 to 8, i.e. corresponding to a change/increase in REE concentrations that would be produced if these melts were generated by 2 – 3% lower degrees of melting of the same sources (Fig. 4..13; Fig. 4.28). The slight positive Eu anomalies displayed by the low-TiO_2 sill samples could be explained by a net addition/accumulation of ~20 wt% plagioclase from an external source to parental melts possessing relatively smooth REE trends (Fig. 4.28). The addition of ~20 wt% plagioclase to melts having REE compositions broadly similar to those of low-TiO_2 sills like the sample 07-JSS-52 would lower their overall REE sample/chondrite ratios of 1 to 2 i.e. corresponding to the change/decrease in these elements that would be associated with 2 – 3% higher degrees of melting of the same sources (Fig. 4.13; Fig. 4.28).

Calculations/modelling (not shown) indicate that fractional crystallisation of ~15 wt% olivine will generate an overall increase in REE concentrations similar to what would be associated with a similar amount of plagioclase fractionation, when Eu is not included (e.g. Fig. 4.28). Consequently, ~20 wt% fractionated olivine should

result in an increase/change in REE concentrations similar to what would be associated with 2 – 3% lesser degrees of partial melting of the same source, meaning that this figure would be 1 – 1.5% for 10 – 15wt% fractional crystallisation of this mineral.

The results from the REE modelling in Fig. 4.27 and Fig. 4.28 have been further tested by means of binary plots of representative sill samples with Nb concentrations being contrasted against Ta, Th, Eu and Sr concentrations where calculations involving both partial melting (equation 8), fractional crystallisation and accumulation (equation 9) have been utilised in order to get a more detailed knowledge about the processes that were active during magma genesis (Fig. 4.29). The configurations of the plotted sill samples in the four diagrams suggest that they perhaps may be further sub-divided according to two distinct melting trends. Combined plots of samples from some of the relatively small sills from this study (The Langaregn, Svínoy-Fugloy and Morskranes? sills) define the first trend i., which display linear trends indicated by thin black dotted lines that are sub-parallel to calculated melting trends (Large grey open arrows labelled with melt percentages and shown on the left side of all part-figures) on the diagrams in Fig. 4.29. Combined plots of samples that represent the larger high-TiO_2 sills (The Eysturoy and Sundini sills) and the larger low-TiO_2 sills (The Kvívík and Streymoy sills) define the second trend ii., which display linear trends shown as thin black dashed lines being sub-parallel to both calculated melting trends and the trends of the first group in the Nb versus Ta and Th diagrams (Fig. 4.29a; Fig. 4.29b). However, when compared to the trends representing the calculated partial melting as well as those that represent the first trend i., the trend representing the second trend ii. displays a slight clockwise rotation in the Nb versus Eu diagram (Fig. 4.29c) and a conspicuous anticlockwise rotation in the Nb versus Sr diagram (Fig. 4.29d). The fixed configurations of the first trend i. relative to calculated partial melting trends in all diagrams of Fig. 4.29 seem to suggest that if these sills experienced fractional crystallisation following their genesis by partial melting; it affected them all in broadly similar proportions. Fractional crystallisation calculations show that fractionation trends for minerals common in typical basalts such as olivine and clinopyroxene are sub-parallel to the calculated partial melting trends for all the elements used in the diagrams of Fig. 4.29. Consequently, fractional crystallisation of only olivine or clinopyroxene cannot explain the rotation of linear trends representing the second trend ii. relative to

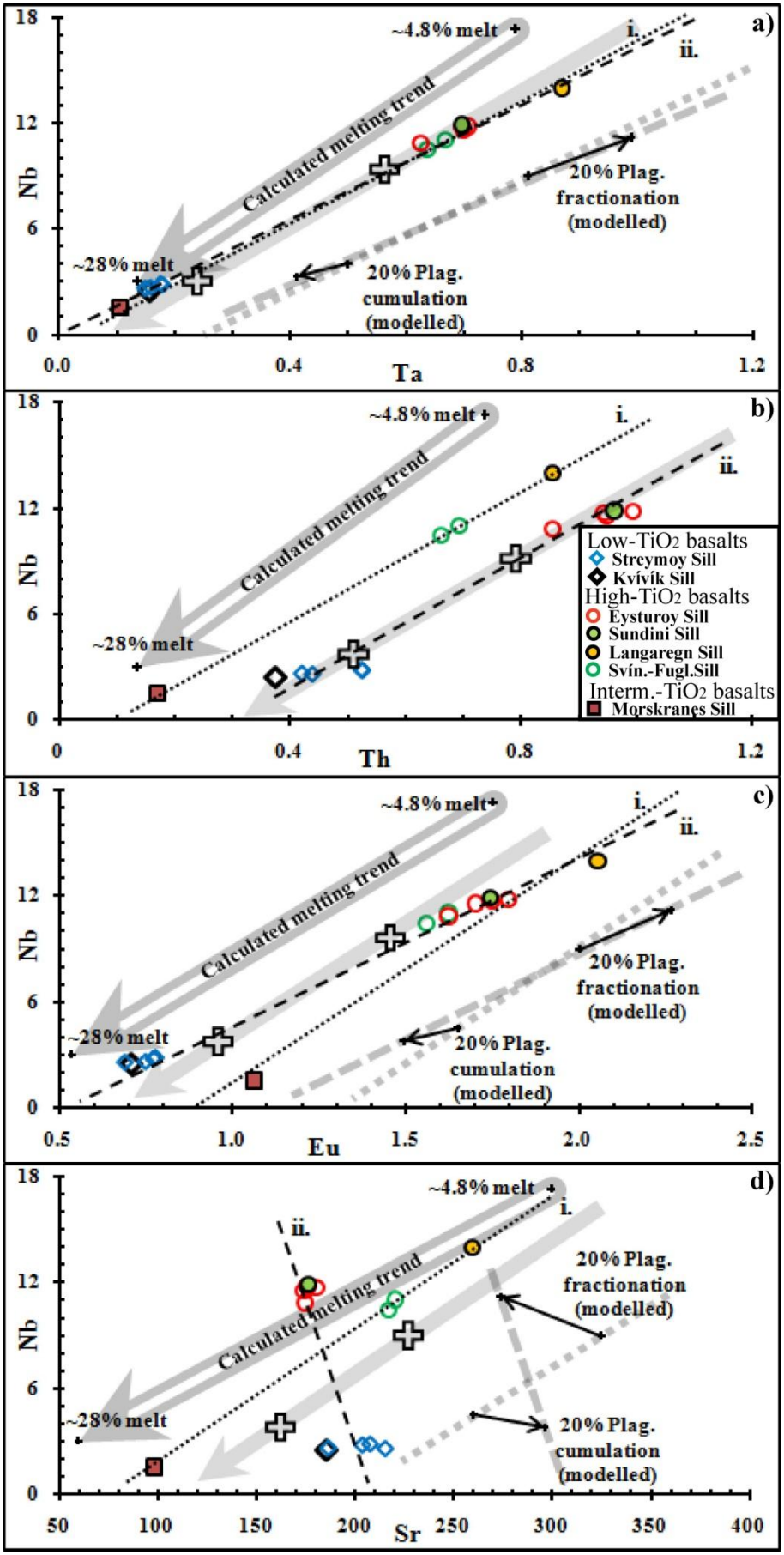
a)
~4.8% melt
i.
ii.
Calculated melting trend
20% Plag. fractionation (modelled)
~28% melt
20% Plag. cumulation (modelled)
Nb
Ta
b)
Low-TiO2 basalts
Streymoy Sill
Kvívík Sill
High-TiO2 basalts
Eysturoy Sill
Sundini Sill
Langaregn Sill
Svín.-Fugl.Sill
Interm.-TiO2 basalts
Mørskranes Sill
Th
c)
Eu
d)
Sr

Figure 4.29. (Previous page). Thick open grey arrows shown on left side of all diagrams indicate 4.8 to 28% calculated partial melting with residual mineral assemblages: 76% Ol + 16% Opx + 8% Cpx (Mineral abbreviations are as in Fig. 4.9). Initial elemental concentrations used in partial melting calculations of Nb = 0.85 ppm; Ta = 0.04 ppm; Th = 0.038 ppm; Eu = 0.17 ppm; Sr = 17 ppm are encompassed by analyses of samples 1 – 6 encountered in fertile spinel leherzolites (Lesnov et al., 2009). The sill samples can be categorised into trend i. (thin black dotted lines) and trend ii. (thin black dashed lines) according to the configurations of their plots on all diagrams. Lines representing trend i. are sub-parallel to the calculated melting trends on all diagrams whereas this is true for trend ii. in diagrams shown in a) and b) only. Trend ii. displays a slight clockwise rotation in the diagram shown in c) and a conspicuous anticlockwise rotation in the diagram shown in d) relative to trend i. and relative to the calculated melting trends. Calculations shown to the right in diagrams a), c) and d) indicate that high-TiO_2 sills (high Nb) of trend ii. could have evolved by ~20 wt% plagioclase fractionation whereas low-TiO_2 sills (low Nb) could have evolved by ~20 wt% net accumulation from an external source from/to their respective primary melts. The bold grey dotted lines that indicate trends chosen to represent parental melts, from which fractionation/accumulation of plagioclase are calculated, are sub-parallel to the thin dotted lines representing trend i. and to the calculated melting trends on the actual diagrams. Bold grey dashed lines connecting the points that resulted from calculated fractionation/accumulation of plagioclase are parallel to the black thin dashed lines representing trend ii. on the actual diagrams. The presumed initial concentrations of parental melts to sills in trend ii. are indicated by large open crosses and the presumed melting trends of their parental melts are indicated by thick grey shaded arrows. Partition coefficients used in the calculations are shown in Table 4.5. (Results from modelling are shown in appendix 5.9). See text.

calculated partial melting trends in the Nb versus Eu and Sr diagrams. Calculated trends representing fractional crystallisation of plagioclase are sub-parallel to the calculated partial melting trends in the Nb versus Ta and Th diagrams (vector shown in the right side of Fig. 4.19a only), but relative to the calculated melting trends calculated trends from fractionation of plagioclase display a slight clockwise rotations in a Nb versus Eu diagram and a considerable anticlockwise rotation in a Nb versus Sr diagram (calculated vectors shown to the right in Fig. 4.19c and Fig. 4.19d). Hence, the involvement of plagioclase seems to offer a satisfactory explanation with respect to the trends of the second group ii. in Fig. 4.19. However, if selective removal of plagioclase alone was to count for all the observed characteristics of group ii., around 40 wt% plagioclase fractionation from parental melts to the high-TiO_2 sills (Open and filled circles) would be needed in order to recreate the observed element configurations (calculations not shown). This figure is unrealistically high and is not supported by petrographic observations or by the trace

element and REE characteristics (e.g. Fig. 4.12; Fig. 4.13). Fractional crystallisation of ~20 wt% plagioclase from parental melts to the high-TiO_2 sills together with the addition of ~20 wt% accumulated plagioclase from an external source to melts being parental to the low-TiO_2 sills (calculated vectors shown in the right sides of Fig.4.29a; Fig. 4.29c; Fig. 4.29d) would be a more suitable explanation and would be in accordance both with the petrographic evidences i.e. ubiquitous plagioclase phenocrysts in the low-TiO_2 sills, with trace element and REE characteristics (Fig. 4.12; Fig. 4.13) and with the modelling as shown in Fig. 4.27 and Fig. 4.28. A process where cumulate plagioclases in the low-TiO_2 sills originate from external sources are fully in accordance with a recent isotope study on plagioclase crystals from the Early Cenozoic basaltic lavas on the Island of Skye, NW Britain, which suggested that individual crystals had been aggregated in magmas from different sites of storage and differentiation during magma ascent (Font et al., 2008).

As the sub-parallel trends representing the first group i. (dotted thin black lines) versus trends inferred to represent parental magmas to the sills in the second group ii. (indicated by thick full grey arrows in Fig. 4.29b; Fig. 4.29c and Fig. 4.29d) display slight lateral displacements relative to each other, slight compositional differences of their mantle reservoirs may be envisaged.

Least square mass-balance calculations involving most major elements suggest that fractionation/accumulation of plagioclase from/to basaltic melts would chiefly affect their Al_2O_3, Fe_2O_3 and MgO concentrations (Table 4.6; see also Fig. 4.9). These backtrack/reiteration calculations show that if some of the high-TiO_2 sills evolved by ~20 wt% fractionation and the low-TiO_2 sills evolved by ~20 wt% accumulation of this mineral from/to their respective parental melts, as suggested by the trace element modelling, the Al_2O_3 and the Fe_2O_3 contents of the high-TiO_2 sills would be lower and higher respectively compared to their parental melts whereas the Al_2O_3 and the Fe_2O_3 contents of the low-TiO_2 sills would be higher and lower respectively compared to their parental melts (Table 4.6; Fig. 4.30). Another noticeable consequence associated with these inferred fractionation/accumulation processes would be inverted relative abundances of Al_2O_3 and the Fe_2O_2 in parental melts to high-TiO_2 versus low-TiO_2 sill relative to measured relative abundances of these oxides in the actual sills (Table 4.6; Fig. 4.30). Hence, in contrast with the measured relative abundances of Al_2O_3 and Fe_2O_2 in the high-TiO_2 versus low-TiO_2 sills, the relative abundances of calculated Al_2O_3 and Fe_2O_2 in the precursor melts to these

Table 4.6. Least square mass-balance calculations of plagioclase fractionation and plagioclase accumulation in basaltic melts.

Major elements	[a]Plag	[b]High-TiO_2 sill (08-JES-11)	[c] Parent 1 (Calculated)	[b]Low-TiO_2 sill (07-JSS-52)	[d]P arent 2 (Calculated)
SiO_2	49.60	49.59	49.50	50.29	50.50
Al_2O_3	32.14	13.39	17.15	16.95	13.90
Fe_2O_3	0.27	14.69	11.80	10.42	12.45
MgO	0.20	6.55	5.28	6.86	8.20
CaO	15.38	11.19	12.03	13.22	12.80
Na_2O	2.57	2.33	2.38	2.00	1.90
K_2O	0.17	0.30	0.27	0.20	0.20
TiO_2	0.00	2.01	1.61	0.82	1.00
Sr		174.40	204.60	203.60	178.70
Eu		1.55	1.34	0.74	0.84
Th		0.85	0.71	0.53	0.62
Nb		10.85	8.74	2.81	3.35
Ta		0.63	0.51	0.18	0.21

[a]Plagioclase composition used in the mass-balance calculations is from Table 38, sample 6 in the compilation of Deer et al. (1992). [b]Sill compositions from Table 4.2; [c]Values are found by backtrack/reiteration calculations on the high-TiO_2 sill sample 08-JES-11 on the assumption that parent 1 represents its precursor melt prior to ~20 wt% net plagioclase fractionation; [d]Values are found by backtrack/reiteration calculations on the low-TiO_2 sill sample 07-JSS-52 on the assumption that parent 2 repreents its precursor melt prior to net accumulation of ~20 wt% plagioclase. Sums of squared differences were ~0.001 during both calculations. See text.

sills define trends that are in accordance with the production of parental melts to some of the high-TiO_2 sills by low degrees of melting and formation parental melts to the low-TiO_2 sills by higher degrees of partial melting of broadly similar mantle sources (Fig. 4.30), i.e. these calculated data support the inferences from the trace element modelling above and are also in agreement with experimental results on basalt formation by various degrees of partial melting (Table 1.1; Fig. 1.5). The relative abundances displayed by most of the remaining major elements in the high-TiO_2 and low-TiO_2 sills are maintained in their calculated parental melts i.e. abundances of MgO and CaO are higher and abundances of Na_2O and TiO_2 are lower in the calculated parental melts to the low-TiO_2 sills compared to the calculated parental melts to the high-TiO_2 sills (Table 4.6). Hence, the compositions of the major elements in the calculated parental melts all support the inferences suggesting increasing degrees of melting in going from high-TiO_2 to low-TiO_2 sills. Plots of the calculated melts from Table 4.6 would straddle the border between calc-alkaline basalt and high-MgO tholeiite basalt in a classification diagram similar to that of Fig.

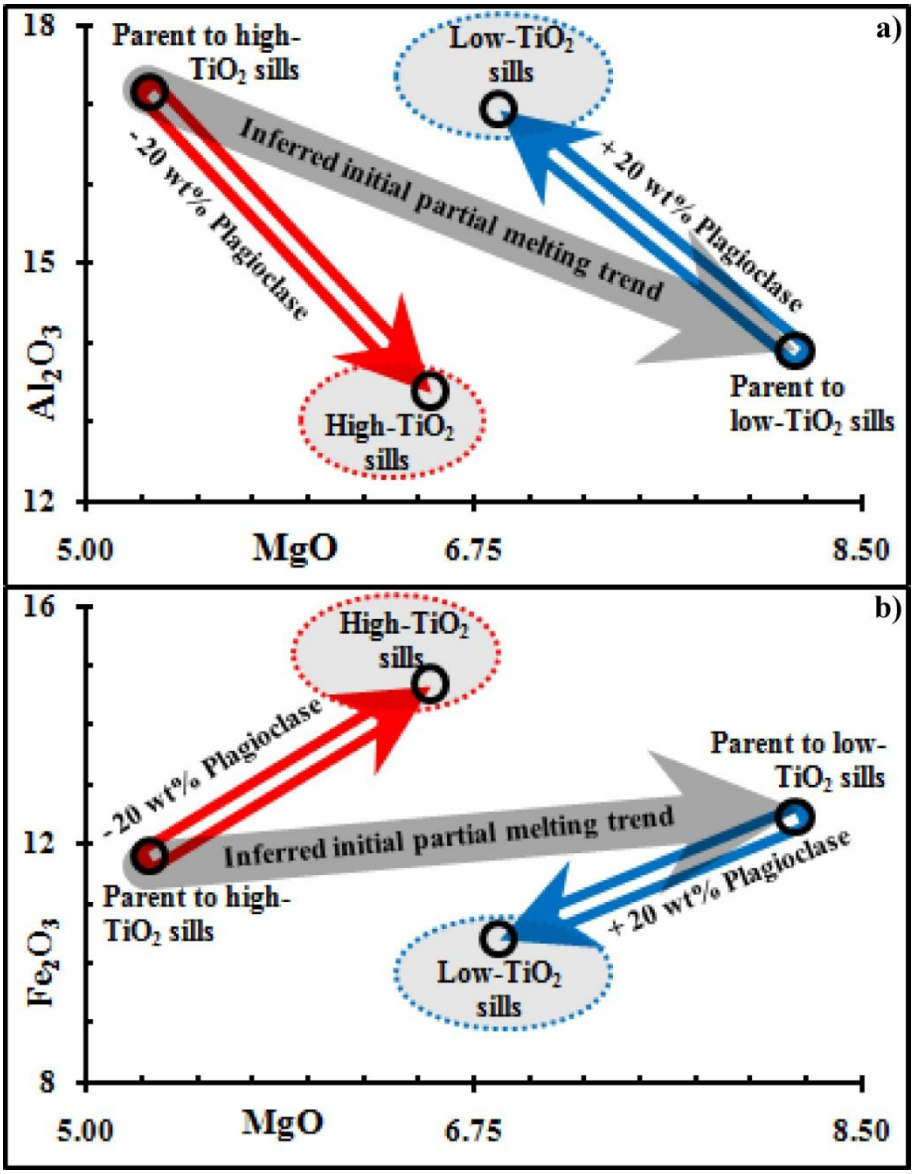

Figure 4.30. Some of the results from the backtrack/reiteration calculations shown in Table 4.6. As olivine fractionation is not accounted for in this figure, the inferred initial partial melting trends would have been located at higher MgO values in a more realistic scenario. a) If some of the high-TiO_2 sills evolved by ~20 wt% plagioclase fractionation and the low-TiO_2 sills evolved by ~20 wt% plagioclase accumulation, their relative concentrations in Al_2O_3 would be inverted when compared to their respective calculated parental melts, i.e. the calculated partial melting trend would define a negative slope. b) A similar scenario would apply for the Fe_2O_3 concentrations of these sills, the difference only being that the relative Fe_2O_3 contents in the high-TiO_2 versus low-TiO_2 sills are opposite to their Al_2O_3 contents and the same would apply for their respective calculated parental melts, i.e. the calculated partial melting trend would define a positive slope. See text.

4.8b, but they would form a tighter cluster compared to the actual measured data from the sills shown in Fig. 4.8b.

Mass-balance calculations show that ~2 wt% olivine fractionation can count for a ~1.5 wt% decrease in the MgO content of mafic melts (Fig. 4.9), i.e. the entire range of MgO observed within the investigated sills of the Faroe Islands (6.15 to 8.25 wt%) can be covered by 3 to 4 wt% olivine (Forsterite) fractionation from melts with compositions similar to the most primitive sill samples (Fig. 4.9).

Interpretations on MgO compositions of primary magmas to Early Cenozoic basalts of the NAIP from previous studies have yielded various results where estimates for W Greenland vary from 10.0 – 13.0 wt% MgO (Yaxley, 2000) to 17.0 – 18.5 wt% MgO (Larsen and Pedersen, 2009). MgO contents of primary melts to basalts of the Faroe Islands have been estimated at 16.0 – 18 wt% earlier (Holm et al., 2001), whereas 12.0 – 13.6 wt% MgO have been inferred for primary melts to basalts from E Greenland (Momme et al., 2006) compared to 13.0 – 15.0 wt% for primary melts that gave rise to Early Cenozoic basalts on the Isle of Skye, NW Britain (Scarrow and Cox, 1995).

As the SiO_2 content of olivines and clinopyroxenes in MgO-rich mafic rocks produced by partial melting of peridotitic lithologies commonly range from 40 – 42 wt% and 51 – 54 wt% respectively (e.g. Falloon et al., 1999; Dasgupta et al., 2007), fractional crystallisation of clinopyroxenes from primary mafic magmas comprising ~46.3 wt% SiO_2 and ~15.4 wt% MgO (similar to the picrite sample 121456 from the Faroe Islands of Søager and Holm., 2011) would have resulted in further silica depletion meaning that olivine probably would be more suitable as a fractionation phase, which could have modified such MgO-rich melts towards silica contents of 49 to 50 wt% being typical for the sills of the Faroe Islands. Mass balance calculations of olivine fractionation (Table 4.7) show that while fractionation of 15 – 20 wt% olivines with 41 – 42 wt% SiO_2 from potential primary melts with compositions comparable to some of the picrites encountered in the Faroe Islands (~46.3 wt% SiO_2 and ~15.4 wt% MgO) could generate the calculated (and measured) span in MgO values as presented in Table 4.6, such fractionation would fail to produce the calculated (and measured) silica levels as presented in Table 4.6. Hence, some additional fractionation of silica deficient phases (magnetite?) seems to be required as well in order to explain observed SiO_2 contents, if primary melts to the actual sills indeed had compositions comparable to picrites encountered in the Faroe Islands.

As both petrographic observations in sills from this study and the high silica content of clinopyroxenes in general seem to suggest that his mineral mainly crystallised

Table 4.7. Least square mass-balance calculations of olivine fractionation from potential primary magmas comparable in composition to observed picrites of the Faroe Islands.

Major Elements	[a]Observed picrite	[b]Olivine	[c]High-TiO_2 sill precursor	[d]Calc. Basalt 1	[e]Low-TiO_2 sill precursor	[f]Calc. Basalt 2
SiO_2	46.34	41.85	49.50	47.46	50.50	47.13
Al_2O_3	12.93	0	17.15	16.16	13.90	15.21
Fe_2O_3	11.16	2.05	11.8	13.44	12.45	12.77
MgO	15.36	56.17	5.28	5.16	8.20	8.16
CaO	10.46	0	12.03	13.08	12.80	12.31
Na_2O	1.74	0	2.38	2.18	1.90	2.05
K_2O	0.06	0	0.27	0.08	0.20	0.07
TiO_2	1.06	0.07	1.61	1.31	1.00	1.23

[a]Picritic lava of the Faroe Islands (Sample 121456 of Søager and Holm., 2011); [b]Olivine composition used in the mass-balance calculations is from Table 1, sample 1 in the compilation of Deer et al. (1992). [c]Calculated sill parent 1 from Table 4.6; [d]Values are calculated assuming 20 wt% olivine fractionation from magmas similar to observed picrite sample 121456. [e]Calculated sill parent 2 from Table 4.6; [f]Values are calculated assuming 15 wt% olivine fractionation from magmas similar to observed picrite sample 121456. Sums of squared differences for calculated basalts 1 and 2 were 9.1 and 13.5 respectively. See text.

during relatively late stages of magma solidification, their selective removal/fractionation from primary melts that gave rise to the sills of the Faroe Islands was probably not a dominating factor during evolution of these melts.

The density of olivine (Forsterite) is around 3.2 g/cm^3 compared to 2.76 g/cm^3 for pure anorthites (Deer et al., 1992), meaning that if these minerals crystallised from a typical tholeiitic magma at ~1250° C and with a density of around 2.6 g/cm^3 (Hall, 1996) the olivine would be far more susceptible to gravitational settling compared to the plagioclase, a fact that would also be in accordance with the general scarcity of olivine phenocrysts in sills from this study. However, in order to explain the petrographic observations as well as the inferred effects of plagioclase fractionation/accumulation on the geochemistry of most of the investigated sills, some settling of plagioclase crystals, which resulted in layers of mostly residual melts from plagioclase fractionation on top of magma layers rich in cumulate plagioclase, may be a requirement. Selective extraction/removal of residual melts following plagioclase fractionation, which left an excess of cumulate plagioclase crystals in the affected magma chambers, could also be an alternative explanation.

When fractional crystallisation of clinopyroxene during early stages of magma evolution is considered to have been relatively insignificant and corrections are made for fractional crystallisation of ~15 wt% olivine from primary melts to all the investigated sills, in addition to fractional crystallisation of ~20 wt% plagioclase

from primary melts to some of the high-TiO_2 sills and accumulation of ~20 wt% plagioclase to parental melts to all the low-TiO_2 sills, and when uncertainties with respect to exact compositions of potential moderately fertile spinel lherzolite sources (e.g. Lesnov et al., 2009) are accounted for, melting percentages of 20 – 22% for low-TiO_2 sills and 10 – 12% for high-TiO_2 sills seem to be reasonable estimates. If the depleted Morskranes Sill is corrected for similar amounts of olivine fractionation, 8 – 10% melting of a depleted mantle (Workman and Hart, 2005) could account for the observed trace element compositions. However, if the Morskranes Sill experienced 10 – 12 wt% plagioclase fractionation as well, as suggested by its calculated Eu/Eu* ratio and the fractionation modelling shown in Fig. 4.27, then 9 – 11% melting of depleted mantle material may well be a more correct estimate for this intrusion, i.e. broadly similar to what is inferred for the high-TiO_2 sills.

While the 20 to 22% partial melting that is inferred to have generated the primary magmas to the low-TiO_2 sills from this study broadly resemble estimates of melting percentages inferred previously for primary magmas that gave rise to low-TiO_2 basalts of W Greenland (Larsen and Pedersen, 2009), E Greenland (Momme et al., 2006) and the Faroe Islands (Holm et al., 2001), the 10 to 12% partial melting proposed for primary magmas to the high-TiO_2 sills in question is slightly higher than comparable estimates for other high-TiO_2 basalts of the Faroe Islands (Holm et al., 2001) and E Greenland (Momme et al., 2006). However, as most of the sills from this study being termed high-TiO_2 basalts display TiO_2 compositions of only ~2.1 wt% compared to 2.5 to 3.5 wt% TiO_2 for other high-TiO_2 basalts of e.g. the Faroe Islands (Holm et al., 2001), the melting percentages obtained during the current work for primary magmas to this sill group broadly resemble the results for similar rock types of other basalts from e.g. E Greenland and the Faroe Islands.

4.6.6. Constraining depth(s) of formation

Production of geochemically distinct basalts by different degrees of partial melting of broadly similar source-rocks, as is inferred for many of the high-TiO_2 versus the low-TiO_2 sills from this study, could result from slight differences in T or in P between source regions to the respective basalts or differences in the compositions of source materials (Table 1.1). The very limited lateral distances between geochemically distinct sills from the Faroe Islands (Fig. 3.2) renders it unlikely that there existed any significant differences in T between their source regions at depth if they formed

broadly contemporaneously. Instead, the low-TiO_2 sills could have formed in response to partial melting at slightly shallower depths and lesser P compared to those of the high-TiO_2 sills, but differences in degrees of metasomatism in the respective source regions could perhaps also have resulted in uneven melt production.

As the upper limit of the plagioclase stability field in rocks of lherzolitic composition is defined by a P of ~0.9 GPa (Borghini et al., 2010) and as the products from partial melting of fertile plagioclase-bearing lherzolites are expected to be of quartz tholeiitic compositions (Kushiro, 1996, 2001), the olivine tholeiites building up the sills of the Faroe Islands probably formed at P greater than ~0.9 GPa. Also, the formation of the bulk of the primary melts that gave rise to the investigated sills can probably be constrained to a P at the lower limit of the garnet stability field or slightly below it, as the previous modelling suggest that only very small amounts of garnet could have been involved in the melt formation if any at all, i.e. these melts were probably produced at pressures between ~0.9 GPa and ~2.8 GPa (Garnet stability field from Robinson and Wood, 1998) corresponding to depths in the range from ~30 to ~85 km. The common occurrences of ophitic to subophitic clinopyroxenes poikilitically enclosing plagioclase laths in samples from these same intrusions suggest that these clinopyroxene grains mostly formed during the latest stages of crystallisation following plagioclase crystallisation. This inference is strongly supported by the predominance of plagioclase crystals at chilled margins of feeder dykes to the Streymoy Sill (Fig. 4.7). As crystallisation of plagioclase prior to clinopyroxene crystallisation only occurs at P lower than ~0.5 GPa (Grove et al., 1992; Korenaga and Keleman, 2000), initiation of plagioclase crystallisation in parental melts to many of the sills from the Faroe Islands probably took place at P lower than 0.5 GPa corresponding to depths less than ~18 km. However, as clinopyroxene (Augite) has a density of around 3.37 g/cm^3 (Deer et al., 1992), grains of this mineral that potentially crystallised early in the evolution process may have fractionated out of the actual magmas thus still rendering it possible that initiation of plagioclase crystallisation occurred at greater depths.

4.6.7. Geochemical constraints on potential mantle sources

The previous calculations strongly suggests that the geochemical compositions of most sills from the Faroe Islands can be explained by partial melting of moderately

fertile mantle material whereas one of the investigated sills, in addition to a few the lava flows, probably owe their geochemical characteristics to melting of more depleted mantle sources. There is a general consensus amongst many geologists that depleted mantle material probably represents residue(s) following partial melting of primordial mantle reservoirs to produce basaltic melts (Wood, 1979; Rampone et al., 2004; Workman and Hart, 2005). The geochemical compositions of fertile mantle material are sometimes interpreted to result from metasomatic processes, where a primordial mantle is contaminated with ascending low-degree basaltic magmas or with fluids expelled from these (Wood, 1979; Dupuy et al., 1991; Grégoire et al., 2003; Lesnov et al., 2009). Other authors suggest that fertile mantle material can evolve in response to assimilation of recycled oceanic crustal material (Kogiso et al., 1998; Korenaga and Keleman, 2000; Yaxley, 2000; Kogiso et al., 2004) perhaps associated with earlier subduction or delamination processes (e.g. Meyer et al., 2007 and references therein). With respect to compositions of major elements, the enrichment of iron (Expressed as FeO_{tot}) in a basaltic melt is commonly taken as an indication of contamination with mafic crustal material, where average FeO_{tot} values of around 13 wt% (HIMU basalts) suggest a strong signature of recycled oceanic crust (Kogiso et al., 1998). Although the investigated high-TiO_2 sills display average Fe_2O_3 contents of ~14.5 wt%, the calculated/inferred parental melts to some of the high-TiO_2 and the low-TiO_2 sills of the Faroe Islands display Fe_2O_3 values ranging from 11.8 to ~12.45 wt% (Table 4.6; Fig. 4.30), i.e. well within the ranges displayed by both mid ocean ridge basalts and ocean island tholeiites (Blatt and Tracy, 1995). Hence, if the results from the calculations shown in Table 4.6 give reliable indications of major element compositions of the primary melts that gave rise to some of the investigated sills, the makeup of these elements do not hint to any significant recycling/involvement of oceanic crustal material during mantle melting to produce these sills. However, as the Langaregn and Svínoy-Fugloy sills display weaker negative Sr and Eu anomalies compared to the Eysturoy and Sundini sills (Fig. 4.12c; Fig. 4.13c), their relatively high Fe_2O_3 contents (Table 4.2; Fig. 4.9) could potentially in part stem from sources that are more enriched relative to those that gave rise to the two latter sills.

Negative Nb and Ta anomalies in normalised multi-element diagrams representing basaltic rocks have often been linked to subduction-zone environments where the partial melting in the presence of fluids to produce these Nb and Ta depleted basalts

are inferred to have occurred. These elements are thought to be retained in mineral phases that are stabilised by fluids/elements from subducted material, which metasomatise the mantle wedge(s) above subducting oceanic slabs and sediments (e.g. Thompson et al., 1983). Conversely, a residual dry mantle with a previous history of metasomatism followed by dehydration melting and magma extraction could be relatively enriched with respect to Nb and Ta (Thompson et al., 1983). Also, partial melting of sources that have experienced different sorts of mantle metasomatism could result in the generation of igneous products possessing negative versus positive Nb and Ta anomalies (Thompson et al., 1983). Nb and Ta troughs in normalised multi-element diagrams that represent suites of low-TiO_2 flood basalts from the Siberian Traps, some of which display geochemical compositions that are virtually identical to those of the low-TiO_2 sills from this study, have previously been interpreted to result from partial melting in the upper mantle following metasomatism from percolation of fluids originating in segments of stagnant ancient subducted slabs stored at greater depths (Ivanov et al., 2008).

The moderately positive/negative Nb and Ta anomalies displayed by some of the sills of the Faroe Islands (Fig. 4.12c; Fig. 4.12d) most probably reflect characteristics of their respective source regions, as neither different degrees of partial melting of moderately fertile mantle material nor fractionation/accumulation of e.g. plagioclase

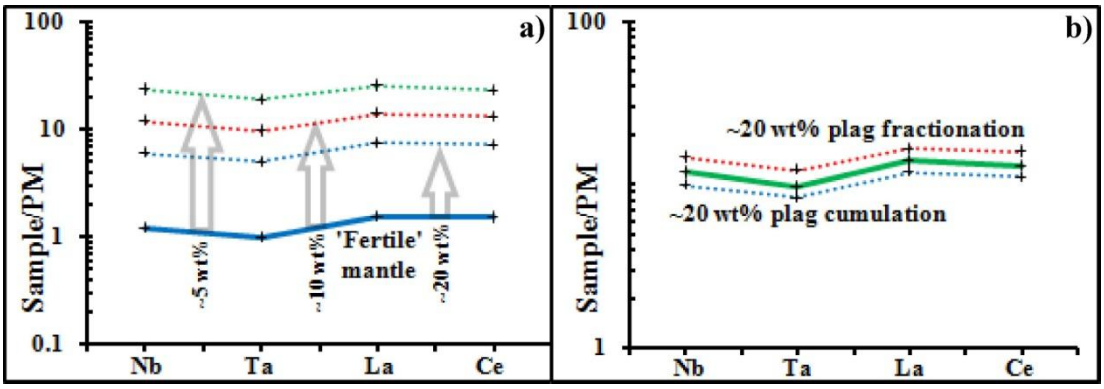

Figure 4.31. a) 5, 10 and 20% partial melting of a moderately fertile mantle (Lesnov et al., 2009), leaving residual mineral assemblages composed of 76 wt% Ol + 16 wt% Opx + 8 wt% Cpx (Abbreviations are as in Fig. 4.9), do not result in fractionation of Nb and Ta relative to La and Ce. b) 20 wt% fractionation/accumulation of plagioclase from a basaltic melt (green line = 10% melt from 4.31a) do not produce any Nb and Ta fractionation relative to La and Ce. Partition coefficients used in the calculations are from Table 4.5 and normalising values are as in Fig. 4.12. (Results from modelling are shown in appendix 5.10). See text.

(or olivine, calculations not shown) from/to basaltic melts can explain any potential fractionation of Nb and Ta relative to e.g. La and Ce (Fig. 4.31).

If melting of a metasomatised mantle, which retained Nb and Ta during magma extraction, also produced the low-TiO_2 sills of the Faroe Islands that display moderately negative Nb and Ta anomalies, the moderately positive Nb and Ta anomalies displayed by the Langaregn and Svínoy-Fugloy sills (Fig. 4.12c) could in theory indicate magma tapping from a dryer Nb and Ta enriched mantle reservoir representing residual material from partial melting as envisaged by Thompson et al. (1983). Also, the previous inferences based on calculations/modelling, suggesting production of the low-TiO_2 sills by higher percentages of partial melting compared to the melting percentages that generated their high-TiO_2 counterparts, would be in accordance with higher degrees of metasomatism (hydration?) in sources to the low-TiO_2 sills compared to sources to the high-TiO_2 sills (See also Table 1.1). Therefore, it seems reasonable to assume that the sources to the low-TiO_2 sills could have experienced moderate metasomatism of some sort prior to the partial melting event. However, as all the investigated high-TiO_2 sills are enriched with respect to the LREE (Fig. 4.13), the formation of the Langaregn and Svínoy-Fugloy sills by low-degree melting of a relatively dry Nb and Ta enriched source that had already experienced a partial melting event may appear to be problematic at a first glance, as the incompatible LREE of these source rocks would have been strongly partitioned into the first melts (See also Table 4.5) leaving the Nb and Ta enriched residue relatively depleted in LREE. This apparent paradox regarding provenance of the Nb and Ta enriched high-TiO_2 sills can perhaps be evaded if one of two possible scenarios are envisaged for their mantle source(s): 1. Refertilisation of a residual Nb and Ta enriched mantle, which had already experienced a metasomatic and a partial melting event, by means of metasomatism with highly LREE enriched alkali-basalts from very low degrees of melting that had occurred at deeper mantle levels resulted in a moderately fertile Nb and Ta enriched mantle; 2. Metasomatism of a moderately fertile mantle by very low-degree melts selectively enriched with respect to Nb and Ta, which were derived from a Nb and Ta enriched residual mantle reservoir that had already experienced an earlier metasomatic and partial melting event, resulted in a moderately fertile Nb and Ta enriched mantle. Of these two hypothetical options the second one appears to be the most appealing as it invokes one initial metasomatic event in the entire region that stabilised Nb and Ta bearing mineral phases,

potentially affecting both a moderately fertile source to the low-TiO_2 sills and the source from where a second generation of low-degree melts in turn metasomatised a moderately fertile source to the high-TiO_2 sills. It is not clear whether either of these two suggested options could have involved enrichment in Fe_2O_3 of the sources that gave rise to the relatively high-Fe_2O_3 Langaregn and Svínoy-Fugloy sills as well. If not, components of ancient recycled oceanic crust could in theory have contaminated their mantle source(s) during earlier magmatic events. However, the low Pb isotopic ratios in all sills from this study (Table 4.4, Fig. 4.14) are dissimilar to the relatively high Pb isotopic ratios typical for basalts interpreted to result from melting of mantle sources containing clear HIMU signatures (e.g. compilation of Rollinson (1998; Day et al., 2010), i.e. components of recycled oceanic crust are included in such sources. Hence, in accordance with some of the Eu/Eu* ratios recorded for these two sills (e.g. Fig. 4.27), some plagioclase fractionation most likely affected their parental melts too albeit probably at smaller scales compared to what is inferred for melts parental to the Eysturoy and Sundini sills.

In the context of Nb and Ta systematic it is perhaps of some relevance that rutile, into which these two elements are strongly partitioned from basaltic melts (Klemme et al., 2005), is not a stable mineral phase at T higher than ~1200° C (Xiong et al., 2005), i.e. it is unlikely that this mineral contributed to the observed Nb and Ta anomalies. Apart from the Morskranes Sill that has a Nb/Ta ratio of ~14.7, most of the investigated sill samples display relatively uniform super-chondritic ratios with average values of ~16.5 (Table 4.3), thus perhaps strengthening inferences regarding relatively homogeneous fertile mantle sources for the majority of the investigated sills. In theory, the occurrence of metasomatised and/or depleted mantle sources to the sills of the Faroe Islands could be in accordance with the local geological history, in which these intrusions represent the latest known phase(s) of igneous activity in a region that had already experienced extensive basaltic magmatism with associated mantle melting and magma tapping, as both mantle metasomatism and formation of depleted mantle material are natural consequences being associated with partial melting and magma tapping (Wood, 1979). However, metasomatic activities associated with other igneous events that occurred in the local mantle prior to the well documented Early Cenozoic magmatism of this region could be an alternative explanation.

The occurrence of low-TiO_2 sills in lavas of the Malinstindur and Enni formations that are dominated by high-TiO_2 basalts (e.g. Søager and Holm, 2009) and of high-TiO_2 sills adjacent to low-TiO_2 dykes and lavas occurring in the northern parts of the archipelago (e.g. Hald and Waagstein, 1991; Søager and Holm, 2011) may suggest that, unless some of the magmas that gave rise to these basalts experienced noticeable lateral transport, different degrees of partial melting occurred at the same localities but at different depths. This could in turn point to different sort of metasomatism at different mantle levels in these particular locations.

As both fertile and depleted naturally occurring peridotites reported worldwide commonly display compositional variations (Dupuy et al., 1991; Grégoire et al., 2003; Rampone et al., 2004; Workman and Hart, 2005; Lesnov et al., 2009), the results obtained from calculations/modelling on partial melting carried out in this chapter probably give reliable indications of relevant rock-forming processes, but slight uncertainties in quantification of these processes should be expected.

4.6.8. Isotopic constraints on potential mantle source(s)

If some of the variations in isotopic ratios observed in samples representing the sills of this study do not result from crustal contamination, they must point to some sort of isotopic heterogeneity in mantle sources to the primary melts that ultimately gave rise to these basalts. Relative isotopic enrichments of samples from this study are signified by systematic increases of $^{206}Pb/^{204}Pb$, $^{207}Pb/^{204}Pb$ and $^{208}Pb/^{204}Pb$ ratios with increasing $^{87}Sr/^{86}Sr$ ratios and decreasing $^{143}Nd/^{144}Nd$ ratios respectively (Fig. 4.18a-e). Most ordinary basalt samples (presumably not significantly affected by contamination) from the Faroe Islands plot slightly below the Northern Hemisphere Reference Line (NHRL) in a $^{206}Pb/^{204}Pb$ versus $^{207}Pb/^{204}Pb$ diagram whereas all samples plot slightly above the NHRL line in a $^{206}Pb/^{204}Pb$ versus $^{208}Pb/^{204}Pb$ diagram (Fig. 4.32). The close proximity of Pb isotope ratios representing the actual samples to ratios representing sources to N-MORB could perhaps point to a genetic link, but potential isotopic contributions from a primitive N Atlantic end-member mantle source (NAEM) reservoir (Ellam and Stuart, 2000) and/or from enriched sources of isotopic compositions comparable to HIMU, EM II or EM I reservoirs (Zindler and Hart, 1986; Hart, 1988) need some attention too (Fig. 4.32). The sample 08-JMS-14 of the depleted Morskranes Sill (Red square with black outline) could potentially have developed from a source that possessed a Pb isotope composition

similar to that of N-MORB mixed with a source comparable to EM I, but the collective Pb isotopic compositions of the other sill samples do not seem to be in accordance with an origin from a N-MORB-like isotopic composition mixed with any of the enriched mantle reservoirs shown in Fig. 4.32. As all the sill samples apart from 08-JMS-14 of the Morskranes Sill define broadly linear trends between the NAEM and HIMU sources (Fig. 4.32), development of primary melts to these basalts by different degrees of isotopic enrichments of a NAEM source with e.g. HIMU-like material remains a theoretical possibility. While Ellam and Stuart (2000) argued in favour of Pb isotopic enrichment by the addition of lithospheric components into NAEM sources of the BTIP, Stracke et al. (2003) more specifically concluded that the spread in Pb isotopic compositions of Icelandic lavas mainly resulted from contamination of depleted mantle sources possessing Pb isotopic compositions comparable to those of picrites from Theistareykir, Iceland, with HIMU-like components, i.e. containing recycled oceanic crust. If a comparable isotopic enrichment process, which involved contributions from a HIMO-like source to potential NAEM-like primary melts to sills of the Faroe Islands, was active in Early Cenozoic times, increasing degrees of HIMO contribution could perhaps be expressed as: depleted source $\rightarrow$ Morskranes Sill $\rightarrow$ high-TiO_2 sills $\rightarrow$ low-TiO_2 sills. The deviation of the sample 08-JMS-14 of the Morskranes Sill (red square with black outline) from the trend defined by the other sills in $^{206}Pb/^{204}Pb$ versus $^{207}Pb/^{204}Pb$ diagrams (Fig. 4.32a; Fig. 4.32a*) could in theory result from a slight involvement of a source similar to EM I, but as a similar association of this sample with an EM I reservoir is not observed in $^{206}Pb/^{204}Pb$ versus $^{208}Pb/^{204}Pb$ diagrams (Fig. 4.32b; Fig. 4.32b*), contributions from other isotopic sources seem to be needed in order to explain the Pb isotopes of the actual sample. The discussion above on trace element and REE characteristics of the sill samples in question suggested two main melting regimes as the main mechanism that generated distinct trends/clusters for high-TiO_2 versus low-TiO_2 sills, but slight differences in metasomatism or source rock compositions were also indicated by variations in e.g. Nb and Ta concentrations and slight positive versus negative anomalies of these. The relative enrichments in Pb isotopes displayed by the Streymoy Sill relative to e.g. the Eysturoy Sill as shown in Fig. 4.32 could be a potential result of an origin from a more metasomatised/enriched mantle source of the former sill as tentatively

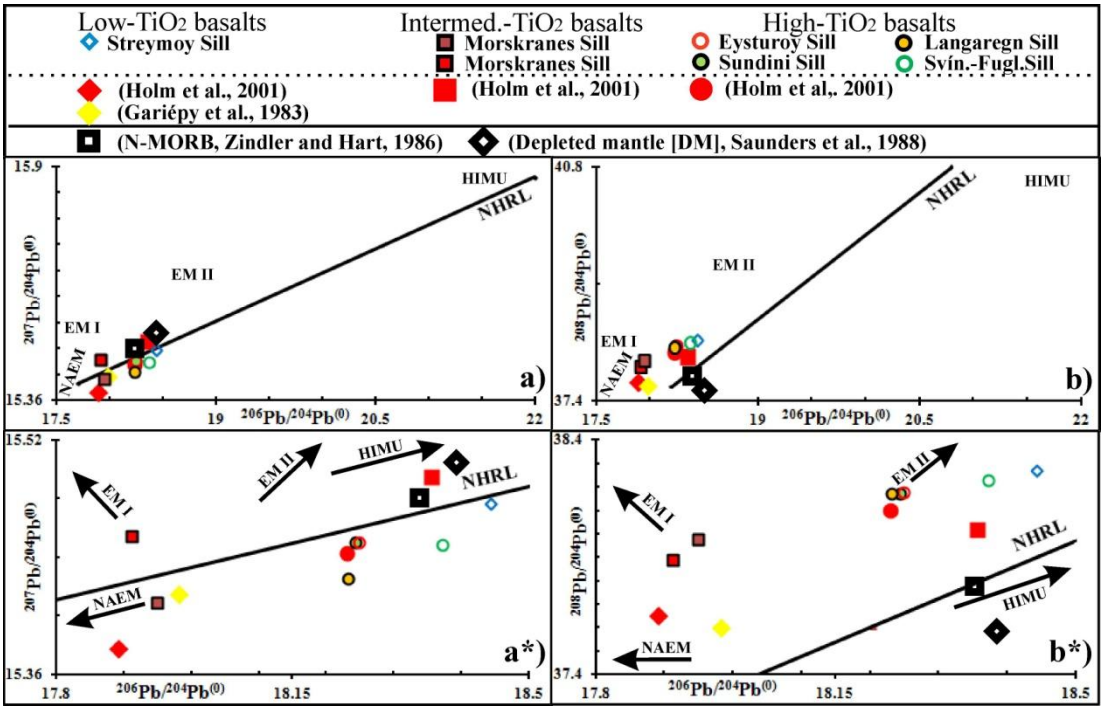

Figure 4.32. a) and b) Sill samples as well as selected dykes and lava flows of the Faroe Islands straddle the NHRL line when plotted in Pb isotope diagrams. a*) and b*) Closer view of a) and b). Isotopic compositions of Northern Hemisphere Reference Line (NHRL), HIMU, EM II, and EM I are based on Zindler and Hart (1986); Hart (1988). Isotopic composition of North Atlantic end-member NAEM is from Ellam and Stuart (2000). See text.

suggested previously. However, the observed differences in Pb isotopes between the Svínoy-Fugloy Sill and the Langaregn Sill as shown in Fig. 4.32 do not seem to be in accordance with an origin of these two sills from a completely uniform mantle source as might be suggested by multi element plots of these sills (Fig. 4.12c), but may point to a slightly heterogeneous source. Then again, these differences between their Pb isotopes do not preclude similar mechanisms in the sources to both of these two sills, as potential metasomatising/enrichment agents could themselves originate from slightly different sources. If the slight isotopic variations between most of the sills that possess gentle/steep negative REE slopes do indeed originate in mantle sources that were affected by enrichment processes, small-degree melts or fluids from some of the sources to the lavas/dykes of the Faroe Islands could be potential candidates, as these basalts possess a much wider range in Pb isotopic compositions compared to the sills in question (Fig. 4.15c; Fig. 4.15d).

As the Morskranes Sill displays depleted signatures with respect to both trace elements (Fig. 4.12a) and REE (Fig. 4.13d), as well as showing depleted signatures

for some radiogenic isotopes (e.g. Fig. 4.18a), it seems reasonable to assume that its primary melts could have developed from a relatively depleted mantle reservoir, perhaps comparable in composition to the source of other depleted lavas/dykes of the Faroe Islands (e.g. red and yellow rhombuses in Fig. 4.18a and Figure 4.32). In theory, the marked differences in $^{87}Sr/^{86}Sr$, $^{143}Nd/^{144}Nd$ and $^{207}Pb/^{204}Pb$ ratios between the two samples that represent the small Morskranes Sill could result from crustal contamination (See previous discussion), but source heterogeneity due to e.g. metasomatism remains an alternative explanation. A process with metasomatic enrichments of the mantle source of the Morskranes Sill with small-degree melts from mantle sources to basaltic lavas/dykes of the Faroe Islands or from sources displaying Pb isotopic compositions similar to those that produced basalts of other North Atlantic regions is not likely to explain the observed Pb isotopic range of this small sill, as none of these basalts display sufficiently large excess Pb isotopic ranges for both $^{206}Pb/^{204}Pb$ versus $^{207}Pb/^{204}Pb$ ratios and $^{206}Pb/^{204}Pb$ versus $^{208}Pb/^{204}Pb$ ratios relative to both these sill samples (Fig. 4.15c; Fig. 4.15d).

Potential implications from similarities/covariance in Pb isotopes of the actual sills with those from other regions of the North Atlantic area e.g. Iceland, E Greenland, W Greenland and other basalts of the Faroe Islands (e.g. Fig. 4.15c; Fig. 4.15d) will be briefly discussed in chapter 5.

4.7. Summary and concluding remarks

4.7.1. Concluding remarks and summary on isotopic characteristics

This chapter has dealt with relevant isotopes of the elements Sr, Nd and Pb representing basaltic sills of the Faroe Islands and these have been contrasted with isotopes of selected basement samples from NW Britain, the Rockall Plateau, E Greenland and other basalts (lavas/dykes) of the Faroe Islands as well as relevant isotopic mantle reservoirs. Due to the limited isotopic dataset on the sills of the Faroe Islands, it has not been possible to determine whether there exist isotopic variations within individual sills and the lack of Pb isotope data on the Kvívík Sill renders it impossible to examine whether the observed differences in Sr and Nd isotopic compositions between this sill and the geochemically identical Streymoy Sill are reflected by their Pb isotopic ratios too.

It is unclear whether specific reservoirs from the literature like HIMU, EM I or EM II did have any bearing on the isotopic compositions of the high/low-TiO_2 sills from

this study or if very slight crustal contamination played any role. The relatively tight clustering of all samples representing high/low-TiO_2 sills in Sr versus Nd isotope ratio plots (Fig. 4.16a) seems to suggest that the primary magmas that gave rise to these intrusions could have been tapped from broadly similar (only slightly heterogeneous) mantle sources. A slightly relatively homogeneous mantle source for all investigated sills, apart from the Morskranes Sill, is also suggested by their fairly uniform Nb/Ta ratios averaging ~16.5 (Table 4.3). Hence, partial melting of a very slightly heterogeneous and isotopically depleted mantle source with Pb isotopic compositions not very different from that of N-MORB (Zindler and Hart, 1986) and DM (Saunders et al., 1988) could have produced the bulk of the high/low-TiO_2 sills sills (Relatively LREE enriched) whereas the LREE-depleted Morskranes Sill probably originates from a more depleted mantle source with an isotopic composition that are closer to NAEM (Ellam and Stuart, 2000) or DMM (Zindler and Hart, 1986). The slight relative enrichments in $^{87}Sr/^{86}Sr$ and $^{207}Pb/^{204}Pb$ ratios between the samples 08-JMS-17 and 08-JMS-14 respectively of the Morskranes Sill might point to very slight contamination of these two samples by two different crustal sources. If true, such isotopic differences between two individual samples collected within short distances of the same small sill could in theory point not only to slight compositional heterogeneities in potential contamination sources, but may also indicate differences in the absolute ages of such sources. Consequently, potential assimilation of basement material by primary melts to the Morskranes Sill could have occurred at different stratigraphic levels, as the crust/lithosphere is expected to be isotopically stratified depending on ages of formation (e.g. Gariépy et al., 1983; Peate et al., 2008).

It is evident that the strongly enriched isotopic signatures of the 4 samples of silicic basaltic lavas utilised in this chapter probably originate from contamination with crustal material (Gariépy et al., 1983; Holm et al., 2001), but the entire range in isotopic compositions of these rocks cannot be recreated by contamination of ordinary basalts of the Faroe Islands with material possessing isotopic composition similar to any individual basement specimen from any of the neighbouring regions (Table 4.4). More likely, contamination of tholeiitic basalts with material originating at various lateral or vertical sections in an isotopically heterogeneous basement region resulted in the observed isotopic span of the contaminated silicic basalt samples. Contamination with crustal material comparable in Sr and Nd isotopic

composition to the average of the basement samples from the Rockall Plateau could explain the range in $^{87}Sr/^{86}Sr$ versus $^{143}Nd/^{144}Nd$ ratios of all these 4 specimens of contaminated silicic basalts, but contributions to the actual basalts of Pb isotopes similar to any combinations of basement material from this region would fail to account for the observed Pb isotopic compositions of any of the actual samples. In theory, assimilation of crustal rocks, displaying isotopic compositions similar to a combination of those representing the plotted basement samples of NW Britain, could explain the Sr and Nd isotopic compositions of all the 4 contaminated silicic basalt samples as well as potentially explaining the Pb isotopic compositions of two of these (red circle and triangle), but would fail to reproduce the isotopic compositions of any of these rocks when these are plotted in Pb versus Nd isotopic ratio diagrams. Contamination (~10 to ~ 20 %) of presumed uncontaminated basalts from the Faroe Islands with material possessing isotopic compositions resembling various combinations of basement samples from E Greenland could reproduce the entire Sr, Nd and Pb isotopic range of all the 4 samples of contaminated silicic basalts, but assimilation of material from two distinct basement sources would be required in order to explain the marked differences in $^{208}Pb/^{204}Pb$ ratios in particular between some of the contaminated silicic basalt samples (e.g. Fig. 4.21b*; Fig. 4.21c*). As average Th/U ratios are much higher for mafic material relative to felsic rocks, i.e. ~2.75 and ~1.55 respectively (Haack, 1983), the noticeable higher $^{208}Pb/^{204}Pb$ ratios in 2 of these contaminated basalts relative to the other 2, could indicate mafic versus felsic contaminants. Alternatively, different ages (i.e. different stratigraphic levels) of assimilated material could be a potential explanation of these variations in $^{208}Pb/^{204}Pb$ ratios.

4.7.2. Concluding remarks and summary on geochemical characteristics

In this chapter it has been shown that the sills of the Faroe Islands are composed of tholeiitic basalts, which can be divided into three main groups according to their TiO_2 contents where the large Streymoy Sill and the smaller Kvívík Sill define a low-TiO_2 group in contrast to the large Eysturoy Sill, the Sundini Sill, the Langaregn Sill and the Svínoy-Fugloy Sill that all define a high-TiO_2 group. The TiO_2 composition of the Morskranes Sill is positioned in between these two main groups. Comparable correlations also exist between most of the other major elements from these sills apart from SiO_2 and MgO. The investigated sills also define three distinct

groups in terms of their trace elements including their REE where each group display REE configurations that resemble each of those that define basalt types 1, 2 and 3 that have been reported from widespread regions of the NAIP (Kerr, 1995). The modelling carried out in this study suggest that observed differences in TiO_2 contents for most sills as well as Sr and Eu anomalies can be explained by differences in the degrees of partial melting of their mantle sources in addition to modification of primary melts by fractional crystallisation of olivine and plagioclase and accumulation of plagioclase. Moderately positive and negative Nb and Ta anomalies displayed by some of the actual sills seem to suggest that their mantle sources could have been affected by different sorts of metasomatism.

More specifically, it is suggested that the sills of the Faroe Islands developed in response to the petrogenetic processes outlined below and indicated in the simplified profile shown in Fig. 4.33.

(1) Partial melting of moderately fertile and slightly metasomatised mantle material, taking place at depths and pressures corresponding to the upper limits of the spinel stability field and perhaps also approaching the lower limits of the garnet stability field could have generated the primary basaltic magmas that eventually gave rise to most of the saucer-shaped sills exposed in the Faroe Islands. Differences in the degrees of partial melting probably resulted in much of the compositional diversity displayed by the investigated intrusions, where low degrees of melting (7 to 8%) could explain the directly observable geochemical compositions of most high-TiO_2 sills, while the measured geochemical compositions of the low-TiO_2 sills that may be explained by higher degrees (~23%) of mantle melting. Also, ~4.5% partial melting of slightly fertile mantle material can reproduce the compositions of some of the very high-TiO_2 dykes reported from earlier studies of the Faroe Islands.

(2) Low degrees of partial melting (7 to 8%) of a moderately depleted mantle, occurring at depths and pressures corresponding to the upper limits of the spinel stability field can explain most of the measured depleted REE signatures that characterise the Morskranes Sill and some lava flows of the Enni Formation. Alternatively, lesser degrees of partial melting ($4 \pm 1\%$) of more depleted mantle material occurring at similar depths can explain the REE compositions of these rocks. However, hybridisation of these latter low-degree melts with around 5 to 10% of magmas having compositions broadly similar to those of some of the

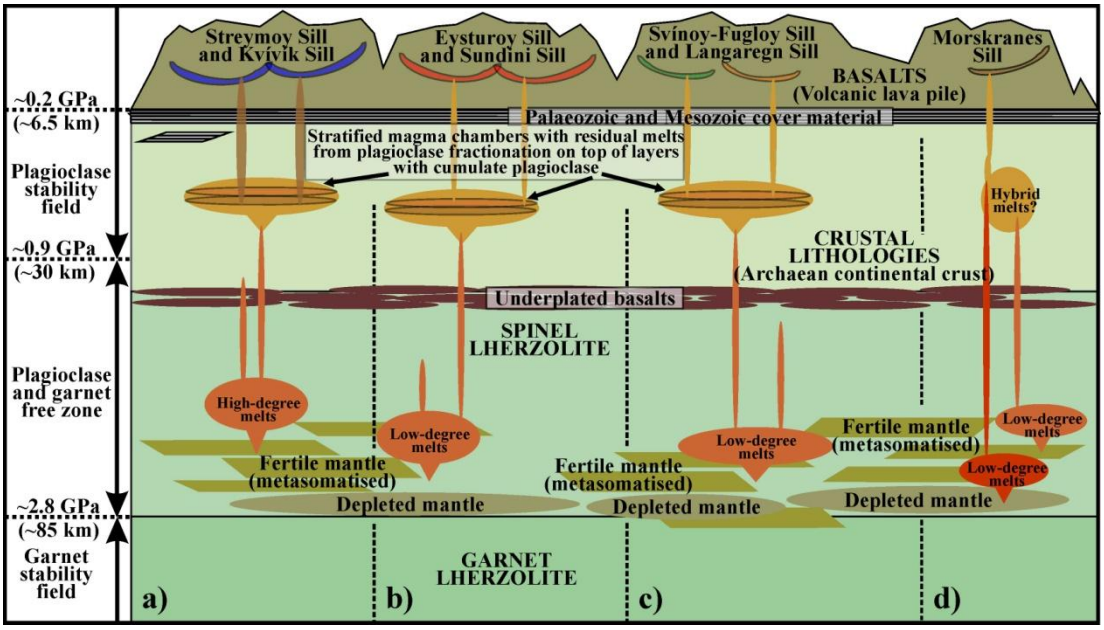

Figure 4.33. The simplified profile summarises inferred petrogenetic processes during formation of the sills of the Faroe Islands. Vertical distances are drawn at arbitrary scales. a) Primary magmas to the Streymoy and Kvívík sills form in response to high-degree melting of a moderately fertile mantle, during ascent they experience fractional crystallisation of mainly olivine followed by net accumulation of plagioclase at depths of <~18 km prior to the ultimate emplacement. b) Primary magmas to the Eysturoy and Sundini sills form in response to low-degree melting of a moderately fertile mantle, during ascent they experience fractional crystallisation of mainly olivine followed by fractional crystallisation of plagioclase at depths of <~18 km prior to the ultimate emplacement. c) The processes that generated the Svínoy-Fugloy and Langaregn sills were probably broadly similar those envisaged under b), but with a slightly different composition of moderately fertile mantle material and perhaps lesser degrees of plagioclase fractionation. d) Primary magmas to the Morskranes Sill form in response to low-degree melting of depleted mantle material. During ascent these magmas experience fractional crystallisation of mainly olivine perhaps probably followed by by some plagioclase fractionation. Slight hybridisation with more fertile liquids and very minor amounts of contamination with crustal material could have occurred during ascent of these depleted melts. The garnet stability field is from Robinson and Wood (1998) and the compilation of Presnall et al. (2002). The plagioclase stability field is from Borghini et al. (2010) and the compilation of Presnall et al. (2002). The thickness of the lava pile is from Rasmussen and Noe-Nygaard (1970); Waagstein (1988); Passey and Bell (2007); Passey and Jolley (2009). The inferred crustal thickness and crustal lithologies are from Bott et al. (1974) and Richardson et al. (1998).

high-TiO_2 sills seems to be a requirement in order to fully explain the observed LREE compositions of these depleted basalts.

(3) Fractional crystallisation of olivine (15 ± 2 wt%) probably modified parental melts to most of the sills from this study. The changes in REE concentrations

associated with this amount of olivine fractionation would correspond to 1 – 1½ % change in the degree of partial melting, i.e. all calculated partial melting percentages (Fig. 4.24) should probably be adjusted upward by 1 – 1½%. Plagioclase fractionation (~20 wt%?) from parental melts to many of the high-TiO_2 sills best explain the observed negative Eu and Sr anomalies in these intrusions as well as their relative depletion in Al_2O_3 and relative enrichment in Fe_2O_3. It is noteworthy that changes in REE concentrations associated with fractional crystallisation of ~20 wt% plagioclase, in addition to ~15% olivine fractionation, from magmas having compositions broadly similar to the high-TiO_2 sills from this study, would correspond to 2 or 3% change in the degree of partial melting, i.e. the partial melting percentages calculated for the high-TiO_2 sills (Fig. 4.24a) can probably be adjusted upwards to 10 ± 2%.

(4) The positive Eu and Sr anomalies displayed by samples representing the low-TiO_2 sills, their relative enrichment in Al_2O_3 and relative depletion in Fe_2O_3 in addition to the ever-present plagioclase phenocrysts are best explained by net accumulation of plagioclase (~20 wt%) into their parental melts. Around 20 wt% plagioclase cumulation, in addition to ~15% olivine fractionation, would result in a modification of REE concentrations in melts having compositions broadly similar to the low-TiO_2 sills from this study that correspond to a 2 or 3% change in partial melting, i.e. the partial melting percentages calculated previously for the low-TiO_2 sills (Fig. 4.24a) can probably be adjusted downwards to 20 ± 2%.

(5) Parental magmas to some parts the Morskranes Sill may have experienced very slight crustal contamination in the course of their evolutions.

Chapter Five

5. Synopsis

5.1. Prelude to chapter five

The current study on the sills of the Faroe Islands offers a good opportunity to compare, contrast and evaluate the obtained results/interpretations, as presented in preceding chapters, with established theories and propositions from previous studies.

The previous interpretations of particular physical features that crop out at various scales within the investigated sills (chapter 3) have led to proposals of applicable emplacement theories as well as measurements of post magmatic stress/deformation orientations within the area in question. These findings can be contrasted and evaluated against emplacement theories established previously for sills occurring in a number of locations worldwide, where the main points from the results obtained in this study may be compared to interpretations of similar features of sills from these earlier works. Also, the observed deformation characteristics within the sills from the current study can be compared to other structural works on basalts occurring within the actual region in an attempt to establish the status of these deformation structures in a regional context.

The geochemical and isotopic parts of this work (chapter 4) offer a wider range of potential outcomes and some of the proposed petrogenetic processes that occurred at depths in the mantle/crust could thus be interpreted slightly differently if e.g. other partition coefficients were used in the trace element modelling or if different values of mantle sources for the same modelling were chosen. Similarly, the general scarcity of isotope analyses representing ancient basement samples from NW Britain and the Rockall Plateau in particular could mean that the isotopic data from these regions being used in this study are not entirely representative of ther actual basement make-up. However, based on the assumption that the geochemical/isotopic interpretations of this study provide fairly reliable indications on the petrogenetic processes that gave rise to the sills in question, these results can be evaluated and contrasted with previous studies on flood basalts from Large Igneous Provinces in general (e.g. chapter 2) and also evaluated in the context of earlier studies on the host basalts of the Faroe Islands.

In this chapter, the proposed sill emplacement theory is briefly contrasted against earlier models of sill intrusions into sedimentary strata and potential applications of these models during sill emplacement into different settings are briefly considered (5.2). The structural measurements from chapter 3 are compared/contrasted against published results on tectonic events within the actual area (5.3). Potential links between earlier basaltic magmatism in the actual region and sill geochemistry is evaluated using trace element compositions, (5.4). Isotopic compositions of sills and dykes/lavas of the Faroe Islands together with earlier models on dykes/lavas from this region are contrasted against Icelandic data and earlier theories on these (5.5). A brief outline on potential future research topics, which could test many of the inferences made in this work complete this Ph.D. thesis (5.6).

5.2. Assessment of sill emplacement mechanisms

Despite the many similarities between the saucer-shaped sills from this study and sills intruded into sedimentary successions worldwide e.g. in terms of their sizes, thicknesses and general geometries, some aspects of the sill emplacement mechanisms proposed in this thesis are at odds with some of the interpretations proposed in earlier studies on the subject. Some of the major issues and potential differences regarding emplacement mechanisms and developments of saucer-shaped sills, being discussed in chapter 3, include: i) Propagation directions and geometries of developing sills are governed by differences in the mechanical properties of stratified host-rocks (Bradley, 1965; Pollard, 1973; Kavanagh et al., 2006; Thomson, 2007; Burchardt, 2008; Menand, 2008; Gudmundsson, 2011). ii) Sill climbing is initiated and maintained in response to uplift, folding and perhaps also faulting of entire sill overburdens (Pollard and Holzhausen, 1979; Fialko, 2001; Galland et al., 2003; Malthe-Sørensen et al., 2004; Hansen and Cartwright, 2006; Thomson, 2007; Goulty and Schofield, 2008; Galland et al., 2009; Galland, 2012). iii) Processes/mechanisms at more local scales, associated with small-scale inflation within the developing sills themselves, explain most characteristics observed in these kinds of intrusions, as tentatively proposed in chapter 3. iv) Saucer-shaped sills are fed by central feeders (Rasmussen and Noe-Nygaard, 1970; Malthe-Sørensen et al., 2004; Thomson, 2007) or by peripheral/marginal feeder dykes/sheets (Francis, 1982; Chevallier and Woodford, 1999; Goulty, 2005).

It is not uncomplicated to determine with any degrees of certainty, which of these mechanisms could have been in action during emplacement of the actual sills and which should be rejected alltogether, as some of these could have contributed to local characteristics within the actual intrusions. The scenario under i) is well documented from naturally occurring sills emplaced in sedimentary successions and from numerical and mechanical experiments, while sills intruded at sub-horizontal rock interfaces in volcanic settings are best documented in Iceland. The concordant Njardvik Sill (intruded at unknown depth and fed by peripheral inclined sheets) in NE Iceland was emplaced at the sub-horizontal interface between a rhyolitic unit and underlying basaltic lava flows (Burchardt, 2008), while another concordant basaltic sill (intruded at ~1200 m depth and fed by central sub-vertical dykes) from E Iceland was emplaced at the interface between sub-horizontal lava flows and tuff horizons (Gudmundsson, 2011). Althoug these two sills are intruded into settings comparable to those of the Faroe Islands, the only feeder/sill parts of these that bear resemblance to equivivalent intrusive systems within the investigated area are the inclined feeder sheets to the Njardvik Sill. It should be noted however, that these two sills from Iceland never reached scales, which are comparable to those typical for the sills of the Faroe Islands, and so may not give a correct picture of large-scale sill intrusion in this kind of settings? With respect to climbing of sheet intrusions between sub-horizontal layers of presumed different competences (Thomson, 2007; Menand, 2008), the best example from this study is displayed by the inferred feeder sheet to the NW segment of the Streymoy Sill (Fig. 3.14a), while the best examples from the actual sills themselves are displayed, where their margins seem to have been guided along sub-vertical dyke/fracture systems locally at high stratigraphic levels (Fig. 3.3a; Fig. 3.3f). There are no clear field evidences to suggest that the sub-horizontal basal sections of the investigated sills should primarily have been emplaced at interfaces between sub-horizontal layers of contrasting competences; rather the basal sections of these sills commonly cut such layers at very low angles. The scenario under ii) could in theory be responsible for the features associated with the larger sills from this study in particular, as these two intrusions undoubtedly have displaced their entire overburdens in sub-vertical directions (Fig. 3.24). Also, the linear dip of the discordant NE rim of the NW segment of the Streymoy Sill (Fig. 3.14a) could in theory point to abrupt tensile failure above a propagating intrusive margin due to sill inflation, in a similar fashion that what was described by Goulty and Schofield

(2008). Then again, apart from this solitary example, all exposed parts of the investigated sills display continuous and gradual upward-curving geometries from base to rim (Fig. 3.6). Moreover, there are no field evidences to suggest any systematic doming and associated sub-vertical fracturing of sill overburdens in response to sill inflation, as might be expected in arched semi-brittle basaltic overburden material (e.g. Pollard and Johnson, 1973). Obviously, the exact mechanism of fracture propagation, during evolution of embryonic sills, is a pertinent issue that need to be evaluated too. The splitting of host-rocks along extension fractures may occur as single fractures, as brittle faulting or as ductile faulting (Pollard, 1973). The two latter fracturing styles or a combination of these typically result from the propagation of blunt sill margins that result in multiple jointing of host-rocks around propagating sill tips (Pollard, 1973), while single fractures, in accordance with their very nature, are not expected to leave much traces in their host-rocks. As host-rocks immediately at intrusive margins to sills from this study do not appear to be significantly fractured/faulted, propagation via single fractures may have been the dominating mechanism during growth of these intrusions, as suggested in chapter 3. This inference is supported by the wedge-shaped terminations of protrusions and sills from this study (Fig. 3.8; Fig. 3.9a). If most of the smaller sills of this study indeed represent typical early stages of sill evolution in volcanic settings, as tentatively suggested in chapter 3, the slightly saucer-shaped geometries that characterise all parts these intrusions (Fig. 3.4f; Fig. 3.5) may be an argument in favour of the small-scale intrusion model under scenario iii) above, as tentatively proposed in chapter 3. This inference is chiefly based on the fact, that although the thinnest parts of these sills display clear upward-curving geometries (e.g. left hand side in Fig. 3.4f), no clear evidences of uplifts/folding are detected above these, as should be expected according to scenario ii) above.

The principal differences between the scenario, under ii) and that under iii) above, are the distinct scales and zones of elastic deformation within host-rocks to sills in each of these scenarios. Doming-folding of free surfaces above inflating large sills or laccolithic intrusions is expected to result in large-scale elastic stretching, oriented sub-parallel to the upper contacts of the developing intrusions, within the overburdens (Pollard and Johnson, 1973; Pollard and Holzhausen, 1979; Goulty and Schofield, 2008) (Fig. 5.1a). The model proposed in this study would involve small-scale sill inflation and elastic stretching within their overburdens that are sub-parallel

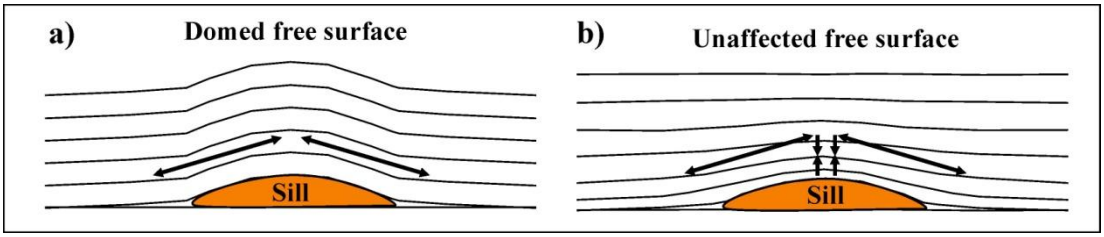

Figure 5.1. The simplifyed cartoons portray potential effects of sill inflation/dilation on their overburdens. a) Elastic deformation/stretching of overburden occur in planes sub-parallel to sill contacts during large-scale inflation and doming of the free surface. b) Same as in a), but with associated sub-vertical elastic compression components that affect host rocks relatively close to sill contacts during small-scale sill inflation. Large double-sided arrows indicate relative elastic extension while vertical double arrow sets in b indicate relative elastic compression. See text.

to intrusive contacts, in addition to elastic compression of host-rocks, being oriented broadly orthogonal to sill contacts (Fig. 5.1b). Hence, the capacity of sill overburdens to compress elastically in sub-vertical directions prior to wholesale doming/folding will in part control whether the intrusion style under scenario ii) or that under scenario iii) will prevail during sill climbing. Systematic elastic compaction/thinning of strata on either side of developing sill intrusions, the magnitude of which decrease with increasing distance from sill contacts, in response to compressive forces from sill dilation, have also been reported in earlier studies (Pollard, 1973, his Fig. 26c; Pollard and Johnson, 1973, their Fig. 18b). However, the single most important mechanism, required to generate the inferred asymmetries necessary for sill climbing to occur in the model from this study, would still be the systematic depth-dependent variations of Young's modulus in wet basaltic crust (Fig. 3.29), as reported by Schultz et al. (2006). The most obvious differences and similarities between emplacement mechanisms, inferred under scenarios ii) and iii) above, can briefly be outlined as follows:

In scenario ii), the entire sub-horizontal basal sill section is formed prior to any noticeable inflation and associated displacement of surrounding sedimentary strata (Fig. 5.2a). The subsequent asymmetrical large-scale sill inflation primarily affects sedimentary strata in the overburden, causing it to dome/fold all the way to the free surface (Fig. 5.2b). The stretching of sedimentary layers within the domed overburden will in turn generate local asymmetries of least principal stress axes σ_3 at sill margins, thus abruptly initiating sill climbing (Fig. 5.2c).

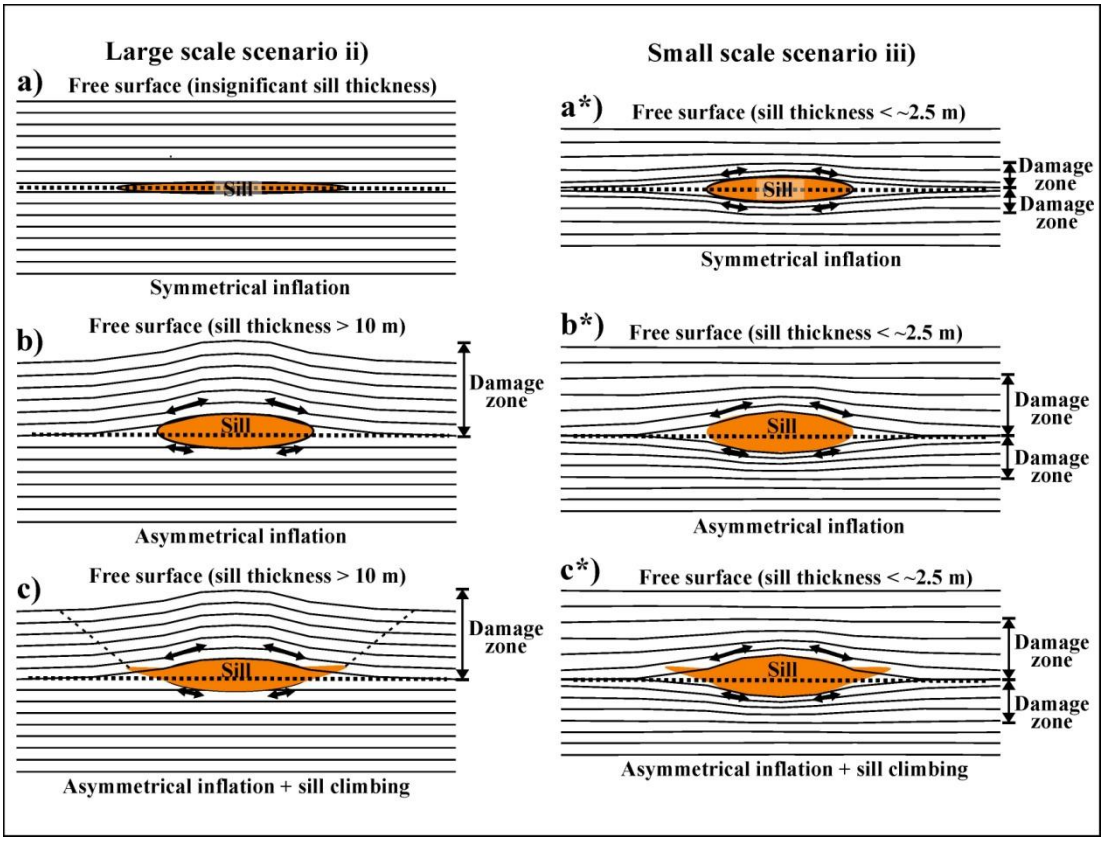

Figure 5.2. The simplified profiles portray two styles of sill emplacement mechanisms (a, b and c versus a*, b* and c*). Vertical/horizontal distances are not drawn at realistic scales. a) A thin sill propagates in sedimentary strata without displacing surrounding layers. a*) A thin sill propagates in volcanic strata thus symmetrically displacing surrounding layers. b) Wholesale uplift/folding of overburden in response to large-scale asymmetrical sill inflation. b*) Disproportional displacement of volcanic strata surrounding a sill, experiencing asymmetrical small-scale inflation. c) Sill starts climbing due to asymmetries in σ_3 at propagating margins, triggered by large-scale asymmetrical inflation. c*) Sill starts climbing due to asymmetries in σ_3 at propagating margins, triggered by small-scale asymmetrical inflation. a), b) and c) are developed from profiles presented by Pollard and Holzhausen (1979); Malthe-Sørensen et al. (2004) and Goulty and Schofield (2008) while a*), b*) and c*) are developed from profile presented by Pollard and Johnson (1973). Double-sided arrows indicate sizes and directions of relative elastic extension triggered by sill inflation. Dashed lines in c indicate potential fractures/faults while horizontal dotted lines indicate initial planes of sill emplacement/propagation. "Damage zone" refer to the sub-vertical extent of folding/doming. See text.

In scenario iii), an embryonic sill, intruded into volcanic strata, immediately start to inflate slightly and displace its host rocks, but the inflation is not large enough at first to generate any large damage zones, and hence no noticeable effects from differences in Young's modulus, on either side of intrusions (Fig. 5.2a*). A sill, intruded into volcanic strata, experience small-scale asymmetric inflation due to variations of

Young's modulus, thereby displacing host strata on either side disproportionally, i.e. the damage zone above the intrusion is larger than the damage zone below it (Fig. 5.2b*). The disproportionate sill inflation generates relatively larger stretching of volcanic strata above the intrusion than below it, thus resulting in local asymmetries of least principal stress axes σ_3 at sill margins, which initiate gradual sill climbing (Fig. 5.2c*).

As is indicated in Fig. 5.2, that the model from scenario ii) and the model proposed in this thesis differ mainly with respect to the scales at which sill inflation initiate sill climbing and with respect to the elastic/mechanical properties of their host rocks. As scenario ii) have been reported from sedimentary settings compared to the volcanic settings for scenario iii) from this study, the inferred differences in their intrusion styles could just reflect the variations in mechanical properties of sedimentary versus crystalline rock suites. Also, the extent of the damage zones on both sides of an inflating sill (e.g. Fig. 5.2) will determine the differences in average values of Young's modulus above and below the actual intrusion, as is indicated in Fig. 3.29. Some sorts of experiments may be needed in order to further constrain these theories.

With respect to scenario iv) above, the asymmetrical geometries displayed by some of the smaller sills of the Faroe Islands (Kvívík, Morskranes and Sundini sills), characterised by very thin basal sections that gradually give way to much thicker inclined rims, may at a first glance appear to be in accordance with the early stages of intrusion processes that are initiated from marginal feeders at inclined sill margins, in a similar manner to that proposed earlier for sills being intruded into sedimentary strata (e.g. Francis, 1982; Chevallier and Woodford, 1999). However, as it has been established in the course of this study, that these smaller asymmetric sills probably were fed from central feeders via their basal sections, intrusion processes broadly similar to those suggested by these two authors are not likely to have controlled the emplacements of the actual saucer-shaped sills.

The question whether aspects of the emplacement theories proposed in this thesis also could be applicable to some sills intruded into sedimentary successions remains an interesting, but unanswered possibility at the present time. Nevertheless, seismic profiles showing images of saucer-shaped sills from a number of offshore sedimentary basins worldwide commonly indicate gradual and continuous upward-curving geometries for some of these intrusions (e.g. Hansen et al., 2004; Hansen and

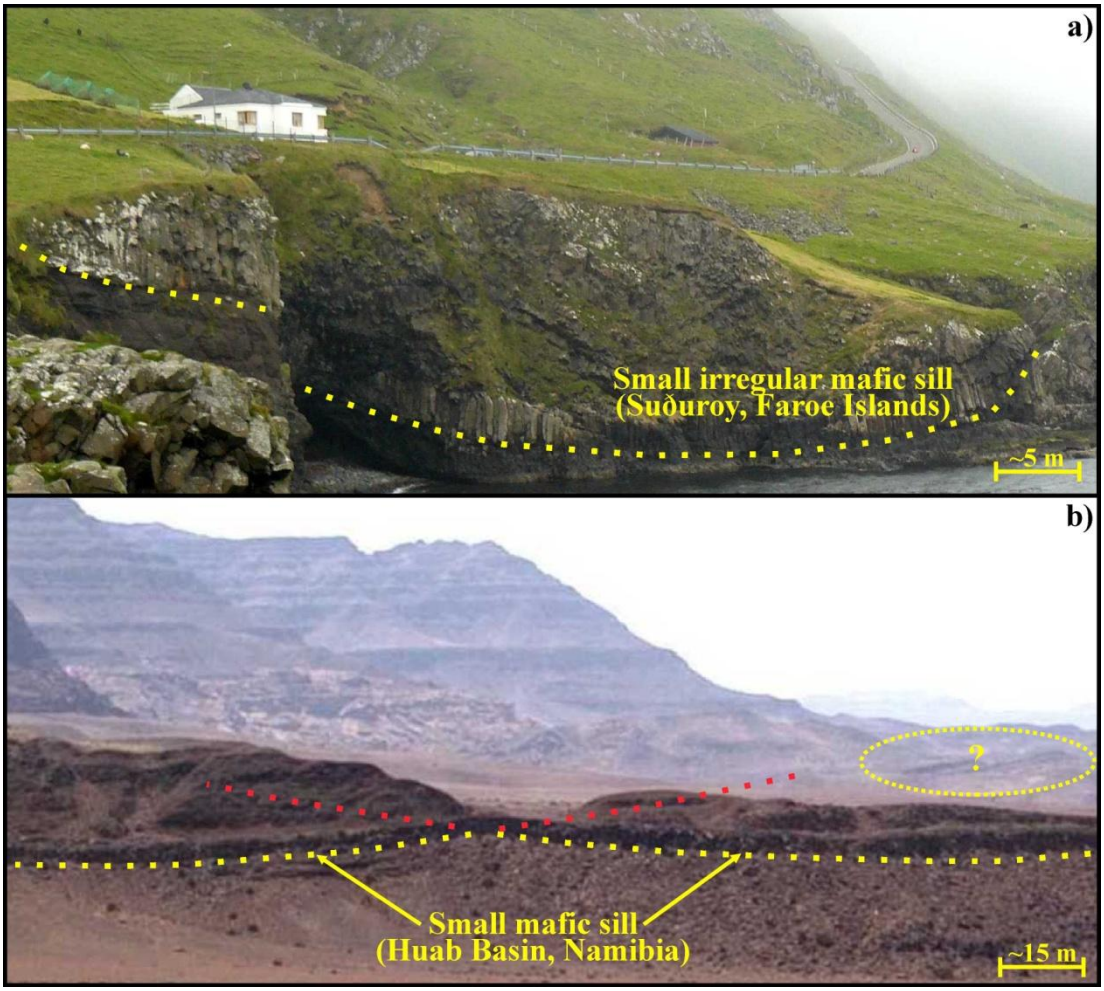

Figure 5.3. a) A small/thin irregular sill, which was intruded into a sedimentary sequence within the basaltic lava pile of the Faroe Islands, displays gradual and continuous upward-curving geometry toward both ends. b) A thin sill (segmented?), being intruded into sedimentary successions within the Huab Basin, Namibia, displays gradual and continuous upward-curving geometry from two sides toward a common point. Yellow dotted lines on both images indicate lower sill contacts. Red dotted lines indicate extrapolated continuations of lower sill contacts. Area enclosed by the densely dotted elliptic line could be a potential site of other inclined sills? See text.

Cartwright, 2006; Rocchi et al., 2007), i.e. these features are in accordance with geometries displayed by all the sill intrusions from this study. Direct evidences of gradual and continuous upward-curving geometries displayed by small mafic sills intruded into sedimentary strata can be observed in some onshore outcrops found in the Faroe Islands and in the Huab Basin, Namibia (Fig. 5.3). It is not known at which crustal depths the sills in the Huab Basin (Fig. 5.3b) were intruded, but field relationships suggest that some of the irregular small sills of the Faroe Islands (Fig. 5.3a) were emplaced at very shallow levels. The curved geometries displayed by all parts of these two small sills seem to suggest that the stress fields around their

margins were asymmetrical during all stages of propagation. Vertical differences in compressibility (Young's modulus) of host-rocks on both sides of these intrusions could potentially have resulted in the inferred continuous stress asymmetries, but continuous uplifts of entire overburdens at infinitesimal intervals immediately above the propagating edges of these intrusions during emplacements also remains an alternative explanation.

5.3. Sill deformation structures in a regional context

Faults and fractures are conspicuous features within many of the saucer-shaped sills of the Faroe Islands and in host-rocks adjacent to these. Measurements have been done on some of the most prominent/visible of these deformation structures, but as the current project is not aiming at structural interpretations in particular, features that would have been detected in a more extensive structural study may not have been recorded in the course of this work. Relative to the actual sills the recorded deformation structures could have been produced by syn-magmatic and/or post-magmatic processes (chapter 3). Many of the sub-vertical structures/displacements in host-rocks immediately at sill contacts (e.g. Fig. 3.23) probably originate from processes related to the emplacements of these intrusions, but deformation structures within the sills themselves (e.g. Fig. 3.24; Fig. 3.25) can only be grouped according to their relative ages. As absolute ages have not been determined on any of these intrusions at the present time, establishments of potential correlations between measured structures/features observed within these sills and measurements and interpretations of comparable structures recorded outside these sills during earlier studies may help to ascertain their status in a local or regional context.

A recent comprehensive structural study on the basalts of the Faroe Islands has pointed to the occurrence of a broadly E–W directed regional shortening event at ~55 Ma, which also affected some of the saucer-shaped sills in the actual area (Walker et al., 2011, stage 4 in their Fig. 14b). The broadly WNW–ESE directed reverse movements recorded in the Streymoy Sill in the course of this study (e.g. Fig. 3.26) seems to be in accordance with this compressional event and the same seems to be the case for the broadly E–W directed pervasive fracturing/jointing observed within most sills (e.g. Fig. 3.25). As extrusion of the uppermost parts of the lava pile of the Faroe Islands (the Enni Formation) took place at ~55 Ma. (Storey et al., 2007), deformation of some of the sills of the Faroe Islands by the recorded E–W shortening

event would mean that these were emplaced shortly following the cessation of extrusive activity in the area, if the age estimate of ~55 Ma for this deformation episode is reliable within reasonable margins.

The deformation phase involving broadly NW–SE directed extension, inferred to have generated sub-vertical NE–SW trending faults/fractures in some of the investigated sills (e.g. Fig. 3.25), would be in agreement with the direction of minimum horizontal stress suggested to have occurred in the actual region during an estimated time span from chrons 24 to 21, i.e. ~55 to ~48 Ma (Geoffroy et al., 1994, their Fig. 5c) as well as corresponding to more recent interpretations of extension in the same area estimated at ~48 Ma (Walker et al., 2011, stage 5 in their Fig. 14c). If this recorded NW–SE directed extension event at ~48 Ma or earlier indeed produced the observed NE–SW faults/fractures observed within the actual sills, additional deformation episodes that must have occurred subsequent to ~48 Ma resulted in: i) strike-slip movements along NE–SW trending sub-vertical fractures that produced fibre lineation (Fig. 3.24c), ii) overprinting of these lineation features at an even later stage by E–W directed strike-slip movements in the sub-horizontal plane (Fig. 3.24c) and iii) strike-slip movements along E–W trending sub-vertical fractures that resulted in slight sinistral displacements of intersecting NE–SW trending sub-vertical fractures (Fig. 3.24b). Previous studies have argued in favour of an Oligocene N–S directed compressional event to the east of the Faroe Islands (Boldreel and Andersen, 1998) and a single WNW–ESE extensional pulse in areas around and within the Norwegian Sea in Oligocene–Miocene times (Doré et al., 1999) while other studies

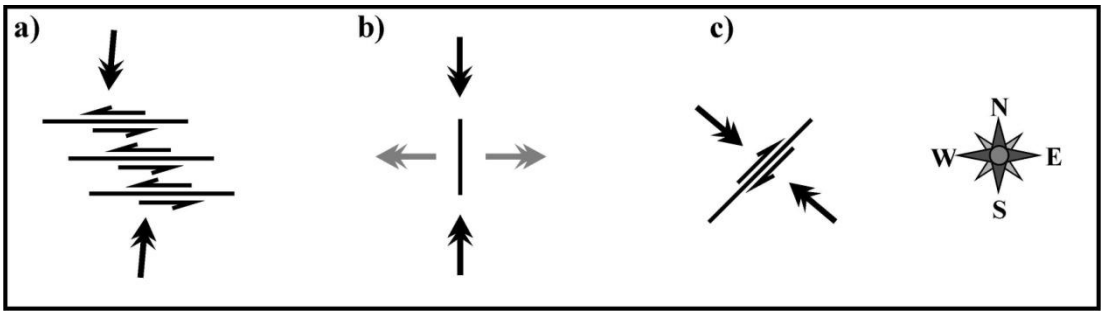

Figure 5.4. a) N–S directed Oligocene compression and associated transpression generates sinistral strike-slip movements in reactivated E–W trending fractures. b) Minimum E–W directed horizontal stress from N–S directed Oligocene shortening result in N–S trending sub-vertical normal faults. c) NW–SE directed Miocene compression/transpression generates dextral strike-slip movements in reactivated NE–SW trending fracture. Full black arrows indicate regional compression. Grey arrows indicate minimum horizontal stress. One sided arrows indicate strike-slip movements. See text.

have suggested an episode with Miocene NW–SE oriented compression in the region around and within the Faroe Islands (Boldreel and Andersen, 1998; Walker et al., 2011, stage 6 in their Fig. 14d). It is unclear whether the inferred Oligocene–Miocene extensional pulse (Doré et al., 1999) could have affected the region encompassing the Faroe Islands. However, local sinistral transpression from the suggested N–S directed Oligocene compression event could have reactivated some E–S trending fractures within some of the investigated sills (Fig. 5.4a), N–S trending normal faults occurring at some inclined sill margins could potentially have formed in response to the reported Oligocene N–S compression (Fig. 5.4b), although local sagging could be an alternative explanation. The Miocene NW–SE oriented compression event could have resulted in local dextral transpression and reactivation of E–W trending fractures, thus producing dextral movements in some sub-vertical specimen of these (Fig. 5.4c). The slip movements that produced the E–W directed fibre lineation observed in some sub-horizontal fractures may be related to one of these events, they could also result from a later regional event has not been recorded yet or they may have a more local origin.

5.4. Evaluation of sill geochemistry in a wider framework

The mantle/lithosphere in many regions of the North Atlantic Igneous Province (NAIP) could have been affected by the complex geological history of this part of the northern hemisphere during tectonic/igneous events that preceded the bulk of magmatism that eventually gave rise to the Early Cenozoic igneous products encountered in this province. Such potential effects on the mantle/lithosphere could result from contamination with recycled (subducted/delaminated) crustal material, from various sorts of mantle metasomatism and/or from earlier melting events that may have resulted in compositional heterogeneities in the mantle/lithosphere and lithospheric weakening (chapter 2). Previous theories on basalt petrogenesis within the NAIP have suggested melt formation from a variety of potential sources including mantle plumes of various sizes and depths of origin and/or upper mantle sources possessing various degrees of heterogeneities with respect to both rock compositions and/or fluid contents (chapter 2; chapter 4).

The inferred petrogenesis of the sills from this study by melting of a variously metasomatised sub-continental lherzolitic mantle (chapter 4; see also Fig. 2.4c) is at odds with earlier theories that argue in favour of magma supplies from a deep-rooted

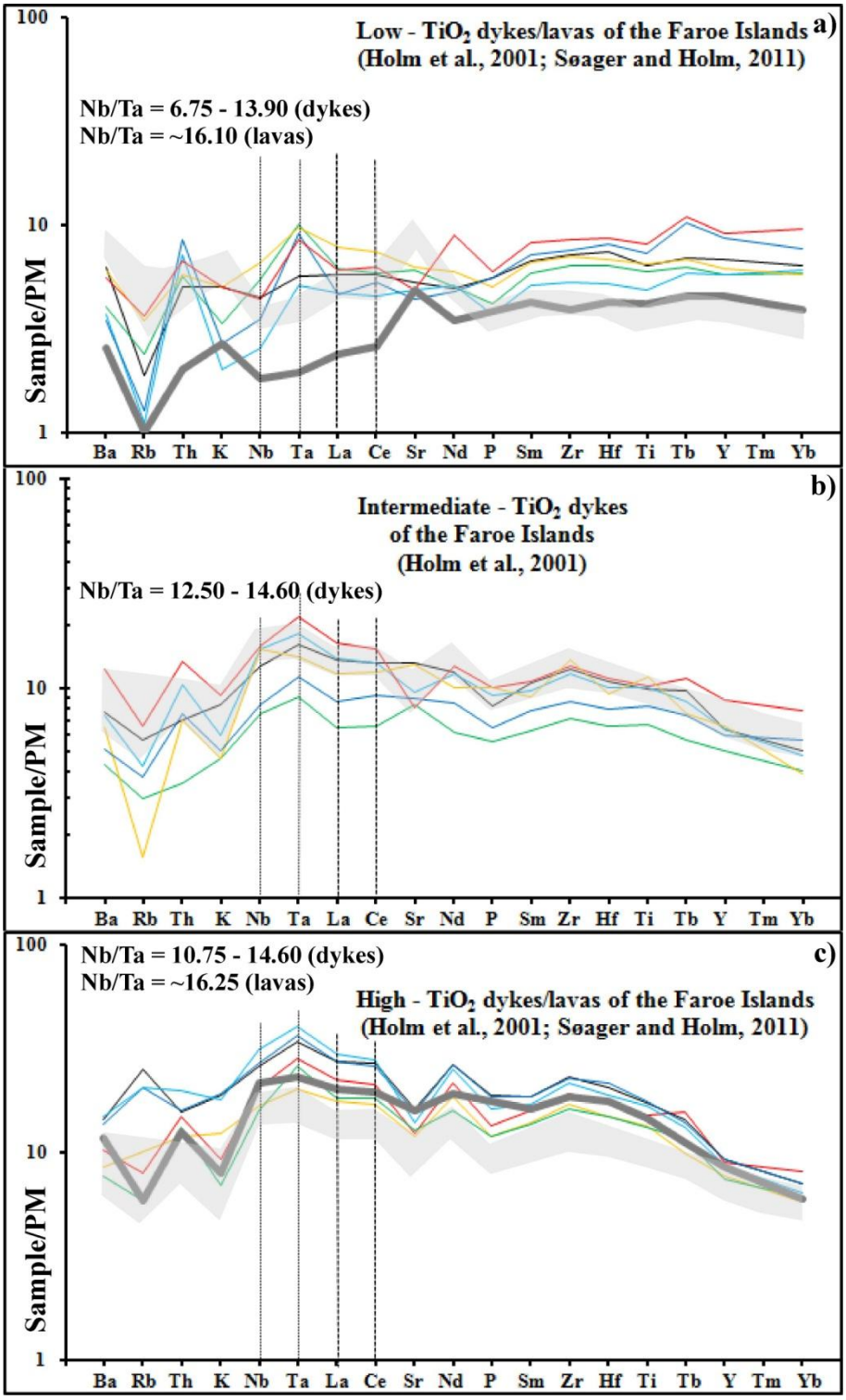

Figure 5.5. a) Representative low-TiO_2 dykes of the Faroe Islands (coloured lines) display strong depletion in Nb and enrichment in Ta relative to La and Ce whereas equivalent lavas (bold grey line) are moderately depleted with respect to Nb and Ta. Shaded field represents low-TiO_2 sills. b) Representative intermediate-TiO_2 dykes from the same region display strong enrichment in Ta and slight enrichment in Nb for some samples relative to La and Ce. Shaded field represents high-TiO_2 sills. c) Samples representing high-TiO_2 dykes from the actual area display Ta and Nb characteristics relative to La and Ce that are broadly similar to those of the intermediate-TiO_2 dykes while equivalent

lavas (bold grey line) are moderately enriched in these elements. Shaded field represents high-TiO_2 sills. Normalising values are as in Fig. 4.12. See text.

mantle plume during formation of lavas/dykes of the Faroe Islands (Holm et al., 2001; Søager and Holm., 2011; see also Fig. 2.4a).

The sills from this study are generally not very different from most of the (older) basaltic dykes/lavas of the Faroe Islands with respect to major element compositions (Fig. 4.10). Comparisons of trace elements representing sills from this study with representative lava/dyke samples from the actual area as presented in multi-element diagrams normalised to primitive mantle values (Sun and McDonough, 1989), reveal substantial differences between trends representing low-TiO_2 sill samples and those representing low-TiO_2 dykes (Fig. 5.5a) whereas high-TiO_2 sills display trends that are broadly similar to those of many samples from the intermediate-TiO_2 and high-TiO_2 dykes although the overall concentrations in the actual elements in sills versus dykes may differ somewhat (Fig. 5.5b; Fig. 5.5c). Low-TiO_2 lavas from the actual region display overall lower concentrations in their incompatible elements relative to the sills (Fig. 5.5a) while high-TiO_2 sills and lavas display broadly similar trace element characteristics (Fig. 5.5c). Some of the most notable differences in trace element compositions between sills and dykes irrespective of their TiO_2 contents include their relative Nb and Ta concentrations, where those representing the sills show relatively flat normalised trends compared to relatively steep positive slopes for these two elements in most of the normalised dyke samples (Fig. 5.5). The Nb/Ta ratios in the low-TiO_2 dykes range from 6.75 to 13.90 whereas ratios for these elements range from 10.75 to 14.60 in dykes with high and intermediate TiO_2 compositions (Fig. 5.5). Only the Morskranes Sill displays a comparable low Nb/Ta ratio of ~14.7 whereas all the other investigated sills display relatively uniform slightly super-chondritic ratios with average values of ~16.5 (Table 4.3). The lavas shown in Fig. 5.5 display Nb/Ta ratios (16.10 – 16.25) that are broadly similar to those of most sills from this study. The wide range in Nb/Ta ratios displayed by the dykes may point to mantle sources that are significantly more heterogeneous compared to the mantle sources to most of the sills in question. As fractionation of Nb versus Ta towards lower Nb/Ta ratios commonly is interpreted to occur in response to processes associated with Ti-bearing minerals such as rutile and the subduction of oceanic crust (e.g. Münker, 1998; Xiong et al., 2005), the low Nb/Ta

ratios in many basaltic dyke samples from the Faroe Islands could reflect the presence of components originating from ancient recycled oceanic crust or a mantle wedge. At a first glance, the large differences in Nb/Ta ratios for sills versus local basaltic dykes seem to suggest that the potential metasomatism inferred to have influenced the mantle sources to most sills from this study was not significantly affected by previous local Early Cenozoic basaltic magmatism, like it is tentatively suggested in chapter 4. However, as the ratios of these two elements in both high-TiO_2 and low-TiO_2 lava samples from the actual area resemble those of equivalent sills (Fig. 5.5a; Fig. 5.5c), lavas and sills could originate from common sources, or the fluids originating from the lava sources may have metasomatised the sill sources. It is puzzling that most high/intermediate/low-TiO_2 basalt samples from the study of Holm et al. (2001) display Nb/Ta ratios markedly different from those obtained in the study of Søager and Holm (2011) and those of the current study, but it is unclear whether potential differences in analytical techniques could have played any role in yielding these contrasting results. If the inferred mantle metasomatism originated from sources other than local magmatism this could point to the activities of other geological events within this part of the North Atlantic area prior to the igneous activity that generated the local lava pile (chapter 2). If mantle sources to both sills/lavas and dykes indeed were contaminated/enriched by different mantle processes being linked to previous tectonic/igneous events and perhaps also to recycled material from earlier episodes with crustal subduction or delamination, the complex geological history of the North Atlantic region could have imposed control on some of the geochemical signatures observed in Early Cenozoic igneous products of the Faroe Islands.

A mechanism with production of high-TiO_2 and low-TiO_2 sills by low and high degrees of partial melting respectively, as proposed for sills from this study, would be in accordance with results from earlier studies on basalts from E Greenland and the Faroe Islands, but it would be at odds with previous studies suggesting continuous replenishment/tapping/fractionation (RTF) as the main process that resulted in the generation of high-TiO_2 basalts from low-TiO_2 basaltic magmas in Early Cenozoic basalts of W Greenland (Larsen and Pedersen, 2009). A similar evolution of high-TiO_2 sills in the Faroe Islands by RTF from low-TiO_2 magmas could explain much of the differences in trace element and REE concentrations between these two basalt groups. However, as Nb and Ta are not noticeably

fractionated relative to e.g. La and Ce during partial melting to produce basalts or during fractional crystallisation of typical basaltic minerals (e.g. Fig. 4.31a; Fig. 4.31b), it is not likely that the moderately negative Nb and Ta anomalies in low-TiO_2 sills within the actual region could have developed into the moderately positive Nb and Ta anomalies that characterise most of the high-TiO_2 sills from this study by RTF processes (e.g. Fig. 4.12).

5.5. Evaluation of isotope compositions in a wider framework

The very limited amount of isotopic data from the current work renders it problematic to be conclusive about possible pre-magmatic developments in potential mantle sources, but based on the observed characteristics a few inferences can be made. As the $^{207}Pb/^{204}Pb$ versus $^{208}Pb/^{204}Pb$ ratios of sill samples from the Faroe Islands are encompassed by fields that represent ratios of these isotopes in basalts/picrites encountered in lavas from Iceland and dykes/lavas exposed in the Faroe Islands (Fig. 5.6), previous interpretations on source characteristics from these regions may be pertinent to the current study.

Holm et al. (2001) proposed that the development of Pb isotopic variations among presumed uncontaminated picritic/basaltic magmas of the Faroe Islands originated from three main mantle components being a Faroe Islands main plume source, a depleted plume source and a high $^{206}Pb/^{204}Pb$ ratio plume source (Fig. 5.6). More specifically, they suggested the derivation of low-TiO_2 magmas from the depleted mantle source, the derivation of high-TiO_2 magnesian lavas from mixtures of this depleted source with a high $^{206}Pb/^{204}Pb$ ratio source and the derivation of basaltic high-TiO_2 dykes from the main Faroe Islands plume component (Fig. 5.6). Holm et al. (2001) used Pb isotopic compositions of low-TiO_2 picrites to define the isotopic composition of their inferred depleted mantle source, but the Pb isotopic range of these picrites also reach values defined by average $^{207}Pb/^{204}Pb$ ratios of Theistareykir basalts and NAEM (Figure 5.6). Low-TiO_2 basalts from the study of Holm et al. (2001) mostly plot adjacent to average values of Theistareykir/NAEM and their main plume component. Isotopic compositions of the basaltic high-TiO_2 dykes mostly straddle the inferred main Faroe Islands plume source (Holm et al., 2001). Based on the assumption that crustal contamination was insignificant during evolution of most basalts from the Faroe Islands, Holm et al. (2001) further suggested that their proposed Faroe Islands main plume source and depleted plume source were not

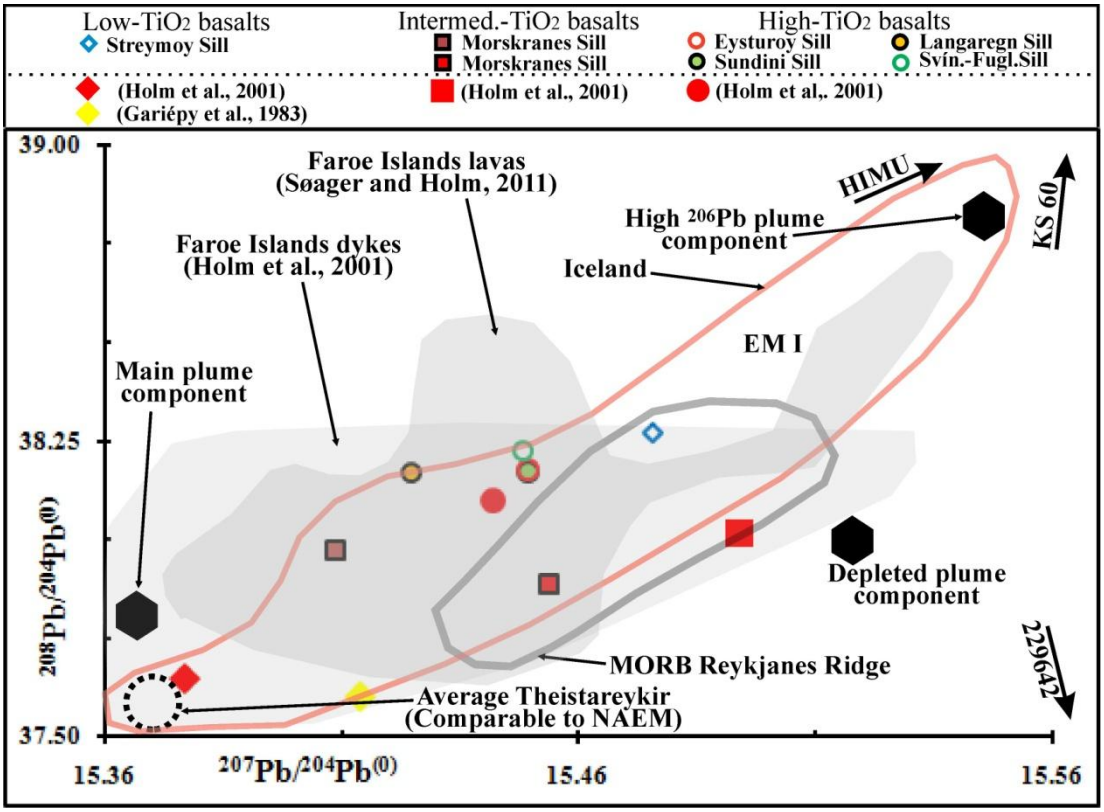

Figure 5.6. Holm et al. (2001) invoked a three-component model in order to explain the Pb isotopic compositions of dykes/lavas of the Faroe Islands. Large octagons indicate their proposed end-member mantle sources while dashed line points towards their inferred crustal contaminants. Light grey shaded field indicates Pb isotopic ratios of dykes/lavas of the Faroe Islands (Holm et al., 2001) while darker grey shaded field indicates Pb isotopic ratios of high-TiO_2 and low-TiO_2 lavas from the same area (Søager and Holm, 2011). Red and grey outlines indicate isotopic data from Iceland and Reykjanes Ridge respectively (Mertz and Haase, 1997). Dotted circle represent average isotopic data from Theistareykir, Iceland (Mertz and Haase, 1997; Stracke et al., 2003). Arrows labelled KS 60 and 229642 indicate directions to isotope ratios of these two basement samples from E Greenland. See text.

represented in later Icelandic and Reykjanes Ridge rocks/magmas, but were particular features that occurred only in the Faroe Islands region. Søager and Holm (2011) invoked a broadly similar scenario with basalt genesis from three end-member mantle plume sources possessing isotopic components similar to NAEM and an enriched EM-type component as well as a component somewhere intermediate between those two. Other interpretations of potential mantle sources giving rise to basalts within the actual region have pointed to the probable existence of two distinct depleted upper mantle sources perhaps including the sub-continental lithospheric mantle (Gariépy et al., 1983).

A model with three mantle components has also been suggested in an earlier study in order to explain the entire isotopic range of volcanic rocks encountered in Iceland (Hanan and Schilling, 1997), but where the Pb isotopic range outlined by the individual mantle components display a wider span toward more depleted and enriched Pb isotopic compositions respectively than the three end-members that have been inferred for the Faroe Islands earlier (Fig. 5.6). These three Icelandic end-member mantle sources labelled p, d and e by these authors have been estimated at: p $\rightarrow$ $^{207}Pb/^{204}Pb$ = 15.59, $^{208}Pb/^{204}Pb$ = 39.45; d $\rightarrow$ $^{207}Pb/^{204}Pb$ = 15.13, $^{208}Pb/^{204}Pb$ = 35.60; e $\rightarrow$ $^{207}Pb/^{204}Pb$ = 15.85, $^{208}Pb/^{204}Pb$ = 39.00, where p is assumed to represent an EM I-like reservoir (Hanan and Schilling, 1997). However, Stracke et al. (2003) attributed the impressive correlation observed between radiogenic isotope ratios of Icelandic basalts to contributions from a HIMU-like component to a depleted end-member source comparable in Pb composition to Theistareykir picrites, perhaps also with the involvement of small amounts of an enriched component similar to an enriched mantle EM I- type source. Hence, Stracke et al. (2003) infer a mechanism and an initial uncontaminated depleted end-member mantle source that fits parts of the model proposed earlier for the generation of basalts of the BTIP (Ellam and Stuart, 2000). Although the $^{208}Pb/^{204}Pb$ ratios of most sills from this study plot at the upper limit of the isotopic field representing Icelandic basalts, they define the same good isotopic correlation (Fig. 5.6), thus perhaps implying similarities in pre-magmatic mantle processes between these two regions. Apart from the wider range of Pb isotopic ratios of the Icelandic basalts/picrites compared to those of similar rocks from the Faroe Islands, the main differences in the Pb isotopic ratios between these two regions are exhibited by slightly more elevated $^{208}Pb/^{204}Pb$ ratios at low $^{207}Pb/^{204}Pb$ ratios and slightly lower $^{208}Pb/^{204}Pb$ ratios at higher $^{207}Pb/^{204}Pb$ ratios in rocks from the Faroe Islands compared to those encountered in Iceland and in part also at the Reykjanes Ridge (Fig. 5.6). According to Holm et al. (2001), these differences could be ascribed to differences in end-member mantle sources, provided that no crustal contamination was involved. The discussion in the isotope part of chapter 4 strongly suggested the involvement of local crustal contaminants heavily enriched with respect to their $^{208}Pb/^{204}Pb$ ratios during evolvement of two of the four contaminated silicic basalt samples of the Faroe Islands (Yellow circle and red rhombus in: Fig. 4.21d; Fig. 4.21f; Fig. 4.23e; Fig. 4.23f). Also, contamination with high $^{207}Pb/^{204}Pb$ ratio (and low $^{208}Pb/^{204}Pb$ ratio) crustal material could potentially

explain the observed variations of these isotopes within parts of the Morskranes Sill (Fig. 4.22). Mixing calculations in chapter 4 further demonstrated that assimilation of even very small amounts (< 0.5%) of virtually any kind of basement material could affect isotopic compositions of individual samples noticeably (Fig. 4.20b). Hence, contributions to some of the basalt samples presented in Holm et al. (2001) with only fractions of a percent of materials possessing Pb isotopic compositions comparable to e.g. basement samples KS60 or 229642 from E Greenland, could in theory generate enrichments or depletions in the $^{208}Pb/^{204}Pb$ ratios of individual basalt/picrite samples of the Faroe Islands at scales that could account for many of the observed differences in $^{208}Pb/^{204}Pb$ ratios between rocks from this region and those encountered in Iceland (Fig. 5.6). In general, ~0.5% assimilation of basement material, with ~15 ppm Pb and with $^{208}Pb/^{204}Pb$ ratios being ~5 higher/lower than those of contaminated basalts possessing Pb concentrations of ~0.5 ppm, would result in a ~0.65 increase/decrease in values of $^{208}Pb/^{204}Pb$ ratios of the target basalts. However, it is not straightforward to test potential small-scale assimilation by means of e.g. REE compositions, as LREE enrichments from crustal contamination at such insignificant scales would hardly be detectable in contrast to the LREE enrichment associated with the 10 – 15% basement assimilation encountered by the contaminated silicic basalt sample K-1 of the Faroe Islands (large yellow circle, Fig. 4.13e: Fig. 4.20a).

As the observed systematic correlation in $^{207}Pb/^{204}Pb$ versus $^{208}Pb/^{204}Pb$ ratios of most sills from this study is in good accordance with the trend observed for these isotope ratios in Icelandic basalts (Fig. 5.6), similar processes could have modified the mantle sources of both regions. Hence, a process with systematic isotopic enrichments of a depleted end-member primitive mantle source comparable in isotopic composition to NAEM or Theistareykir picrites (e.g. Ellam and Stuart, 2000; Stracke et al., 2003) may be applicable for mantle sources to the actual sills, although local mantle metasomatism (e.g. chapter 4) could have played some role too. Some MgO-rich rocks of the Faroe Islands display Pb isotopic compositions akin to those of isotopically depleted rocks from Theistareykir, Iceland (red and yellow rhombuses in Fig. 5.6) while samples representing the Morskranes Sill in turn display depleted $^{206}Pb/^{204}Pb$ and $^{87}Sr/^{86}Sr$ ratios that are broadly similar to these same local MgO-rich rocks (Fig. 4.18a). Hence, an origin from a depleted source may be envisaged for the Morskranes Sill. Although the possibility of hybridisation between melts of the Morskranes Sill and melts with compositions comparable to some of the high-TiO_2

sills of this study was left open in chapter 4 (e.g. Fig. 4.24c; Fig. 4.25), the lack of systematic correlations in Pb versus Sr and Nd isotopic ratios of the Morskranes Sill with any of the other (LREE enriched) sills of the Faroe Islands (Fig. 4.18) renders this scenario rather unlikely. Hence, there is no robust evidence to suggest that the opserved spread in $^{207}Pb/^{204}Pb$ ratios within the small Morskranes Sill (Fig.5.6) should result from various input of magmas from two distinct mantle sources. Instead, it is tentatively suggested that the higher $^{208}Pb/^{204}Pb$ and $^{207}Pb/^{204}Pb$ ratios displayed by samples of this sill relative to local MgO-rich rocks (and rocks of Theistareykir) as well as the observed internal isotopic differences resulted from very slight (< 0.5%) contamination with crustal material.

5.6. Potential future research topics

A number of interpretations and inferences on geochemical, isotopic and physical aspects, thought to have been associated with the petrogenesis and emplacement of seven saucer-shaped sills of the Faroe Islands, have been made in the course of the current Ph.D. project. However, in order to further constrain a few of the proposed processes and models, some additional analyses and testing would be desirable in a potential future continuation of the current work. Such future research topics could include:

(1) Whole-rock ICP-MS analyses of additional sill samples in order to get a better coverage of the trace element (including the REE) compositions of these intrusions. Whole-rock isotope analyses of additional sill samples in order to reveal potential internal isotopic variations within individual sills.

(2) Microprobe analyses of selected minerals in order to detect the provenance of unknown minerals of the Morskranes Sill. Microprobe analyses of selected minerals (plagioclase and clinopyroxene) and their melt inclusions in order to perform geothermobarometric calculations and to detect paths of melt evolution.

(3) Absolute dating of all the investigated sills by means of the argon–argon and/or the rhenium–osmium methods in order to establish potential differences in emplacement ages between individual sills and to establish the geochronological status of the actual sills in a regional and provincial context.

(4) Geochemical analyses of vertical profiles from selected sills of this study in order to detect potential multiple magma pulses and to investigate if in-situ fractional crystallisation had any bearing on geochemical/mineralogical distributions.

(5) A series of comprehensive mechanical experiments/modelling in order to test the effect of systematic depth-related variations of Young's modulus on sill emplacement processes.

References

Abdel-Rahman, A-F. M. and Nassar, P. 2004. Cenozoic volcanism in the Middle East: petrogenesis of alkali basalts from northern Lebanon. Geological Magazine 141(5), 545-563.

Abrahamsen, N. 2006. Palaeomagnetic results from the Lopra-1/1A re-entry well, Faroe Islands. Geological Survey of Denmark and Greenland Bulletin 9, 51-65.

Aigner-Torres, M., Blundy, J., Ulmer, P. and Pettke, T. 2007. Laser Ablation ICPMS study of trace element partitioning between plagioclase and basaltic melts: an experimental approach. Contributions to Mineralogy and Petrology 153, 647–667.

Albarede, F. and Van der Hilst, R. D. 2002. Zoned mantle convection. Philosophical Transactions of the Royal Society, London.A. 360, 2569-2592.

Anderson, D. L. 1982. Isotopic evolution of the mantle: a model. Earth and Planetary Science Letters 57, 13-24.

Anderson, D. L. 2005. Large igneous provinces, delamination, and fertile mantle. Elements 1, 271-275.

Anderson, D. L. 2006. Speculations on the nature and cause of mantle heterogeneity. Tectonophysics 416, 7-22.

Archer, S. G., Bergman, S. C., Iliffe, J., Murphy, C. M. and Thornton, M. 2005. Palaeogene igneous rocks reveal new insights into the geodynamic evolution and petroleum potential of the Rockall Trough, NE Atlantic Margin. Basin Research 17, 171-201.

Baer, G. 1991. Mechanisms of dike propagation in layered rocks and in massive, porous sedimentary rocks. Journal of Geophysical Research 96(B7), 11911-11929.

Baer, G., Beyth, M. and Reches, Z. 1994. Dikes emplaced into fractured basement, Timna Igneous Complex, Israel. Journal of Geophysical Research 99(B12), 24039-24050.

Baker, M. B. and Stolper, E. M. 1994. determining the composition of high-pressure mantle melts using diamond aggregates. Geochimica et Cocmochimicia Acta 58(13), 2811-2827.

Barrat, J. A., Fourcade, S., Jahn, B. M., Cheminée, J. L. and Capdevila, R. 1998. Isotope (Sr, Nd, O) and trace-element geochemistry of volcanics from the Erta'Ale range (Ethiopia). Journal of Volcanology and Geothermal Research 80, 85-100.

Barton, A. J. and White, R. S. 1997. Crustal structure of Edoras Bank continental margin and mantle thermal anomalies beneath the north Atlantic. Journal of Geophysical Research 102(B2), 3109-3129.

Bédard, J. H. 2005. Partitioning coefficients between olivine and silicate melts. Lithos 83, 394–419.

Beier, C., Haase, K. M., Abouchami, W., Krienitz, M-S. and Hauff, F. 2008. Magma genesis by rifting of oceanic lithosphere above anomalous mantle: Terceira Rift, Azores. Geochemistry Geophysics Geosystems 9(12), Q12013, 1-26.

Bell, B. and Butcher, H. 2002. On the emplacement of sill complexes: evidence from the Faroe-Shetland Basin. From: Jolley, D. W. & Bell, B. R. (eds) The North

Atlantic Igneous Province: Stratigraphy, Tectonic, Volcanic and Magmatic Processes. Geological Society, London, Special Publications 197, 307-329.

Berlo, S., Turner, J. and Blundy, C. H. 2004. The extent of U-series disequilibria produced during partial melting of the lower crust with implications for the formation of the Mount St. Helens dacites. Contributions to Mineralogy and Petrology 148, 122-130.

Berndt, C., Planke, S., Alvestad, E., Tsikalas, F. and Rasmussen, T. 2001. Seismic volcanostratigraphy off the Norwegian margin: constraints on tectonomagmatic break-up processes. Journal of the Geological Society, London 158, 413-426.

Bernstein, S. 1994. High-pressure fractionation in rift-related basaltic magmatism: Faeroe plateau basalts. Geology 22, 815-818.

Bernstein, S., Brooks, C. K. and Stecher, O. 2001. Enriched component of the proto-Icelandic mantle plume revealed in alkaline Tertiary lavas from East Greenland. Geology 29(9), 859–862.

Blatt, H. and Tracy, R. J. 1995. Petrology, Igneous, Sedimentary, and Metamorphic. Second edition. W. H. Freeman and Company, New York. pp. 529.

Blichert-Toft, J., Lesher, C. E. and Rosing, M. T. 1992. Selectively contaminatcd magmas of the Tertiary East Greenland macrodyke complex. Contributions to Mineralogy and Petrology 110, 154-172.

Blystad, P., Brekke, H., Faerseth, R. B., Larsen, B. T., Skogseid, J. and Tørrudbakken, B. 1995. Structural elements of the Norwegian continental margin. Norwegian Petroleum Directorate Bulletin No 8.

Boldreel, L. O. and Andersen, M. S. 1993. Late Paleocene to Miocene compression in the Faeroe-Rockall area. Petroleum Geology of Northwest Europe: Proceedngs of the 4th.Conference Geological Society, London 1025-1034.

Boldreel, L. O. and Andersen, M. S. 1998. Tertiary compressional structures on the Faroe-Rockall Plateau in relation to northeast Atlantic ridge-push and Alpine foreland stresses. Tectonophysics 300, 13-28.

Bonatti, E. 1990. Not so hot "hot spots" in the oceanic mantle. Science 250, 107-110.

Borghini, G., Fumagalli, P. and Rampone, E. 2010. The stability of plagioclase in the upper mantle: Subsolidus experiments on fertile and depleted lherzolite. Journal of Petrology 51(1-2), 229-254.

Boström, K. and Bach, W. 1995. 10.Data report: Chemical analyses of basaltic rocks: An interlaboratory comparison. In: Batiza, R., Storms, A. and Allan, J. F. (eds) 1995. Proceedings of the Ocean Drilling Program. Scientific Results 142, 75-81.

Bott, M. H. 1985. Plate tectonic evolution of the Icelandic Transverse Ridge and adjacent regions. Journal of Geophysical Research 90(B12), 9953-9960.

Bott, M. H. P. 1987. The continental margin of central East Greenland in relation to North Atlantic plate tectonic evolution. Journal of the Geological Society, London 144, 561-568.

Bott, M. H. P., Sunderland, J., Smith, P. J., Casten, U. and Saxov, S. 1974. Evidence for continental crust beneath the Faeroe Islands. Nature 248, 202-204.

Bradley, J. 1965. Intrusion of major dolerite sills. Transactions of the Royal Society of New Zealand, 3, 27–54.

Brekke, H., Dahlgren, S., Nyland, B. and Magnus, C. 1999. The prospectivity of the Vøring and Møre basins on the Norwegian Sea continental margin. Petroleum Geology of Northwest Europe: Proceedngs of the 5th.Conference, Geological Society, London 261-274.

Brown, P. E., Parsons, I. and Becker, S. M. 1987. Peralkaline volcanicity in the Arctic Basin-the Kap Washington Volcanics, petrology and palaeotectonics. Journal of the Geological Society, London 144, 707-715.

Bryan, S. E. and Ernst, R. E. 2008. Revised definition of Large Igneous Provinces (LIPs) Earth-Science Reviews 86, 175–202.

Bugge, T., Prestvik, T. and Rokoengen, K. 1980. Lower Tertiary volcanic rocks off Kristiansund, mid Norway. Marine Geology 35, 277-286.

Bull, J. M. and Masson, D. G. 1996. The southern margin of the Rockall Plateau: stratigraphy, Tertiary volcanism and plate tectonic evolution. Journal of the Geological Society, London 153, 601-612.

Burchardt, S. 2008. New insights into the mechanics of sill emplacement provided by field observations of the Njardvik Sill, Northeast Iceland. Journal of Volcanology and Geothermal Research 173, 280-288.

Burke, K. and Dewey, J. F. 1973. Plume-generated triple junctions: key indicators in applying plate tectonics to old rocks. Journal of Geology 81, 406-433.

Callot, J-P., Geoffroy, L. and Brun, J-P. 2002. Development of volcanic passive margins: three-dimensional laboratory models. Tectonics 21(6), 2.1- 2.13.

Campell, I. H. and Griffits, R. W. 1990. Implications of mantle plume structure for the evolution of flood basalts. Earth and Planetary Science Letters 99, 79-93.

Cartwright, J. and Hansen, D. M. 2006. Magma transport through the crust via interconnected sill complexes. Geology 34(11), 929-932.

Chalmers, J. A. 1991. New evidence on the structure of the Labrador Sea/Greenland continental margin. Journal of the Geological Society, London 148, 899-908.

Chalmers, J. A. 1997. The continental margin off southern Greenland: along-strike transition from an amagmatic to a volcanic margin. Journal of the Geological Society, London 154, 571-576.

Chalmers, J. A., Larsen, L. M. and Pedersen, A. K. 1995. Widespread Palaeocene volcanism around the North Atlantic and Labrador Sea: evidence for a large, hot, early plume head. Journal of the Geological Society, London 152, 965-969.

Chalmers, J. A. and Laursen, K. H. 1995. Labrador Sea: the extent of continental and oceanic crust and the timing of the onset of seafloor spreading. Marine and Petroleum Geology 12, 205–217.

Chambers, L. M., Pringle, M. S. and Parrish, R. R. 2005. Rapid formation of the Small Isles Tertiary centre constrained by precise $^{40}Ar/^{39}Ar$ and U-Pb ages. Lithos 79, 367-384.

Charlier, B. L. A., Ginibre, C., Morgan, D., Nowell, G. M., Pearson, D. G., Davidson, J. P. and Ottley, C. J. 2006. Methods for the microsampling and high

precision analysis of strontium and rubidium isotopes at single crystal scale for petrological and geochronological applications. Chemical Geology 232, 114-133.

Chevallier, L. and Woodford, A. 1999. Morpho-tectonics and mechanism of emplacement of the dolerite rings and sills of the western Karoo, South Africa. South African Journal of Geology 102(1), 43-54.

Choi, S. H. and Kwon, S-T. 2005. Mineral chemistry of spinel peridotite xenoliths from Baengnyeong Island, South Korea, and its implications for the paleogeotherm of the uppermost mantle. The Island Arc 14, 236-253.

Clift, P. D., Turner, J. and ODP LEG 152 Scientific Party. 1995. Dynamic support by the Iceland Plume and its effect on the subsidence of the northern Atlantic margins. Journal of the Geological Society, London 152, 935-941.

Cocks, L. R. M. 2005. Presidential Address 2005: where was Britain in the Palaeozoic? Proceedings of the Geologists' Association 116, 117-127.

Coffin, M. F. and Eldholm, O. 1992. Volcanism and continental break-up: a global compilation of large igneous provinces. From Storey, B. C., Alabaster, T. And Pankhurst, R. J. (eds), Magmatism and the causes of continental break-up, Geological Society Special Publication No. 68, 17-30.

Cole, J. E. and Peachey, J. 1999. Evidence for pre-Cretaceous rifting in the Rockall Trough: an analysis using quantitative plate tectonic modelling. Petroleum Geology of Northwest Europe: Proceedings of the 5th Conference, Geological Society, London 359-370.

Connelly, J. N., Thrane, K., Krawiec, A. W., and Garde, A. A. 2006. Linking the Palaeoproterozoic Nagssugtoqidian and Rinkian orogens through the Disko Bugt region of West Greenland. Journal of the Geological Society, London 163, 319-335.

Conrad, C. P. 2000. Convective instability of thickening mantle lithosphere. Geophysical Journal International 143, 52-70.

Cope, J. C. W. 1994. A Latest Cretaceous hotspot and the southeasterly tilt of Britain. Journal of the geological Society, London 151, 905-908.

Correa-Gomes, L. C., Souza Filho, C. R., Martins, C. J. F. N. And Oliveira, E. P. 2001. Development of symmetrical and asymmetrical fabrics in sheet-like igneous bodies: the role of magma flow and wall-rock displacements in theoretical and natural cases. Journal of Structural Geology 23, 1415-1428.

Corti, G., Bonini, M., Innocenti, F., Manetti, P. and Mulugeta, G. 2001. Centrifuge models simulating magma emplacement during oblique rifting. Journal of Geodynamics 31, 557-576.

Courtillot, V., Davaille, A., Besse, J. and Stock, J. 2003. Three distinct types of hotspots in the Earths mantle. Earth and Planetary Science Letters 205, 295-308.

Cox, K. G. 1980. A model for flood basalt vulcanism. Journal of Petrology 21(4), 629-650.

Cox, K. G. 1988. Numerical Modelling of a Randomized RTF Magma Chamber: A Comparison with Continental Flood Basalt Sequences. Journal of Petrology 29(3), 681-697.

Dasgupta, R., Hirschmann, M. M. and Smith, N. D. 2007. Partial melting experiments of peridotite + CO_2 at 3 GPa and genesis of alkalic ocean island basalts. Journal of Petrology 48(11), 2093-2124.

Day, J. M. D., Pearson, D. G., Macpherson, C. G., Lowry, D. and Carracedo, J. C. 2010. Evidence for distinct proportions of subducted oceanic crust and lithosphere in HIMU-type mantle beneath El Hierro and La Palma, Canary Islands. Geochimica et Cosmochimica Acta 74, 6565-6589.

Dean, K., McLachlan, K. and Chambers, A. 1999. Rifting and the development of the Faeroe-Shetland Basin. In: Fleet, A.J. & Boldy, S.A.R. (eds). Petroleum Geology of Northwest Europe: Proceedings of the 5th Conference. Geological Society, London, 533-544.

Deer, W. A., Howie, R. A. and Zussman, J. 1992. An introduction to the rock forming minerals. Second edition. Longman pp. 696.

Delaney, P. T., Pollard, D. D., Ziony, J. I. and McKee, E. H. 1986. Field relations between dikes and joints: emplacement processes and paleostress analysis. Journal of Geophysical Research 91(B5), 4920-4938.

DePaolo, D. J. 1981. Trace element and isotopic effects of combined wallrock assimilation and fractional crystallisation. Earth and Planetary Science Letters 53, 189-202.

DePaolo, D. J. and Wasserburg, G. J. 1979. Petrogenetic mixing models and Nd – Sr isotopic patterns. Geochimica et Cocmochimica Acta 43, 615-627.

Dickin, A. P. 1981. Isotope geochemistry of Tertiary igneous rocks from the Isle of Skye. Journal of Petrology 22, 155-189.

Dickin, A. P. 1992. Evidence for an Early Proterozoic crustal province in the North Atlantic Region. Journal of the Geological Society, London 149, 483-486.

Dixon, J. E., Leist, L., Langmuir, C. and Schilling, J. G. 2002. Recycled dehydrated lithosphere observed in plume-influenced mid-ocean-ridge basalt. Nature 420, 385-389.

Donnelly, K. E., Goldstein, S. L., Langmuir, C. H. and Spiegelman, M. 2004. Origin of enriched ocean ridge basalts and implications for mantle dynamics. Earth and Planetary Science Letters 226, 347-366.

Doré, A. G., Lundin, E. R., Fichler, C. and Olesen, O. 1997. Patterns of basement structure and reactivation along the NE Atlantic margin. Journal of the Geological Society, London 154, 85-92.

Doré, A. G., Lundin, E. R., Jensen, L. N., Birkeland, Ø., Eliassen, P. E. and Fichler, C. 1999. Principal tectonic events in the evolution of the Northwest European Atlantic margin. In: Fleet, A. J. & Boldy, S. A. R. (eds) Petroleum Geology of Northwest Europe: Proceedings of the 5th Conference. 41-61.

Dowall, D. P., Nowell, G. M. and Pearson, D. G. 2003. Chemical pre-concentration procedures for high-precision analysis of Hf-Nd-Sr isotopes in geological materials by plasma ionisation multi-collector mass spectrometry (PIMMS) techniques. In: Holland, J.G. and Tanner, S.D. Eds. Plasma Source Mass Spectrometry: Applications and Emerging Technologies, The Royal Society of Chemistry, Cambridge, 321-337.

Downes, H. 1990. Shear zones in the upper mantle-relation between geochemical enrichment and deformation in mantle peridotites. Geology 18, 374-377.

Dupuy, C., Mével, C., Bodinier, J-L. and Savoyant, L. 1991. Zabargad peridotite: Evidence for multistage metasomatism during Red Sea rifting. Geology 19, 722-725.

Edwards, J. W. F. 2002. Development of the Hatton-Rockall Basin, North-East Atlantic Ocean, Marine and Petroleum Geology 19, 193-205.

Einsele, G., Gieskes, J. M., Curray, J., Moore, D. M., Aguayo, E., Aubry, M-P., Fornari, D., Guerrero, J., Kastner, M., Kelts, K., Lyle, M., Matoba, Y., Molina-Cruz, A., Niemitz, J., Rueda, J., Saunders, A., Schrader, H., Simoneit, B. and Vacquier, V. 1980. Intrusion of basaltic sills into highly porous sediments, and resulting hydrothermal activity. Nature 283, 441-445.

Eldholm, O. and Grue, K. 1994. North Atlantic volcanic margins: dimensions and production rates. Journal of Geophysical Research 99(B2), 2955-2968.

Eldholm, O., Thiede, J. and Taylor, E. 1989. Evolution of the Vøring volcanic margin. Proceedings of the Ocean Drilling Program, Scientific Results 104, 1033-1065.

Elkins-Tanton, L. T. 2005. Continental magmatism caused by lithospheric delamination. Geological Society of America, Special Paper 388, 449-461.

Ellam, R. M. and Stuart, F. M. 2000. The sub-lithospheric source of north Atlantic basalts: evidence for, and significance of, a common end-member. Journal of Petrology 41(7), 919-932.

Elliot, G. M. and Parson, L. M. 2008. Influence of margin segmentation upon the break-up of the Hatton Bank rifted margin, NE Atlantic. Tectonophysics 457(3-4), 161-176.

Ellis, D., Passey, S.R., Jolley, D.W. and Bell, B.R. 2009. Transfer zones: The application of new geological information from the Faroe Islands applied to the offshore exploration of intra basalt and sub-basalt exploration. In: Varming, T. & Ziska, H. (eds). Faroe Islands Exploration Conference: Proceedings of the 2nd Conference. Annales Societatis Scientiarum Færoensis, Tórshavn, 50, 205-226.

England, R. W. 1988. The Early Tertiary stress regime in NW Britain: evidence from the patterns of volcanic activity. Geological Society, London, Special Publication 39, 381-389.

Ernst, R.E., Buchan, K.L. and Campbell, I.H. 2005. Frontiers in Large Igneous Province research. Lithos 79, 271-297.

Estrada, S., Höhndorf, A. and Henjes-Kunst, F. 2001. Cretaceous/Tertiary volcanism in North Greenland: the Kap Washington Group. Polarforschung 69, 17-23.

Falloon, T. J., Green, D. H., Danyushevskyi, L. V. and Faul. U. H. 1999. Peridotite Melting at 1·0 and 1·5 GPa: an Experimental Evaluation of Techniques using Diamond Aggregates and Mineral Mixes for Determination of Near-solidus Melts. Journal of Petrology 40(9), 1343-1375.

Falloon, T. J., Green, D. H., Danyushevsky, L. V. and McNeill, A. W. 2008. The composition of near-solidus partial melts of fertile peridotite at 1 and 1.5 GPa: implications for the petrogenesis of MORB. Journal of Petrology 49(4), 591-613.

Faure, G. 1986. Principles of isotope geology. Second edition. John Wiley & sons pp. 589.

Faure, G. 2001. Origin of igneous rocks: the isotopic evidence. Springer Verlag. Berlin, Heidelberg, New York pp. 495.

Fialko, Y. 2001. On origin of near-axis volcanism and faulting at fast spreading mid-ocean ridges. Earth and Planetary Science Letters 190, 31-39.

Fitton, J. G., Larsen, L. M., Saunders, A. D., Hardarson, B. S. and Kempton, P. D. 2000. Paleogene continental to oceanic magmatism on the SE Greenland continental margin at 63ºN: a review of the results of Ocean Drilling Program Legs 152 and 163. Journal of Petrology 41(7), 951-66.

Foland, K. A., Gibb, F. G. F. and Henderson, C. M. B. 2000. Patterns of Nd and Sr isotopic ratios produced by magmatic and post-magmatic processes in the Shiant Isles Main Sill, Scotland. Contributions to Mineralogy and Petrology 139, 655-671.

Font, L., Davidson, J. P., Pearson, D. G., Nowell, G. M., Jerram, D. A. and Ottley, C. J. 2008. Sr and Pb Isotope Micro-analysis of Plagioclase Crystals from Skye Lavas: an Insight into Open-systemProcesses in a Flood Basalt Province. Journal of Petrology 49(8), 1449-1471.

Foulger, G. R. 2006. Older crust underlies Iceland. Geophysical Journal International 165, 672-676.

Foulger, G. R. and Anderson, D. L. 2005. A cool model for the Iceland hotspot. Journal of Volcanology and Geothermal Research 141, 1-22.

Foulger, G. R., Natland, J. H. and Anderson, D. L. 2005a. Genesis of the Iceland melt anokmaly by plate tectonic processes. Geological Society of America, Special Paper 388, 595-625.

Foulger, G. R., Natland, J. H. and Anderson, D. L. 2005b. A source for Icelandic magmas in remelted Iapetus crust. Journal of Volcanology and Geothermal Research. 141, 23-44.

Foulger, G. R., Pritchard, M. J., Julian, B. R., Evans, J. R., Allen, R. M., Nolet, G., Morgan, W. J., Bergsson, B. H., Erlendsson, P., Jakobsdottir, S., Ragnarsson, S., Stefansson, R. and Vogtfjörd, K. 2001. Seismic tomography shows that upwelling beneath Iceland is confined to the upper mantle. Geophysical Journal International 146, 504-530.

Fram, M. S. and Lesher, C. E. 1997. Generation and polybaric differentiation of East Greenland Early Tertiary flood basalts. Journal of Petrology 38(2), 231-275.

Francis, E. H. 1982. Magma and sediment-I. Emplacement mechanism of late Carboniferous tholeiitic sills in northern Britain. Journal of the Geological Society, London 139, 1-20.

Frei, D., Liebscher, A., Franz, G., Wunder, B., Klemme, S. and Blundy, J.2009. Trace element partitioning between orthopyroxene and anhydrous silicate melt on the lherzolite solidus from 1.1 to 3.2 GPa and 1,230 to 1,535° C in the model system Na_2O–CaO–MgO–Al_2O_3–SiO_2. Contributions to Mineralogy and Petrology 157, 473-490.

Fyfe, W. S., Price, N. J. and Thompson, A. B. 1978. Fluids in the Earth's crust. Amsterdam,Elsevier, pp. 383.

Galer, S. J. G. and Abouchami, W. 1998. Practical application of lead triple spiking for correction of instrumental mass discrimination, Mineralogical Magazine 62A, 491-492.

Galerne, C. Y., Neumann, E-R. and Planke, S. 2008. Emplacement mechanisms of sill complexes: Information from the geochemical architecture of the Golden Valley Sill Complex, South Africa. Journal of Volcanology and Geothermal Research 177, 425–440.

Galland, O. 2012. Experimental modelling of ground deformation associated with shallow magma intrusions. Earth and Planetary Science Letters 317-318, 145-156.

Galland, O., Cobbold, P. R., Hallot, E., D'Ars, J. D. B. and Delavaud, G. 2006. Use of vegetable oil and silica powder for scale modelling of magmatic intrusion in a deforming brittle crust. Earth and Planetary Science Letters 243, 786-804.

Galland, O., D'Ars, J. D. B., Cobbold, P. R. and Hallot, E. 2003. Physical models of magmatic intrusion during thrusting. Terra Nova 15, 405-409.

Galland, G., Planke, S., Neumann, E-R. and Malthe-Sørenssen, A. 2009. Experimental modelling of shallow magma emplacement: Application to saucer-shaped intrusions Earth and Planetary Science Letters 277, 373-383.

Gamble, J. A., Wysoczansky, R. J. and Meighan, I. G. 1999. Constraints on the age of the British Tertiary Volcanic Province from ion microprobe U-Pb (SHRIMP) ages for acid igneous rocks from NE Ireland. Journal of the Geological Society, London 156, 291-299.

Garfunkel, Z. and Beyth, M. 2006. Constraints on the structural development of Afar imposed by the kinematics of the major surrounding plates. From: Yirgu, G., Ebinger, C. J. & Maguire, P. K. H. (eds) 2006. The Afar Volcanic Province within the East African Rift System. Geological Society, London, Special Publications, 259, 23-42.

Gariépy, C., Ludden, J. and Brooks, C. 1983. Isotopic and trace element constraints on the genesis of the Faeroe Lava pile. Earth and Planetary Science Letters 63, 257-272.

Geoffroy, L. 2005. Volcanic passive margins. C. R. Geoscience 337, 1395-1408.

Geoffroy, L., Bergerat, F. and Angelier, J. 1994. Tectonic evolution of the Greenland-Scotland ridge during the Paleogene: new constraints. Geology 22, 653-656.

Geoffroy, L., Bergerat, F. and Angelier, J. 1996. Brittle tectonism in relation to the Palaeogene evolution of the Thulean/NE Atlantic domain: a study in Ulster. Geological Journal 31, 259-269.

Geoffroy, L., Callot, J-P., Scaillet, S., Skuce, A., Gélard, J. P., Ravilly, M., Angelier, J., Bonin, B., Cayet, C., Perrot, K. and Lepvrier, C. 2001. Southeast Baffin volcanic margin and the North American-Greenland plate separation. Tectonics 20(4), 566-584.

George, R. M. and Rogers, N. W. 2002. Plume dynamics beneath the African plate inferred from the geochemistry of the Tertiary basalts of southern Ethiopia. Contributions to Mineralogy and Petrology 144, 286-305.

Gernigon, L., Olesen, O., Ebbing, J., Wienecke, S., Gaina, C., Mogaard, J. O., Sand. M. and Myklebust, R. 2008. Geophysical insights and early spreading history in the vicinity of the Jan Mayen Fracture Zone, Norwegian–Greenland Sea. Tectonophysics TECTO-124188 (Pages 21), doi:10.1016/j.tecto.2008.04.025.

Gerya, T. V. and Yuen, D. A. 2003. Rayleigh-Taylor instabilities from hydration and melting propel ´cold plumes´ at subduction zones. Earth and Planetary Science Letters 212, 47-62.

Gibb, F. G. F. and Henderson, C. M. B. 2006. Chemistry of the Shiant Isles Main Sill, NW Scotland, and wider implications for the petrogenesis of mafic sills. Journal of Petrology 47(1), 191-230.

Gibson, S. A. 2002. Major element heterogeneity in Archean to recent mantle plume starting heads. Earth and Planetary Science Letters 195, 59-74.

Gibson, S. A., Thompson, R. N., Dickin, A. P. and Leonardos, O. H. 1995. High-Ti and low-Ti mafic potassic magmas: Key to plume-lithosphere interactions and continental flood-basalt genesis. Earth and Planetary Science Letters 136, 149-165.

Gill, R. C. O., Holm, P. M. and Nielsen, T. F. D. 1995. Was a short-lived Baffin Bay plume active prior to initiation of the present Icelandic plume? clues from high-Mg picrites of West Greenland. Lithos 34, 27-39.

Goulty, N. R. 2005. Emplacement mechanism of the Great Whin and Midland Valley dolerite sills. Journal of the Geological Society, London 162, 1047-1056.

Goulty, N. R. and Schofield, N. 2008. Implications of simple flexure theory for the formation of saucer-shaped sills. Journal of Structural Geology 30, 812-817.

Green, P. F., Duddy, I. R., Bray, R. J. and Lewis, C. L. E. 1993. Elevated palaeotemperatures prior to Early tertiary cooling throughout the UK region: implications for hydrocarbon generation. Petroleum Geology of Northwest Europe: Proceedings of the 4th Conference, Geological Society, London 1067-1074.

Green, D. H. and Falloon, T. J. 2005. Primary magmas at mid-ocean ridges, ”hotspots,” and other intraplate settings: Constraints on mantle potential temperature. in Foulger GR, Natland JH, Presnall DC, Anderson DL, eds., Plates, plumes, and paradigms: Geological Society of America Special Paper 388, 217-247.

Grégoire, M., Bell, D. R. and Le Roex, A. P. 2003. Garnet lherzolites from the Kaapvaal Craton (South Africa): trace element evidence for a metasomatic history. Journal of Petrology 44 (4), 629-657.

Grove, T. L., Kinzler, R. J. and Bryan, W. B. 1992. Fractionation of mid-ocean ridge basalt (MORB), in: Mantle flow and generation at mid-ocean ridges. American Geophysical Union 71, 281-310.

Gudfinnson, G. H. and Presnall, D. C. 1996. Melting relations of model lherzolite in the system CaO-MgO-Al_2O_3-SiO_2 at 2.4-3.4 GPa and the generation of komatiites. Journal of Geophysical Research 101 (B12), 27701-27709.

Gudlaugsson, S. T., Gunnarsson, K., Sand, M. and Skogseid, J. 1988. Tectonic and volcanic events at the Jan Mayen Ridge microcontinent. Geological Society, London, Special Publications 39, 85-93.

Gudmundsson, A. 1986. Formation of crustal magma chambers in Iceland. Geology 14, 164-166.

Gudmundsson, A. 2011. Deflection of dykes into sills at discontinuities and magma-chamber formation. Tectonophysics 500, 50-64.

Gudmundsson, A. and Marinoni, L. B. 1999. Geometry, emplacement, and arrest of dykes. Annales Tectonicæ XIII(1-2), 71-92.

Haack, U. 1983. On the content and vertical distribution of K, Th and U in the continental crust. Earth and Planetary Science Letters 62, 360-366.

Haase, K. M. and Dewey, C. W. 1994. The petrology and geochemistry of Vesteris Seamount, Greenland Basin-an intraplate alkaline volcano of non-plume origin. Journal of Petrology 35(2), 295-328.

Haase, K. M., Dewey, C. W., Mertz, D. F., Stoffers, P. and Garbe-Shönberg, D. 1996. Geochemistry of lavas from Mohns Ridge, Norwegian-Greenland Sea: implications for melting conditions and magma sources near Jan Mayen. Contributions to Mineralogy and Petrology 123, 223-237.

Hald, N. and Tegner, C. 2000. Composition and age of tertiary sills and dykes, Jameson Land Basin, East Greenland: relation to regional flood volcanism. Lithos 54, 207-233.

Hald, N. and Waagstein, R. 1983. Silicic basalts from the Faeroe Islannds: evidence of crustal contamination. In: Bott MHP, Saxov S, Talvani M, Thiede J (eds) Structure and development of the Greenland-Scotland Ridge. New methods and concepts. Plenum New York, 343-349.

Hald, N. and Waagstein, R. 1984. Lithology and chemistry of a 2-km sequence of Lower Tertiary tholeiitic lavas drilled on Suðuroy, Faeroe Islands (Lopra-1). In: Berthelsen O, Noe-Nygaard A, Rasmussen J (eds) The deep drilling project 1980-1981 in the Faeroe Islands. Annales Societatis Scientiarum Færoensis, Tórshavn, Supplementum IX, 15-38.

Hald, N. and Waagstein, R. 1991. The dykes and sills of the Early Tertiary Faeroe Island basalt plateau. Transactions of the Royal Society of Edinburg: Earth Sciences 82, 373-388.

Hall, A. 1996. Igneous Petrology. © Longman Group Limited, England. Second Edition pp. 551.

Hanan, B. B. and Schilling, J-G. 1997. The dynamic evolution of the Iceland mantle plume: the lead isotope perspective. Earth and Planetary Science Letters 151, 43-60.

Hanghøj, K., Storey, M. and Stecher, O. 2003. An isotope and trace element study of the East Greenland Tertiary dyke swarm: constraints on temporal and spatial evolution during continental rifting. Journal of Petrology 44(11), 2081-2112.

Hansen, D. M. 2006. The morphology of intrusion-related vent structures and their implications for constraining the timing of intrusive events along the NE Atlantic margin. Journal of the Geological Society, London 173, 789-800.

Hansen, K. and Brooks, C. K. 2002. The evolution of the East Greenland margin as revealed from fission-track studies. Tectonophysics 349, 93-111.

Hansen, D. M. and Cartwright, J. A. 2006. Saucer-shaped sill with lobate morphology revealed by 3D seismic data: implications for resolving a shallow-level sill emplacement mechanism. Journal of the Geological Society, London 163, 509-523.

Hansen, D. M., Cartwright, J. A. and Thomas, D. 2004. 3D seismic analysis of the geometry of igneous sills and sill junction relationships. Davies, R. J., Cartwright, J. A., Stewart, S. A., Lappin, M. & Underhill, J. R. (eds) 2004. 3D Seismic Technology: Application to the Exploration of Sedimentary Basins. Geological Society, London, Memoirs 29, 199-208.

Harrison, J. C., Mayr, U., McNeil, D. H., Sweet, A. R., McIntyre, D. J., Eberle, J. J., Harington, C. R., Chalmers, J. A., Dam, G. and Nøhr-Hansen, H. 1999. Correlation of Cenozoic sequences of the Canadian Arctic region and Greenland; implications for the tectonic history of northern North America. Bulletin, Canadian Petroleum Geology 47(3), 223-254.

Harry, D. L. and Bowling, J. C. 1999. Inhibiting magmatism on nonvolcanic rifted margins. Geology 27(10), 895-908.

Hart, S. R. 1988. Heterogeneous mantle domains: signatures, genesis and mixing chronologies. Earth and Planetary Science Letters 90, 273-296.

Hatcher, R. D. 1995. Structural Geology, Principles, Concepts, and Problems. Prentice Hall, Englewood Cliffs, New Jersey 07632. pp. 525.

Hedlin, M. A. H., Shearer, P. M. and Earle, P. S. 1997. Seismic evidence for small-scale heterogeneity throughout the Earth's mantle. Nature 387, 145-150.

Helffrich, G. and Wood, B. 2001. The Earth's Mantle, Nature 412, 501-507.

Higgins NC, Solomon M, Varne R. 1985. The genesis of the Blue Tier Batholith, northeastern Tasmania. Lithos 18: 129-149.

Hirose, K. and Kawamoto, T. 1995. hydrous partial melting of lherzolite at 1 GPa: The effect of H_2O on the genesis of basaltic magmas. Earth and Planetary Science Letters 133, 463-473.

Hirose, K. and Kushiro, I. 1993. Partial melting of dry peridotites at high pressures: Determination of compositions of melts segregated from peridotite using aggregates of diamond. Earth and Planetary Science Letters 114, 477-489.

Hirth, G. and Kohlstedt, D. L. 1996. Water in the oceanic upper mantle: implications for rheology, melt extraction and the evolution of the lithosphere. Earth and Planetary Science Letters 144, 93-108.

Hitchen, K. 2004. The geology of the UK Hatton-Rockall margin. Marine and Petroleum Geology 21, 993-1012.

Hitchen, K., Morton, A. C., Mearns, E. W., Whitehouse, M. and Stoker, M. S. 1997. Geological implications from geochemical and isotopic studies of Upper

Cretaceous and lower Tertiary igneous rocks around the northern Rockall Trough. Journal of the Geological Society, London 154, 517-521.

Hitchen, K. and Ritchie, J. D. 1993. New K-Ar ages, and a provisional chronology, for the offshore part of the British Tertiary Igneous Province. Scottish Journal of Geology 29(1), 73-85.

Hofmann, A. W. 1997. Mantle geochemistry: the message from oceanic volcanism. Nature 385, 219-229.

Holdsworth, R. E., Butler, C. A. and Roberts, A. M. 1997. The recognition of reactivation during continental deformation. Journal of the Geological Society, London 154, 73-78.

Holm, P. M., Hald, N. and Waagstein, R. 2001. Geochemical and Pb-Sr-Nd isotopic evidence for separate hot depleted and Iceland plume mantle sources for the Paleogene basalts of the Faroe Islands. Chemical Geology 178, 95-125.

Huppert, H. E. and Sparks, R. S. J. 1985. Komatiites I: Eruption and flow. Journal of Petrology 26(3), 694-725.

Ionov, D. A. 2010. Petrology of mantle wedge lithosphere: new data on supra-subduction zone peridotite xenoliths from the Andesitic Avacha Volcano , Kamchatka. Journal of Petrology 51(1-2), 327-361.

Ivanov, A. V., Demonterova, E. I., Rasskazov, S. V. and Yasnygina, T. A. 2008. Low-Ti melts from the southeastern Siberian Traps Large Igneous Province: Evidence for a water-rich mantle source. Journal of Earth System Science 117(1), 1-21.

Jackson, J., McKenzie, D., Priestley, K. and Emmerson, B. 2008. New views on the structure and rheology of the lithosphere. Journal of the Geological Society, London 165, 453-465.

Jamtveit, B., Brooker, R., Brooks, C. K., Larsen, L. M. and Pedersen, T. 2001. The water content of olivines from the North Atlantic Volcanic Province. Earth and Planetary Science Letters 186, 401-415.

Japsen, P. and Chalmers, J. A. 2000. Neogene uplift and tectonics around the North Atlantic: overview. Global and planetary Change 24, 165-173.

Japsen, P., Green, P. F. and Chalmers, J. A. 2005. Separation of Palaeogene and Neogene uplift on Nuussuaq, West Greenland. Journal of the Geological Society, London 162, 299-314.

Jerram, D. A., Single, R. T., Hobbs, R. W. and Nelson, C. E. 2009. Understanding the offshore flood basalt sequence using onshore volcanic facies analogues: an example from the Faroe-Shetland basin . Geological Magazine 146 (3), 353-367.

Jerram, D.A. and Widdowson, M. 2005. The anatomy of Continental Flood Basalt Provinces: geological constraints on the processes and products of flood volcanism. Lithos 79: 385-405.

Jolivet, L. and Faccenna, C. 2000. Mediterranean extension and the Africa-Eurasia collision. Tectonics 19(6), 1095-1106.

Jones, S. M., White, N. and Lovell, B. 2001. Cenozoic and Cretaceous uplift in the Porcupine Basin and its relationship to a mantle plume. The Petroleum

Exploration of Ireland's Offshore Basins. Geological Society, London, Special Publications 188, 345-360.

Jørgensen, O. 2006. The regional distribution of zeolites in the basalts of the Faroe Islands and the significance of zeolites as palaeotemperature indicators. In Chalmers, J. A. & Waagstein, R. (eds) Scientific Results from the Deepened Lopra-1 Borehole, Faroe Islands. Geological Survey of Denmark and Greenland Bulletin 9, 123–156.

Kalsbeek, F. 1995. Geochemistry, tectonic setting, and poly-orogenic history of Palaeoproterozoic basement rocks from the Caledonian fold belt of North-East Greenland. Precambrian Research 72, 301-315.

Kanaris-Sotiriou, R., Morton, A. C. and Taylor, P. N. 1993. Palaeogene peraluminous magmatism, crustal melting and continental breakup: the Erlend complex, Faeroe-Shetland Basin, NE Atlantic. Journal of the Geological Society, London 150, 903-914.

Karson, J. A. and Brooks, C. K. 1999. Structural and magmatic segmentation of the tertiary East Greenland volcanic rifted margin. Mac Niocaill, C & Ryan, P. D.(eds). Continental Tectonics. geological Society, London, Special Publications 164, 313-338.

Karson, J. A., Brooks, C. K., Storey, M. and Pringle, M. S. 1998. Tertiary faulting and pseudotachylites in the east Greenland volcanic rifted margin: seismogenic faulting during magmatic construction. Geology 26(1), 39-42.

Kavanagh, J. L., Menand, T. and Sparks, R. S. J. 2006. An experimental investigation of sill formation and propagation in layered elastic media. Earth and Planetary Science Letters 245, 799-813.

Kays, M. A., Goles, G. G. and Grover, T. W. 1989. Precambrian sequence bordering the Skaergaard Intrusion. Journal of Petrology 30 (2), 321-361.

Kay, R. W. and Kay, S. M. 1993. Delamination and delamination magmatism. Tectonophysics 219, 177-189.

Keranen, K. and Klemperer, S. L. 2008. Discontinuous and diachronous evolution of the main Ethiopian Rift: Implications for the development of continental rifts. Earth and planetary Science Letters 265, 96-111.

Kerr, A. C. 1994. Lithospheric thinning during the evolution of continental large igneous provinces: A case study from the North Atlantic Tertiary province. Geology 22, 1027-1030.

Kerr, A. C. 1995. The melting processes and composition of the North Atlantic (Iceland) plume: geochemical evidence from the Early Tertiary basalts. Journal of the Geological Society, London 152, 975-978.

Kerr, A. C., Kempton, P. D. and Thompson, R. N. 1995. Crustal assimilation during turbulent magma ascent (ATA); new isotopic evidence from the Mull Tertiary lava succession, N. W. Scotland. Contributions to Mineralogy and Petrology 119, 142-154.

Kimbell, G. S., Ritchie, J. D., Johnson, H. and Gatliff, R. W. 2005. Controls on the structure and evolution of the NE Atlantic margin revealed by regional 3D gravity modelling. In Doré. A. G & Vining. B. A. (eds) Petroleum Geology: North-West

Europe and Global Perspectives-Proceedings of the 6th Petroleum Geology Conference. Geological Society. London 933-947.

Kitagawa, H., Kobayashi, K., Makishima, A. and Nakamura, E. 2008. Multiple pulses of the Mantle Plume: Evidence from Tertiary Icelandic Lavas. Journal of Petrology 49(7), 1365-1396.

Klemme, S., Prowatke, S., Hametner, K. and Günther, D. 2005. Partitioning of trace elements between rutile and silicate melts: Implications for subduction zones. Geochimica et Cosmochimica Acta 69(9), 2361–2371.

Knott, S. D., Burchell, M.T., Jolley, E. J. and Fraser, A. J. 1993. Mesozoic to Cenozoic plate reconstructions of the North Atlantic and hydrocarbon plays of the Atlantic margins. Petroleum Geology of Northwest Europe: Proceedings of the 4th Conference, Geological Society, London 953-974.

Kodaira, S., Mjelde, R., Gunnarson, K., Shiobara, H. and Shimamura, H. 1998. Structure of the Jan Mayen microcontinent and implications for its evolution. Geophysical Journal International 132, 383-400.

Kogiso, T. and Hirschmann, M. 2006. Partial melting experiments of bimineralic eclogite and the role of recycled mafic oceanic crust in the genesis of ocean island basalts. Earth and Planetary Science Letters 249, 188-199.

Kogiso, T., Hirschmann, M. M. and Pertermann, M. 2004. High-pressure partial melting of mafic lithologies in the mantle. Journal of Petrology 45(12), 2407-2422.

Kogiso, T., Hirose, K. and Takahashi, E. 1998. Melting experiments on homogeneous mixtures of peridotite and basalt: application to the genesis of ocean island basalts. Earth and Planetary Science Letters 162, 45-61.

Kohlstedt, D. L., Evans, B. and Mackwell, S. J. 1995. Strenght of the lithosphere: constraints imposed by laboratory experiments. Journal of Geophysical Research 100(B9), 17587-17602.

Korenaga, J. 2004. Mantle mixing and continental breakup magmatism Earth and Planetary Science Letters 218, 463-473.

Korenaga, J. and Keleman, P. B. 2000. Major element heterogeneity in the mantle source of the North Atlantic Igneous Province. Earth and Planetary Science Letters 184, 251-268.

Kushiro, I. 1996. Partial melting of a fertile mantle peridotite at high pressures: An experimental study using aggregates of diamond. Geophysical Monograph 95, 109-122.

Kushiro, I. 2001. Partial melting experiments on peridotite and origin of mid-ocean ridge basalts. Annual Review of Earth and Planetary Science 29, 71-107.

Kusznir, N. J. and Park, R. G. 2002. The extensional strength of the continental lithosphere: its dependence on geothermal gradient, and crustal composition and thickness. Geological Society, London, Special Publications 28, 35-52.

Larsen, L. M., Fitton, J. G. and Fram, M. S. 1998. Volcanic rocks of the Southeast Greenland margin in comparison with other parts of the North Atlantic Tertiary Igneous Province. Proceedings of the ODP. Scientific Results 152, 315-330.

Larsen, H. C. and Jakobsdóttir, S. 1988. Distribution, crustal properties and significance of seawards-dipping sub-basement reflectors off E Greenland. Geological Society, London, Special Publications 39, 95-114.

Larsen, H. C. and Marcussen, C. 1992. Sill-intrusion,flood basalt emplacement and deep crustal structure of the Scoresby Sund region, East Greenland. Geological Society, London, Special Publications 68, 365-386.

Larsen, L. M. and Pedersen, A. K. 2009. Petrology of the Paleocene Picrites and Flood Basalts on Disko and Nuussuaq,West Greenland. Journal of Petrology 50(9), 1667-1711.

Larsen, L. M., Rex, D. C., Watt, W. S. and Guise, P. G. 1999a. $^{40}Ar/^{39}Ar$ dating of alkali basaltic dykes along the south-west coast of Greenland: Cretaceous and Tertiary igneous activity along the eastern margin of the Labrador Sea. Geology of Greenland, Survey Bulletin 184, 19-29.

Larsen, L. M., Waagstein, R., Pedersen, A. K. and Storey, M. 1999b. Trans-Atlantic correlation of the Palaeocene volcanic successions in the Faeroe Islands and East Greenland. Journal of the Geological Society, London 156, 1081-1095.

Larsen, H. C. and Saunders, A. D. 1998. Tectonism and volcanism at the southeast Greenland rifted margin: a record of plume impact and later continental rupture. Proceedings of the ODP, Scientific Results 152, 503-533.

Larsen, L. M. and Watt, W. S. 1985. Episodic volcanism during break-up of the North Atlantic: evidence from the East Greenland plateau basalts. Earth and Planetary Science Letters 73, 105-116.

Lay, T. 2005. The deep mantle thermo-chemical boundary layer: the putative mantle plume source Geological Society of America, Special Paper 388, 193-205.

Lenoir, X., Feraud, G. and Geoffroy, L. 2003. High-rate flexure of the East Greenland volcanic margin: constraints from $^{40}Ar/^{39}Ar$ dating of basaltic dykes. Earth and Planetary Science Letters 214, 515-528.

Lesnov, F. P., Koz'menko, O. A., Nikolaeva, I. V. and Palesskiiet, S. V. 2009. Residence of incompatible trace elements in a large spinel lherzolite xenolith from alkali basalt of Shavaryn Tsaram-1 paleovolcano (western Mongolia). Russian Geology and Geophysics 50, 1063–1072.

Lister, J. R. and Kerr, R. C. 1991. Fluid-mechanical models of crack propagation and their application to magma transport in dykes. Journal of Geophysical Research 96(B6), 10049-10077.

Lugmair, G. W. and Marti, K. 1978. Lunar initial $^{143}Nd/^{144}Nd$: differential evolution of the lunar crust and mantle. Earth and Planetary Science Letters 39, 349-357.

Lundin, E. R. and Doré, A. G. 1997. A tectonic model for the Norwegian passive margin with implications for the NE Atlantic: Early Cretaceous to break-up. Journal of the Geological Society, London 154, 545-550.

Lundin, E. R. and Doré, A. G. 2002. Mid-Cenozoic post-breakup deformation in the "passive" margins bordering the Norwegian-Greenland Sea. Marine and Petroleum Geology 19, 79-93.

Lundin, E. R. and Doré, A. G. 2005a. Fixity of the Iceland "hotspot" on the Mid-Atlantic Ridge: observational evidence, mechanisms, and implications for Atlantic volcanic margins. Geological Society America, Special Paper 388, 627-651.

Lundin, E. R. and Doré, A. G. 2005b. NE Atlantic break-up: a re-examination of the Iceland mantle plume model and the Atlantic-Arctic linkage. Petroleum Geology of Northwest Europe: Proceedings of the 6th Conference, Geological Society, London 735-754.

Lustrino, M. 2005. How delamination and detachment of lower crust can influence basaltic magmatism. Earth-Science Reviews 72, 21-38.

Lyle, P. 2000. The eruption environment of multi-tiered columnar basalt lava flows. Journal of the Geological Society, London 157, 715-722.

Maaløe, S. 2003. Melt dynamics of a partially molten mantle with randomly oriented veins. Journal of Petrology 44(7), 1193-1210.

MacDonald, G. A. 1968. Composition and origin of Hawaiian lavas. In: Coats R. R., Hay R. L. and Anderson C. A. (eds), Studies in Volcanology: a memoir in honour of Howel Williams. Geological Society of America Memoirs 116, 477-522.

Mackay, L. M., Turner, J., Jones, S. M. and White, N. J. 2005. Cenozoic vertical motions in the Moray Firth Basin associated with initiation of the Iceland Plume. Tectonics 24, TC5004, 1-23.

Maclennan, J. and Jones, S. M. 2006. Regional uplift, gas hydrate dissociation and the origins of the Paleocene-Eocene thermal maximum. Earth and Planetary Science Letters 245, 65-80.

Malthe-Sørenssen, A., Planke, S., Svensen, H. and Jamtveit, B. 2004. Formation of saucer-shaped sills. From: Breitkreuz, C. & Petford, N. (eds) 2004. Physical Geology of High-Level Magmatic Systems. Geological Society, London, Special Publications 234, 215-227.

Masson, F, Hauser, F. and Jacob, A. W. B. 1999. The lithospheric trace of the Iapetus Suture in SW Ireland from teleseismic data. Tectonophysics 302, 83-98.

Mathiesesn, A., Bidstrup, T. and Christianden, G. 2000. Denudation and uplift history of the Jameson Land basin, East Greenland-constrained from maturity and apatite fission track data. Global and Planetary Change 24, 275-301.

Meibom, A., Anderson, D. L., Sleep, N. H., Frei, R., Chamberlain, C. P., Hren, M. T. and Wooden, J. L. 2003. Are high $^{3}He/^{4}He$ ratios in oceanic basalts an indicator of deep-mantle plume components? Earth and Planetary Science Letters 208, 197-204.

Menand, T. and Tait, S. R. 2002. The propagation of a buoyant liquid-filled fissure from a source under constant pressure: An experimental approach. Journal of Geophysical Research 107(B11), 2306, ECV 16.1 – ECV 16.14.

Mertz, D. F. and Haase, K. M. 1997. The radiogenic isotope composition of the high-latitude North Atlantic mantle. Geology 25(5), 411-414.

Meyer, R., Nicoll, G. R., Hertogen, J., Troll, V. R., Ellam, R. M. and Emelius, C. H. 2009. Trace element and isotope constraints on crustal anatexis by upwelling mantle melts in the North Atlantic Igneous Province: an example from the Isle of Rum, NW Scotland. Geological Magazine 146(3), 382-399.

Meyer, R., Van Wijk, J. and Gernigon, L. 2007. The North Atlantic Igneous Province: A review of models for its formation. The Geological Society of America, Special Paper 430, 525-552.

Mjelde, R., Breivik, A. J., Raum, T., Mittelstaedt, E., Ito, G. and Faleide, J. I. 2008. Magmatic and tectonic evolution of the North Atlantic. Journal of the Geological Society, London 165, 31-42.

Momme, P., Tegner, C., Brooks, C. K. and Keays, R. R. 2006. Two melting regimes during Paleogene flood basalt generation in East Greenland: combined REE and PGE modelling. Contributions to Mineralogy and Petrology 151, 88-100.

Morency, C. and Doin, M-P. 2004. Numerical simulations of the mantle lithosphere delamination. Journal of Geophysical Research 109(B03410), 1-17.

Morgan, J. P. 1997. The generation of a compositional lithosphere by mid-ocean ridge melting and its effect on subsequent off-axis hotspot upwelling and melting. Earth and Planetary Science Letters 146, 213-232.

Morgan, J.V. and Barton, P. J. 1990. A geophysical study of the Hatton Bank volcanic margin: a summary of the results from a combined seismic, gravity and magnetic experiment. Tectonophysics 173, 517-26.

Morton, A. C., Hitchen, K., Ritchie, J. D., Hine, N. M., Whitehouse, M. and Carter, S. G. 1995. Late Cretaceous basalts from Rosemary Bank, Northern Rockall Trough. Journal of the Geological Society, London 152, 947-952.

Morton, A. C. and Taylor, P. N. 1991. Geochemical and isotopic constraints on the nature and age of basement rocks from Rockall Bank, NE Atlantic. Journal of the Geological Society, London 148, 631-634.

Motoki, A. and Sichel, S. E. 2008. Hydraulic fracturing as a possible mechanism of dyke-sill transitions and horizontal discordant intrusions in trachytic tabular bodies of Arraial do Cabo, State of Rio de Janeiro, Brazil. Geofísica Internacional 47(1), 13-25.

Mudge, D. C. and Jones, S. M. 2004. Paleocene uplift and subsidence events in the Scotland-Shetland and North Sea region and their relationship to the Iceland Plume. Journal of the Geological Society, London 161, 381-386

Münker, C. 1998. Nb/Ta fractionation in a Cambrian arc/back arc system, New Zealand: source constraints and application of refined ICPMS techniques. Chemical Geology 144, 23-45.

Nadin, P. A., Kuznir, N. J. and Cheadle, M. J. 1997. Early Tertiary plume uplift of the North Sea and Faeroe-Shetland Basins. Earth and Planetary Science Letters 148, 109-127.

Nakamura, N. 1974. Determination of REE, Ba, Fe, Mg, Na and K in carbonaceous and ordinary chondrites. Geochimica et Cocmochimica Acta 38, 757-775.

Natland, J. H. and Winterer, E. L. 2005. Fissure control on volcanic action in the Pacific. Geological Society of America, Special Paper 388, 687-710.

Naylor, P. H., Bell, B. R., Jolley, D. W., Durnall, P. and Fredsted, R. 1999. Palaeogene magmatism in the Faeroe-Shetland Basin: influences on uplift history and sedimentation. Petroleum Geologu of Northwest Europe: Petroleum Geology

of Northwest Europe: Proceedings of the 5th Conference, Geological Society, London 545-558.

Nichols, A. R. L., Carroll, M. R. and Höskuldsson, Á. 2002. Is the Iceland hot spot also wet? Evidence from the water contents of undegassed submarine and subglacial pillow basalts. Earth and Planetary Science Letters 202, 77-87.

Nielsen, T. F. D. 1987. Tertiary alkaline magmatism in East Greenland: a review. From: Fitton, J. G. and Upton, B. G. J (eds), Alkaline Igneous Rocks, Geological Society Special Publication 30, 489-515.

Nielsen, T. K., Larsen, H. C. and Hopper, J. R. 2002. Contrasting rifted margin styles south of Greenland: implications for mantle plume dynamics. Earth and Planetary Science Letters. 200, 271-286.

Nielsen, S. B., Stephenson, R. and Thomsen, E. 2007. Dynamics of mid-Paleocene north Atlantic rifting linkked with European intra-plate deformations. Nature 450, 1071-1073.

Noe-Nygaard, A. and Rasmussen, J. 1968. Petrology of a 3,000 metre sequence of basaltic lavas in the Faeroe Islands. Lithos 1, 286-304.

Nowell, G. M., and Parrish, R. R. 2002. Simultaneous acquisition of isotope compositions and parent/daughter ratios by non-isotope dilution solution-mode Plasma ionisation Multi-collector Mass Spectrometry (PIMMS). In: Holland, J. G. & Tanner, S.D., Eds. Plasma Source Mass Spectrometry The New Millenium, The Royal Society of Chemistry, 298-310.

Obata, M. and Morten, L. 1987. Transformation of Spinel Lherzolite to Garnet Lherzolite in Ultramafic Lenses of the Austridic Crystalline Complex, Northern Italy. Journal of Petrology 28(3): 599-623.

O´Connor, J. M., Stoffers, P., Wijbrans, J. R., Shannon, P. M. and Morrissey. T. 2000. Evidence from episodic seamount volcanism for pulsing of the Iceland plume in the past 70 Myr. Nature 408, 954-958.

O'Hara, M. J. and Mathews, R. E. 1981. Geochemical evolution in an advancing, periodically replenished, periodically tapped, continuously fractionated magma chamber Journa of the Geological Society, London 138, 237-277.

Ohanian, H. C. 1989. Physics. Second edition, expanded. W. W. Norton & Company. New York – London. pp. 1148.

Olesen, O., Ebbing, J., Lundin, E., Mauring, E., Skilbrei, J. R., Torsvik, T. H., Hansen, E. K., Henningsen, T., Midbøe, P. and Sand. M. 2007. An improved tectonic model for the Eocene opening of the Norwegian-Greenland Sea: Use of modern magnetic data. Marine and Petroleum Geology 24, 53-66.

Ordóñez-Calderón, J. C., Polat, A., Fryer, B. J., Gagnona, J. E., Raith, J. G. and Appel, P. W. U. 2008. Evidence for HFSE and REE mobility during calc-silicate metasomatism, Mesoarchean (~3075 Ma) Ivisaartoq greenstone belt, southern West Greenland. Precambrian Research 161: 317–340.

O´Reilly, B.M., Readman, P. W. and Hauser, F. 1998. Lithospheric structure across the western Eurasian plate from a wide-angle seismic and gravity study: evidence for a regional thermal anomaly. Earth and Planetary Science Letters 156, 275-280.

Orihashi, Y., Al-Jailani, A and Nagao, K. 1998. Dispersion of the Afar plume: Implications from the Spatiotemporal Distribution of the Late Miocene to Recent Volcanics, Southwestern Arabian Peninsula. Gondwana Research 1(2), 221-234.

Ottley, C. J., Pearson, D. G. and Irvine, G. J. 2003. A routine method for the dissolution of geological samples for the analysis of REE and trace elements via ICP –MS. In: Plasma Source Mass Spectrometry, Applications and Emerging Technologies, (J.G. Holland, S.D. Taner, Eds.). The Royal Society of Chemistry 221–230.

Park, R. G. 1995. Geological structures and moving plates. Blackie Academic & Professional, an Imprint of Chapman & Hall, pp. 337.

Passey, S. R. and Bell, B. R. 2007. Morphologies and emplacement mechanisms of the lava flows of the Faroe Islands Basalt Group, Faroe Islands, NE Atlantic Ocean. Bulletin of Volcanology 70, 139-156.

Passey, S. R. and Jolley, D. W. 2009. A revised lithostratigraphic nomenclature for the Palaeogene Faroe Islands Basalt group, NE Atlantic Ocean. Earth and Environmental Science Transactions of the Royal Society of Edinburg 99, 127-158.

Peate, D. W., Barker, A. K., Riishuus, M. S. and Andreasen, R. 2008. Temporal variations in crustal assimilation of magma suites in the East Greenland flood basalt province: Tracking the evolution of magmatic plumbing systems. Lithos 102, 179-197.

Peate, D. W., Baker, J. A., Blichert-Toft, J., Hilton, D. R., Storey, M., Kent, A. J. R., Brooks, C. K., Hansen, H., Pedersen, A. K. and Duncan, R. A. 2003. The Prinsen of Wales Bjerge Formation lavas, East Greenland: the transition from tholeiitic to alkalic magmatism during Paleogene continental break-up. Journal of Petrology 44(2), 279-304.

Peate, D. W. and Hawkesworth, C. J. 1996. Lithospheric to asthenospheric transition in Low-Ti flood basalts from southern Paraná, Brazil. Chemical Geology 127, l-24.

Peate, I. U., Larsen, M. and Lesher, C. E. 2003. The transition from sedimentation to flood volcanism in the Kangerlussuaq Basin, East Greenland: basaltic pyroclastic volcanism during initial Palaeogene continental break-up. Journal of the Geological Society, London 160, 759-772.

Peate, D. W. and Stecher, O. 2003. Pb isotope evidence for contributions from different Iceland mantle components to Palaeogene East Greenland flood basalts. Lithos 67, 39-52.

Planke, S., Rasmussen, T., Rey, S. S. and Myklebust R. 2005. Seismic characteristics and distribution of volcanic intrusions and hydrothermal vent complexes in the Vøring and Møre basins. Petroleum Geology of Northwest Europe: Proceedings of the 6th Conference, Geological Society, London 833-844.

Pollard, D. D. 1973. Derivation and evaluation of a mechanical model for sheet intrusions. Tectonophysics 19, 233-269.

Pollard, D. D. and Holzhausen, G. 1979. On the echanical interaction between a fluid-filled fracture and the Earth's surface Tectonophysics 53, 27-57.

Pollard, D. D. and Johnson, A. M. 1973. Mechanics of growth of some laccolithic intrusions in the Henry Mountains, Utah, II. Bending and failure of overburden layers and sill formation. Tectonophysics 18, 311-354.

Polteau, S., Mazzini, A., Galland, O., Planke, S. and Malthe-Sørensen, A. 2008. Saucer-shaped intrusions: Occurrences, emplacement and implications. Earth and Planetary Science Letters 266, 195-204.

Presnall, D. C., Gudfinnsson, G. H. and Walter, M. J. 2002. Generation of mid-ocean basalts at pressures from 1 to 7 GPa. Geochimica et Cocmochimica Acta 66, 2073-2090.

Price, S., Brodie, J., Whitham, A. and Kent, R. 1997. Mid-Tertiary rifting and magmatism in the Traill Ø region, East Greenland. Journal of the Geological Society, London 154, 419-434.

Prytulak, J. and Elliott, T. 2007. TiO_2 enrichment in ocean island basalts. Earth and Planetary Science Letters 263, 388-403.

Raddick, M. J., Parmentier, E. M. and Scheirer, D. S. 2002. Buoyant decompression melting: a possible mechanism for intraplate volcanism. Journal of Geophysical Research 107(B10), ECV 7.1-7.14.

Rampone, E., Romairone, A. and Hofmann, A. W. 2004. Contrasting bulk and mineral chemistry in depleted mantle peridotites: evidence for reactive porous flow. Earth and Planetary Science Letters 218, 491-506.

Rasmussen, J. and Noe-Nygaard, A. 1969. Beskrivelse til geologisk kort over Færøerne i målestok 1:50000, Geological Survey of Denmark 1. Series No. 24.

Rasmussen, J. and Noe-Nygaard, A. 1970. Geology of the Faeroe Islands. Geological Survey of Denmark I. Series No. 25, 1-142.

Redfield, T. F., Torsvik, T. H., Andriessen, P. A. M. and Gabrielsen, R. H. 2004. Mesozoic and Cenozoic tectonics of the Mære Trøndelag Fault Complex, central Norway: constraints from new apatite fission track data. Physics and Chemistry of the Earth 29, 673-682.

Ren, S., Faleide, J. I., Eldholm, O., Skogseid, J. and Gradstein, F. 2003. Late Cretaceous-Paleocene tectonic development of the NW Vøring Basin. Marine and Petroleum Geology 20, 177-206.

Richardson, K. R., Smallwood, J. R., White, R. S., Snyder, D. B. and Maguire, P. K. H. 1998. Crustal structure beneath the Faroe Islands and the Faroe-Iceland Ridge. Tectonophysics 300, 159-180.

Richter, F. M. 1986. Simple models for trace element fractionation during melt segregation. Earth and Planetary Science Letters 77, 333-344.

Rickwood, P. C. 1989. Boundary lines within petrologic diagrams which use oxides of major and minor elements. Lithos 22, 247-263.

Ritchie, J. D., Hitchen, K. and Edwards, J. W. F. 1997. The Sigmundur Complex, a ?Tertiary igneous centre in the northern Rockall Trough. Scottish Journal of Geology 33(2), 97-103.

Roberts, D. 2003. The Scandinavian Caledonides: event chronology, palaeo-geographic settings and likely modern analogues. Tectonophysics 365, 283-299.

Roberts, D. G. and Searle, R. C. 1979. The western Rockall Plateau: stratigraphy and structural evolution. Initial Reports of the Deep Sea Drilling Project XLVIII, 1061-1088.

Robinson, J. A. C. and Wood, B. J. 1998. The depth of the spinel to garnet transition at the peridotite solidus. Earth and Planetary Science Letters 164, 277–284.

Rocchi, S., Mazzotti, A., Marroni, M., Pandolfi, L., Costantini, P., Giuseppe, B., Di Biase, D., Federici, F. And Lô, P. G. 2007. Detection of Miocene saucer-shaped sills (offshore Senegal) via integrated interpretation of seismic, magnetic and gravity data. Terra Nova 19, 232-239.

Roest, W. R. and Shrivastava, S. P. 1989. Sea-floor spreading in the Labrador Sea: a new reconstruction. Geology 17, 1000-1003.

Rogers, N., Macdonald, R., Fitton, J. G., George, R., Smith, M. and Barreiro. 2000. Two mantle plumes beneath the East African rift system: Sr, Nd and Pb isotope evidence from Kenya Rift basalts. Earth and Planetary Science Letters 176, 387-400.

Rohrman, M. and Van der Beek, P. 1996. Cenozoic postrift domal uplift of North Atlantic margins: an asthenospheric diapirism model. Geology 24(10), 901-904.

Rollinson, H., 1998. Using geochemical data: evaluation, presentation, interpretation. Longman pp. 352.

Rosenbaum, G., Lister, G. S. and Duboz. 2002. Relative motions of Africa, Iberia and Europe duriing alpine orogeny. Tectonophysics 359, 117-129.

Rubin, A. M. 1995. Propagation of magma-filled cracks. Annual Reviews, Earth and Planetary Sciences 23, 287-336.

Rudge, J. F., Champion, M. E. S., White, N., McKenzie, D. and Lovell, B. 2008. A plume model of transient diacronous uplift at the Earth's surface. Earth and Planetary Science Letters 267, 146-160.

Rumph, B., Reaves, C. M., Orange, V. G. and Robinson, D. L. 1993. Structuring and transfer zones in the Faeroe Basin in a regional tectonic context. Petroleum Geology of Northwest Europe: Proceedings of the 4th Conference, Geological Society, London 999-1009.

Ryan, P. D. and Dewey, J. F. 1997. Continental eclogites and the Wilson Cycle. Journal of the Geological Society, London 154, 437-442.

Saunders, A. D., Fitton, J. G., Kerr, A. C., Norry, M. J. and Kent, R. W. 1997. The North Atlantic Igneous Province. Geophysical Monograph 100, 45-93.

Saunders, A. D., Jones, S. M., Morgan, L. A., Pierce, K. L., Widdowson, M. and Xu, Y. G. 2007. Regional uplift associated with continental large igneous provinces: the roles of mantle plumes and the lithosphere. Chemical Geology 241, 282-318.

Saunders, A. D., Norry, M. J. and Tarney, J. 1988. Origin of MORB and chemically depleted mantle reservoirs: trace element constraints. Journal of Petrology, Special Lithosphere Issue, 415-445.

Scarrow, J. H. and Cox, K. G. 1995. Basalts generated by decompressive adiabatic melting of a mantle plume: A case study from the Isle of Skye, NW Scotland. Journal of Petrology 36, 3-22.

Schultz, R. A., Okubo, C. H. and Wilkins, S. J. 2006. Displacement-length scaling relations for faults on terrestrial planets. Journal of Structural Geology 28, 2182-2193.

Sears, J. W., George, G. M. St. and Winne, J. C. 2005. Continental rift systems and anorogenic magmatism. Lithos 80, 147-154.

Sheth, H. C. 2007. 'Large Igneous Provinces (LIPs)': Definition, recommended terminology, and a hierarchical classification. Earth-Science Reviews 85, 117-124.

Shrivastava, S. P. and Tapscott, C. R. 1986. Plate kinematics of the North Atlantic. The Geology of North America, Magasin, 379-404.

Single, R.T. and Jerram, D.A. 2004. The 3-D facies architecture of flood basalt provinces and their internal heterogeneity: examples from the Palaeogene Skye Lava Field. Journal of the Geological Society, London, 161: 911-926.

Sinton, C. W. and Duncan, R. A. 1998. ^{40}Ar-^{39}Ar ages of lavas from the Southeast Greenland margin, ODP leg 152, and the Rockall Plateau, DSDP leg 81. Proceedings of the ODP, Scientific Results 152, 387-401.

Sinton, C. W., Hitchen, K. and Duncan, R. A. 1998. ^{40}Ar/^{39}Ar geochronology of silicic and basic volcanic rocks on the margins of the North Atlantic. Geological Magazine 135(2), 161-170.

Skaarup, N., Jackson, H. R. and Oakey, G. 2006. Margin segmentation of Baffin Bay/Davis Strait, eastern Canada based on seismic reflection and potential field data. Marine and Petroleum Geology 23, 127-144.

Skaarup, N. and Pulvertaft, C. R. 2007. Aspects of the structure on the coast of the West Greenland volcanic province revealed in seismic data. Bulletin of the Geological Society of Denmark 55, 65-80.

Skogseid, J., Pedersen, T., Eldholm, O. and Larsen, B. T. 1992. Tectonism and magmatism during NE Atlantic continental break-up: the Vøring Margin. Geological Society, London, Special Publications 68, 305-320.

Skogseid, J., Planke, S., Faleide, J. I., Pedersen, T., Eldholm, O. and Neverdal, F. 2000. NE Atlantic continental rifting and volcanic margin formation. Geological Society, London, Special Publications 167, 295-326.

Sobolev, A. V., Hofmann, A. W. and Nikogosian, I. K. 2000. Recycled oceanic crust observed in ghost plagioclase within the source of Mauna Loa lavas. Nature 404, 986-990.

Sonder, L. J. and England, P. C. 1989. Effects of a temperature-dependent rheology on large scale continental extension. Journal of Geophysical Research 94(B6), 7603-7619.

Sparks, R. S. J. 2003. Dynamics of magma degassing. From: Oppenheimer, C., Pyle, D. M. & Barclay, J. (eds) Volcanic Degassing. Geological Society, London, Special Publications 213, 5-22.

Speight, J. M., Skelhorn, R. R., Sloan, T. and Knaap, R. J. 1982. The dyke swarms of Scotland. Igneous Rocks of the British Isles. edited by D. S. Sutherland © 1982 John Wiley & Sons Ltd. Chapter 33, 449-459.

Srivastava, S. P. 1985. Evolution of the Eurasian Basin and its implications to the motion of Greenland along Nares Strait. Tectonophysics 114, 29-53.

Steiger, R. H. and Jäger, E. 1977. Subcommission on geochronology: convention of the use of decay constants in geo- and cosmochronology. Earth and Planetary Science Letters 36, 359-362.

Storey, M., Duncan, R. A., Pedersen, A. K., Larsen, L. M. and Larsen, H. C. 1998. $^{40}Ar/^{39}Ar$ geochronology of the West Greenland Tertiary volcanic province. Earth and Planetary Science Letters 160, 569-586.

Storey, M., Duncan, R. A. and Tegner, C. 2007. Timing and duration of volcanism in the North Atlantic Igneous Province: implications for geodynamics and links to the Iceland hotspot. Chemical Geology 241, 264-281.

Stracke, A., Zindler, A., Salters, V. J. M., McKenzie, D., Blichert-Toft, J., Albaréde, F. and Grønvold, K. 2003. Theistareykir revisited. Geochemistry Geophysics Geosystems 4(2), pp. 49.

Sun, S-s. and McDonough, W. F. 1989. Chemical and isotopic systematics of oceanic basalts: implications for mantle composition and processes. In Saunders AD, Norry MJ (eds) Magmatism in the ocean basins, Geological Society Special Publication 42, 313-345.

Surlyk, F. 1990. Timing, style and sedimentary evolution of Late Palaeozoic–Mesozoic extensional basins of East Greenland. From: Hardman, R. F. P. & Brooks, J. (eds), Tectonic Events Responsible for Britain's Oil and Gas Reserves, Geological Society Special Publication 55, 107-125.

Surlyk, F., Clemmensen, L. B. and Larsen, H. C. 1981. Post-Paleozoic evolution of the east Greenland continental margin. In: Kerr, J. W. & Fergusson, A. J. (eds) Geology of the North Atlantic Borderland. Canadian Society of petroleum Geologists, Memoir 7, 611-645.

Søager, N. and Holm, P. M. 2009. Extended correlation of the Paleogene Faroe Islands and East Greenland plateau basalts. Lithos 107, 205-215.

Søager, N. and Holm, P. M. 2011. Changing compositions of the Icfeland plume; Isotopic and elemental constraints from the Paleogene Faroe flood basalts. Chemical Geology 280, 297-313.

Takahashi, E. and Kushiro, I. 1983. Melting of a dry peridotite at high pressures and basalt magma genesis. American Mineralogist 68, 859-879.

Tate, M. P., Dodd, C. D. and Grant, N. T. 1999. The Northeast Rockall Basin and its significance in the evolution of the Rockall - Faeroes/East Greenland rift system. Petroleum Geology of Northwest Europe: Proceedings of the 5th Conference, Geological Society, London 391-406.

Taylor, P. N., Kalsbeek, F. and Bridgwater, D. 1992. Discrepancies between neodymium, lead and strontium model ages from the Precambrian of southern East Greenland: Evidence for a Proterozoic granulite-facies event affecting Archaean gneisses. Chemical Geology (Isotope Geoscience Section) 94, 281-291.

Tegner, C., Brooks, C. K., Duncan, R. A., Heister, L. E. and Bernstein, S. 2008. ^{40}Ar-^{39}Ar ages of intrusions in East Greenland: Rift-to-drift transition over the Iceland hotspot. Lithos 101, 480-500.

Tegner, C. and Duncan, R. A. 1999. ^{40}Ar-^{39}Ar chronology for the volcanic history of the Southeast Greenland rifted margin. Proceedings of the ODP, Scientific Results 163, 53-62.

Tegner, C., Duncan, R. A., Bernstein, S., Brooks, C. K., Bird, D. K. and Storey, M. 1998a. ^{40}Ar-^{39}Ar geochronology of Tertiary mafic intrusions along the East Greenland rifted margin: relation to flood basalts and the Iceland hotspot track. Earth and Planetary Science Letters 156, 75-88.

Tegner, C., Lesher, C. E., Larsen, L. M. and Watt, W. S. 1998b. Evidence from the rare-earth-element record of mantle melting for cooling of theTertiary Iceland Plume. Nature 395, 591-594.

Tesfaye, S., Harding, D. J. and Kusky, T. M. 2003. Early continental breakup boundary and migration of the Afar triple junction, Ethiopia. Geological Society of America Bulletin 115(9), 1053-1067.

Thirlwall, M. F., Gee, M. A. M., Taylor, R. N. and Murton, B. J. 2004 Mantle components in Iceland and adjacent ridges investigated using double-spike Pb isotope ratios. Geochimica et Cosmochimica Acta 68(2), 361-386.

Thompson, R. N., Dickin, A. P., Gibson, I. L. and Morrison, M. A. 1982. Elemental fingerprints of isotopic contamination of Hebridean Palaeocene mantle derived magmas by Archean sial. Contributions to Mineralogy and Petrology 79, 159-168.

Thompson, R. N., Gibson, S. A., Dickin, A. P. and Smith, P. M. 2001. Early Cretaceous basalt and picrite dykes of the southern Etendeka region, NW Namibia: windows into the role of the Tristan mantle plume in Paraná – Etendeka magmatism. Journal of Petrology 42 (11), 2049-2081.

Thompson, R. N., Morrison, M. A., Dickin, A. P., Gibson, I. L. and Harmon, R. S. 1986. Two contrasting styles of interaction between basic magmas and continental crust in the British Tertiary Igneous Province. Journal of Geophysical Research 91 (B6), 5985-5997.

Thompson, R. N., Morrison, M. A., Dickin, A. P. and Hendry, G. L. 1983. Continental flood basalts . . . Arachnids Rule OK? In: Hawkesworth CJ, Norry MJ (eds) Continental flood basalts and mantle xenoliths, Shiva, Nantwick, UK 158-185.

Thompson, R.N., Ottley, C.J., Smith, P.M., Pearson, D.G., Dickin, A.P., Morrison, M.A., Leat, P.T. and Gibson, S.A. 2005. Source of the Quaternary alkalic basalts, picrites and basanites of the Potrillo Volcanic Field, New Mexico, USA – lithosphere or convecting mantle? Journal of Petrology 46, 1603-1643.

Thompson, R. N., Riches, A. J. V., Antoshechkina, P. M., Pearson, D. G., Nowell, G. M., Ottley, C. J., Dickin, A. P., Hards, V. L., Nguno, A.-K. and Niku-Paavola. V. 2007. Origin of CFB Magmatism: Multi-tiered intracrustal picrite-rhyolite magmatic plumbing at Spitzkoppe, Western Namibia, during Early Cretaceous Etendeka magmatism. Journal of Petrology, 48(6), 1119-1154.

Thomson, K. 2004. Sill complex geometry and internal architecture: a 3D seismic perspective. From Breitkreuz, C. & Petford, N. (eds) 2004. Physical Geology of High-level Magmatic Systems. Geological Society, London, Special Publications 234, 229-232.

Thomson, K. 2007. Determining magma flow in sills, dykes and laccoliths and their implications for sill emplacement mechanisms. Bulletin of Volcanology 70, 183-201.

Thomson, K., Green, P. F., Whitham, A. G., Price, S. P. and Underhill, J. R. 1999. New constraints on the thermal history of North-East Greenland from apatite fission track analysic. Geological Society of America, Bulletin 111(7), 1054-1068.

Thomson, K. and Hutton, D. 2004. Geometry and growth of sill complexes: insights using 3D seismic from the North Rockall Trough. Bulletin of Volcanology 66, 364-375.

Thrane, K. 2002. Relationships between Archaean and Palaeoproterozoic crystalline basement complexes in the southern part of the East Greenland Caledonides: an ion microprobe study. Precambrian Research 113, 19-42.

Torske, T. and Prestvik, T. 1991. Mesozoic detachment faulting between Greenland and Norway: inferences from Jan Mayen Fracture Zone system and associated alkalic volcanic rocks. Geology 19, 481-484.

Torsvik, T. H., Mosar, J. and Eide, E. A. 2001. Cretaceous-Tertiary geodynamics: a North Atlantic Exercise. Geophysical Journal International 146, 850-866.

Torsvik, T. H., Van der Voo, R., Meert, J., Mosar, J. and Walderhaug, H. J. 2001. Reconstructions of the continents around the North Atlantic at about the 60th parallel. Earth and Planetary Science Letters 187, 55-69.

Trude, J., Cartwright, J., Davies, R. J. and Smallwood, J. 2003. New technique for dating igneous sills. Geology 31(9), 813-816.

Trønnes, R. G., Planke, S., Sundvoll, B. and Imsland, P. 1999. Recent volcanic rocks from Jan Mayen: low-degree melt fractions of enriched northeast Atlantic mantle. Journal of Geophysical Research 104(B4), 7153-7168.

Tsikalas, F., Eldholm, O. and Faleide, J. I. 2002. Early Eocene sea floor spreading and continent-ocean boundary between Jan Mayen and Senja fracture zones in the Norwegian–Greenland Sea. Marine Geophysical Researchers 23, 247-270.

Ulmer, P. 2001. Partial melting inj the mantle wedge – the role of H_2O in the genesis of mantle-derived 'arc-related' magmas. Physics of the Earth and Planetary Interiors 127, 215-232.

Upton, B. G. J. 1988. History of Tertiary igneous activity in the N Atlantic borderlands. Geological Society, London, Special Publications 39, 429-453.

Upton, B. G. J., Emeleus, C. H., Rex, D. C. and Thirlwall, M. F. 1995. Early Tertiary magmatism in NE Greenland. Journal of the Geological Society, London 152, 959-964.

Upton, B. G. J., Skovgaard, A. C., McClurg, J., Kirstein, L., Cheadles, M., Emeleus, C. H., Wadsworth, W. J. and Fallick, A. E. 2002. Picritic magmas and the Rum ultramafic complex, Scotland. Geological Magazine 139(4), 437-452.

Valentine, G. A. and Krogh, K. E. C. 2006. Emplacement of shallow dikes and sills beneath a small basaltic volcanic center – The role of pre-existing structure (Paiute Ridge, southern Nevada, USA). Earth and Planetary Science Letters 246, 217-230.

Van Wijk, J. W., Huismans, R. S., Ter Voorde, M. and Cloetingh, S. A. P. L. 2001. Melt generation at volcanic continental margins: no need for a mantle plume. Geophysical Research Letters 28(20), 3995-3998.

Varga, R. J., Gee, J. S., Staudigel, H. and Tauxe, L. 1998. Dike surface lineations as magma flow indicators within the sheeted dike complex of the Troodos Ophiolite, Cyprus. Journal of Geophysical Research 103(B3), 5241-5256.

Viereck, L. G., Taylor, P. N., Parson, L. M., Hertogen, J., Gibson, I. L. and the ODP Leg 104 Scientific Party. 1988. Origin of the Paleogene Vøring Plateau volcanic sequence. Geological Society, London, Special Publications 39, 69-83.

Waagstein, R. 1988. Structure, composition and age of the Faeroe basalt plateau. Geological Society, London ,Special Publications 39, 225-238.

Waagstein, R., Guise, P. and Rex, D. 2002. K/Ar and $^{39}Ar/^{40}Ar$ whole-rock dating of zeolite facies metamorphosed flood basalts: the upper Paleocene basalts of the Faroe Islands, NE Atlantic. Geological Society, London, Special Publications 197, 219-252.

Walker, G. P. L. 1992. "Coherent intrusion complexes" in large basaltic volcanoes – a new structural model. Journal of Volcanology and Geothermal Research 50, 41-54.

Walker, J. A., Carr, M. J., Feigenson, M. D. and Kalamarides, R. I. 1990. The petrogenetic significance of interstratified high- and low-Ti basalts in central Nicaragua. Journal of Petrology 31(5), 1141-1164.

Walker, R. J., Holdsworth, R. E., Imber, J., and Ellis, D. 2011. Onshore evidence for progressive changes in rifting directions during continental break-up in the NE Atlantic. Journal of the Geological Society, London, 168, 27–48.

Weaver, B. L. and Tarney, J. 1980. Rare earth geochemistry of Lewisian granulite-facies gneisses, northwest Scotland: implications for the petrogenesis of the Archaean lower continental crust. Earth and Planetary Science Letters 51, 279-296.

Weis, D., Kieffer, B., Maerschalk., C., Pretorius, W. and Barling, J. 2005. High precision Pb-Sr-Nd-Hf isotopic characterisation of USGS BHVO-1 and BHVO-2 reference materials. Geochemistry Geophysics, Geosystems 6.

White, R. and McKenzie, D. 1989. Magmatism at Rift Zones: the generation of volcanic continental margins and flood basalts. Journal of the Geophysical Research 94(B6), 7685-7729.

Wilson, M. 1997. Thermal evolution of the Central Atlantic passive margins: continental break-up above a Mesozoic super-plume. Journal of the Geological Society, London 154, 491-495.

Wolfenden, E., Ebinger, C., Yirgu, G., Deino, A. and Ayalew, D. 2004. Evolution of the northern Main Ethiopian rift: birth of a triple junction. Earth and Planetary Science Letters 224, 213-228.

Wood, D. A., 1979. A variably veined suboceanic upper mantle – Genetic significance for mid-ocean ridge basalts from geochemical evidence. Geology 7, 499-503.

Woods, A. W. and Cardoso, S. S. S. 1997. Triggering basaltic volcanic eruptions by bubble-melt separation. Nature 385, 518-520.

Wood, D. A., Gibson, I. L. and Thompson,R. N. 1976. Elemental mobility during zeolite facies metamorphism of the Tertiary basalts of eastern Iceland. Contributions to Mineralogy and Petrology 55, 241-254.

Workman, R. K. and Hart, S. R. H. 2005. Major and trace element composition of the depleted MORB mantle (DMM). Earth and Planetary Science Letters 231, 53–72.

Xiao, L., Xu, Y. G., Mei, H. J., Zheng, Y. F., He, B. and Pirajno, F. 2004. Distinct mantle sources of low-Ti and high-Ti basalts from the western Emeishan large igneous province, SW China: implications for plume-lithosphere interaction. Earth and Planetary Science Letters228, 525-546.

Xiong, X. L., Adam, J. and Green, T. H. 2005. Rutile stability and rutile/melt HFSE partitioning during partial melting of hydrous basalt: Implications for TTG genesis. Chemical Geology 218, 339-359.

Yasuda, A., Fujii, T. and Kurita, K. 1994. Melting phase relations of an anhydrous mid-ocean ridge basalt from 3 to 20 GPa: Implications for the behavior of subducted oceanic crust in the mantle. Journal of Geophysical Research 99(B5), 9401-9414.

Yaxley, G. M. 2000. Experimental study of the phase and melting relations of homogeneous basalt + peridotite mixtures and implications for the petrogenesis of flood basalts. Contributions to Mineralogy and Petrology 139, 326-338.

Yoder, H. S. and Tilley, C. E. 1962. Origin af basalt magmas: an experimental study of natural and synthetic rock systems. Journal of Petrology 3, 342-532.

Zegers, T. E. and Van Keken, P. E. 2001. Middle Archean continent formation by crustal delamination. Geology 29(12), 1083-1086.

Zhao, D. 2004. Global tomographic images of mantle plumes and subducting slabs: insight into deep Earth dynamics. Physics of the Earth and Planetary Interiors 146, 3-34.

Ziegler, P. A. 1989. Evolution of the North Atlantic-An Overview. The American Association of Petroleum Geologists (AAPG) Memoir 46, 111-129.

Ziegler, P. A. 1992. Plate tectonics, plate moving mechanisms and rifting. Tectonophysics 215, 9-34.

Zindler, A. and Hart, S. 1986. Chemical geodynamics. Annual Review of Earth Planetary Sciences 14, 493-571.

Appendix 1

Outline of the workflow employed during transfer of field data to 3D electronic maps (ArcGIS software)

Loading maps: Printed topographic maps containing relevant field measurements were scanned, saved as jpg files and subsequently loaded in the **ArcCatalog** program by selecting → folder → new → layer → new layer → browse jpg file → save under new selected/chosen file name.

Assigning coordinate systems to loaded maps: Relevant coordinate systems were assigned to loaded maps in the **ArcMap** program by selecting → add data → folder → open relevant file (from ArcCatalog) → map appear on screen → right click on mouse while cursor is positioned on map → data frame properties → coordinate system → predefined → projected coordinate systems → UTM → WGS 1984 → WGS 1984 UTM zone 29N (*WGS_1984_UTM_zone_29N; Projection: Transverse_Mercator; False_Easting: 500000; False_Northing: 0; Central_Meridian: -9; Scale_Factor: 0.9996; Latitude_of_Origin: 0; Linear Unit: Meter)* → select no frame in data view → right click on mouse while cursor is positioned on map → properties → grids → new grid → measured grid → assign intervals on x/y axes e.g. 1000 metres → next → finish (grid appear on screen) → right click on mouse while cursor is positioned on map (again) → properties → assign origin in x/y space e.g. 0.0 → OK → data frame → fixed extent → assign the same four coordinates that define four preselected corners of the actual map section → OK (numbered meridians appear on grid) → activate GeoReferencing function in → view → toolbars → GeoReferencing (if map is out of frame then select → GeoReferencing → fit to display) → add control points → left click on mouse while cursor is positioned on preselected coordinates that represent one corner of map → left click on mouse while cursor is positioned on grid coordinates that correspond to those just selected for map corner → repeat this process on the remaining three map/grid corners → select GeoReferencing → update GeoReferencing → right click on Layers → file → save as layer file → select/choose new file name → OK.

Creating shapefiles: New shapefiles were created in **ArcCatalog** by selecting → folder → new → shapefile → select/choose new file name → polyline → edit → predefined coordinate system (then assigning the same coordinate system as above i.e. WGS-1984, UTM-29N) → OK.

Producing geological surfaces/layers: Maps with assigned coordinate systems were used to produce surfaces of individual geological formations and sills in **ArcMap** by selecting → add data → open empty shapefile (from ArcCatalog) → editor → start editing → sketch tool → draw outline with cursor/mouse → save edits. Alternatively surfaces of individual geological formations and sills can be produced in e.g. CorelDRAW and then assigned relevant coordinate systems using the procedure described above for maps.

Draping of surfaces onto electronic 3D topographic maps: Predefined electronic topographic data that represent the Faroe Islands (WGS-1984, UTM 29N, 10 metres height intervals) were supplied from the company of MUNIN, Tórshavn, Faroe Islands and stored as layer files in ArcCatalog. These topographic data were conversed to TIN surfaces in **ArcMap** by selecting → add data → open file (with topographic map from ArcCatalog) → create TIN from features → select/choose new file name for output TIN (height source = Z values; triangulate as hard line) → OK → save as layer or as ArcMap project.

Draping of surfaces to produce 3D geological maps were done in **ArcScene** by selecting → add data → open TIN file → add data (again) → open file with a geological formation or sill → use mouse to position/drag this latter file on the top of the TIN file in the left panel of the screen → right click on layer → properties → base heights → obtain heights for layer from surface → rendering → shade areal features relative to the scene's light position → OK → save draped feature.

The draped features will appear as 3D electronic geological maps that can be rotated and viewed from any angles in ArcScene. These features can be converted to jpg images. Examples are shown in Fig. 2.3; Fig. 3.2; Fig. 3.3 (orthogonal views) and Fig. 3.4 (oblique views).

Appendix 2

C1 X-Ray Fluorescence (XRF) analysis methodology

The geochemical datasets used in chapter 4 of this thesis are based on whole-rock analyses of samples representing basaltic sills and a few of their feeders. More than 400g of the fine to medium grained basalt samples were crushed to fine gravel/sand (< 0.5 cm) using standard crushing techniques. Around 100g of each of the crushed samples were subsequently ground to fine powder using an agate ball mill at Durham University. In order to avoid/reduce any kind of contamination, thorough cleaning on all used instruments was carried out between the processing of each sample.

Major elements and selected trace elements (Table 4.2) for samples and standards were measured on an ARL 8420+ dual goniometer wavelength dispersive XRF spectrometer in the X.R.F. Laboratory at the Department of Earth Sciences, Open University, Milton Keynes, United Kingdom.

Major elements: For XRF analyses of major elements a suitable amount of finely ground rock powder from each sample and a suitable amount of flux (lithium metaborate/tetraborate, Johnson Matthey Spectroflux 100B) were dried overnight in an oven at ~110° C. Exactly 0.7 g of each dry sample and 3.5 g of flux (1:5 ratio) were weighed out and mixed in Pt crucibles. Following stirring, each mixed sample was fused at 1100° C for 15-20 minutes during which the crucibles were swirled every 5 minutes or so to ensure thorough mixing. The melted samples were subsequently poured into pre-heated brass moulds and pressed to form glass discs. Glass discs for two well known standards (WS-E and G94) were produced parallel to the rock samples and both were analysed together with every batch of samples.

Potential losses of fluids/volatiles (H_2O and/or CO_2) during fusion were determined by means of 1 to 2g of dried powder from each sample being heated for 30 to 45 minutes at 1000°C in a muffle furnace. Loss on ignition (LOI) for individual samples was then calculated to two decimal places using the expression:

$$Percentage\ Loss\ on\ Ignition = \frac{loss\ or\ gain\ in\ weight\ of\ rock\ powder}{original\ weight\ of\ rock\ powder} \times 100$$

The reproducibility of major element concentrations on the standards during the analyses was usually better than 1% (See the table Appendix 2.1. below).

Appendix 2.1. Control analyses of major elements of the standards WS-E and G94 during XRF analyses on glass beads (as shown in Table 4.2) at the Open University, Milton Keynes.

wt%	**WS-E Expected**	**WS-E** Average (n=6)	**WS-E** St.Dev.	**G94 Expected**	**G94** Average (n=6)	**G94** St.Dev.
SiO_2	**51.10**	51.13	0.033	**69.95**	69.79	0.023
TiO_2	**2.425**	2.41	0.013	**0.314**	0.31	0.003
Al_2O_3	**13.78**	13.95	0.021	**14.66**	14.65	0.019
Fe_2O_3	**13.25**	13.27	0.016	**3.05**	3.06	0.007
MnO	**0.171**	0.17	0.001	**0.075**	0.08	0.002
MgO	**5.55**	5.55	0.014	**1.04**	1.05	0.011
CaO	**8.95**	9.07	0.009	**1.34**	1.37	0.004
Na_2O	**2.47**	2.44	0.008	**4.60**	4.61	0.019
K_2O	**1.00**	1.00	0.003	**2.96**	2.98	0.008
P_2O_5	**0.302**	0.30	0.002	**0.165**	0.17	0.002
LOI	**0.85**	0.85	0.000	**1.97**	1.97	0.000
Total	**99.85**	100.14	0.059	**100.12**	100.03	0.056

A few of the analysed samples display negative LOI values (Table 4.2). If all preparation steps of the actual samples were done correctly, near-absence of secondary alteration and relative weight gain from the oxidation of FeO (Fe^{++}) to Fe_2O_3 (Fe^{+++}) could be an explanation (Ionov, 2010). This scenario may be supported by the fact that negative LOI values only occur in iron-rich sill samples. Five sill samples display slightly high totals of 101-102%, all of which possess unusually high silica contents of 50.3 to 50.45 wt% (Table 4.2). High totals can result from preferential evaporation of flux during production of the glass beads, but can also reflect uncertainties in the determination of SiO_2 (e.g. Boström and Bach, 1995).

Trace elements: The preparation of samples for XRF analyses of trace elements involved ~9 g of finely ground powder from each sample being thoroughly mixed with ~0.9 ml of polyvinylpyrollidone (P.V.P.) binder. Each mixed sample was then pressed to a powder pellet in a mould at ~5 ton for a few moments and subsequently dried overnight at ~110° C. Powder pellets for four standards (BHVO-1; QLO-1; DNC-1 and W-2 all being United States Geological Survey international reference materials) were produced parallel to the rock samples and analysed for trace elements together with every batch of samples from this study. The reproducibility of each standard during analyses of the trace elements, shown in Table 4.2, was usually better than 4% apart from Y that was usually better than 5 to 10% (See the table Appendix 2.2. below for selected trace elements).

Appendix 2.2. Control analyses of selected trace elements, used in this study, by means of the standards BHVO-1, QLO-1, DNC-1 and W-2 during XRF analyses on pressed powder tablets (as shown in Table 4.2) at the Open University, Milton Keynes.

	BHVO-1	**BHVO-1**	**BHVO-1**	**QLO-1**	**QLO-1**	**QLO-1**	**DNC-1**	**DNC-1**	**DNC-1**	**W-2**	**W-2**	**W-2**
ppm	**Expected**	Average (n=6)	St.Dev.	**Expected**	Average (n=6)	St.Dev.	**Expected**	Average (n=6)	St.Dev.	**Expected**	Average (n=6)	St.Dev.
Sr	**403**	402.65	1.22	**336**	332.82	1.04	**145**	147.72	0.54	**194**	201.08	0.73
Y	**27.6**	27.77	0.44	**24.0**	25.12	0.16	**18.0**	18.85	0.37	**24.0**	23.13	0.8
Zr	**179**	175.22	1.36	**185**	186.82	1.13	**41**	40.12	0.5	**94**	93.32	1.29
Ba	**139**	135.12	3.02	**1370**	1378.73	18.07	**114**	108.52	4.09	**182**	179.12	5.99

Appendix 3

Inductively coupled plasma emission spectrometry (ICP-MS) analysis methodology

Finely ground powder from actual basalt samples and from the international standard NBS 688, each sample weighing 0.100 ± 0.001g, was used for ICP-MS analyses of trace elements and REE (Table 4.2). The powder was dissolved in a mixture of 1 ml HNO_3 (69%) + 4 ml HF (40%) in a Savillex 22 ml PFA vial and left on a hotplate at ~150° C for ~48 hours with the seal on (reflux). The mixture in each sample was subsequently allowed to evaporate to near dryness. 1 ml HNO_3 was applied to each sample, which was again allowed to evaporate to near dryness; this procedure was repeated once. 2.5 ml HNO_3 + 10 ml 18MΩ H_2O was subsequently applied to each sample, which was left on a hotplate at ~100°C overnight with the seal on (reflux). 1 ml of 1 ppm Re and Rh internal 'spikes' was then applied to each of the cooled samples to yield 20 ppb in solution followed by the addition of 18MΩ H_2O until each sample was diluted to exactly 50 ml in order to yield a solution of approximately 3.5% HNO_3. Prior to analyses each sample was diluted 10 fold by the addition of 3 % HNO_3. One standard (NBS 688) and three blanks were prepared parallel with the rock samples. Trace elements and REE in samples, standards and blanks were determined on an Elan 6000 Perkin Elmer-Sciex inductively coupled plasma mass spectrometer (ICP-MS) at the Department of Earth Sciences, Durham University, Durham, United Kingdom. Calibration of the Perkin Elmer Sciex Elan 6000 ICP-MS was achieved via the use of in-house standards and international reference materials (e.g. W-2, BHVO-1, AGV1, BE-N and NBS688), together with procedural blanks. In order to ascertain the magnitude of calibration drift, three blanks and all the five standards were run at the start and at the end of the performed analyses and one blank was run for every 8-10 samples. The reproducibility of trace elements from in-house standards analysed on this apparatus is usually better than 5% and frequently 3% (See table Appendix 3.1. below for control analyses of the standards NBS688, BHVO-1, W-2, AGV1 and BE-N). More details on methods for the dissolution of geological samples for analysis of REE and trace elements via ICP –MS are given in Ottley et al. (2003) and Thompson et al. (2005).

Appendix 3.1. Control analyses of selected trace elements of the standards NBS688, BHVO-1, W-2, AGV1 and BE-N during ICP-MS analyses on dissolved rock samples (as shown in Table 4.3) at the Department of Earth Sciences, Durham University.

ppm	NBS688 Expected	NBS688 Aver.(n=7)	NBS688 St.Dev.	BHVO-1 Expected	BHVO-1 Aver.(n=2)	BHVO-1 St.Dev.	W-2 Expected	W-2 Aver.(n=2)	W-2 St.Dev.	AGV1 Expected	AGV1 Aver.(n=2)	AGV1 St.Dev.	BE-N Expected	BE-N Aver.(n=2)	BE-N St.Dev.
Rb	**1.91**	1.95	0.04	**11.00**	9.62	0.06	**20.00**	20.14	0.05	**67.00**	67.80	1.05	47.00	48.81	0.27
Sr	**169.20**	173.38	3.43	**403.00**	411.27	8.20	**194.00**	199.06	1.67	**662.00**	673.98	20.95	1370.00	1275.72	23.55
Y	**17.00**	21.53	0.43	**27.60**	28.01	0.58	**24.00**	22.60	0.19	**21.00**	20.11	0.33	30.00	30.75	0.65
Zr	**61.00**	56.54	1.09	**179.00**	175.78	1.36	**94.00**	89.81	0.05	**225.00**	231.76	3.09	265.00	277.15	0.80
Nb	**5.00**	4.41	0.11	**19.00**	19.58	0.32	**7.90**	7.63	0.05	**15.00**	14.76	0.10	100.00	119.40	0.90
Ba	**200.00**	185.78	5.89	**139.00**	136.33	6.89	**182.00**	172.12	8.40	**1221.00**	1255.39	47.25	1025.00	1062.49	46.45
La	**5.30**	5.18	0.14	**15.80**	15.65	0.53	**11.40**	10.47	0.42	**38.00**	39.03	0.97	82.00	83.72	2.90
Ce	**13.00**	11.82	0.29	**39.00**	38.14	1.52	**24.00**	22.75	1.08	**66.00**	69.02	2.14	152.00	153.04	6.06
Pr	**2.40**	1.86	0.06	**5.70**	5.84	0.29	**5.90**	3.18	0.17	**6.50**	9.04	0.43	16.90	18.75	0.90
Nd	**9.60**	8.96	0.28	**25.20**	27.10	1.26	**14.00**	13.67	0.48	**34.00**	34.18	1.37	70.00	71.90	2.93
Sm	**2.50**	2.46	0.07	**6.20**	6.50	0.26	**3.25**	3.36	0.15	**5.90**	5.96	0.17	12.00	12.72	0.63
Eu	**1.01**	1.00	0.03	**2.06**	2.11	0.07	**1.10**	1.10	0.06	**1.66**	1.75	0.08	3.60	3.83	0.12
Gd	**3.20**	3.28	0.08	**6.40**	6.77	0.13	**3.60**	3.90	0.02	**5.20**	4.70	0.01	9.00	9.68	0.06
Tb	**0.52**	0.56	0.01	**0.96**	1.01	0.04	**0.63**	0.66	0.01	**0.71**	0.67	0.02	1.30	1.33	0.05
Dy	**3.40**	3.43	0.09	**5.20**	5.48	0.15	**3.80**	3.84	0.06	**3.80**	3.60	0.16	6.29	6.44	0.16
Ho	**0.81**	0.74	0.02	**0.99**	1.01	0.02	**0.76**	0.81	0.04	**0.73**	0.69	0.01	1.03	1.10	0.03
Er	**2.10**	2.09	0.04	**2.40**	2.47	0.02	**2.50**	2.14	0.05	**1.61**	1.73	0.03	2.48	2.42	0.07
Tm	**0.29**	0.33	0.01	**0.33**	0.35	0.00	**0.38**	0.33	0.01	**0.32**	0.26	0.01	0.37	0.32	0.01
Yb	**2.05**	2.10	0.04	**2.02**	2.05	0.01	**2.05**	2.03	0.02	**1.67**	1.65	0.02	1.80	1.83	0.05
Lu	**0.35**	0.35	0.01	**0.29**	0.31	0.01	**0.33**	0.33	0.00	**0.28**	0.27	0.01	0.24	0.28	0.00
Hf	**1.55**	1.52	0.02	**4.38**	4.51	0.09	**2.56**	2.37	0.01	**5.10**	5.16	0.08	5.40	5.86	0.11
Ta	**0.31**	0.28	0.00	**1.23**	1.25	0.01	**0.50**	0.49	0.00	**0.92**	0.91	0.00	5.50	6.13	0.04
Pb	**3.30**	2.89	0.08	**2.60**	2.08	0.03	**9.30**	7.59	0.09	**36.00**	35.80	0.38	4.00	3.99	0.09
Th	**0.33**	0.33	0.01	**1.08**	1.25	0.00	**2.20**	2.16	0.03	**6.50**	6.42	0.03	11.00	10.63	0.09
U	**0.31**	0.26	0.03	**0.42**	0.42	0.01	**0.53**	0.49	0.01	**1.89**	1.91	0.02	2.40	2.42	0.04

Appendix 4

Multi-collector inductively coupled plasma emission spectrometry (MC-ICP-MS) analysis methodology (Adopted from "Electronic Appendix A" of G. Nowell 2010)

Isotope ratios for Sr, Nd and Pb were measured using the AHIGL ThermoElectron Neptune Multi-collector Plasma Mass Spectrometer (MC-ICP-MS) at the Arthur Holmes Isotope Geology Laboratory (AHIGL) Durham University, Durham, United Kingdom. The basic analytical method used for each element on the Neptune comprises a static multi-collection routine of 1 block of 50 cycles with an integration time of 4sec per cycle; total analysis time 3.5mins.

For the **Sr** and **Nd** chemistry, samples were dissolved in Teflon beakers with 1ml l6N HNO_3 and 3mls 29N HF at 120°C for 48hrs. After dissolution Sr and Nd were separated using a combination of cation and anion exchange columns (Dowall et al., 2003).

After chemistry, **Sr** samples were taken up in 1ml of 3% HNO_3 and introduced into the Neptune using an ESI PFA50 nebuliser and a dual cyclonic–Scott Double Pass spraychamber. With this sample introduction set up, and the normal H skimmer cone, the sensitivity for Sr on the Neptune is typically ~60V total Sr ppm-1 at an uptake rate of 90µl min-1. Prior to analysis a small aliquot was first tested to establish the Sr concentration of each sample by monitoring the size of the 84Sr beam (88Sr was too high in non-diluted aliquot to measure directly) from which a dilution factor was calculated to yield a beam of approximately 20V 88Sr. Instrumental mass bias was corrected for using a 88Sr/86Sr ratio of 8.375209 (the reciprocal of the 86Sr/88Sr ratio of 0.1194) and an exponential law. The sill samples from the Faroe Islands were analysed in a single session during which the average 87Sr/86Sr value for the NBS 987 standard was 0.710270 ± 0.000016 (21.8 ppm 2SD; n = 9, see also table appendix 4.1 below).

Following chemistry the REE cuts containing the **Nd** fraction were taken up in 1ml of 3% HNO_3 and introduced into the Neptune using an ESI PFA50 nebuliser and a dual cyclonic–Scott Double Pass spraychamber. With this sample introduction set

up, and the normal H skimmer cone, the sensitivity for Nd on the Neptune is 60-80V total Nd ppm-1 at an uptake rate of 90µl min-1. Instrumental mass bias was corrected using a 146Nd/145Nd ratio of 2.079143 (equivalent to the more commonly used 146Nd/144Nd ratio of 0.7219) and an exponential law. The 146Nd/145Nd ratio is used for correcting mass bias since at Durham Nd isotopes are measured on a total REE-cut from the 1st stage cation columns and this is the only Ce and Sm-free stable Nd isotope ratio. This approach requires a correction for isobaric interferences from Sm on 144Nd, 148Nd and 150Nd. The correction used is based on the method of Nowell and Parrish (2001). The accuracy of the Sm correction method during analysis of a total REE fraction is demonstrated by repeat analyses of BHVO-1, which gave an average 143Nd/144Nd ratio of 0.512982±0.000007 (13.5ppm 2SD, n=13) after Sm correction; identical to the TIMS ratio of 0.512986±0.000009 (17.5ppm 2SD; n=19) obtained by Weis et al. (2005). During analysis of the sill samples from the Faroe Islands the pure and Sm-doped J&M standards gave an average 143Nd/144Nd ratio of 0.511115 ± 0.000014 (26.7 ppm 2SD; n = 9, see also table appendix 4.1. below).

Sill **Pb** was separated using small Sr Spec resin columns (Charlier et al., 2006).

After chemistry, Lead samples were taken up in 1ml of 3% HNO_3. Prior to analysis each sample was tested on the Neptune to determine its Pb concentration and thereby calculate the appropriate amount of tantalum spike to add in order to obtain a Pb/Tl ratio of ~12. After spiking with Tl each sample was introduced into the Neptune using an ESI PFA50 nebuliser and a dual cyclonic–Scott Double Pass spraychamber. With this set-up, and the normal H skimmer cone, the sensitivity for Pb on the Neptune is typically ~100V total Pb ppm-1 at an uptake rate of 90µl min-1. Pb mass bias was corrected for externally using the 205Tl/203Tl ratio of the admixed Tl spike and an exponential law. The 205Tl/203Tl ratio used for correcting the Pb ratios is determined for each analytical session by minimising the difference in offset between the session average Pb ratios (all ratios) and the Galer and Abouchami (1998) values, i.e. it is the ratio that gives the best fit for all the Pb ratios to the values of Galer and Abouchami (1998) simultaneously that is used. Samples were analysed in a single analytical session during which the 205Tl/203Tl ratio used for mass bias correction was 2.38835 and the average 206Pb/204Pb, 207Pb/204Pb and 208Pb/204Pb ratios

for the NBS 981 Pb std were 16.9402 ± 0.0020, 15.4972 ± 0.0024, 36.7176 ± 0.0060 respectively (all 2SD; n=9, see also table appendix 4.1. below).

Calculations of $^{87}Rb/^{86}Sr$ and $^{147}Sm/^{144}Nd$ ratios. As $^{87}Rb/^{86}Sr$ and $^{147}Sm/^{144}Nd$ ratios were not supplied together with the Sr and Nd isotope data, these values had to be calculated separately using the expressions (Faure, 1986, 2001):

$^{87}Rb/^{86}Sr = (Rb/Sr) \times (Ab^{87}Rb \times WSr) / (Ab^{86}Sr \times WRb)$ and

$^{147}Sm/^{144}Nd = (Sm/Nd) \times (Ab^{147}Sm \times WNd) / (Ab^{144}Nd \times WSm)$

where Ab refer to isotopic abundances and W refer to atomic weights. Isotopic abundances of ^{87}Rb and ^{147}Sm are 0.278346 and 0.150000 respectively (Faure, 1986). Calculations of unknown ^{86}Sr and ^{144}Nd (and some other) isotopic abundances can be tabulated as (e.g. Faure, 2001):

	Ratio	Isotope	Abundance
$^{84}Sr/^{88}Sr$	[a]Calculated	$^{84}Sr \rightarrow$	$(^{84}Sr/^{88}Sr)/Sum$
$^{86}Sr/^{88}Sr$	[b] 0.119400	$^{86}Sr \rightarrow$	$(^{86}Sr/^{88}Sr)/Sum$
$^{87}Sr/^{88}Sr$	[c]Calculated	$^{87}Sr \rightarrow$	$(^{87}Sr/^{88}Sr)/Sum$
$^{88}Sr/^{88}Sr$	1.000000	$^{88}Sr \rightarrow$	$(^{88}Sr/^{88}Sr)/Sum$
	[d]Sum		

[a]$(^{84}Sr/^{86}Sr)/(^{86}Sr/^{88}Sr)$ where $^{84}Sr/^{86}Sr = 0.056584$ (Steiger and Jäger, 1977); [b]Value from Steiger and Jäger (1977); [c]$(^{86}Sr/^{88}Sr)/(^{87}Sr/^{86}Sr)_{measured}$; [d]combined value of Sr isotopic ratios.

and

	Ratio	Isotope	Abundance
$^{145}Nd/^{146}Nd$	[a]Calculated	$^{145}Nd \rightarrow$	$(^{145}Nd/^{146}Nd)/Sum$
$^{144}Nd/^{146}Nd$	[b] 1.389535	$^{144}Nd \rightarrow$	$(^{144}Nd/^{146}Nd)/Sum$
$^{143}Nd/^{146}Nd$	[c]Calculated	$^{143}Nd \rightarrow$	$(^{143}Nd/^{146}Nd)/Sum$
$^{146}Nd/^{146}Nd$	1.000000	$^{146}Nd \rightarrow$	$(^{146}Nd/^{146}Nd)/Sum$
	[d]Sum		

[a]$(^{145}Nd/^{144}Nd)/(^{144}Nd/^{146}Nd)$ where $^{145}Nd/^{144}Nd = 0.347280$ (Faure, 2001); [b]Value from Faure (2001); [c]$(^{144}Nd/^{146}Nd)/(^{143}Nd/^{144}Nd)_{measured}$; [d]combined value of Nd isotopic ratios.

Equation used for age correction of $^{87}Sr/^{86}Sr$ ratios (Faure, 1986). $^{87}Rb/^{86}Sr$ ratios may be either measured or calculated (as shown above).

$$(^{87}Sr/^{86}Sr)^{54\ Ma} = (^{87}Sr/^{86}Sr)_{measured} - {}^{87}Rb/^{86}Sr * (EXP(\lambda_{Rb\rightarrow Sr}*54\ Ma) - 1)$$

Equation used for age correction of $^{143}Nd/^{144}Nd$ ratios (Faure, 1986). $^{147}Sm/^{144}Nd$ ratios may be either measured or calculated (as shown above).

$$(^{143}Nd/^{144}Nd)^{54\ Ma} = (^{143}Nd/^{144}Nd)_{measured} - {}^{147}Sm/^{144}Nd * (EXP(\lambda_{Sm\rightarrow Nd}*54\ Ma) - 1)$$

Equation used for age correction of $^{206}Pb/^{204}Pb$ ratios (Faure, 1986). $^{238}U/^{204}Pb$ ratios may me either measured or calculated.

$$(^{206}Pb/^{204}Pb)^{54\ Ma} = (^{206}Pb/^{204}Pb)_{measured} - {}^{238}U/^{204}Pb * (EXP(\lambda_{U\rightarrow Pb}*54\ Ma) - 1)$$

Equation used for age correction of $^{207}Pb/^{204}Pb$ ratios (Faure, 1986). $^{235}U/^{204}Pb$ ratios may me either measured or calculated.

$$(^{207}Pb/^{204}Pb)^{54\ Ma} = (^{207}Pb/^{204}Pb)_{measured} - {}^{235}U/^{204}Pb * (EXP(\lambda_{U\rightarrow Pb}*54\ Ma) - 1)$$

Equation used for age correction of $^{208}Pb/^{204}Pb$ ratios (Faure, 1986). $^{232}Th/^{204}Pb$ ratios may me either measured or calculated.

$$(^{208}Pb/^{204}Pb)^{54\ Ma} = (^{208}Pb/^{204}Pb)_{measured} - {}^{232}Th/^{204}Pb * (EXP(\lambda_{Th\rightarrow Pb}*54\ Ma) - 1)$$

Appendix 4.1. Control analyses of isotopic ratios on the standards NBS 981, NBS 987 and J&M during MC-ICP-MS analyses of dissolved rock samples (as shown in Table 4.4) at the Department of Earth Sciences, Durham University.

Ratios	**NBS 981** $^{206}Pb/^{204}Pb$	**NBS 981** $^{207}Pb/^{204}Pb$	**NBS 981** $^{208}Pb/^{204}Pb$	**NBS 987** $^{87}Sr/^{86}Sr$	**J&M** $^{143}Nd/^{144}Nd$
Expected	16.9405	15.4963	36.7219	0.71024	0.51111
Average	16.940	15.497	36.718	0.71027	0.51112
St.Dev.	0.002	0.002	0.006	0.0000155	0.0000136

Appendix 5

Results from geochemical modelling

Appendix 5.1. Results of 15% 'modal melting' of selected basement samples from NW Britain, Rockall and E Greenland as modelled in **Fig. 4.19**.

Sample	[a]Plag	[a]Qtz	[a]Opx	Rb	K_2O	Th	Nb	Rb/K_20	Th/Nb
KS19A	~55	~40	~5	[b]38	[b]0.96	[b]5.19	[b]7.00	[b]39.58	[b]0.74
				[c]192	[c]4.09	[c]31.79	[c]42.13	[c]46.86	[c]0.75
KS60	~55	~40	~5	[b]28	[b]1.66	[b]31.30	[b]20.00	[b]16.87	[b]1.57
				[c]153	[c]8.25	[c]178.91	[c]103.21	[c]18.53	[c]1.73
B	~60	~10	~30	[b]34	[b]1.45	[b]3.65	[b]8.00	[b]23.45	[b]0.46
				[c]123	[c]6.01	[c]19.31	[c]41.10	[c]20.46	[c]0.47
E	~55	~40	~5	[b]160	[b]4.62	[b]8.75	[b]16.00	[b]34.63	[b]0.55
				[c]808	[c]19.70	[c]53.60	[c]96.30	[c]41.00	[c]0.56
P42	~55	~40	~5	[b]101	[b]4.20	[b]3.99	[b]4.00	[b]24.05	[b]1.00
				[c]551	[c]20.87	[c]24.44	[c]24.07	[c]26.41	[c]1.02

[a]Residual phases used in the calculations with numbers in each column representing percentages of residual minerals. [b]Measured elemental concentrations/ratios in basement samples. [c]Calculated elemental concentrations/ratios from 15% modal melting.

Appendix 5.2. Results of 4.5%, 7-8% and 23% modal melting respectively of a fertile spinel lherzolite (Average of samples 1 to 5, Lesnov et al., 2009) as modelled in **Fig. 4.24a**.

Sample	[a]Ol	[a]Qpx	La	Ce	Nd	Sm	Eu	Gd	Dy	Er	Yb
$1\text{-}5^{4.5\%}$	~76	~24	[b]3.19	[b]3.06	[b]2.94	[b]2.51	[b]2.21	[b]2.50	[b]2.19	[b]2.13	[b]2.05
			[c]60.60	[c]56.12	[c]51.82	[c]41.02	[c]40.19	[c]35.10	[c]25.32	[c]20.18	[c]15.37
$1\text{-}5^{7\text{-}8\%}$	~84	~16	[b]3.19	[b]3.06	[b]2.94	[b]2.51	[b]2.21	[b]2.50	[b]2.19	[b]2.13	[b]2.05
			[c]29.82	[c]28.34	[c]26.86	[c]22.86	[c]21.96	[c]21.05	[c]16.97	[c]15.08	[c]12.82
$1\text{-}5^{23\%}$	~84	~16	[b]3.19	[b]3.06	[b]2.94	[b]2.51	[b]2.21	[b]2.50	[b]2.19	[b]2.13	[b]2.05
			[c]13.52	[c]12.93	[c]12.34	[c]10.45	[c]10.26	[c]10.16	[c]8.59	[c]8.04	[c]7.28

[a]Residual mineral phases used in the calculations with numbers in each column representing percentages of residual minerals. [b]Measured elemental concentrations in spinel lherzolite (Lesnov et al., 2009) normalised to chondrite values of Nakamura (1974). [c]Calculated elemental concentrations from partial melting normalised to chondrite values of Nakamura (1974). Only two decimals are shown in this table while six decimals were used in the actual calculations/figure. For convenience, only olivine and orthopyroxene were used as residual phases in the calculations that resulted in the data shown in this table, but the inclusion of small amounts of clinopyroxene and spinel as additional residual phases could yield broadly similar results.

Appendix 5.3. Results of 7% and 8% modal melting respectively of the average of a depleted MORB mantle (Workman and Hart, 2005) as modelled in **Fig. 4.24b**.

Sample	[a]Ol	[a]Qpx	La	Ce	Nd	Sm	Eu	Gd	Dy	Er	Yb
$DMM^{7\%}$	~84	~16	[b]0.58	[b]0.64	[b]0.92	[b]1.18	[b]1.25	[b]1.30	[b]1.47	[b]1.55	[b]1.66
			[c]7.55	[c]8.11	[c]11.58	[c]14.25	[c]15.07	[c]14.51	[c]14.75	[c]13.71	[c]12.61
$DMM^{8\%}$	~84	~16	[b]0.58	[b]0.64	[b]0.92	[b]1.18	[b]1.25	[b]1.30	[b]1.47	[b]1.55	[b]1.66
			[c]4..54	[c]4.98	[c]7.32	[c]9.63	[c]11.19	[c]13.20	[c]13.63	[c]12.87	[c]10.21

[a]Residual mineral phases used in the calculations with numbers in each column representing percentages of residual minerals. [b]Measured elemental concentrations in DMM (Workman and Hart, 2005) normalised to chondrite values of Nakamura (1974). [c]Calculated elemental concentrations from partial melting normalised to chondrite values of Nakamura (1974). Only two decimals are shown in this table while six decimals were used in the actual calculations/figure. For convenience, only olivine and orthopyroxene are displayed as residual phases in this table while ≤ 2% spinel was used as an additional residual phase in the actual calculations.

Appendix 5.4. Results of 3.5% modal melting of a depleted spinel lherzolite (Sample ETR3, Rampone et al., 2004) mixed with 10% and 20% material similar to sill sample 08-JSVS-22 (Table 4.2) respectively as modelled in **Fig. 4.24c**.

Sample	[a]Ol	[a]Qpx	La	Ce	Nd	Sm	Eu	Gd	Dy	Er	Yb
ETR3+10%	~84	~16	[b]0.05	[b]0.04	[b]0.26	[b]0.58	[b]0.66	[b]0.86	[b]1.12	[b]1.09	[b]1.14
			[c]4.16	[c]3.89	[c]8.30	[c]13.31	[c]14.44	[c]16.06	[c]16.66	[c]13.51	[c]11.44
ETR3+20%	~84	~16	[b]0.05	[b]0.04	[b]0.26	[b]0.58	[b]0.66	[b]0.86	[b]1.12	[b]1.09	[b]1.14
			[c]7.35	[c]7.01	[c]10.95	[c]14.64	[c]15.30	[c]16.53	[c]16.37	[c]13.24	[c]11.38

[a]Residual mineral phases used in the calculations with numbers in each column representing percentages of residual minerals. [b]Measured elemental concentrations in depleted spinel lherzolite (Rampone et al., 2004) normalised to chondrite values of Nakamura (1974). [c]Calculated elemental concentrations from partial melting of depleted spinel lherzolite mixed with more enriched material normalised to chondrite values of Nakamura (1974). Only two decimals are shown in this table while six decimals were used in the actual calculations/figure. For convenience, only olivine and orthopyroxene are displayed as residual phases in this table while ≤ 2% spinel was used as an additional residual phase in the actual calculations.

Appendix 5.5.i. Results of partial melting calculations of a moderately fertile mantle (Lesnov et al., 2009) as modelled in trend i of **Fig. 4.25**.

Ce	Sm	Yb	$(Ce)_N$	$(Sm)_N$	$(Yb)_N$	$(Ce/Sm)_N$	Melt %
140.17	21.79	5.96	162.05	107.33	27.09	1.51	1
91.96	15.33	5.30	106.32	75.51	24.11	1.41	2
68.43	11.82	4.78	79.11	58.24	21.72	1.36	3
54.49	9.62	4.35	62.99	47.40	19.76	1.33	4
45.26	8.11	3.99	52.33	39.96	18.13	1.31	5
31.81	5.83	3.30	36.77	28.70	15.02	1.28	7.5
24.52	4.55	2.82	28.34	22.39	12.82	1.27	10
16.81	3.16	2.18	19.43	15.56	9.92	1.25	15
12.79	2.42	1.78	14.79	11.92	8.09	1.24	20
10.32	1.96	1.50	11.93	9.66	6.83	1.24	25
8.65	1.65	1.30	10.00	8.12	5.91	1.23	30
5.25	1.01	0.84	6.07	4.96	3.84	1.22	50
2.65	0.51	0.45	3.06	2.51	2.05	1.22	100

Residual mineralogy fertile lherzolite: 84% Ol. + 16% Opx. Lowermost row shows initial values. Normalising values from Nakamura (1974).

Appendix 5.5.ii. Results of partial melting calculations of a moderately fertile mantle (Lesnov et al., 2009) as modelled in trend ii of **Fig. 4.25**.

Ce	Sm	Yb	$(Ce)_N$	$(Sm)_N$	$(Yb)_N$	$(Ce/Sm)_N$	Melt %
132.87	19.00	4.44	153.61	93.58	20.19	1.64	1
88.80	13.91	4.08	102.66	68.50	18.53	1.50	2
66.68	10.97	3.77	77.09	54.02	17.12	1.43	3
53.38	9.05	3.50	61.71	44.60	15.91	1.38	4
44.51	7.71	3.27	51.45	37.97	14.86	1.36	5
31.44	5.62	2.81	36.35	27.69	12.76	1.31	7.5
24.30	4.42	2.46	28.10	21.79	11.18	1.29	10
16.72	3.10	1.97	19.32	15.28	8.96	1.26	15
12.74	2.39	1.64	14.73	11.76	7.47	1.25	20
10.29	1.94	1.41	11.90	9.56	6.41	1.24	25
8.63	1.64	1.23	9.98	8.05	5.61	1.24	30
5.25	1.00	0.82	6.07	4.94	3.75	1.23	50
2.65	0.51	0.45	3.06	2.51	2.05	1.22	100

Residual mineralogy fertile lherzolite: 76% Ol. + 24% Opx. Lowermost row shows initial values. Normalising values from Nakamura (1974).

Appendix 5.5.iii. Results of partial melting calculations of a moderately fertile mantle (Lesnov et al., 2009) as modelled in trend iii of **Fig. 4.25**.

Ce	Sm	Yb	$(Ce)_N$	$(Sm)_N$	$(Yb)_N$	$(Ce/Sm)_N$	Melt %
116.25	11.42	4.00	134.39	56.25	18.20	2.39	1
81.13	9.39	3.71	93.79	46.25	16.85	2.03	2
62.30	7.97	3.45	72.02	39.28	15.69	1.83	3
50.57	6.93	3.23	58.46	34.13	14.68	1.71	4
42.55	6.13	3.04	49.19	30.17	13.80	1.63	5
30.48	4.75	2.64	35.23	23.39	11.98	1.51	7.5
23.74	3.88	2.33	27.44	19.10	10.59	1.44	10
16.46	2.84	1.89	19.03	13.98	8.60	1.36	15
12.60	2.24	1.59	14.57	11.02	7.23	1.32	20
10.20	1.85	1.37	11.80	9.09	6.24	1.30	25
8.57	1.57	1.21	9.91	7.74	5.49	1.28	30
5.23	0.99	0.82	6.05	4.85	3.71	1.25	50
2.65	0.51	0.45	3.06	2.51	2.05	1.22	100

Residual mineralogy fertile lherzolite: 76% Ol. + 20% Opx. + 4% Cpx. Lowermost row shows initial values. Normalising values from Nakamura (1974).

Appendix 5.5.v. Results of partial melting calculations of the average of a moderately depleted mantle (Workman and Hart, 2005) as modelled in trend v of **Fig. 4.25**.

Ce	Sm	Yb	$(Ce)_N$	$(Sm)_N$	$(Yb)_N$	$(Ce/Sm)_N$	Melt %
29.09	10.21	4.83	33.63	50.30	21.95	0.67	1
19.09	7.18	4.30	22.07	35.37	19.55	0.62	2
14.20	5.54	3.88	16.42	27.29	17.64	0.60	3
11.31	4.51	3.53	13.08	22.22	16.05	0.59	4
9.39	3.80	3.23	10.86	18.72	14.68	0.58	5
6.60	2.73	2.68	7.63	13.45	12.18	0.57	7.5
5.09	2.13	2.29	5.88	10.49	10.41	0.56	10
3.49	1.48	1.77	4.03	7.29	8.05	0.55	15
2.65	1.13	1.44	3.06	5.57	6.55	0.55	20
2.14	0.92	1.22	2.47	4.53	5.55	0.55	25
1.80	0.77	1.05	2.08	3.79	4.77	0.55	30
1.09	0.47	0.68	1.26	2.32	3.09	0.54	50
0.55	0.24	0.37	0.64	1.18	1.66	0.54	100

Residual mineralogy depleted lherzolite: 84% Ol. + 16% Opx. Lowermost row shows initial values. Normalising values from Nakamura (1974).

Appendix 5.5.vi. Results of partial melting calculations of the average of a moderately depleted mantle (Workman and Hart, 2005) as modelled in trend vi of **Fig. 4.25**.

Ce	Sm	Yb	$(Ce)_N$	$(Sm)_N$	$(Yb)_N$	$(Ce/Sm)_N$	Melt %
8.99	4.30	3.70	10.39	21.18	16.82	0.49	1
7.78	3.67	3.39	8.99	18.08	15.41	0.50	2
6.86	3.20	3.12	7.93	15.76	14.18	0.50	3
6.13	2.84	2.90	7.09	13.99	13.18	0.51	4
5.55	2.55	2.70	6.42	12.56	12.27	0.51	5
4.48	2.03	2.31	5.18	10.00	10.50	0.52	7.5
3.75	1.69	2.02	4.34	8.33	9.18	0.52	10
2.84	1.26	1.61	3.28	6.21	7.32	0.53	15
2.28	1.01	1.34	2.64	4.98	6.09	0.53	20
1.90	0.84	1.15	2.20	4.14	5.23	0.53	25
1.64	0.72	1.01	1.90	3.55	4.59	0.53	30
1.05	0.46	0.67	1.21	2.27	3.05	0.54	50
0.55	0.24	0.37	0.64	1.18	1.66	0.54	100

Residual mineralogy depleted lherzolite: 83% Ol. + 15% Opx. + 2Sp. Lowermost row shows initial values. Normalising values from Nakamura (1974).

Appendix 5.5.vii. Results of partial melting calculations of a depleted mantle (Rampone et al., 2004) as modelled in trend vii of **Fig. 4.25**.

Ce	Sm	Yb	$(Ce)_N$	$(Sm)_N$	$(Yb)_N$	$(Ce/Sm)_N$	Melt %
2.01	5.04	3.31	2.32	24.83	15.05	0.094	1
1.32	3.55	2.95	1.52	17.47	13.39	0.087	2
0.98	2.74	2.65	1.13	13.47	12.07	0.084	3
0.78	2.23	2.42	0.90	10.97	10.98	0.082	4
0.65	1.88	2.22	0.75	9.25	10.07	0.081	5
0.46	1.35	1.84	0.53	6.64	8.34	0.079	7.5
0.35	1.05	1.57	0.41	5.18	7.12	0.078	10
0.24	0.73	1.21	0.28	3.60	5.51	0.077	15
0.18	0.56	0.99	0.21	2.76	4.49	0.077	20
0.15	0.45	0.83	0.17	2.23	3.79	0.077	25
0.12	0.38	0.72	0.14	1.88	3.28	0.076	30
0.08	0.23	0.47	0.09	1.15	2.13	0.076	50
0.04	0.12	0.25	0.04	0.58	1.14	0.076	100

Residual mineralogy depleted lherzolite: 84% Ol. + 16% Opx. Lowermost row shows initial values. Normalising values from Nakamura (1974).

Appendix 5.5.viii. Results of partial melting calculations of a depleted mantle (Rampone et al., 2004) as modelled in trend viii of **Fig. 4.25**.

Ce	Sm	Yb	$(Ce)_N$	$(Sm)_N$	$(Yb)_N$	$(Ce/Sm)_N$	Melt %
1.51	1.94	2.26	1.75	9.57	10.28	0.183	1
1.09	1.68	2.09	1.26	8.27	9.50	0.152	2
0.85	1.48	1.94	0.98	7.29	8.84	0.134	3
0.70	1.32	1.82	0.80	6.51	8.26	0.123	4
0.59	1.20	1.71	0.68	5.89	7.76	0.116	5
0.43	0.96	1.48	0.49	4.75	6.73	0.104	7.5
0.33	0.81	1.31	0.39	3.98	5.94	0.097	10
0.23	0.61	1.06	0.27	3.00	4.81	0.090	15
0.18	0.49	0.89	0.21	2.41	4.04	0.086	20
0.15	0.41	0.77	0.17	2.02	3.48	0.083	25
0.12	0.35	0.67	0.14	1.73	3.06	0.082	30
0.07	0.22	0.45	0.09	1.11	2.06	0.078	50
0.04	0.12	0.25	0.04	0.58	1.14	0.076	100

Residual mineralogy depleted lherzolite: 80% Ol. + 12% Opx. + 8% Cpx. Lowermost row shows initial values. Normalising values from Nakamura (1974).

Appendix 5.5.ix. Results of partial melting calculations of a depleted mantle (Rampone et al., 2004) as modelled in trend ix of **Fig. 4.25**.

Ce	Sm	Yb	$(Ce)_N$	$(Sm)_N$	$(Yb)_N$	$(Ce/Sm)_N$	Melt %
1.52	1.87	1.13	1.76	9.21	5.14	0.191	1
1.09	1.63	1.09	1.26	8.01	4.96	0.157	2
0.85	1.44	1.06	0.98	7.08	4.80	0.139	3
0.70	1.29	1.02	0.81	6.35	4.64	0.127	4
0.59	1.17	0.99	0.68	5.76	4.50	0.119	5
0.43	0.95	0.92	0.49	4.66	4.17	0.106	7.5
0.33	0.80	0.86	0.39	3.92	3.89	0.099	10
0.23	0.60	0.75	0.27	2.97	3.43	0.091	15
0.18	0.49	0.67	0.21	2.39	3.07	0.087	20
0.15	0.41	0.61	0.17	2.00	2.77	0.084	25
0.12	0.35	0.56	0.14	1.72	2.53	0.082	30
0.07	0.22	0.41	0.09	1.10	1.87	0.078	50
0.04	0.12	0.25	0.04	0.58	1.14	0.076	100

Residual mineralogy depleted lherzolite: 80% Ol. + 11% Opx. + 8% Cpx. + 1% Grt. Lowermost row shows initial values. Normalising values from Nakamura (1974).

Appendix 5.6.i. Results of partial melting calculations of a fertile mantle (Lesnov et al., 2009) as modelled in trend i of **Fig. 4.26**.

Zr	Y	TiO_2	Y/TiO_2	Melt %
309.33	111.04	5.18	21.44	1
258.16	92.11	4.22	21.83	2
221.52	78.69	3.56	22.11	3
193.99	68.68	3.08	22.32	4
172.54	60.93	2.71	22.48	5
135.18	47.53	2.09	22.76	7.5
111.12	38.96	1.70	22.93	10
81.95	28.63	1.24	23.15	15
64.91	22.63	0.97	23.27	20
53.73	18.71	0.80	23.35	25
45.84	15.95	0.68	23.41	30
28.88	10.03	0.43	23.54	50
15.00	5.20	0.22	23.64	100

Residual mineralogy fertile lherzolite: 84% Ol. + 16% Opx. Lowermost row shows initial values.

Appendix 5.6.ii. Results of partial melting calculations of a fertile mantle (Lesnov et al., 2009) as modelled in trend ii of **Fig. 4.26**.

Zr	Y	TiO_2	Y/TiO_2	Melt %
242.73	86.25	4.51	19.13	1
210.46	74.52	3.77	19.79	2
185.76	65.59	3.23	20.28	3
166.25	58.58	2.83	20.67	4
150.45	52.92	2.52	20.99	5
121.56	42.63	1.98	21.56	7.5
101.98	35.69	1.63	21.94	10
77.13	26.92	1.20	22.43	15
62.02	21.61	0.95	22.72	20
51.86	18.05	0.79	22.92	25
44.56	15.50	0.67	23.06	30
28.51	9.90	0.42	23.38	50
15.00	5.20	0.22	23.64	100

Residual mineralogy fertile lherzolite: 76% Ol. + 24% Opx. Lowermost row shows initial values.

Appendix 5.6.iii. Results of partial melting calculations of a fertile mantle (Lesnov et al., 2009) as modelled in trend iii of **Fig. 4.26**.

Zr	Y	TiO_2	Y/TiO_2	Melt %
270.46	44.33	3.03	14.62	1
230.76	41.19	2.69	15.34	2
201.23	38.48	2.41	15.97	3
178.39	36.10	2.19	16.52	4
160.22	33.99	2.00	17.00	5
127.69	29.67	1.65	18.00	7.5
106.14	26.32	1.40	18.77	10
79.35	21.48	1.08	19.89	15
63.36	18.14	0.88	20.66	20
52.74	15.70	0.74	21.22	25
45.16	13.83	0.64	21.65	30
28.68	9.38	0.41	22.67	50
15.00	5.20	0.22	23.64	100

Residual mineralogy fertile lherzolite: 76% Ol. + 16% Opx. + 8% Cpx. Lowermost row shows initial values.

Appendix 5.6.iv. Results of partial melting calculations of a fertile mantle (Lesnov et al., 2009) as modelled in trend iv of **Fig. 4.26**.

Zr	Y	TiO_2	Y/TiO_2	Melt %
237.03	29.53	3.51	8.41	1
206.20	28.19	3.05	9.24	2
182.47	26.98	2.70	10.01	3
163.64	25.86	2.42	10.70	4
148.33	24.83	2.19	11.35	5
120.21	22.59	1.77	12.75	7.5
101.05	20.72	1.49	13.92	10
76.63	17.77	1.13	15.77	15
61.71	15.56	0.91	17.15	20
51.66	13.84	0.76	18.23	25
44.42	12.46	0.65	19.09	30
28.47	8.91	0.42	21.32	50
15.00	5.20	0.22	23.64	100

Residual mineralogy fertile lherzolite: 76% Ol. + 19% Opx. + 4% Cpx. + 1% Grt. Lowermost row shows initial values.

Appendix 5.7. Results of plagioclase fractionation/accumulation calculations from/to a melt with a Sr/Nb versus Eu/Eu* ratio intermediate between high/low-TiO_2 sills as modelled in **Fig. 4.27**.

Sr	Nb	Sr/Nb	$(Sm)_N$	$(Eu)_N$	$(Gd)_N$	$(Eu/Eu^*)_N$	
202.5	4.50	45.00	16.13	15.55	15.00	1.00	Initial
187.8	4.99	37.67	17.80	16.68	16.50	0.97	-10% Plag
172.6	5.59	30.89	19.87	18.03	18.35	0.94	-20% Plag
216.8	4.10	52.85	14.76	14.60	13.76	1.02	+10% Plag
230.7	3.77	61.19	13.61	13.79	12.72	1.05	+20% Plag

Uppermost row shows starting values. Normalising values from Nakamura (1974).

Appendix 5.8. Results of 20 wt% plagioclase fractionation and 20 wt% plagioclase accumulation from sample 08-JSVS-22 and to sample 07-JSS-40 respectively as modelled in **Fig. 4.28**.

Sample	[a]Plag	La	Ce	Nd	Sm	Eu	Gd	Dy	Er	Yb
08-JSVS-22	-20 %	[b] 25.75	[b]25.02	[b]26.23	[b]22.28	[b]20.25	[b]19.18	[b]14.68	[b]11.67	[b]11.05
		[c] 30.85	[c]30.52	[c]32.14	[c]27.39	[c]22.99	[c]23.62	[c]18.10	[c]14.44	[c]13.64
07-JSS-40	+20 %	[b]11.00	[b]10.11	[b]10.14	[b]8.73	[b]8.95	[b]8.16	[b]7.37	[b]6.88	[b]6.95
		[c]9.33	[c]8.51	[c]8.52	[c]7.34	[c]7.78	[c]6.85	[c]6.18	[c]5.78	[c]5.86

[a]Active mineral phase used in the calculations with numbers in each column representing fractionating and accumulating percentages. [b]Measured elemental concentrations in actual sill samples normalised to chondrite values of Nakamura (1974). [c]Calculated elemental concentrations from plagioclase fractionation and accumulation normalised to chondrite values of Nakamura (1974).

Appendix 5.9. Results of partial melting calculations in addition to plagioclase fractionation/accumulation calculations as modelled in **Fig. 4.27**.

Nb	**Ta**	**Th**	**Eu**	**Sr**	
0.85	0.04	0.038	0.17	17.0	Initial (partial melting)
17.31	0.79	0.74	1.75	299.6	4.8% melt
3.027	0.14	0.13	0.54	59.7	28% melt
9.00	0.81		2.00	325.0	Initial (Plag fractionation)
11.18	0.99		2.27	273.9	-20% Plag
4.00	0.50		1.65	260.0	Initial (Plag accumulation)
3.27	0.41		1.49	296.2	+20% Plag

Appendix 5.10. Results of the modelling shown in **Fig. 4.31**.

Nb	Ta	La	Ce	Nb	Ta	La	Ce
[a]1.19	[a]0.76	[a]17.18	[a]40.76	[e]11.80	[e]9.51	[e]13.83	[e]13.07
[b]23.34	[b]18.54	[b]25.01	[b]22.96	[f]14.63	[f]12.20	[f]16.61	[f]15.90
[c]11.80	[c]9.51	[c]13.83	[c]13.07	[g]9.87	[g]8.29	[g]11.91	[g]11.13
[d]5.93	[d]4.88	[d]7.31	[d]7.02				

Fig. 4.31a. [a]Elements representing a moderately fertile mantle normalised to primitive mantle (Sun and McDonough, 1989). [b]Mantle normalised values from 5% partial melting of moderately fertile mantle with residual mineral assemblage: 76% Ol + 16% Opx + 8% Cpx. [c]Mantle normalised values from 10% partial melting of moderately fertile mantle with residual mineral assemblage: 76% Ol + 16% Opx + 8% Cpx. [d]Mantle normalised values from 20% partial melting of moderately fertile mantle with residual mineral assemblage: 76% Ol + 16% Opx + 8% Cpx.

Fig. 4.31b. [e]Elements representing a typical basalt (from [c]) normalised to primitive mantle (Sun and McDonough, 1989). [f]Mantle normalised values representing 20 wt% plagioclase fractionation from typical basalt. [f]Mantle normalised values representing 20 wt% plagioclase accumulation to typical basalt.

Subsidiary matter in support of candidate

Geological Magazine 2009

Journal of the Geological Society, London 2011

Geological Magazine

Geol. Mag. **146** (3), *2009, pp. 309–325. © 2009 Cambridge University Press*
doi:10.1017/S0016756809006347 *Printed in the United Kingdom*

The onset of the North Atlantic Igneous Province in a rifting perspective

J. HANSEN*, D. A. JERRAM*, K. J. W. MCCAFFREY* & S. R. PASSEY‡
*Department of Earth Sciences, Durham University, South Road, DH1 3LE, Durham, United Kingdom
‡Jarðfeingi (Faroese Earth and Energy Directorate), Brekkutún 1, P.O. Box 3059, FO-110, Tórshavn, Faroe Islands

(*Received* 25 March 2008; *accepted* 17 February 2009; First published online 25 March 2009)

<u>One reviewer commented:</u>

This is a review manuscript of the processes that are involved in the formation of the North Atlantic Igneous Province. Despite the many reviews that have been written about the NAIP, these authors have actually managed to write the review from an original point of view that really adds value to it. I enjoyed reading the manuscript, and there are some very nice compilations included.

Journal of the Geological Society, London

Journal of the Geological Society, London, Vol. 168, 2011, pp. 159–178.
doi: 10.1144/0016-76492010-012.159

Early Cenozoic saucer-shaped sills of the Faroe Islands: an example of intrusive styles in basaltic lava piles

J. HANSEN[1]*, D. A. JERRAM[1], K. J. W. MCCAFFREY[1] & S. R. PASSEY[2]
[1]Department of Earth Sciences, Durham University, South Road, Durham DH1 3LE, Durham, UK
[2]Jarðfeingi (Faroese Earth and Energy Directorate), Brekkutún 1, P.O. Box 3059, FO-110, Tórshavn, Faroe Islands
*Corresponding author (e-mail: jogvan.hansen@durham.ac.uk or jogvanha@post.olivant.fo)

Received 15 January 2010; revised typescript accepted 9 August 2010.
Scientific editing by Brian Bell.

<u>One reviewer commented:</u>

The paper provides a very good description of saucer-shaped sills in the Faroe Islands. These sills are intruded into a thick basaltic lava pile, which has rarely been described in the literature and as such the paper offers new and important insight into igneous emplacement into non-sedimentary host-rocks.